Investigating the Shear Strength of Infilled Rock Discontinuity Replicas

Matthew Rapa

A dissertation submitted to the Faculty for the Built Environment, University of Malta in part fulfilment of the requirements for the attainment of the degree of Master of Engineering (Structural Engineering)

July 2025

L-Università ta' Malta

FACULTY/~~INSTITUTE/CENTRE/SCHOOL~~ Built Environment

DECLARATIONS BY POSTGRADUATE STUDENTS

(a) Authenticity of Dissertation

I hereby declare that I am the legitimate author of this Dissertation and that it is my original work.

No portion of this work has been submitted in support of an application for another degree or qualification of this or any other university or institution of higher education.

I hold the University of Malta harmless against any third party claims with regard to copyright violation, breach of confidentiality, defamation and any other third party right infringement.

(b) Research Code of Practice and Ethics Review Procedures

I declare that I have abided by the University's Research Ethics Review Procedures. Research Ethics & Data Protection form code BEN-2025-00092.

As a Master's student, as per Regulation 77 of the General Regulations for University Postgraduate Awards 2021, I accept that should my dissertation be awarded a Grade A, it will be made publicly available on the University of Malta Institutional Repository.

Acknowledgements

I would like to express my gratitude towards my supervisor Dr. Adrian Mifsud B.E.&A. (Hons.), M.Sc.(Lon), Ph.D. (Melit.), DIC, Eur.Ing. Perit and co-supervisor Perit Christian Schembri B.E.&(Hons.), M.Sc. (Lond.), DIC for their constant guidance and support through this dissertation.

I would also like to show my sincere appreciation towards Mr Nicholas Azzopardi A.M.I.C.T. (UK), A.I.A.T. and Mr. Alex Falzon A.I.A.T.(UK), Tech. ICT (UK), for their assistance in the Civil Engineering Laboratories. Furthermore, I would like to thank Solidbase Laboratories for kindly providing access to their laboratory facilities and supporting me with their resources. I am also deeply gratefully for the technicians and engineers at the Department of Mechanical Engineering for their precise fabrication of components used throughout this dissertation.

To my family and friends – thanks for always showing me your unwavering love and support, which has been a guiding light not only for this dissertation but for all my studies.

I dedicate this dissertation to the memory of my friend, Julian, who has given me the perseverance to overcome every obstacle. His memory continues to guide and inspire me.

Title:

Investigating the Shear Strength of Infilled Rock Discontinuity Replicas

Abstract:

Understanding shear strength of discontinuities is essential when assessing the stability of excavations or slopes in fractured rock masses. Challenges are seen in Malta where clay-filled joints are present in fractured limestone formations.

This study investigates the shear strength of infilled rock discontinuities by replicating these joints in a controlled laboratory setup. The focus is placed on the effect of Blue Clay, used as the infill material, on the mechanical behaviour of the joint. To isolate the influence of clay infill thickness, the study uses 3d printed moulds which were used to cast plaster specimens of consistent geometry.

Test were conducted on specimens with different thicknesses. Results indicate that infill thickness significantly influences shear strength. The smallest clay volume (1mm) retained asperity interlock, leading to higher peak shear stress. In contrast, shearing the clay alone showed the lowest strength.

These findings demonstrate how geometry and infill material affect shear response, and the relevance of infill thickness in predicting failure mechanisms in real life scenarios.

Keywords:

Shear Strength, Rock Discontinuities, Infill Properties, Blue Clay, Lower Globigerina Limestone

Table of Contents

List of Tables

Glossary

CHILE	Continuous Homogeneous Isotropic Linearly-Elastic
DIANE	Discontinuous Inhomogeneous Anisotropic Not-Elastic
LCL	Lower Coralline Limestone
UGL	Upper Globigerina Limestone
LGL	Lower Globigerina Limestone
MGL	Middle Globigerina Limestone
UCS	Unconfined Compressive Strength
REV	Representative Elementary Volume
RSR	Rock Structure Rating
RMR	Rock Mass Rating
RQR	Rock Quality Designation
GSI	Geological Strength Index
CNS	Constant Normal Stiffness
CNL	Constant Normal Loading
NSD	Normalised Shear Drop
LVDT	Linear Variable Digital Transformer
ISRM	International Society of Rock Mechanics
OCR	Over Consolidation Ratio
JRC	Joint Roughness Coefficient
JCS	Joint Compressive Strength

F	Force
A	Area
σ	Stress
σ_c	UCS
σ_n	Normal Stress
$\sigma_{n'}$	Effective Normal Stress
$\sigma_{1'}$	Maximum Principal Effective Stress
$\sigma_{3'}$	Minimum Principal Effective Stress
$\sigma_{p'}$	Past Vertical Effective Stress
$\sigma_{v'}$	Current Vertical Effective Stress
σ_{cd}	Uniaxial Compressive Strength of diameter d
σ_{ci}	UCS
c	Cohesive Strength
ϕ	Friction Angle
ϕ_b	Friction Angle
ϕ_R	Residual Friction Angle
$\phi_{s\text{-}RM}$	Friction Angle of Soil-Rock Model
ϕ_{sf}	Friction Angle of Sand Files
$\Delta\phi$	Increase in Friction Angle
i	Angle of Inclination
τ	Shear Stress
d_n	Dilation Angle
m_b	Hoeke Brown constant
s	Constant from Hoeke Brown referring to degree of interlocking
a	Constant from Hoeke Brown referring to shape of failure envelope
m_i	Coefficient of determination
D	Degree of blasting
t/a	Thickness/ Height of asperity
α	Constant of material in NSD
β	Constant of material in NSD
r	Rebound number for wet and fractured surfaces
R	Rebound number for dry surfaces
S	Constant relating to mean particle size
e	Void Ratio
V_v	Volume of voids
V_s	Volume of solid
V	Total Volume
V_w	Volume of water
n	Porosity

S	Degree of Saturation
I_p	Plasticity Index
w	Water Content
M_w	Mass of Water
Ms	Mass of Soil
δ	Peak Parameter

List of Figures

1. Introduction

1.1. Insight of Study

It is fundamentally important to understand how the ground behaves in any form of construction. It is important to understand the behaviour of the ground because this influences the design and behaviour of excavations and foundations. Rock, in particular, is peculiar because of its complex behaviour under stress. This behaviour can be understood from the CHILE-DIANE concept. The CHILE concept refers to continuous, homogenous, isotropic, linearly elastic. The DIANE concept refers to discontinuous, inhomogeneous, anisotropic and non-elastic. This concept highlights the multi-faceted nature of rock. Therefore, understanding the behaviour of rock is paramount both from its initial behaviour, often in the form of a rock wedges, and also for its long-term performance under loading and environmental considerations.

In Malta, the ground formation is dominated by weak, fractured sedimentary rocks, one of which is the Globigerina Limestone. The shear strength, particularly in its weathered or jointed state, is very much questioned in the preliminary stages of development. Within an excavation, a rock face is often exposed without any form of lateral confinement. The concern of potential instability of unsupported faces is heightened by the pace of local development, which demands quicker construction processes and timelines. This has unjustifiably limited the time for geotechnical assessment, increasing the risk and raising concerns whether the ground can support the loads imposed by new structures.

A significant challenge in Maltese geotechnical engineering is the presence of discontinuities. These are natural fractures that form planes of weakness, leading to the formation of wedges and blocks that in some cases, could potentially slide out of place, carrying with them the foundations of buildings next door. Therefore, the presence of these discontinuities must be thoroughly assessed. Different failure mechanisms must be identified and subsequently understood for mitigation purposes, typically through retaining embedded piles or bolting to keep potential wedges in place. The stability of the rock mass is dependent on the discontinuities that it contains. Some of the properties of the discontinuities include the infill material, infill thickness and roughness. The dissertation explores the different discontinuity properties which are present and how their shear strength parameters are affected.

The research presented focuses on weak and fractured rock which is typical for the Maltese Islands. Emphasis is given on the mechanical behaviour of discontinuities within Globigerina Limestone. While the study focuses on Globigerina Limestone, the findings are applicable to other weak types of rock with similar characteristics.

The objective is to understand how infill thickness and infill material, specifically Blue Clay, influence the shear strength of a discontinuity. This knowledge could then be applied in geotechnical engineering problems involving the stability of rock wedges, for example when designing or assessing the safety of an excavation.

1.2. Aims and Objectives of Dissertation:

The dissertation aims to investigate the shear strength developed across a rock discontinuity, specifically for the case when soil infill exists between the discontinuity faces. This situation often encountered locally, especially in the case of fissured weak rock, where the fissures have been infilled with surface soils such as clays and terrarossas over the millennia. Discontinuity infill generally consists of myriad materials of different mechanical characteristics, but behaviour is generally controlled by the presence of clays, especially if these are of high plasticity *(Hoek and Bray, 1981).* Locally, one such infill is a derivative of the Blue Clay stratum, a high plastic over consolidated marine clay that is often eroded and reworked as it is transported by sub-surface flow into the fissure's voids and cavities of the underlying layers of the stratigraphic sequence.

Discontinuities locally can also contain terrarossa, calcified deposits, weathered marl or fault gouge. The probable real-life scenario is that the Blue Clay is often mixed with a combination of these, such as Blue Clay mixed with fine particles of terrarossa *(Durn, 2003)*. This instance is probable near the interface of the Blue Clay layer with the underlying limestone. This occurs due to erosion and groundwater transport. Terrarossa is a reddish clay which is formed from the chemical weathering of limestone. This colour is a form of oxidation. In Malta, this is present in fractures and fissures which may be transported through percolating water which is trapped in discontinuities *(Durn, 2003).*

The shear strength plays a crucial role in understanding the stability of slopes, foundations and excavation, especially when there are discontinuities present. Estimating the shear strength of infilled discontinuities is very challenging. This is because of the complexity of analysing the interaction between the rock surfaces and the infill material, and because of the difficulty of sampling these to create appropriate and meaningful undisturbed test specimens. Contrasting this, clean rock joints are often analysed by inspecting and classifying their surface roughness. Several other variables such as infill thickness, moisture content and plasticity influence the failure surface *(Mokhtarian et al., 2024)*.

Testing the shear strength of infilled discontinuities is particularly difficult. This is because of the difficulty in replicating the discontinuity. In reality, the discontinuities are very rough, and other properties such as the infill material, vary considerably. The research aims to simplify these properties and isolate variables using physical models. Direct shear testing will be used in this research on discontinuity models. The testing procedure will consist of simulating Lower Globigerina Limestone through plaster-based rock models and Blue Clay infill of different thicknesses. The laboratory testing will study the shear strength, deformation characteristics and location of artificial failure planes created specifically for the purpose in the laboratory. One of the variables that influences shear resistance can therefore be investigated.

The proposed research therefore seeks to answer the following questions:

- How does infill thickness affect the shear strength of discontinuities?
- Where are the mechanisms of failure in the case of clay-infilled discontinuities?
- How does the interaction between asperities and clay influence joint shear behaviour?

1.3. Dissertation Outline

Literature Review

The literature of the dissertation is split up into 4 sub-chapters. The **first** section aims to give a background to Malta's stratigraphic sequence, highlighting the different rock formations with a focus on the strata that are relevant for this study. The **second** section aims to investigate how a typical rock mass is analysed from a quantitative and qualitative perspective, for the purposes of engineering classification and design. This delves into the differences between intact rock and the associated rock masses, and how these can be assessed. The **third** section describes about how the discontinuity can vary, even with the presence of water. It also describes how different researchers have quantified the interaction between infill materials and rock discontinuities. Lastly, the **fourth** section describes the difficulties present when testing.

Methodology

This chapter describes the approach taken to determine the possible effect of discontinuity infill on the shear characteristics of a rock-to-rock interface, in the laboratory. The equipment used, and the modifications and improvements made to it are described. It then highlights the procedure taken to simulate the local weak rocks using a man-made pourable material: Plaster of Paris, and the rationale adopted to simulate the characteristics of the discontinuities within. This chapter also describes the approach taken and the techniques used to simulate, create and prepare the discontinuity infill, prior to testing.

Results and Discussion

This chapter firstly presents the individual results. These results are then compared with one another. Following this, they are then compared to tests with no infill thickness and with infill thickness greater than the geometry of the asperities.

Conclusions

This last chapter provides an overview of the outcomes which have been found in the results.

Further Research

This section mentions the future studies which can be carried out based on the findings of this dissertation study.

2. Literature Review

The local context of the ground formation is described in this chapter. Firstly, it gives a general overview of how the Maltese archipelago and its stratigraphy was brought into being, highlighting how the location of the archipelago within the Mediterranean Sea has influenced its geology and geomorphology. A brief explanation of the different types of local rocks is given, followed by an introduction to the importance and significance of fractured rock to engineering problems. The existence and origin of these fissures is discussed, with reference to the inherent complexity in the related analytical processes required for engineering interventions.

The difference between rock mass and intact rock is an important concept in rock mechanics. Section 2.2 of this chapter explains the different ways in which a rock mass is analysed. This shows how different researchers have classified rock mass characteristics into quantitative data. The behaviour of rock masses is also discussed here and how its strength can vary based on each respective type of analysis.

Section 2.3 delves into understanding the properties of these discontinuities, which essentially define the rock mass. It investigates about how the intact material properties effect the strength parameters of rock mass, which gives an insight to what test results are of relevance to the related engineering problems.

Different researchers have developed different ways to quantify rock mass characteristics. The literature from Section 2.2 and 2.3 is merged and discussed in Section 2.3.2. Another insight to the strength of rock joints with infill materials is discussed in this section.

2.1. Malta's Stratigraphy

2.1.1. Description of Malta's different rock formations

Maltese rock is made up of five stratigraphic formations which were deposited in marine conditions in the Miocene era, between 5 and 30 million years ago *(ERA, 2025)*. The main formations are all carbonate sediments deposited in different bathymetric conditions, ranging from agitated shallow reefs teeming with life and exposed to bright sunlight, to dark and calm deep-sea conditions beneath several hundred metres of water *(ERA, 2025)*. The locations and order of the main formations can be seen on Figure 2.1 and Figure 2.2.

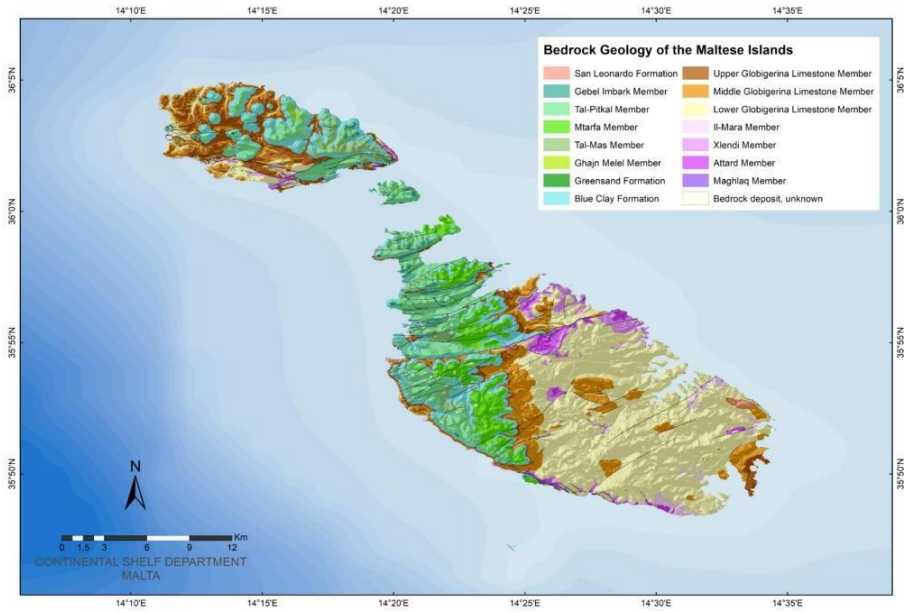

Figure 2.1 - The geological map of Malta

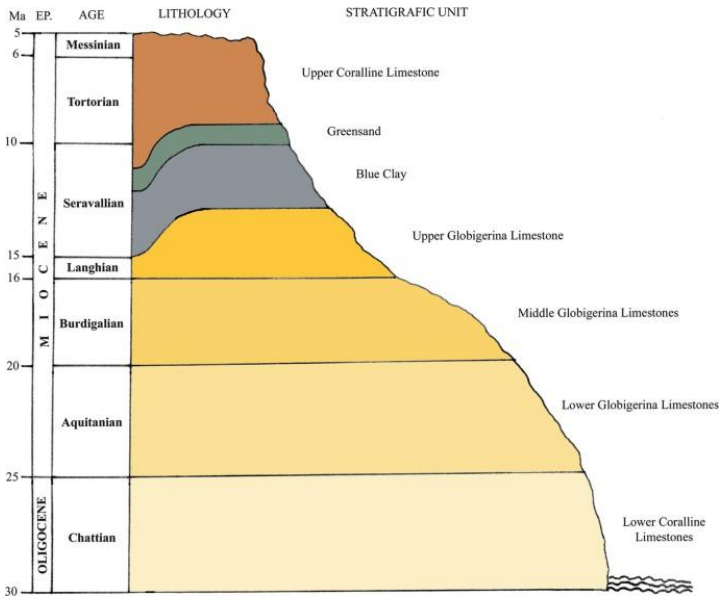

Figure 2.2 - The order of the Maltese rock formations from the youngest to the oldest

The oldest from these rocks is the Lower Coralline Limestone (LCL). It is made up of a hard, pale grey material. It is present in many areas locally including Kalkara, Fgura, Naxxar, Marsascala and in the cliffs of Gozo. This is a strong rock which can exhibit a very high uniaxial compressive strength, however this can vary considerably. LCL is heavily jointed in some areas. The resulting rock mass creates localised zones of weakness that are relevant to this study *(H.M. Pedley et al.,1976).*

The second oldest rock in Malta is the Globigerina Limestone. This geological formation outcrops in around 70% of the surface geology of the Maltese Islands. The shapes of the rock strata formed are very random and cause a very distinctive landscape across the islands *(ERA, 2025)*. It can be characterised as having yellow to grey-coloured outcrops, which vary in thickness across the Maltese archipelago. Globigerina Limestone is divided into 3 further rock formations, namely the Upper Globigerina Limestone, the Middle Globigerina Limestone and Lower Globigerina Limestone, and these members are further subdivided into facies which all have distinct geotechnical behaviour.

The Lower Globigerina Limestone dates back to the late Oligocene. This is normally a yellow-grey colour and it is a weak to moderately weak rock formation. It contains pre-existing fractures from tectonic processes. These can influence the behaviour of the rock during an excavation. This makes it very relevant to this study, with its UCS ranging from around 5 MPa to 15 MPa *(Gauci & Scerri, 2019*). The nature of the rock therefore allows it to fail along a weak plane. the understanding of this rock formation is crucial to slope and excavation assessments. Lower Globigerina Limestone is the “Franka” used in local construction *(Gauci & Scerri, 2019*).

The Middle Globigerina Limestone (MGL) lies stratigraphy between the Lower and Upper Globigerina Limestone layers. Middle Globigerina is finer and contains a small amount of clay *(Baldassini et al., 2015).* This contributes to its lower mechanical strength, rendering it inappropriate for structural construction.

Upper Globigerina Limestone (UGL) is pale yellow and grey coloured. From the different types of limestone, the LGL and MGL are particularly relevant to this research, however the Upper Globigerina Limestone may also influence the rock mass behaviour, especially because it is in contact with the overlying Blue Clay. This is commonly involved in discontinuities. Figure 2.3 shows Upper Globigerina Limestone in Malta.

Figure 2.3 - Upper Globigerina Limestone photographed in Marsaxlokk showing clear erosion

Blue Clay is found on top of the Upper Globigerina Limestone. An important characteristic is its impermeability *(H.M. Pedley et al.,1976)*. However, apart from this, it causes many building constraints because of its plastic properties. This causes it to expand when wet. This change in behaviour of clay causes several cracks and differential settlement in the local scene. The constant swelling and shrinking of Blue Clay causes an undesired ground formation for construction *(Gauci & Scerri, 2019*).

Greensands is known as the green rock when it is unweathered and orange when it is exposed. It is the thinnest rock formation and found mainly in Gozo (Figure 2.1).

Lastly, the youngest rock formation is the Upper Coralline Limestone. It can reach very large thicknesses (160m in Bingemma area) and exhibits similar chemical properties to Lower Coralline Limestone *(ERA, 2025).* The landslides and rock spreading which are present in the North-Western coast of Malta are associated with the UCL overlying Blue Clay. Over here, the clay is acting as a slip plane *(Mantovani et al., 2012)*. This only occurs as the Blue Clay is acting as a foundation for the UCL, making this occurrence only relevant for this rock formation.

From the above-mentioned rock formations, the Lower Globigerina Limestone is the most relevant rock formation for this study, together with the discontinuity infill comprised of Blue Clay. A brief overview of these rocks suggests that their Unconfined Compressive Strength (UCS) ranges are considerably weak. The degree of fracturing and infill varies considerably across the islands.

2.1.2. The geomorphology and structural geology of the Maltese islands.

The Maltese archipelago is located in the Middle of the Mediterranean Sea, 90km south of Sicily. It is made up of 3 main islands which are Malta, Gozo and Comino. The location of Malta is a relatively stable zone seismically, as it sits next to the Sicily Channel Rift Zone on the African Plate *(H.M. Pedley et al.,1976)*. Figure 2.4 shows this location below. This area is associated with the Pantelleria Rift System *(H.M. Pedley et al.,1976).* This system of faults has shaped the nature of Malta's stratigraphy through tectonic uplift and subduction.

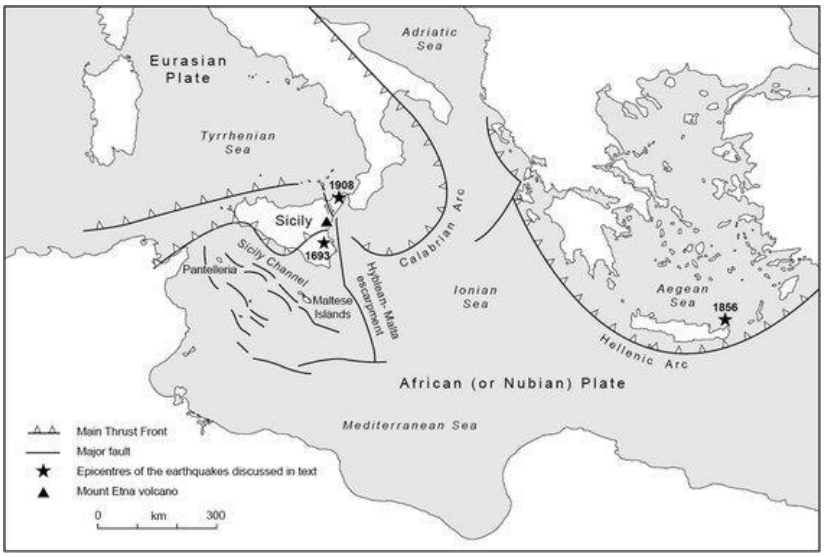

Figure 2.4 - Showing where Malta lies in relation to the tectonic plates (Gauci, 2018)

A prominent feature in Malta is the Great Fault. This is a fault which spans diagonally across the Maltese Islands from Fomm ir-Rih in the North-Western region of Malta to Madliena in the North-East of Malta *(H.M. Pedley et al.,1976)*. This is one of the primary causes of the changes in topography and stratigraphy in Malta *(H.M. Pedley et al.,1976).* In fact, the stratigraphy and terrain even change across short distances. These conditions can affect site-specific design and designs of excavations. This is very depending on the type of rock present in the location.

The tectonic setting combined with weak sedimentary rock has led to fissures in rock masses, that if poorly understood, lead to structural settlement and wedge failure. This has highlighted the importance of an engineering knowledge of the ground, within the construction industry, especially whilst considering the behaviour which is influenced through the discontinuities.

2.2. Rock Mass and Intact Rock

Intact Rock refers to the "perfect" rock sample which is clear of any imperfections within the specimen itself. This would be a homogenous, isotropic, continuous rock specimen *(Evert Hoek, 1997)*. Rock mass refers to a body of rock, which also includes samples of intact rock. The imperfections however cause a very variable type of rock which is very often the rock we find. These imperfections have been caused from several natural events (refer Section 2.1) such as faults and seismic movement *(Bieniawski, 1989)*. Rock masses are less straightforward to understand and analyse because of their non-homogeneous, anisotropic and discontinuous nature *(Hoek, 1997)*.

In theory, it is very difficult to ensure a specimen of intact rock is representative of its intact properties. This is because the rock in the ground is full of variables, containing discontinuities and voids. Naturally, minimizing such variables can be done by reducing the sample size, but this then introduces a new set of testing difficulties which are discussed in Section 2.4.

Reducing the sample size can be problematic. This is addressed in a concept called Representative Elementary Volume (REV). Within rock mechanics, this refers to the minimum rock volume which can be used to determine the overall rock mass properties *(Hudson et al., 1983).* The overall aim is to simplify the heterogeneity of the rock mass with the presence of its discontinuities, whilst providing statistical data. The chosen rock volume for the testing procedure is an important element. This is because the volume needs to be large enough to include several discontinuities for representative rock behaviour, and not too large which will introduce impracticality whilst testing.

REV considers the discontinuity properties which are present in a rock mass. These will be discussed in more detail in Section 2.3 and include the frequency, orientation, roughness, shear strength of joints surfaces, aperture width and infill material *(Hoek and Bray, 1981*). Other contributing factors effecting the rock mass properties include the groundwater, which has a direct effect on the pore pressures and effective stress *(Barton and Choubey, 1977)*. These two parameters will affect the mechanical behaviour of the rock mass.

The difficulty in assessing rock masses has brought about several researchers to analyse rock mass. These methods are called Rock Classification Systems. Examples of these include the Rock Structure Rating (RSR) developed by Wickham et. al. (1972) and the Rock Mass Rating developed by Bieniawski (1989).

2.2.1. Strength of rock mass and intact rock

Rock classification systems need to be applied to estimate the mechanical properties of the rock. This is followed by determining the strength of intact rock through the Uniaxial Compressive Strength (UCS) and Young's modulus *(Aladejare et al., 2022).* The reliability of such properties is questioned because it does not consider the dimensions and natural conditions of the intact rock *(Aladejare et al., 2022)*. As previously mentioned in Section 2.2, approximating rock mass properties and their deformation modulus is more complex and less reliable *(Aladejare et al., 2022).* This makes intact rock strength alone insufficient for fractured rock environments.

The accuracy of rock mass strength is dependent on cost and time. Some examples of these direct tests include plate bearing, flat jack and pressure chamber *(Ulusay et al., 2007*). The rock mass classification systems are therefore used as a cheaper and quicker alternative to approximating rock mass strength. These take into consideration several critical properties relating to discontinuities. Strength estimates are therefore extracted from classification systems by correlating observations to tables and simple tests *(Bienawski, 1989)*.

Therefore, whilst precise rock mass strength is always going to be desired, the impracticality in achieving it, has resulted in the widely adopted use of the rock mass classification systems. These provide a much more feasible approach *(Ulusay et al., 2007*).

2.2.2. Strength Estimates and Failure Criterion

Two of the most important parameters when estimating the shear strength of rocks are cohesive strength, *c*, and the friction angles, *φ*. This information is critical for assessing slope stability, as it can help identify potential slipping surfaces *(Hoek, 1970).* This can also occur in the local context which has been mentioned in Section 2.1.

Hoek and Bray (1974) conducted back analysis of slope failure to derive the c and *φ* parameters of soils. Their findings showed that while these parameters are important, high cohesive materials in rock often do not exhibit stickiness, which differentiates from clay behaviour.

2.2.2.1. Mohr-Coulomb Failure Criterion

This is a widely used equation for determining the equation of the shear strength of rock. However, the Mohr-Coulomb failure criterion is most relevant for soils, This is because soil is a soft material so it will generally fail due to shear and this criterion relates shear strength to normal stress. At high normal stresses, it is assumed that the Coulomb relationship can be developed into the linear approach:

$$\tau = c + \sigma_n \tan \phi \qquad \textit{Eq. 2-1}$$

Importantly, this equation recognises that when the shear strength is zero, the normal stress is zero. These studies showed that a curved envelope for rock discontinuities has been measured and understood. These were obtained by Jaeger *(1959),* Krsmanovic et al*. (1964*), Lane et al*. (1964),* Patton and Byerlee *(1967*).

Experimental results were conducted relating to the friction angle and the slenderness ratio against the dilation angle. This is the angle by which a joint surface expands vertically as it shears, which is a common occurrence in rough discontinuities. The dilation angle is the instantaneous inclination of the

shearing path at peak strength *(Ryland et al., 2017).* When the shear displacement occurs at the instant peak shear strength, maximum dilation occurs.

From the experiments on the relationships mentioned above. The 2 equations were derived:

$$\frac{\tau}{\sigma_n} = tan(2d_n + 30) \qquad \textit{Eq. 2-2}$$

The dilation angle in terms of UCS (σ_c) and normal stress (σ_n) can be expressed as follows:

$$d_n = 10log_{10}(\sigma_c/\sigma_n) \qquad \textit{Eq. 2-3}$$

By eliminating the angle of dilation, the equations above can be merged into:

$$\tau = \sigma_n tan\,(20log_{10}\,(\frac{\sigma_c}{\sigma_n}) + 30) \qquad \textit{Eq. 2-4}$$

From these equations σ_n is the normal force acting on the joint, σ_c is the uniaxial compressive strength of the intact rock, d_n is the dilation angle $\text{and}\ \tau$ is the shear strength. The ratio $\frac{\sigma_c}{\sigma_n}$ is very often used by Barton and Choubey (1977) and it relates how the joint strength is dependent on the ratio between the applied normal stress and the intact rock strength.

Cohesion and friction angles for joints are found through the intercept from the Mohr-Coulomb failure criterion. Importantly, these are not a constant in rocks or soils. However, they are treated as one for mathematical convenience.

2.2.2.2. Hoek-Brown Failure Criterion

The Hoek-Brown Failure Criterion is also typically used to quantify this strength characteristic based on shear and normal stresses acting at the fissured interface *(Hoek & Brown, 2019).* However, this criterion can only be used when isotropic behaviour of rock is present. This isotropic behaviour is simplified to rock masses which have closed spaced discontinuities (*Hoek, 1980)*. This criterion can be characterized by the equation:

$$\sigma_1^{'} = \sigma_3^{'} + \sigma_{ci}\left(m_b \frac{\sigma_3^{'}}{\sigma_{ci}} + s\right)^a \qquad \textit{Eq. 2-5}$$

This equation considers the maximum $(\sigma_1^{'})$ and minimum $(\sigma_3^{'})$ principle effective stresses at failure *(Hoek, 1980)* whilst m_b refers to the Hoeke-Brown constant for the rock mass. The constants *s* and *a* are dependent on the rock mass characteristics.

The normal and shear stresses can be characterised by the principal stresses through the equations published by Balmer (1952*):*

$$\sigma_n^{'} = \frac{\sigma_1^{'} + \sigma_3{'}}{2} - \frac{\sigma_1^{'} + \sigma_3{'}}{2} \cdot \left(\frac{\frac{d\sigma_1^{'}}{d\sigma_3^{'}} - 1}{\frac{d\sigma_1^{'}}{d\sigma_3^{'}} + 1}\right) \qquad \textit{Eq. 2-6}$$

$$\tau = (\sigma_1^{'} - \sigma_3{'})\frac{\sqrt{\frac{d\sigma_1{'}}{d\sigma_2{'}}}}{\left(\frac{d\sigma_1^{'}}{d\sigma_3^{'}} + 1\right)} \qquad \textit{Eq. 2-7}$$

However,

$$\frac{d\sigma_1{'}}{d\sigma_3{'}} = 1 + am_b\left(\frac{m_b\sigma_3^{'}}{\sigma_{ci}} + s\right)^{a-1} \qquad \textit{Eq. 2-8}$$

Therefore, it can be deduced from the above equations that the uniaxial compressive strength of the intact rock (σ_{ci}), the Hoek-Brown constant (m_b) for the intact rocks and the GSI strength index of Section 2.2.3.3, all are needed for the strength to be estimated *(Hoek, 1980).* The triaxial test is a laboratory equipment which is used to determine the σ_{ci} and m_b. m_b , *s* and *a* are found through using GSI (Section 2.2.3.3). m_b reflects the reduced rock mass's reduced frictional strength, s refers to the degree of interlocking and a related to the shape of the failure envelope. These test results are still analysed with caution because of the anisotropic property of rocks. These all help to assess the degree of strength reduction when discontinuities are present.

2.2.3. Rock Classification Systems

2.2.3.1. Rock Structure Rating (RSR)

Understanding the rock mass implies identifying and quantifying a series of characteristics that are likely to influence its engineering behaviour. An example of Rock Classification System is Rock Structure Rating (RSR) and it can be used to quantitatively describe rock simply from logic *(Wickham et al, 1972).* This method can be used in the applications of the slopes present in the North-Western region of Malta which were specified in Section 2.1.

This process divides the rock into 3 main parameters: A, B and C, which are given a rating based on a set of criteria. The formula used is:

$$RSR = A + B + C \qquad \textit{Eq. 2-9}$$

Parameter A is used to describe the geology. This includes the Origin (igneous, metamorphic, sedimentary), which in this case is sedimentary. Parameter A also refers to its hardness and geological structure. The geological structure refers to the presence or absence of faults. Parameter B is used to describe geometry and discontinuity pattern of rock mass. This includes the joint spacing, orientation and direction. Parameter C refers to the presence of water and conditions of the joint. It considers the rock quality based on the Parameters defined in A and B *(Hoek, 1980)*.

The RSR system, together with the Parameters defined A, B and C, present a method of analysing the quality and stability of rock masses. This system is used by engineers and geologists in the design of foundations, excavations and slopes. This system can help extract rock information which can help professionals to take informed decisions on excavation methods and foundation designs.

Locally, sedimentary rock formations often have very complex discontinuity patterns. Therefore the RSR system can help to evaluate the stability of rock wedges.

2.2.3.2. Rock Mass Rating (RMR)

Another classification system is Rock Mass Rating (RMR). This was introduced by Bieniawski (1976). This rating is based upon 6 parameters *(Hoek, 1980)*, which include the Uniaxial Compressive strength of rock material, the rock quality designation (RQD), the discontinuity spacing, the condition of the discontinuity, the groundwater considerations and the orientation of the discontinuities *(Barton and Choubey, 1977).* RMR combines these parameters and gives ranks to the rock mass such that professionals can take informed decisions in the design of foundations, slopes etc.

Locally, discontinuities can vary over very short distances. This may result in an inconsistent RMR rating, especially if the scoring is being based on limited exposure or influenced by surface weathering. The consistency of scoring is difficult to maintain, especially when there is the visual assessment and the subjectivity of the engineer *(Hudson et al., 1983).* Therefore, it can be used as a framework to analyse the small-scale geological variability in local rock masses.

RMR helps to bridge the gap between general specification systems and site-specific geological issues. The importance of this is highlighted locally, due to several ground differences present between adjacent sites. It will also help to identify the differences between parameters, providing not just a descriptive approach but also a critical approach.

2.2.3.3. GSI Strength Index

Another Rock Classification System which can be used to determine the strength of rock mass is the geological strength index (GSI) *(Hoek, 1994).* This was introduced by Hoek (1994) and Kaiser and Bawden (1995) for quantifying and estimating rock mass strength based on different ground conditions. For large discontinuities, the GSI strength index should be used individually *(Hoek, 1994)*.

Before the introduction of the GSI system, the strength of a rock mass was found using the Hoek-Brown failure criterion, which was discussed in Section 2.2.2.2, together with the RMR rating mentioned earlier in Section 2.2.3.2 *(Bienawski, 1989).* Generally, this system gives a largely qualitative set of data, which many engineers find cumbersome to transfer into quantitative data (*Hoek, 1980).*

From the table above, a value of GSI is chosen based on investigation. This value is then used to find:

$$m_b = m_i exp\,(\frac{GSI - 100}{28 - 14D}) \qquad \textit{Eq. 2-10}$$

$$s = exp\,(\frac{GSI - 100}{9 - 3D}) \qquad \textit{Eq. 2-11}$$

$$a = \frac{1}{2} + \frac{1}{6}\,(e^{-GSI/15} - e^{-20/3}) \qquad \textit{Eq. 2-12}$$

In the above equation, m_b is the reduced value of the Hoek-Brown constant, m_i refers to the coefficient of determination and D refers to the degree of disturbance in blasting (*Hoek, 1981)*.

These classification systems provide a critical base for assessing slop stability, which is spoken about in the next section.

2.2.4. Rock Slope Stability

Unloading is present in real-life scenarios through excavations and erosion. This reduces the confinement, increasing the chances of having clay-filled joints supporting a wedge. This can be seen on Figure 2.5:

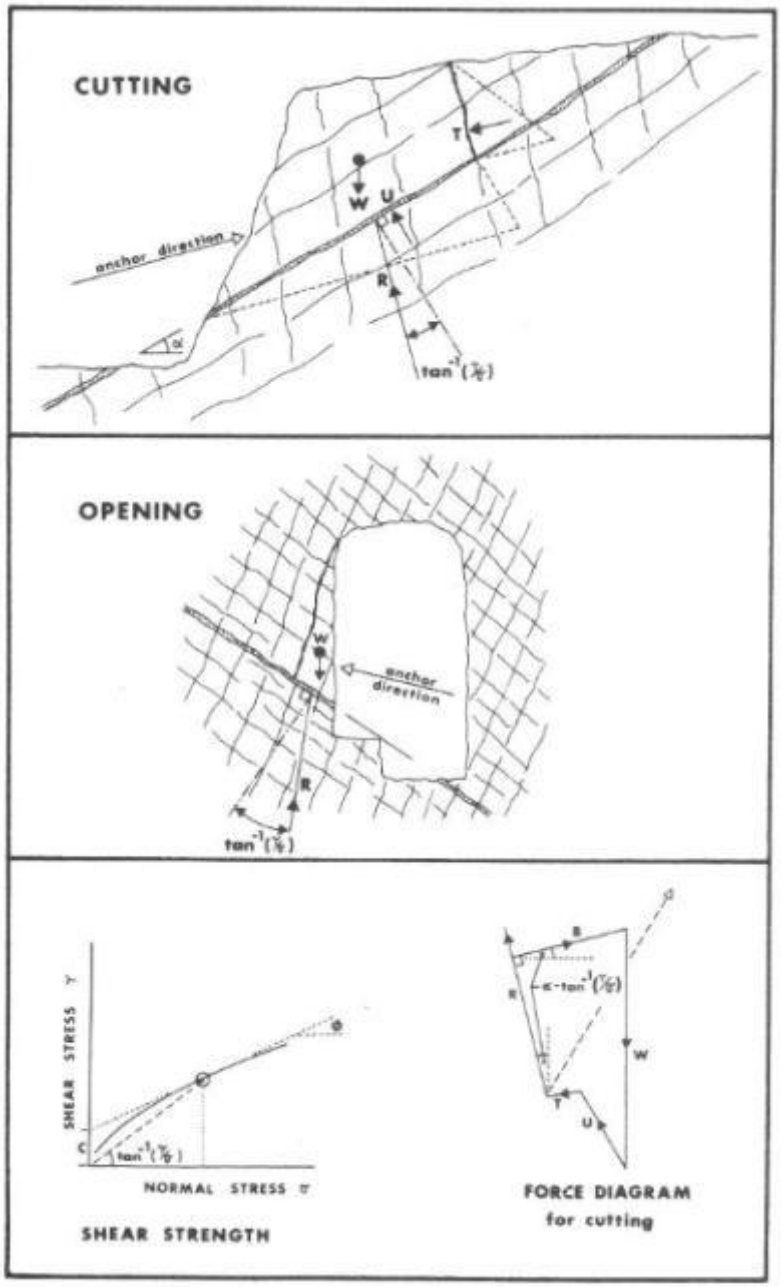

Figure 2.5 - Diagrams depicting the filled discontinuities and force diagrams of joints (Barton, 1973)

Figure 2.5 shows how during an excavation, intersecting discontinuities can separate a block of rock in the shape of a wedge. These form when the natural discontinuities intersect and define a block of rock. The lateral confinement can be removed and hence can freely move. Therefore, in order to get a cohesive understanding of this concept, the concept of kinematic feasibility needs to be implemented *(Hoek & Bray, 1981)*. This refers to the geometric conditions that allow a wedge to slide. The wedges will not all move. They will only move if the orientation of the discontinuity and direction of sliding

align with each other *(Hoek & Bray, 1981)*, allowing the wedge to displace. Figure 2.5 shows how the geometries affect wedge mobility.

The stability is determined from a balance of forces between the disturbing and resisting forces. The self-weight of the wedge acts vertically downwards. This can therefore be resolved in components which are parallel and perpendicular to the sliding face. The parallel component slides the wedge down the sliding plane, whilst having an opposing force in friction and cohesion *(Hoek & Bray, 1981)*. It is geometrically understood how a steeper inclination angle will result in a greater sliding force parallel to the face. This is the basis of the Coulomb Wedge Theory, where an interplay between shear strength and normal stress is present.

As the wedge starts sliding, the infill material will also be under shear and normal stress *(Hoek & Bray, 1981)*. The permeability of this infill material is important. In low permeability plastic clay, the pore water pressure will not be able to dissipate as quickly. This causes a delayed reaction as the shear interaction is not immediately mobilised. This shows how short-term conditions will reflect lower stability from elevated pore-pressures. This contrasts with long-term conditions which show increased strength as drainage and pore pressures reduce *(Terzaghi, 1963)*.

The above concept shows the importance of time-dependency when analysing rock wedges *(Terzaghi, 1963)*. Stabilising these said wedges can be done through interventions such as rock bolts and anchors. These add confining forces or change the direction of resultant forces. These may prove to be costly, so studying in-fissure behaviour is also economically beneficial.

Initially, the shear strength will be greater than the downwards component of the wedge's weight. *(Barton, 1973)*. The short-term increase because of the drop in water pressure during unloading and increased shear strain. The long-term increase in shear strength is associated with reduced pore-water pressure *(Barton ,1973)*. As time passes, the pore water pressure continues to increase, which results in the clay softening and swelling. This results in a decrease in stability. Early signs of failure can be found in tension cracks above the surface. However, caution must be taken because they can become hidden because of rainfall *(Barton, 1973).*

The rate at which these discontinuities are sheared affects the drainage. Fast shearing will reduce the possibility of drainage. The actual effect is very much dependent on the plasticity index of the clay. This property also has a relation to the reduction in strength properties over time. Some studies by Skempton and Hutchinson (1969) showed a 10-15% reduction in drained strength over a long period of time. The residual strength, however, only had a 0.5% - 2% decrease.

Drained tests can represent in-situ conditions, as they allow for the pore pressures to dissipate. When the infill thickness becomes less than the amplitude of the rock wall roughness, rock-rock contact becomes present and this affects the strength *(Barton, 1973).* The rock wall refers to the surrounding intact rock, where the surface geometry influences how the clay behaves.

Plasticity also affects the residual strength. High clay plasticity may have residual friction angles as low as 5 to 12 *(Terzaghi and Peck, 1967)*. Low plasticity clays, on the contrary, may have residual friction angles as high as 30. The difference in shear strengths, whether the clay is present in its intact form, on an artificial cut surface or on a non-planar surface, can be seen from the results of Skempton and Petley (1968) on Figure 2.6.

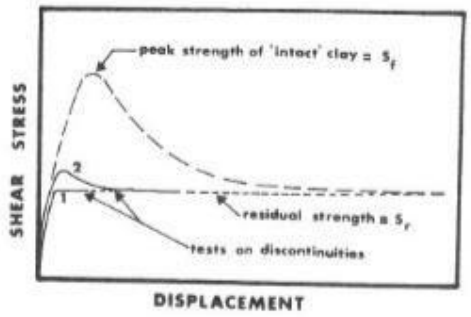

Figure 2.6 - A graph showing the Stress-Displacement based on the findings of Skempton and Petley (1968)

Slope stability for clay-filled discontinuities is also particular. In general, the main contributing factor for slope stability is the cohesion of the slope being excavated *(Barton, 1973)*. When excavating, negative pore pressures will be developed because of the reduction in the normal stress. The other factor contributing to these negative pore pressures is if the clay discontinuities are found in their heavily over consolidated state. This is because they expand during shear, increasing the volume and decreasing the negative pore pressure. The negative pore pressures will draw water into the unloaded zone *(Barton, 1973)*.

When water is present, the strength of rock will either be unaffected or increased for low-medium stress levels. However when there are natural or rough joints present, the strength is reduced between 5-30% *(Barton, 1976)*. The rock is weakened because of its adverse effect on the tensile strength on brittle materials. At great depth, the presence of water reduces the effective confining pressure, thereby shifting the brittle-ductile transition to greater depths. Brace (1968) showed how pore water pressure within a saturated rock falls if the loading rate exceeds the rate at which fluid can flow into the stressed region *(Barton, 1976)*.

There is a reduction in effective stress with the presence of water *(Barton, 1976)*. The mechanical strength of the rock is lowered because of a reduction in the surface energy and crystal strength of the rock mass. This will reduce the shear strength for non-planar joints during shearing *(Barton, 1976)*. However, if the rock contains several crystal structures, the frictional coefficient increases with the presence of water, subsequently increasing the shear strength.

Most of the smooth surfaces are unaffected or increase their shear strength when wet whilst most of the natural or rough joint surfaces reduce in strength when wet.

2.3. Discontinuity parameter analysis

There are several characteristics of discontinuities that have a bearing on shear strength, especially when this is relevant to the stability of a wedge of rock. These characteristics include orientation of the main discontinuity sets size, in terms of discontinuity aperture, the nature of the materials forming the discontinuity sides and the infill, the presence of water, and the height of asperities within the discontinuity surfaces. With reference to this chapter and the Methodology in Chapter 3, particular detail is given to the infill material and thickness from the variables.

2.3.1. Infill Thickness

Sliding complications may occur because of fillings of different grades. When a filled joint is sheared whilst controlling the lateral displacement, the volume will remain constant. Rock contact here will occur eventually, allowing for dilation to take place, decreasing the pore water pressure *(Barton, 1973)*. The pore water pressure may even be negative unless shearing is very low. The effects of this will be greatly felt when the discontinuity is very thin, increasing its volume tremendously as it is sheared. The effects of this will be felt less and less as the filling thickness increases *(Barton, 1973)*.

The thickness of a soil is crucial in the shear behaviour of a discontinuity. This property needs to be analysed in tangent with the amplitude of the joint roughness. A thin infill relative to the amplitude induces rock-to-rock contact, increasing joint strength. Thicker soil will adversely isolate the rock surfaces, where the shear resistance becomes dominated by the clay's properties. This can be characterised through the Figure 2.7:

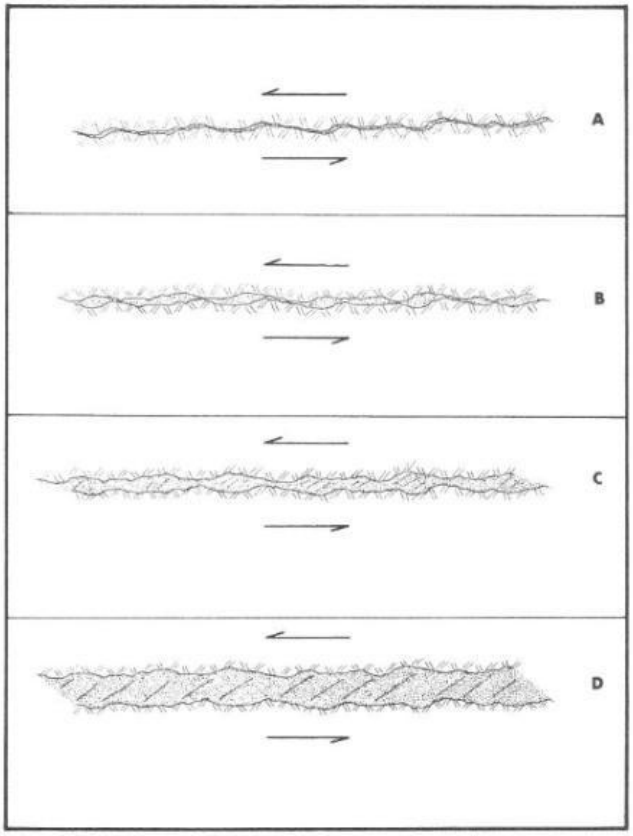

Figure 2.7 - Discontinuity filling thickness (Barton, 1973)

From Figure 2.7, Section A is immediate contact. Shear strength is almost the same when the discontinuity is unfilled because of the immediate contact. Section B is similar to Section A, but the displacement will be larger. Dilation will be reduced, and negative pore water pressures will be reduced too. Section C will have a build-up of stress in the infill part as the rock asperities come closer to each other. When shearing is slowly done, consolidation and drainage will occur. Section D is when the influence of the rock walls completely disappears because the infill thickness is far greater than the asperity amplitude. Soil mechanics can be followed to determine the shear strength behaviour.

However, Rocha (1964) suggests that when low stresses are present in joint filling, the influence of the filling material is low too. Under low normal stress, the mobilised shear strength is dominated by the rock wall geometry and the residual friction at the interface rather than by any cohesive or frictional contribution from the clay *(Hoek & Bray, 1981)*. The Coulomb Wedge theory explains how the normal stress acting perpendicular to the sliding surface governs the shear strength. A low normal stress would therefore indicate that shear resistance is being governed only by the residual friction.

Many fissured surfaces have been undergoing displacement for several years. Within this scenario, the joint surfaces have most likely reached residual strength conditions. Therefore, the displacement will not mobilise any peak shear strength and only the residual friction angle of the infill governs this response *(Lupini et al., 1981)*.

Filled joints and the influence of displacement and loading history are conveniently divided into 2 groups: the ones which have already undergone shear displacement, meaning they will be close to their residual strength, and the ones which have not been displaced yet *(Barton, 1973)*. The first group are present due to faults.

The history of loading on the discontinuity will be completely independent of the residual shear strength. In drained tests on soils, the residual shear strength will be almost identical regardless of loading history. On the other hand, the peak shear strength will be greatly affected by the loading history *(Barton, 1973)*.

Normally consolidated soil fillings are when the existing effective normal stress in situ is equal or greater than the effective pre-consolidation pressure *(Barton, 1973)*. At surface, most discontinuities will almost always be in their over consolidated state. Normally consolidated discontinuities occur due to surface weathering *(Barton, 1973)*.

Testing on soils will need to be done very slowly because of their low permeability. This will help to prevent pore pressures from arising.

Soft silty clayey soils do not show much of a difference between their residual strength and their peak strength *(Barton, 1973)*. This contrasts with higher clay contents, which have a larger difference. Skempton (1964) did suggest that residual strength is the same for both normally and over-consolidated clays.

Apart from the properties of what makes up the infill material itself, the most important parameter is the thickness of the infill material itself *(Indraratna, 2010).* This is because the shear strength will decrease as the infill thickness increases up until a critical value where the infill thickness will not affect the behaviour anymore *(Indraratna, 2010).* When the critical value is exceeded, the shear strength of the infill material prevails over that of the rock *(Indraratna, 2010).* The comparison between the

thickness and height of the joint is given by the t/a ratio, where the t represents the infill thickness, whereas a represents the height of the joint asperity *(Indraratna, 2010).*

Under Constant Normal Stiffness Test (CNS), a Normalised Shear Drop (NSD) represents a decrease in peak shear stress when compared to peak shear stresses for smooth rock joints. CNS tests simulate in-site boundary conditions more realistically than conventional shear tests. This is because the normal load is allowed to vary with joint dilation *(Indraratna, 2010)*. The NSD speaks about the drop in shear strength from the infill material. This can be quantified by:

$$NSD = \frac{t/a}{\alpha\left(\frac{t}{a}\right) + \beta}$$

Eq.. 2-13

Where α and β are constants dependent on the infill material. The t/a ratio refers to the thickness of the infill material (t) compared with the asperity height of the joint (a).

2.3.2. Quantifying shear strength of rock and rock joints

This was already introduced in Section 2.2.2.1, when talking about the Mohr-Coulomb Failure Criterion, however this section shows how it has been developed further by other researchers.

2.3.2.1. Patton's approach

As discussed earlier, discontinuities are rather random and contain several geometric imperfections. However, excavations can very often be engineered in many different shapes. Patton's study is one where he analysed the shear strength of rock discontinuities mimicking a saw-tooth approach *(Patton, 1966)*.

The equation derived by Patton to describe the shear strength for rock discontinuities of this shape is;

$$\tau = \sigma_n \tan(\phi_b + i) \qquad \textit{Eq. 2-14}$$

This equation represents how the shear strength within the discontinuity is dependent on the friction angle of the surface and the angle of the saw-tooth geometric discontinuity. In reality, the shear displacement is caused by the surface moving up the inclined face. This causes an increase in volume (dilation) *(Hoek, 1980)*.

The value for *i* is difficult to estimate without testing. Patton suggested that it will be only the first-order irregularities which affect the shear strength of joints in natural slopes *(Barton, 1976).* Below surface-weathered zones, all roughness, *i*, is important to characterise. These terms can be seen on Figure 2.8, Figure 2.9 and Figure 2.10.

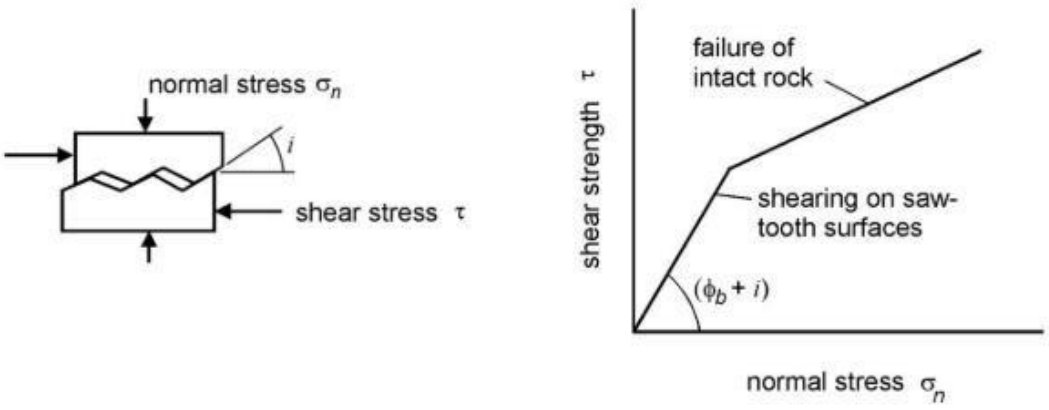

Figure 2.8 - Patton's experiment on saw-tooth specimens (Evert Hoek, Shear strength of rock discontinuities, pg 4)

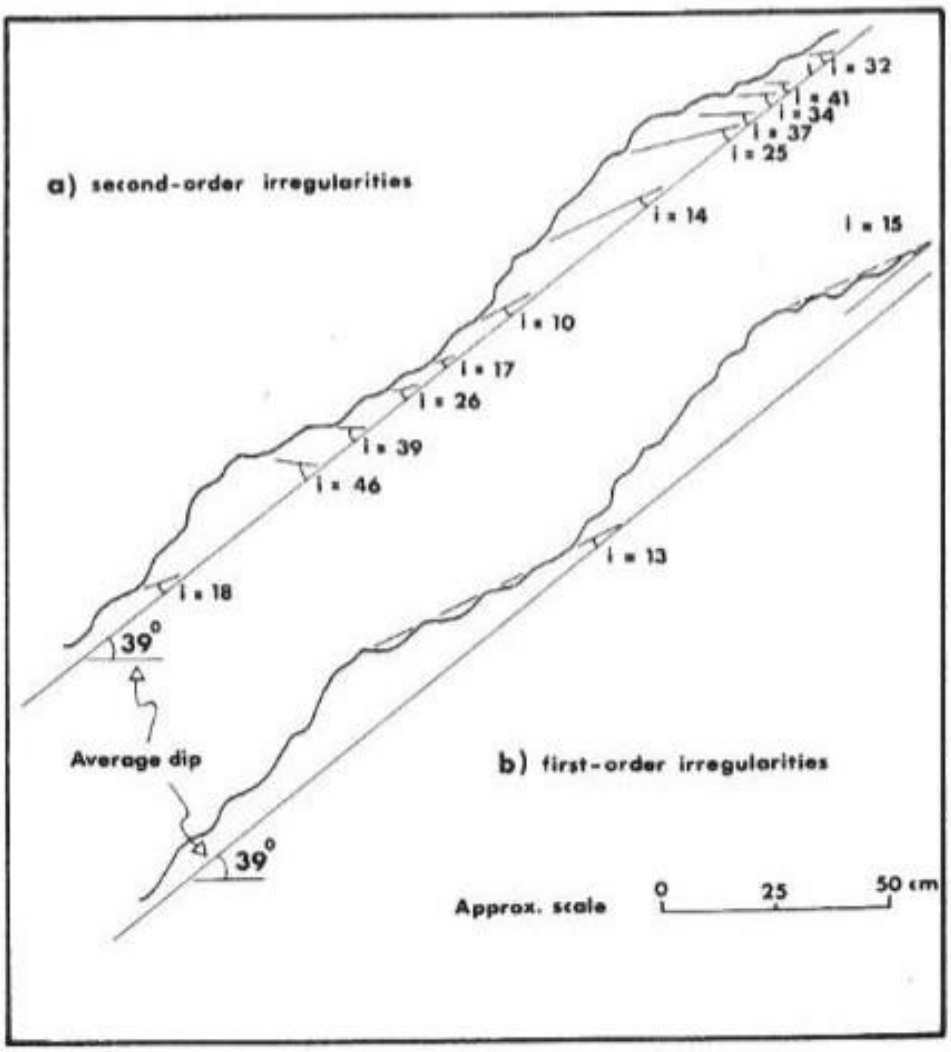

Figure 2.9 - A diagram explaining the first and second order asperities of rough undulating joints (Patton,1966)

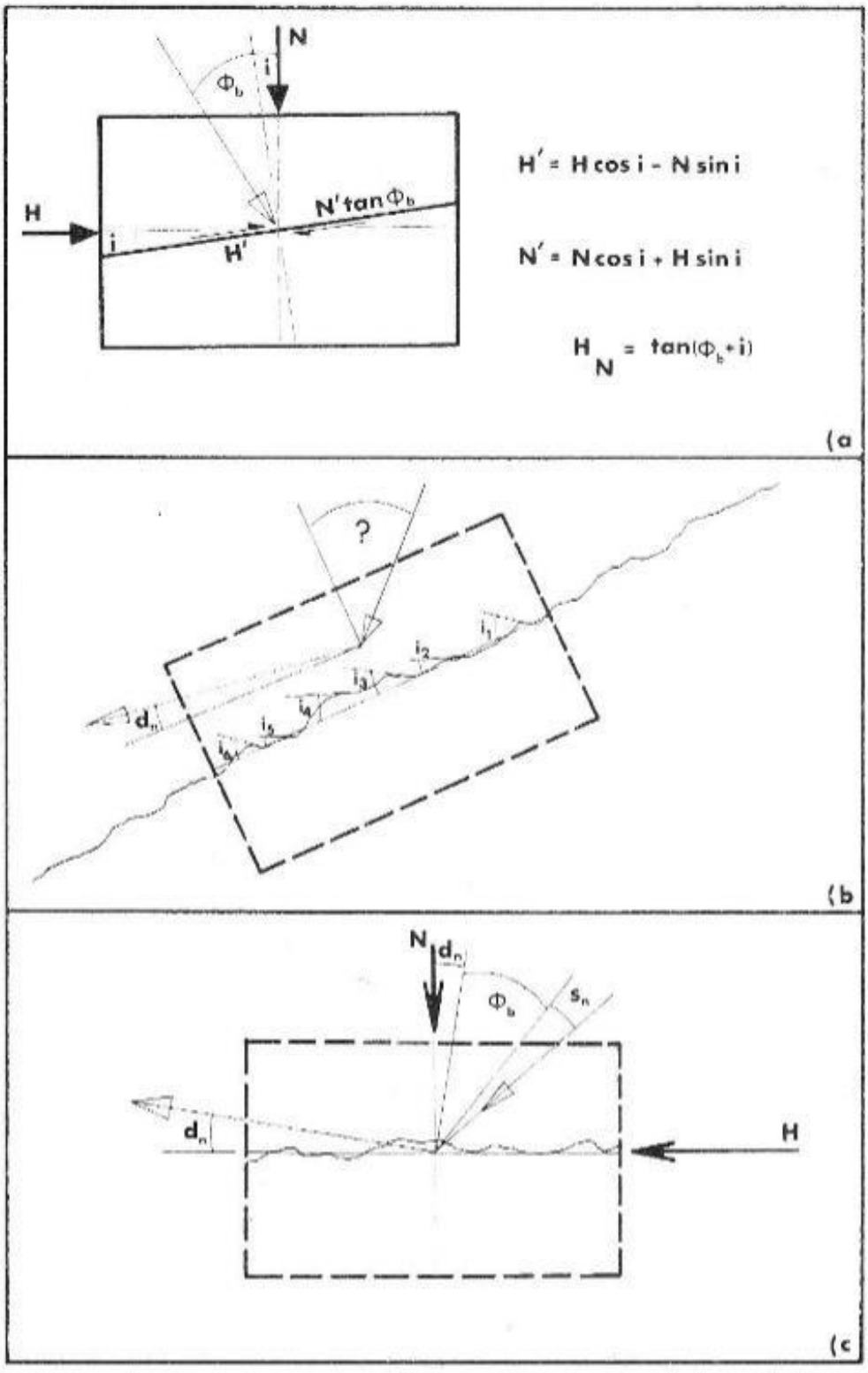

Figure 2.10 - Diagrams representing important elements such as dilation angles (dn) and friction angles (φb) as explained by Barton (1973)

2.3.2.2. Roughness Coefficient and Wall Compressive Strength

As mentioned earlier, discontinuities present in the ground are random, and so is their geometry. This makes Patton's approach not very accurate in reality (*Barton, 1973)*. Barton (1973) readjusted the equation such that it takes into consideration the joint roughness coefficient (JRC) and the joint wall compressive strength (JCS). This is often a result of weathering, which is mentioned in more detail towards the end of the chapter.

The JRC is a sliding scale of roughness (Figure 2.11) which varies from 20 being the roughest to 0 being the smoothest *(Barton, 1976).* The JCS is the unconfined compression strength of the rock if the joint is unweathered. This can be reduced to 1/4th of the value if the rock is weathered *(Barton, 1976)*. The equation will be written as follows:

$$\tau = \sigma_n \tan\left(\phi_b + JRC log_{10}\left(\frac{JCS}{\sigma_n}\right)\right) \qquad \textit{Eq. 2-15}$$

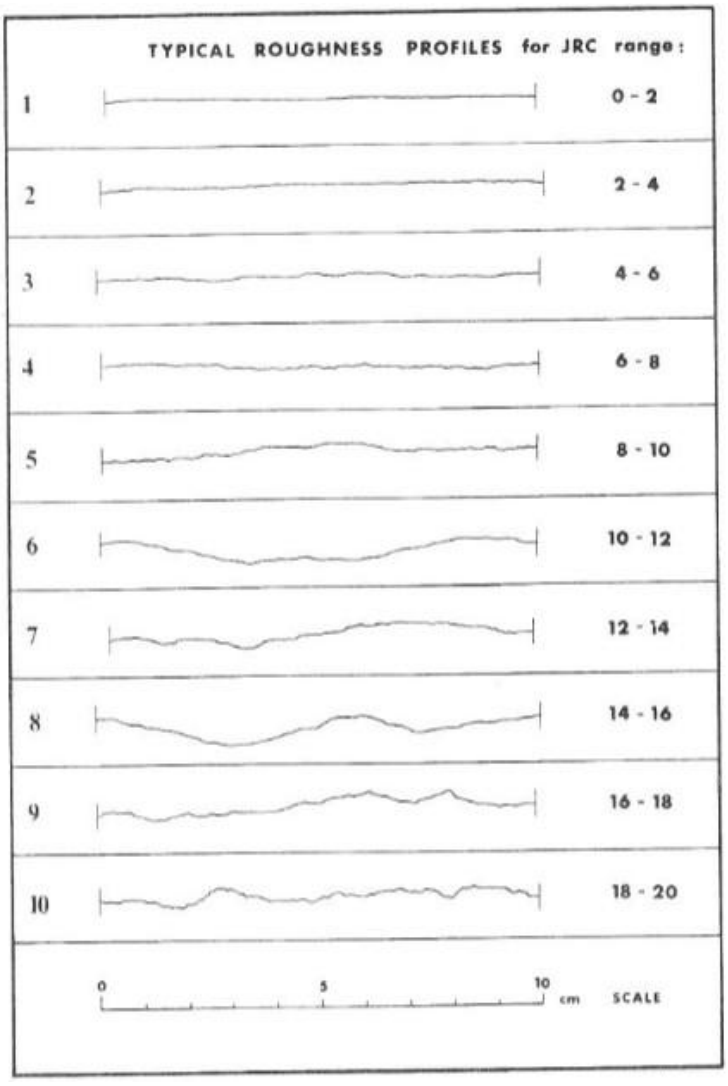

Figure 2.11 - Roughness profiles and JRC values (Barton and Choubey, 1977)

As the specimen is sheared, the contact area increases, causing the compressive strength to increase too. This rearranges the equation to:

$$\tau = \sigma_n \tan\left(\phi_b + JRC log_{10}\left(\frac{\sigma_1 - \sigma_3}{\sigma_n}\right)\right) \qquad \textit{Eq. 2-16}$$

In this case, σ_1 is the axial stress at failure and σ_3 is the effective controlling pressure, which when it is zero, takes us back to the original equation.

However, a non-linear approach of distinguishing the shear strength of rock joints was developed by further studies of Barton and Choubey (1977), which the above equation to:

$$\tau = \sigma_n tan\left(\phi_r + JRC log_{10}\left(\frac{JCS}{\sigma_n}\right)\right) \qquad \textit{Eq. 2-17}$$

This equation now takes into account the residual friction angle.

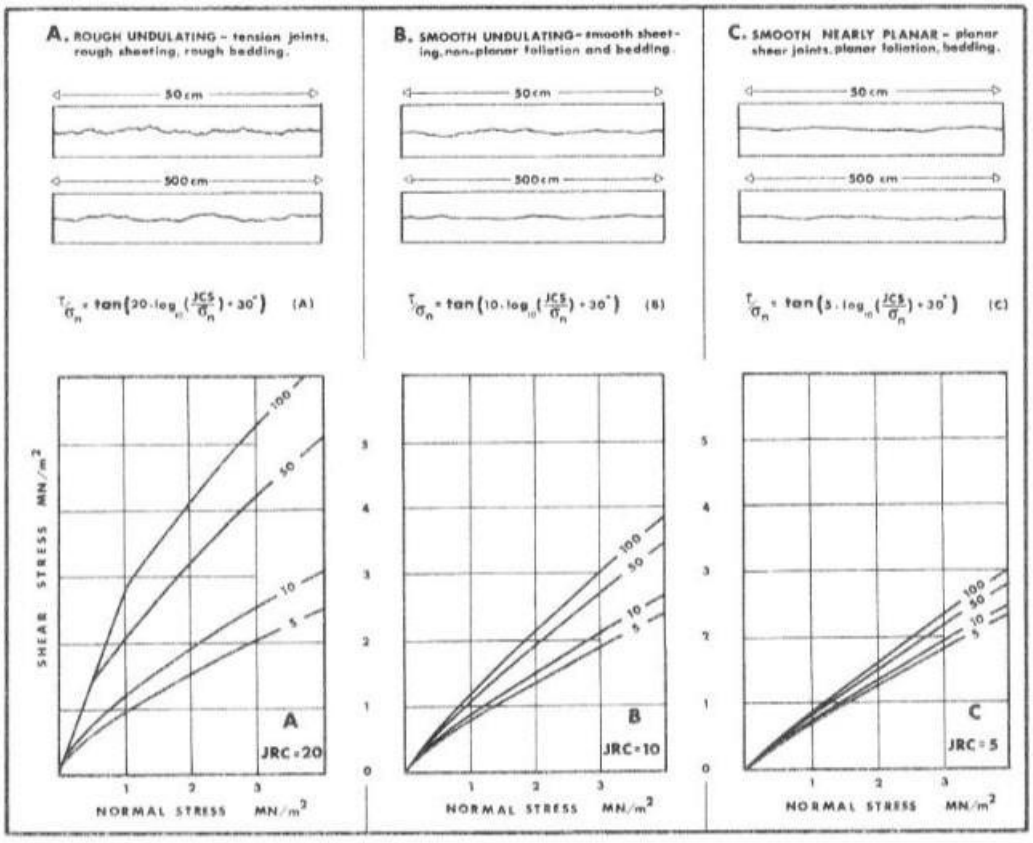

Figure 2.12 - A graph depicting the empirical law for different undulating joints as explained in the description (Barton and Choubey, 1977)

Normally, the JCS value will be lower than the σ_c *(Barton and Choubey, 1977)*. This value can be found using the Schmidt hammer test on the exposed part of the rock. Miller's method (1965) is used to gather compressive strength parameters from the rebound value. If the tests were done with saturated joints or infill, then the JCS value can be assumed to be even lower, sometimes even up to 20% lower.

The previous equation makes use of the $\phi_r$which is the residual friction angle, which is calculated by taking into account the rebound from the Schmidt hammer test in the equation:

$$\phi_r = (\phi_b - 20) + 20\ (r/R) \qquad \textit{Eq. 2-18}$$

In this case, r is the rebound number for wet and fracture surfaces, and R is the rebound number for dry surfaces *(Hoek, 1980)*.

The process of weathering also effects the shear strength. Weathering occurs different within different types of rock formations. This is because it is dependent on the mineralogy of the rock. This can be seen in Lower Globigerina Limestone which produces horizontal fissures during weathering *(Gatt, 2005)*. This creates a space where soil can later be infilled. Contrasting this, the Middle Globigerina Limestone disintegrates more thoroughly in the weathering process. This forms a soil-like material *(Gatt, 2005)*, highlighting the differences of weathering in different rock formations.

The shear strength of weathered joints will be lower than those in unweathered joints, because of a lower compressive strength *(Barton, 1976*). In Malta, weathering has a greater effect on the upper and lower rock formations rather than the impermeable Blue Clay.

The alteration index *(Hamrol, 1961*) is an old and outdated approach which was used to understand the mechanical properties of rock during weathering. This terms the weight of water absorbed by the rock in an absorption test which is then divided by the dry weight of the rock giving a percentage. This is an indirect measure of porosity *(Barton, 1976).*

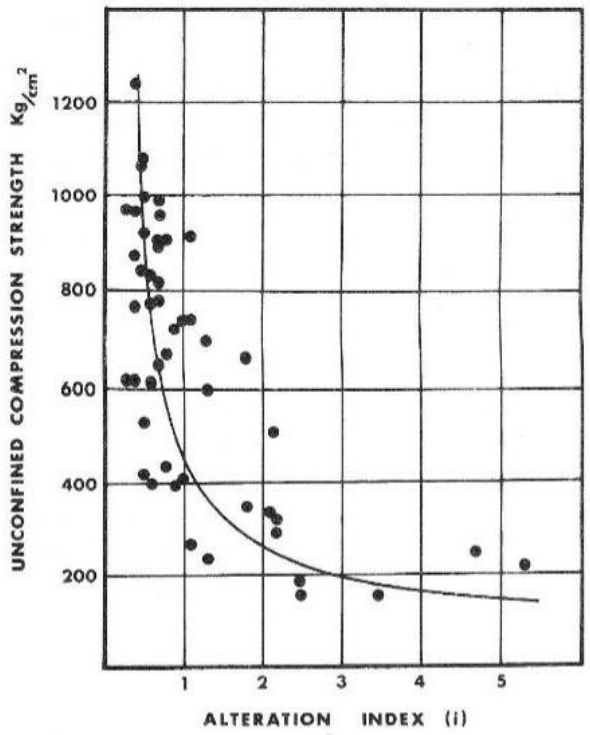

Figure 2.13 - A graph of the how compressive strength varies with the alternation index (Serafim, 1964)

Figure 2.13 is showing the inverse relationship between the alteration index and unconfined compressive strength. This graph can be visually seen to support the idea of how more weathering (alteration index increases) results in the compressive strength decreasing.

The first step of the weathering process of rock is when the is a reduction in joint wall strength. When this occurs, JCS becomes less than σ_c. The second step is when there is a penetration of joint weathering into rock block. When this occurs, σ_c starts to be reduced. The third stage occurs during advanced weathering stages. When this occurs, there is more uniformity in σ_c.

2.3.2.3. Barton-Bandis Model

The Barton-Bandis Model is a method used for quantifying the non-linear shear and deformation of the joints *(Ryland et al., 2019).* The non-linearity is a cause of the differences present within the discontinuity. Such differences include surface roughness and the deformation and permeability of joints *(Ryland et al., 2019)*. The ISRM has included the infill material as a key element which characterises rock discontinuities. The research presented by Indraratna (2010) in Section 2.3.1 also briefly mentions this.

This will introduce basic stress-displacement-dilation of joints in shear *(Ryland et al., 2019).* Residual peaks will be very difficult to achieve with only a few millimetres of shearing *(Ryland et al., 2019).* These are normally achieved through the Schmidt Hammer test *(Ryland et al., 2019).* The tests shown in Rylands research (2019), show how the internal friction angle is reduced. This is a cause of weathering.

Another way of estimating the shear strength is through a soil-rock model *(Venkateswarlu et al., 2022)*. This can be done through the equation *(Irfan et al. 1993):*

$$\phi_{S-RM} = \phi_{sf} + \Delta\phi \qquad \textit{Eq. 2-19}$$

In the above equation, the ϕ_{S-RM} refers to the friction angle of the soil-rock model, the ϕ_{sf} refers to the friction angle of the sand fines and the $\Delta\phi$ refers to the increase in friction angle.

2.3.2.4. Barton-Kjaernsi Model

This model was further developed through comparing the approaches in Section 2.3.2 with the infill properties.

Therefore, another way of estimating the shear strength of a soil-rock model is through the Barton-Kjaernsi model. This is used to analyse rock infill materials as a way of quantifying a soil-rock mixture *(Venkateswarlu et al., 2022).* It was presented that rock fragments will offer higher shear resistance, due to the interlock between them *(Venkateswarlu et al., 2022).* This will however, make it more complex to quantify, because of the translations which will occur as the specimen is sheared. Since often these real-life models are scaled down to fit laboratory apparatus, inaccuracies due to size-related dilation will be present *(Venkateswarlu et al., 2022).* This can be expressed as:

$$\tau_f = \sigma_n \tan\left(R log_{10}\left(\frac{S}{\sigma_n}\right) + \phi_r\right) \qquad \textit{Eq. 2-20}$$

$R log_{10}\left(\frac{S}{\sigma_n}\right) + \phi_r$ refers to the peak friction angle of a rock infill material *(Venkateswarlu et al., 2022).* R is the equivalent roughness of the rock infill, and this is quantified through empirical charts which take into consideration the porosity, roundedness, smoothness and particle mixture of the infill. S is another parameter which is quantified through the mean particle size and the uniaxial compressive strength (UCS) *(Venkateswarlu et al., 2022).*

The test results from Venkateswarlu (2022) confirm that the larger the rock infill, the greater the shear strength. This was done by varying different gravel contents. This can be seen from their results on Figure 2.14.

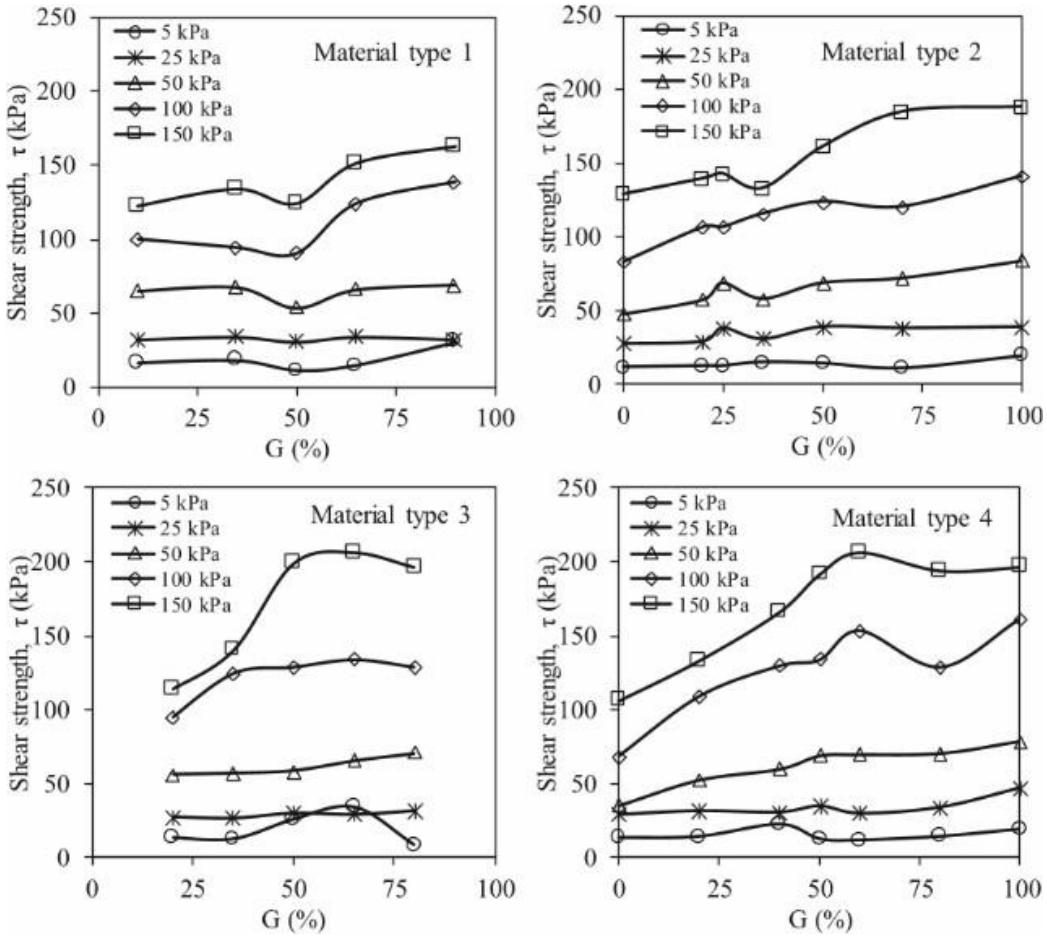

Figure 2.14 - The above shows how the gravel content (G) is changed for 4 different types of material. At higher G values, the test results showed higher shear strength values. This showed an almost linear behaviour in many cases.

Determining such values is done through triaxial and direct shear testing. Normally, direct shear is very widely used because it is very easy to use and provides instantaneous results *(Venkateswarlu et al., 2022).* However, as a form of experimentation, it contains a few inaccuracies.

Firstly, the failure occurs within a plane of shear. This means that the shear test will not take into account the inhomogeneity of the soil within its geometry. Different soil particles will also fail at different shear stress levels *(Venkateswarlu et al., 2022)*. Therefore, when analysing a particular soil infill, it is important to keep the particles as uniform as possible for the test, so that the true particles will be tested.

This has also been discussed in more detail with relation to the direct shear box used in Section 4.

2.3.3. Infill material

The infill material can vary based on several factors and is very often considered to be the weakest material in a rock discontinuity *(Al-Obaidi, 2018).* The infill material can typically be soils, including clays and silts. These are soft, finely grained and have distinct mechanical behaviours when compared to intact rock. Their behaviour falls under the scope of soil mechanics. Water content, particle-size distribution and the material (sand or rock) are some of these factors *(Mokhtarian et al., 2024)*. These factors are some of the elements which influence the properties of the infill materials and therefore their mechanical response.

There are also three important volume relationships. These help to understand how much void is present within the soil itself, and it is directly related to the size of the grains of soil *(Mokhtarian et al., 2024)*. These relationships are:

The void ratio:

$$e = \frac{V_v}{V_s} \qquad \textit{Eq. 2-21}$$

where V_s is the volume of the solid particles and V_v is the volume of voids.

Porosity:

$$n = \frac{V_v}{V} \qquad \textit{Eq. 2-22}$$

where V_v is the volume of voids and V is the total volume.

Degree of Saturation:

$$S = \frac{V_w}{V_v} \qquad \textit{Eq. 2-23}$$

where V_w is the volume of water in voids and V_v is the volume of voids. In practice, the infill material will not be present under one fixed ratio, but under a range.

2.3.3.1. Soil Infill

From defining the properties from the phase relationships of Section 2.3.3, the strength behaviour can be analysed, both at a residual and peak level.

The strength of soil originates from interparticle interaction and friction. This governs its ability to resist shear. Peak shear strength occurs when the soil reaches its maximum resistance before failure. The interparticle friction, effective stress, packing, and dilation/contraction of the soil mass are all contributing factors which influence the peak shear strength. They determine how the soil will interact and rearrange under a load. This is the foundation of strength analysis in soil.

Over consolidation increases the peak strength of this layer above the residual strength. After normal consolidation, brittle behaviour is seen when it is sheared for the first time *(Bishop et al. 1971).* The undrained strength for over-consolidated clays is dependent on the over consolidation ratio *(Barton,1973)*. This ratio is the value of the past vertical effective stress σ'_p and the current vertical effective stress σ'_v.

Therefore:

$$OCR = \frac{\sigma'_p}{\sigma'_v} \qquad \textit{Eq. 2-24}$$

If the ratio lies between 1 and 4, it would be considered relatively low for a discontinuity filling *(Barton, 1973)*. Over here, the volume will decrease whilst shearing, and the undrained strength will be less than the drained strength. With very large ratios above 8, the clay will dilate whilst shearing, resulting in the pore pressure decreasing. In this case, the undrained strength will be greater than the drained strength. This helps engineers deduce that the short-term stability of slopes above heavily over consolidated fills is greater than long-term stability *(Barton, 1973)*.

For normally consolidated fills of clay particles, the undrained strength will be smaller than the drained strength, because of the volume contractions during shearing *(Barton, 1973)*.

When the rock is displaced, the rock surface will be in contact with each other when sheared. This will initiate the process where the shear strength will now be dependent on the asperities and the rock strength. However, when the specimen is sheared, dilation occurs. This dilation is dependent on the normal force applied *(Indraratna, 2010).* The asperities will then start to break *(de Toledo et al., 1993).* In the beginning, the shear stresses start rapidly increasing until they reach their first peak, which refers to the infill peak. The compression and dilation will be dependent on the infill material. However, de Toledo et al. (1993) said that shearing may occur at constant volume. This occurs when soil is moved from a loaded to an unloaded area.

The presence of water through the concept of effective stress also influences this behaviour. The effective stress is defined as the difference between the total stress and pore water pressure *(Terzaghi, 1963)*. This controls the interparticle forces that resist the shearing forces. Undrained and drained conditions can therefore provide very different resistances. In the undrained conditions, the pore pressures within the clay will rise during the loading phase, resulting in a temporary loss in shear strength. Conversely, the drained conditions will allow water to dissipate, which allows the soil to resist load more effectively *(Terzaghi, 1963)*.

Understanding the brittleness and post-shear structure of soil is important to determine the mode of shear *(Lupini et al., 1981).* These are studied on cohesive soils, and the transition from one to another is dependent on the packing and porosity (Section 2.3.3) of the particles present.

Soils with a large cohesion produce large deformation *(Hvorslev, 1936).* However, at larger displacements, a constant strength is present *(Tiedman, 1937).* The soil will exhibit an ultimate point of stress behaviour *(Haefeli, 1938*) and will then decrease its shearing resistance. Haefeli (1938), suggested that the drop in strength from peak to residual increased with the liquid limit in clays.

The residual strength varies based on the soils having platy to rotund particles and the coefficient of interparticle friction between them *(Lupini et al., 1981)*. The 3 modes of residual shear are turbulent, sliding and transitional modes.

Moreover, soils having turbulent shear behaviour show a high residual strength. This mainly occurs when ϕ_R' is greater than 25. The residual state involves shear at constant volume without orientation.

Residual behaviour becomes significant at large strains. The less the platy particles, the residual strength is essentially from the rotund particles. Higher platy particles, therefore mean greater separation between rotund particles. Skinner (1969) studied the residual shearing resistance of granular soil and found that it is independent of the friction angle. Therefore, the reduction in strength is due to the increase in clay content. The increasing separation of clay particles is also due to this, rather than from a reduction in sliding resistance between the clay particles.

Residual shear behaviour changes significantly as the clay content of cohesive soil increases. Lupini (1981) studied this by artificially preparing soils for such an experiment.

Transitional behaviour involves discontinuous sliding shear surfaces and pockets of soil behaving in the turbulent mode *(Lupini et al., 1981)*. If soil behaves like this, the residual strength is likely to be sensitive to small changes in grading. Increasing the normal stresses will reduce the residual friction angle in sliding and, at the same time, cause a denser pack of round particles and more interference between them. Increasing stress on the residual friction angle may be a product of two opposing mechanisms *(Lupini et al., 1981)*.

Additionally, Chattopadhyay (1972*)* studied the relationship between residual strength and particle shape. Low residual friction angles with platy particles. Sub-angular and needle-shaped particles gave high residual friction angles. Fleischer (1972) and Voight (1973) studied the shearing angle and plasticity index *Ip* for stiff clays. The results showed that the residual shearing angle was independent of initial soil structure and stress history an independent of normal effective stress.

Bucher (1975) used 2 different stress devices to study stress history, stress level, shear rate and temperature on residual friction angle. Friction angle did not affect the temperature change. Shear displacement increased the residual strength in clays. Wesley's (1977) results showed an atypical relationship between residual friction with clay fraction and *Ip*. This concluded the importance of the clay particle shape.

Plasticity in soil, however, does not have a relationship with the residual shearing angle *(Kenney, 1967)*. Kenney (1967) did however highlight how the residual strength is more dependent on the soil composition rather than the size or plasticity of the grains. This behaviour can be seen on Figure 2.15 below:

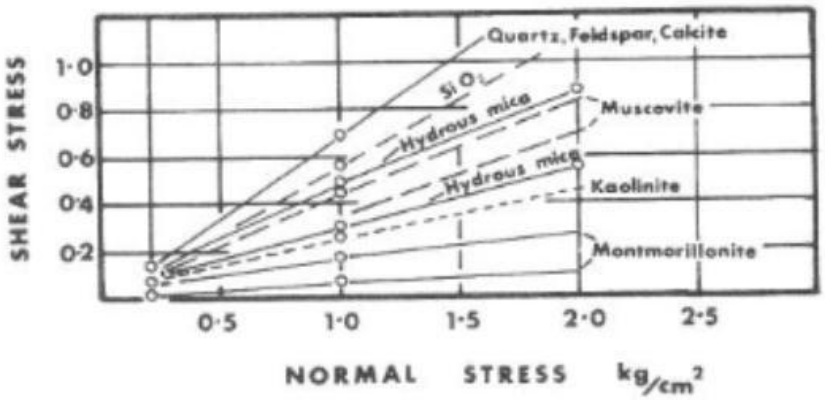

Figure 2.15 - Graphs depicting how the residual strength is dependent on the mineralogy (Kenney, 1967)

The results show that the largest residual stresses occurred when there were large quantities of clay minerals of the mica family. However, the coarse particles will tend to increase ϕ_r above the clay particles *(Barton, 1973)*.

Borowicka (1965) reported that as the brittleness increased in soils, the residual shearing angle decreased with increasing clay fraction. However, testing was done using ring tests, triaxial tests and shear box tests. Hermmann and Wolfskill (1966) suggested that from these tests, the triaxial tests normally display the higher strengths.

Lupini et al.(1981) also mentions the distinct relationship between residual strength and plasticity index, which is evident in cohesive soils. The plasticity index is a value which quantifies the range of water content values for the plastic behaviour of clay. This influences the ability of clay to realign and slide under shear. Soils which contain a high plasticity exhibit lower residual friction angle because of how the soils form oriented shear surfaces. This is relevant to the research on Blue Clay, as the Blue Clay has a high plasticity index, suggesting these trends should be present. The residual friction angle and clay fraction relationship can be seen on the Figure 2.16 below.

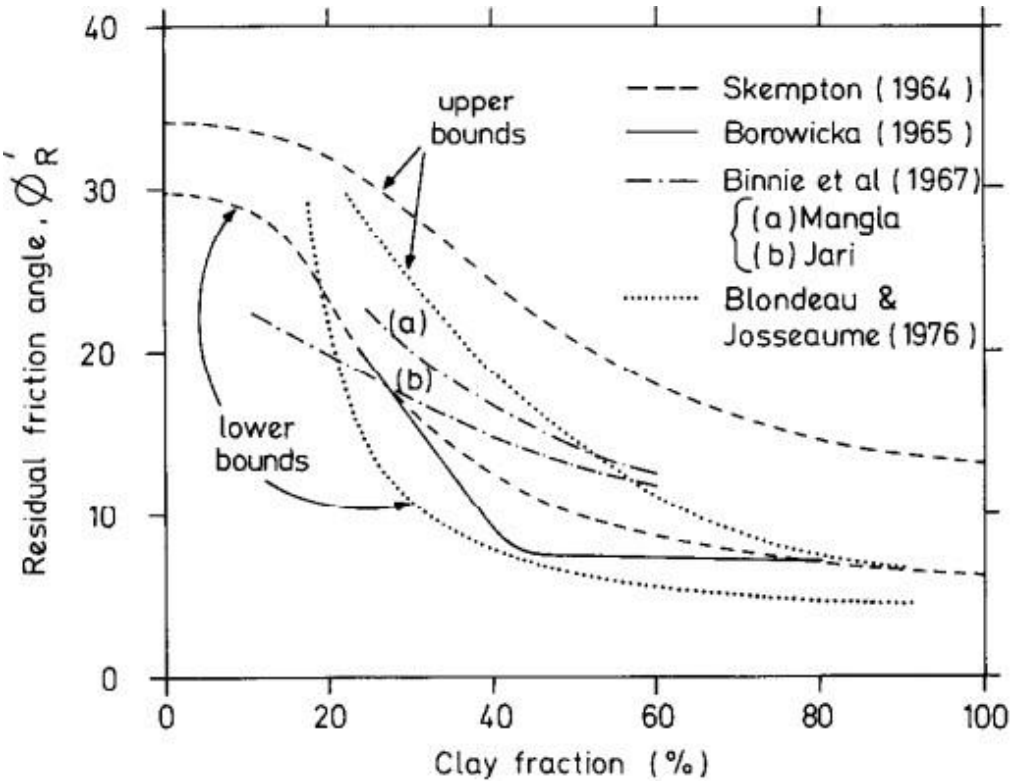

Figure 2.16 - The variations of residual strength with clay fractions in soils (Lupini et al., 1981)

Chandler (1969) focused his studies on low plasticity soils. His studies deduced that the clay fraction in the residual shear surface was higher than in the adjacent soil. This confirmed the results of Skempton (1964). Binnie et al.(1967), Early and Skempton (1972) studies soils which displayed low residual friction angles whilst also having a high plasticity.

Residual strength is low in soils when an oriented shear surface is formed. This has a significant impact on the bulk properties of soil. These surfaces are hazardous.

2.4. Testing Difficulties

2.4.1. Sample Size

It is assumed that when the sample size increases, the strength decreases. It was already mentioned earlier in Section 2.2 how the size may determine strength properties. Hoek and Brown (1980) familiarised this approach through the equation whereby the uniaxial compressive strength, σ_{cd} (where d is the diameter in mm of the specimen under test) varies through the equation:

$$\sigma_{cd} = \sigma_{c50} \left(\frac{50}{d}\right)^{0.18} \qquad \textit{Eq. 2-25}$$

The above equation relates the compressive strength of a specimen with the compressive strength of a specimen with a known diameter of 50mm.

Eventually, a constant value for strength is reached for larger specimens (*Hoek, 1980).* This is because the size of the small rocks formed will be very small in comparison to the large rock strata (*Hoek, 1980).*

Therefore, through such literature, there exists a transition phase from when rock is considered as an anisotropic material to an isotropic material. The shear strength and stiffness reduce as the block size is larger because of the effective joint roughness *(Ryland & Bandis, 2016)*. The deformation which occurs is also relative to the block size under test.

The stress-shear displacement curves change their shape in larger sample sizes because the reduced effective roughness and increased contact areas change the shape, as seen in Figure 2.17.

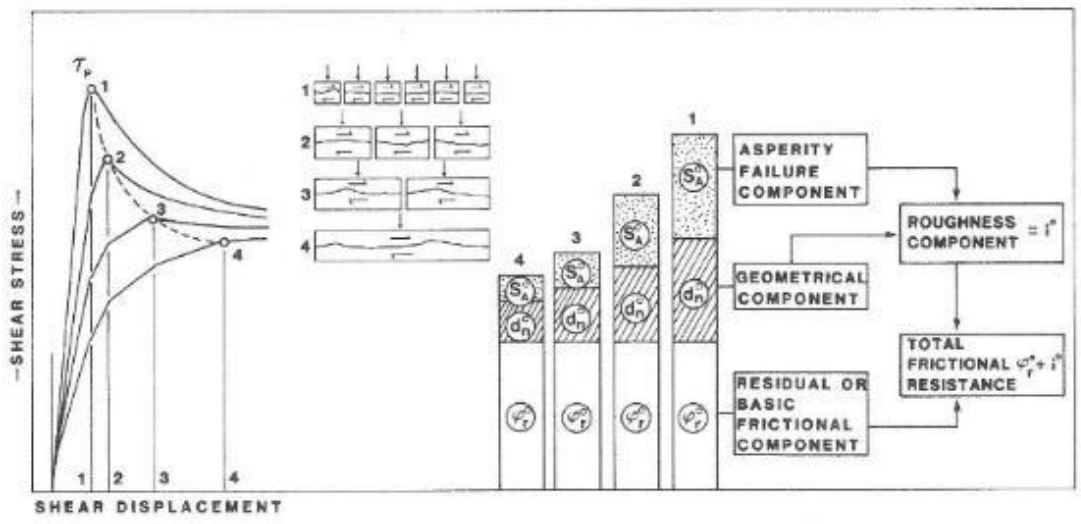

Figure 2.17 - Graphs showing how a larger joint sampled will produce a reduced asperity strength, reduced dilation, and increased displacement (Bandis et al., 1981)

Figure 2.17 shows how the curve is flattened as the sample increases. Bandis (1981) stated that the JCS and JRC values decrease with an increased block size. This reduction is seen mostly in the roughest joint surfaces.

The peak parameter δ becomes greater with greater rock samples. An approximation can be given below through the formula:

$$\delta = \frac{L}{500} \cdot \left(\frac{JRC}{L}\right)^{0.33} \qquad \textit{Eq. 2-26}$$

Therefore, increased block size results in an increase δ, reduced JRC and a reduced JCS. A gradual flattening of the normal stress will occur with increasing block size. When the size of the sample becomes larger than the natural block size, the effect of the size will then become redundant *(Ryland & Bandis, 2016).*

Several studies *(Goodman, 1970; Bandis et al., 1983)* have shown that joint deformability and strength are scale-dependent, with smaller samples often underestimating displacements and stiffness reductions observed at field scale. The limited specimen dimensions in this study may not fully replicate field-scale behaviour, particularly for infilled joints subjected to normal displacement and closure effects.

Understanding these mechanism equip engineers to make better decisions when dealing with clay-rich discontinuities, especially in slope stability in complex geological conditions.

3. Methodology

3.1. Introduction

This study investigates the shear strength behaviour of clay-filled rock discontinuities. Characterisation of rock discontinuities presents significant challenges due to their inherent natural variability. The complexity and diversity of discontinuity parameters make in-situ testing particularly difficult, reinforcing the importance of controlled laboratory testing to characterise shear strength with some reliability and effectiveness

Shear strength testing on rock discontinuities requires a well-planned experimental strategy. The variability of natural rock introduces issues related to repeatability, representativeness, and a variety of parameters. While the testing program cannot capture the full spectrum of natural variability, it is designed to isolate and evaluate the influence of specific factors on shear strength behaviour.

The direct shear box test apparatus available at the University of Malta (refer to Section 8.2 for Equipment Specifications) was employed. This apparatus was selected for its ability to provide controlled boundary conditions and for its relevance to established shear failure criteria. The equipment was modified and upgraded to enable digital data acquisition rather than analogue, improving the precision and reliability of the results. Each test set comprises three specimens subjected to varying normal stresses, as per standard practice. To ensure consistency, each trio of specimens within a test set was prepared to be as identical as possible.

This study builds upon previous work by Barbieri (2021), who modelled the Lower Globigerina Limestone using Plaster of Paris, a material selected for its similar mechanical properties and the ability to be cast into moulds for improved repeatability. Barbieri's research focused on roughness and interlock in unfilled discontinuities.

In contrast, the present study examines discontinuities filled with Blue Clay, varying the infill thickness to assess its effect on shear strength. Blue Clay is a prominent geological material in Malta and is commonly observed within rock discontinuities. Although clay infill in the field often coexists with other constituents such as gravel and sand, this study isolates the effect of Blue Clay by using it exclusively as the infill material. The clay was sourced from Santa Maria Estate, Mellieha, that is the material that was tested in Cassar (2020) research.

The geometry of the discontinuity surfaces was kept constant throughout the study. Saw-tooth-shaped discontinuities were prepared, adopting a geometry similar to that proposed by Patton (1966). This approach ensured consistency in roughness, asperity height, and interlock, allowing this study to focus specifically on the impact of clay infill thickness.

3.2. The Direct Shear Box Test Apparatus

A Direct Shear Box was used to conduct trial tests in order to become familiar with the apparatus and its limitations. The trial test was carried out on a Lower Globigerina Limestone specimen which was sourced from the Solid Base laboratory. The Lower Globigerina Limestone was selected because, as highlighted in Section 2, its weathering process produces horizontal fissures which were often clay-filled. The strength of these fissures could be tested with the direct shear box test.

However, the main aim of this trial test was to grasp an understanding of the equipment. This process also served as an opportunity to look at different ways in which the testing procedure could be improved.

The direct shear box has several advantages and disadvantages. One of its limitations is that it includes a predetermined failure plane. However, in this case, the failure plane is aligned with the plane that is prepared for testing. Other disadvantages include how a non-uniform stress distribution is present, pore water pressure cannot be measured, and drainage control is also not possible. The sample size is also restricted to the size of the equipment which introduces the possibility of scale effects. The advantage of using a direct shear box include its suitability to test interface behaviour and its instant and direct results.

The direct shear box test apparatus is presented in Figure 3.1 – Figure 3.1, Figure 3.2, and Figure 3.3. The hydraulic pumps (Figure 3.2) are used to apply a vertical and shearing force on the test specimen within the equipment.

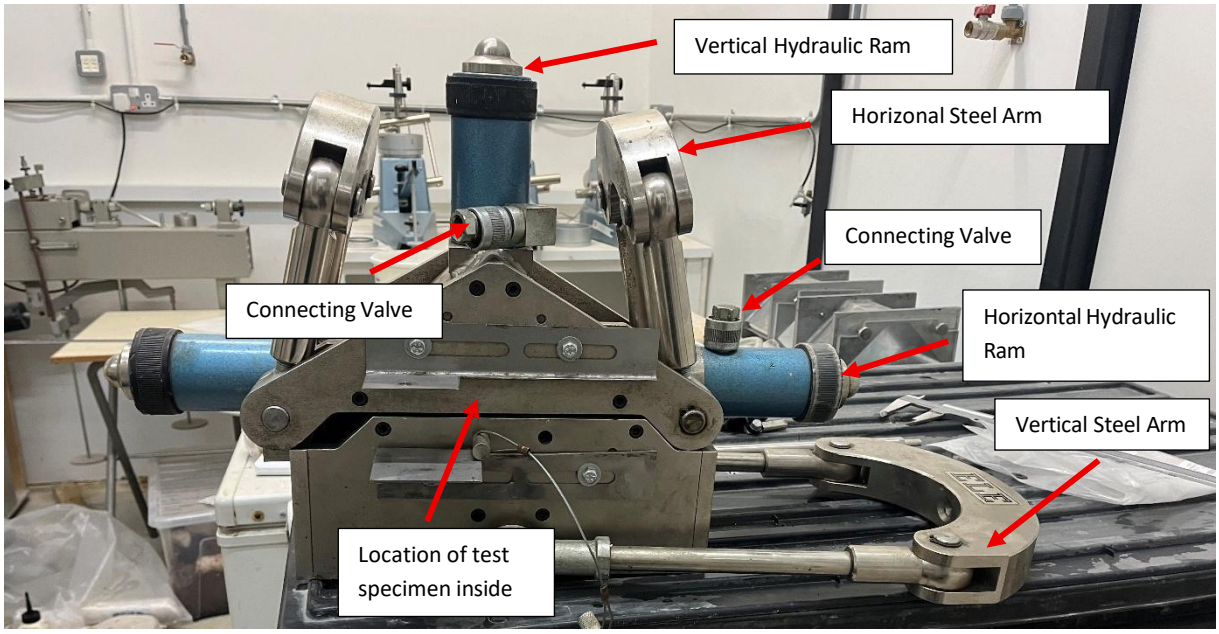

Figure 3.1 – Direct Shear Box test apparatus prior to adjustments.

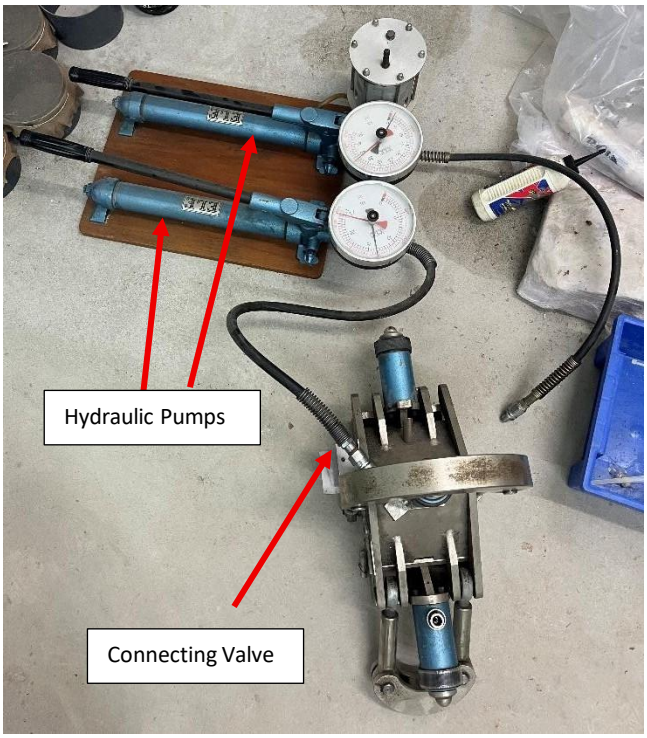

Figure 3.2 - Current shear box set-up connected to hydraulic pumps

One of the pumps was connected to the vertical ram. For the hydraulic pumps to influence the ram, the valve on the hydraulics has to be closed. This ensured that the pressure within the hydraulic pump was not altered. A manual up and down movement was applied on the lever of the hydraulic pump and this ensured that the oil within the hydraulics was transferred to the ram. This resulted in the hydraulic ram extending upwards. Since this was locked in place by the steel arm, the steel arms would want to move upwards too, however this was locked to the bottom of the shear box. This therefore induced a force on the specimen in test, which was termed as the normal force.

The other hydraulic pump was used to apply the horizontal force, through the connecting valve. This was applied by having a steel arm which was connected to the horizontal ram. The same motion was applied for this lever. Since this hydraulic ram was locked in place with the steel arm, the extension would therefore induce the horizontal force on the specimen as it tried to move sideways. This was termed as the shear force.

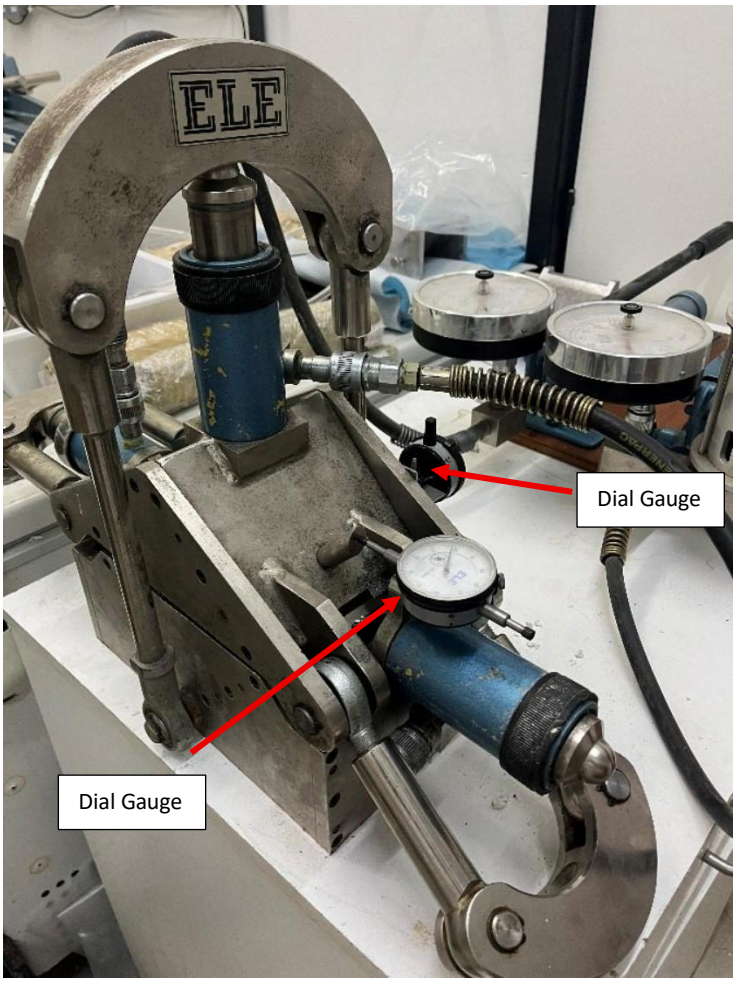

Figure 3.3 – The location of the dial gauges which can be seen during a test

One dial gauge was used to measure the vertical displacement. This provided a measure of dilation and/or contraction. The other dial gauge was used to measure the horizontal displacement, also termed the shear displacement. The shear displacement was then converted to a shear strain (%) where the displacement in relation to the shearing length of the specimen was analysed.

3.2.1. ISRM Testing Procedure

The testing procedure followed the ISRM manual for shearing rock joints *(Muralha, 2014)*.

Following the set-up of the direct shear box (see Figure 3.4), both valves were closed so that the manual up and down motion on the lever arms was applied. This induced a normal and shear force on the test specimen. Importantly, only a small force was applied so that the steel arms would lock in place with the hydraulic rams.

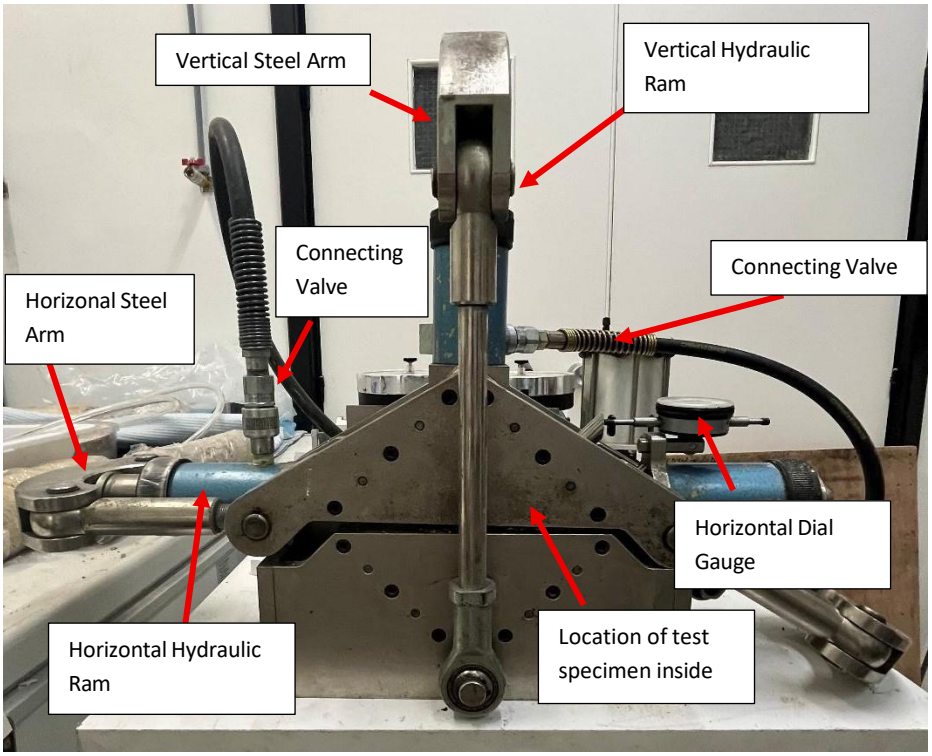

Figure 3.4 - The rock specimen under test during the trial experimentation

A normal force was then applied. The rate at which a normal force was applied was in accordance with the ISRM manual for Constant Normal Stiffness, where rates of 0.01 MPa/s or less were applied. A set initial normal force was applied, and this force could be checked on the dial gauges of the hydraulic pumps. The readings on both dial gauges were then noted, so that any zeroing could be done at this stage.

Any load which was also imposed on the test specimen was taken into consideration. This included the self-weight of the rock sample and the self-weight of the top part of the shear box.

The shear load was then applied once the normal force was stabilized. The value of the shear force being applied was given by the reading on the hydraulic pump. While the displacement rate was set in accordance with ISRM standards (0.1-0.2mm/min), the maximum strain achieved during the test was approximately 6%. This falls slightly short of the typical ISRM target strain range of 10-15%. However, this was due to equipment limitations which is discussed in Section 4 and Section 6.

The dial gauges, as explained previously, were used to measure the normal and shear displacements simultaneously. These measurements, together with the normal force and shear force values, were tabulated manually. The stresses were calculated from the formula:

$$\sigma = \frac{F}{A} \qquad \textit{Eq. 3-1}$$

The force value was the tabulated result from the experimentation. The normal force would produce the normal stress within this equation and the Shear Force would produce the Shear Stress within this equation. The area was the same for both equations and it was the contact area of the two specimens against eachother.

Following the results, four graphs were plotted, which were Shear Strain vs Shear Stress, Normal Stress vs Shear Stress, Normal Displacement vs Shear Strain and Shear Strain vs Time. Apart from a quantitative set of data was recorded, several photos were taken before, during and after the experiment to log visual data.

Following an explanation of the testing procedure and the individual elements, several limitations in the experimental set-up became apparent during this phase. These limitations included accuracy and data synchronisation which prompted a full conversion to a digital system.

3.3. Conversion of apparatus from Analogue to Digital

From the preliminary tests, several equipment flaws were highlighted. Within this test, the normal force was kept constant on the rock specimen whilst shearing in incremental values. This provided results only at the incremental values, occasionally giving only three readings for a whole experiment. This provided very inaccurate results as graphs were drawn up with only three sparse measurements.

Readings from the dial gauges were also difficult to tabulate. This was because the analogue meter of the dial gauge would constantly be moving. The readings of both gauges, and both applied forces needed to be synchronised. This was very difficult and impractical.

It was then decided to go for a digital set-up. The digital system offered several advantages when compared to the analogue set-up. The first advantage is having an improved set of data accuracy. The digital system will continuously record data, including many points within a single test. The second advantage is that it is easier to log data. This is because manual tabulation of data does not need to be carried out. Lastly, there is much better synchronisation between all four sets of data.

The new digital set-up, which was set-up, consisted of two load cells, one for the normal force and one for the shear force, and two LVDTS, one for the vertical displacements and one for the horizontal displacements. An NI 9237 data logger was used to transfer the readings from the load cells and LVDTs to a dedicated PC. They were connected to the data logger through four RJ50 inputs (see Figure 3.5), one input for each apparatus. Each component was connected to its designated input to ensure reliable data acquisition.

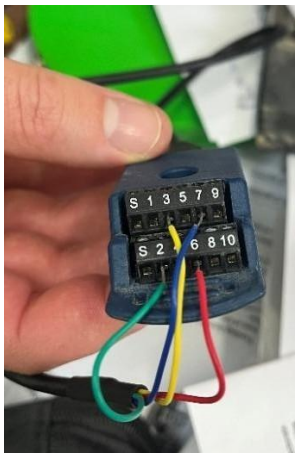

Figure 3.5 - A photo of the LVDT sensor connected to the RJ50 input, which was directly connected to the data logger

3.3.1. New Equipment Installation

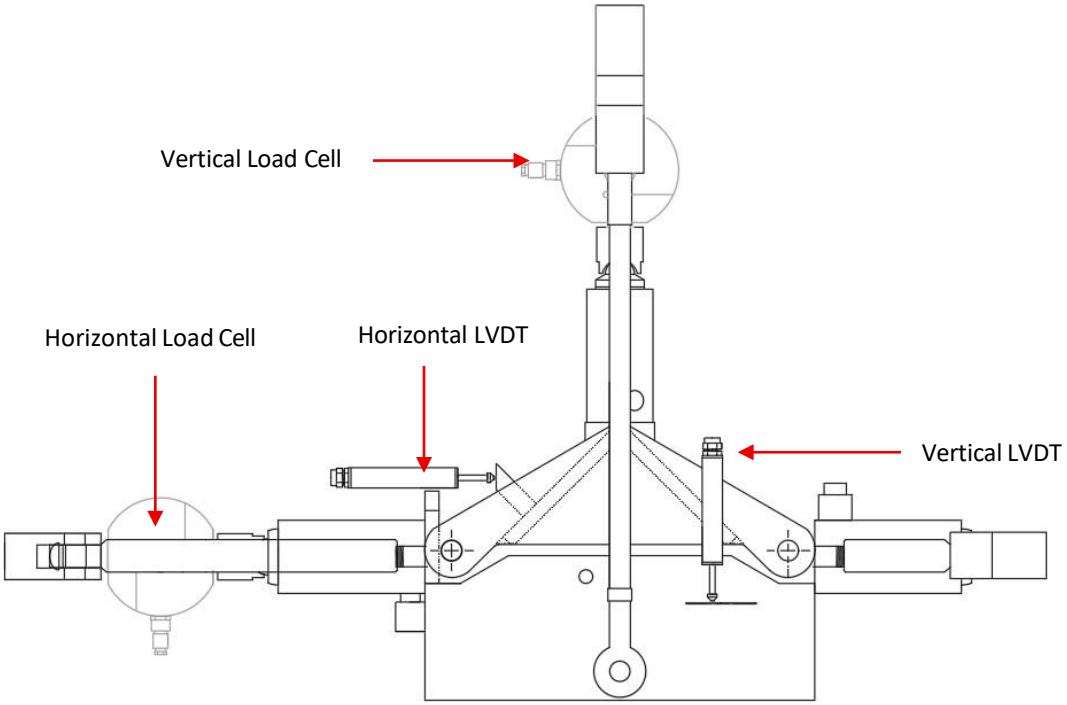

Figure 3.6 - The locations of the 2 load cells and 2 LVDTS

The accuracy of the experimentation was enhanced from the installation of the load cells and LVDTs (see Figure 3.6 for their locations).

The compression load cell uses strain gauges to detect deformation caused by applied loads. As the load is applied, the strain gauges experience a change in resistance which is converted into a measurable voltage using a Wheatstone bridge circuit. This voltage is then interpreted to determine the force applied. The measured force is then converted to stress by dividing it by the contact area between the two specimens.

Two load cells were installed, a vertical load cell to calculate the eventual normal stress and a horizontal load cell to calculate the eventual shear force.

The LVDT (linear variable digital transformer) operates through the principles of electromagnetism. The core within the LVDT moves in relation to the response of the motion of the shear box, outputting a voltage proportionally. A precise measure of linear movement is measured through this sensor. The sign of the voltage indicates the displacement direction, and the magnitude calculates the strain.

An LVDT was added to the shear box apparatus to accurately and continuously measure displacement during the shear testing. Two LVDTs were required, one to measure the vertical movement and one to measure the horizontal movement. These were used to calculate strain and assess the deformation behaviour of the specimen. The vertical displacement captured whether dilation or compression occurred during testing.

All four of these new sensors needed to be calibrated so that their voltage can be correlated to accurate displacement and force readings.

3.4. Equipment Calibration

A pre-set software was written on LabVIEW to read the voltage of both load cells and both LVDT sensors. This voltage reading needed to be calibrated such that the change in voltage can be interpreted as the accurate displacement of the LVDTs and the accurate applied force within the Load Cells (see Figure 3.7).

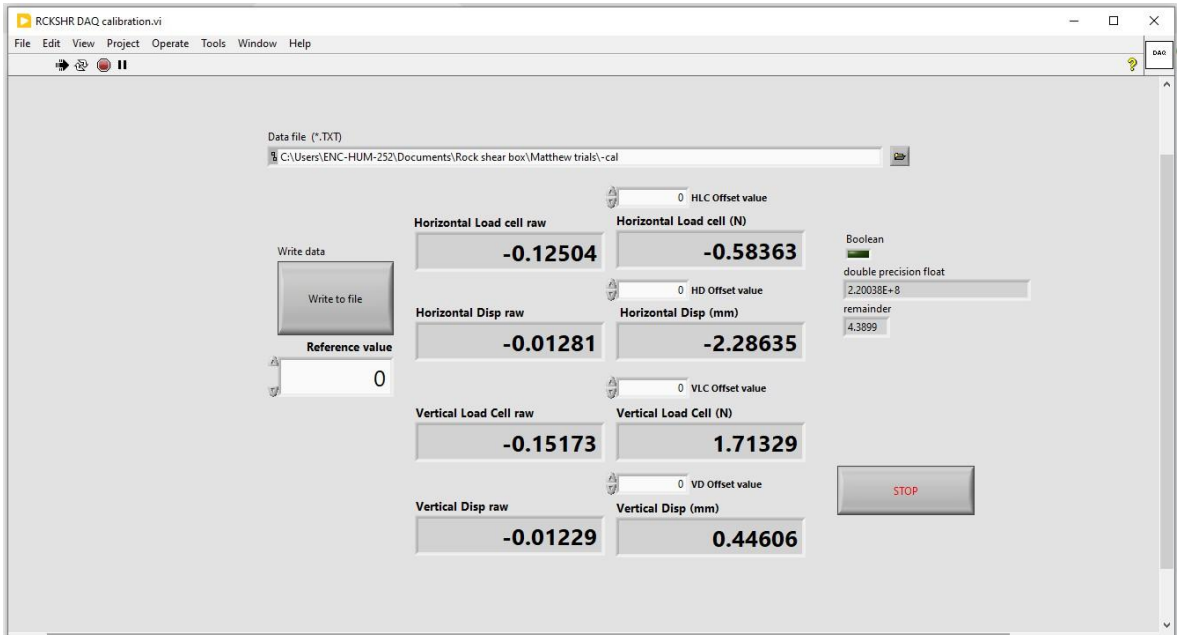

Figure 3.7 - The calibration file on LabVIEW

This new set-up allowed for a more accurate set of readings to be taken, which should be perfectly synchronised. The number of readings taken per experiment was dependent on how the software was run. This was always much more than in the original analogue set-up, reducing errors from few readings.

The calibration of the LVDT was done using the micrometre, as seen on Figure 3.8 (see Appendix 8.3 for calibration certificate). Over here, the distance of the LVDT was increased in increments of 2mm from 0 to 24mm, and back to 0mm. At each distance, the voltage which the software was reading was recorded from the preset calibration file on LabVIEW. Three repeated readings were done for each interval.

Figure 3.8 - The LVDT was attached to the micrometre where readings start being recorded. At this current instance the measured displacement from the micrometre was of 18mm.

The results of these were then plotted as a straight-line graph on excel. The root mean square determined the accuracy of the system. This needed to have its first four or five decimal points to be 9, to be deemed sufficiently accurate for experimentation. Figure 3.9 shows this.

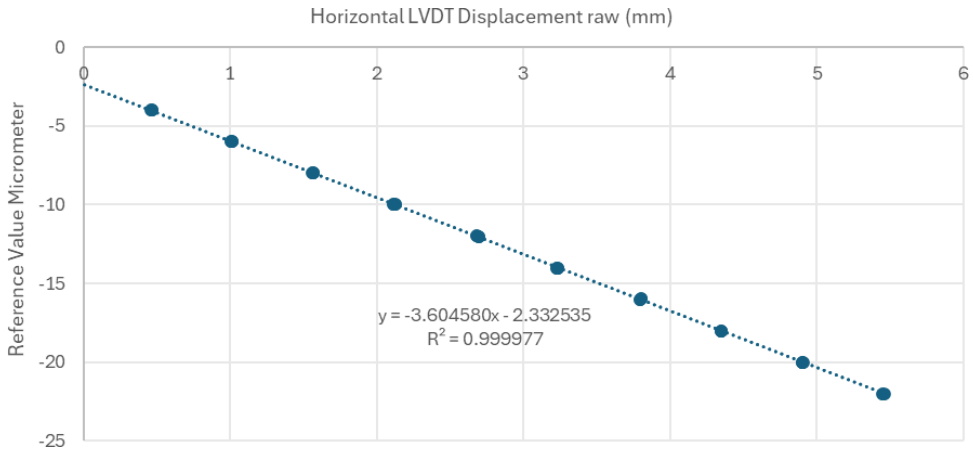

Figure 3.9 - A photo of the tabulated readings for the calibration of the Horizontal LVDT

After the calibration was done, the equation of the best straight line was inputted into the LabVIEW software. Now, the output should give the exact displacement which is present on the LVDT. This was checked by plotting a graph of the new output against the reference value. The gradient of this straight line should be as close to 1 as possible (seen Figure 3.10 below). The intercept within the equation represents the offset value.

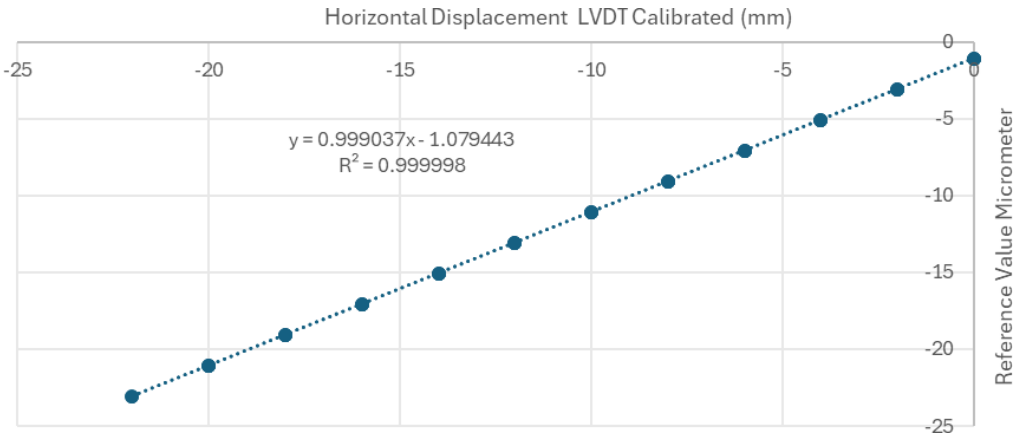

Figure 3.10 -The gradient of the plotted line is 1 when corrected to 3 d.p. giving a fairly accurate representation of the sensor. This is because in this scenario, the equipment is calibrated.

The calibration of the load Cell was done on the compression machine. The compression machine was set such that a force of between 0kN-50kN was applied (see Figure 3.11). This was applied in 5kN increments, and the load cell was loaded in the 0kN-50kN-0kN order, with multiple readings taken at each interval.

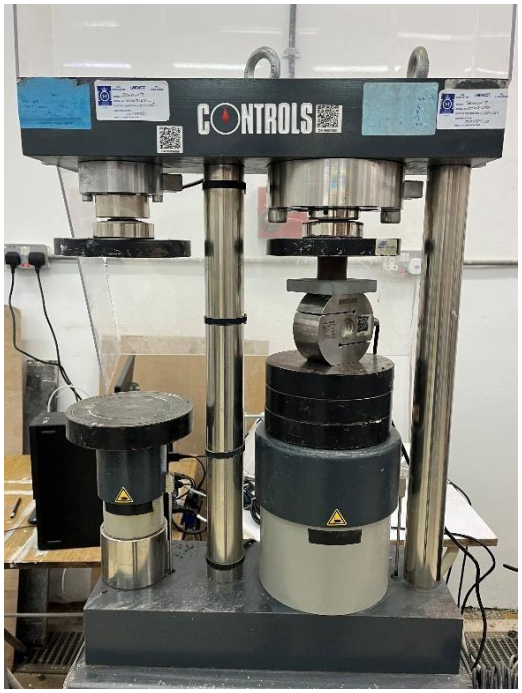

Figure 3.11 - A photo of the load cell placed under the compression machine where a known force is applied.

At every set interval, the corresponding readings on the LabVIEW software were recorded at multiple instances to calibrate the load cells accordingly. These values were inputted into an excel sheet where the best straight line was drawn to match the reading on the software with the actual force applied. The root mean square was also found to showcase the accuracy of the readings.

Following this, the equation was inputted into the LabVIEW software to correlate the applied force with the actual value the software was reading. The gradient of this relationship should be as close to 1 as possible.

After the calibration was successful and complete, the individual elements were then assembled on the direct shear box set-up. This ensured that the apparatus was accurate, synchronised under the ISRM guidelines and with all sensors providing reliable data.

3.4.1. Connection of the load cell in set-up

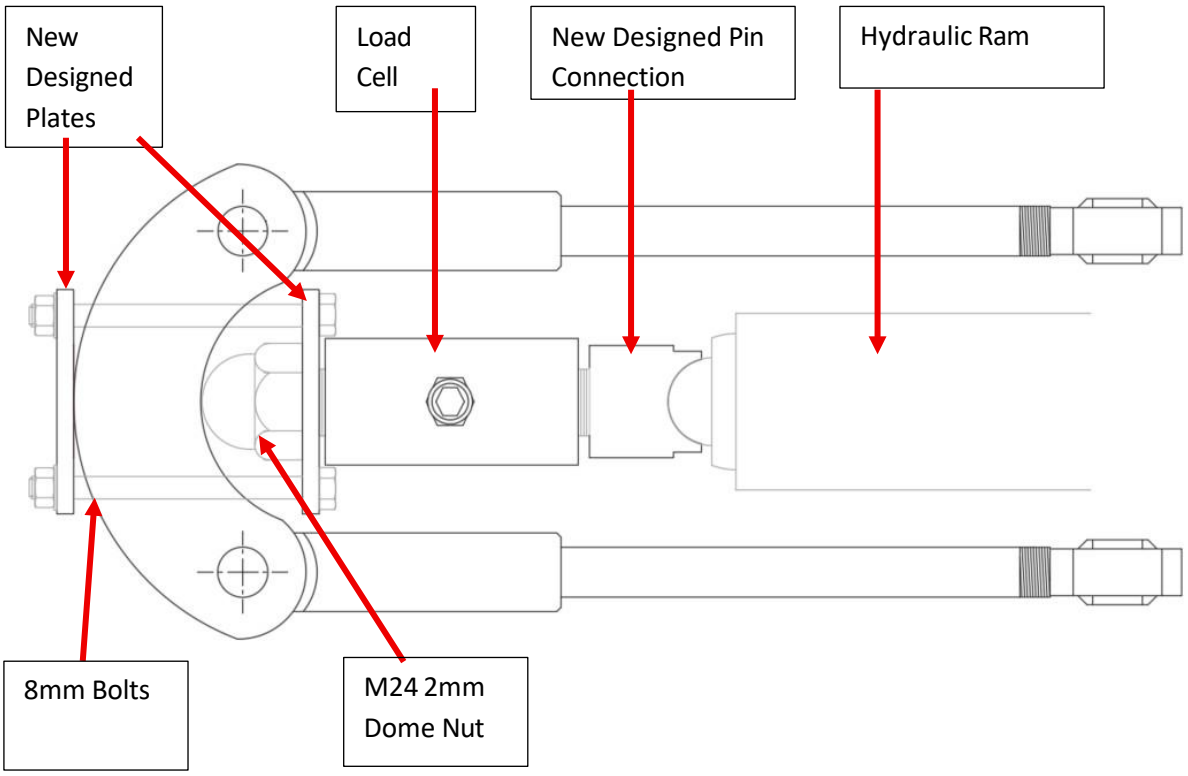

Figure 3.12 - A photo showing the plan view of the complete set-up. This set-up was done for the vertical and horizontal hydraulic rams

The load cell needed to be connected in a suitable way to the overall set-up. Firstly, it was important to analyse the specifications of the load cell. The top and bottom of the load cell allowed an M24 bolt with a 2mm bolt thread to be connected to it. This load cell needed to have a pinned connection to the hydraulic ram on one side and a fixed connection to the steel arm on the other side.

The hydraulic ram to load cell connection needed to be manufactured at the Engineering Faculty. This was because the connection needed to be custom-made to fit the specifications of both the ram and the load cell (as show in Figure 3.1, Figure 3.2, Figure 3.3). This connection was specifically designed and manufactured for the purpose of this research.

The diameter of the ram was first measured using a Vernier Calliper. This provided an accurate measurement of 31mm. A mild steel 40mm cylindrical block was bought so that a hemispherical ball of 31mm diameter can be cut out from this. This would allow the connection to hug the hydraulic ram. Importantly, the centre of the radius to cut the sphere was offset outwards. This was because of ease of fabrication, as the perpendicular edges of a hemisphere are harder to manufacture than smaller geometries. On top of the cut-out hemisphere, 2 indented zones were cut out. This was so that following the experiment, plyers can easily be attached to the connection so that it can be unscrewed from the load cell.

The other side of the connection was a M24 thread with a 2mm pitch cut into the steel cylinder. This was used so that a bolt of the same dimensions would connect this manufactured connection to the

load cell directly. These drawings can be seen on Figure 3.13 and Figure 3.14, where it could be seen manufactured on Figure 3.15.

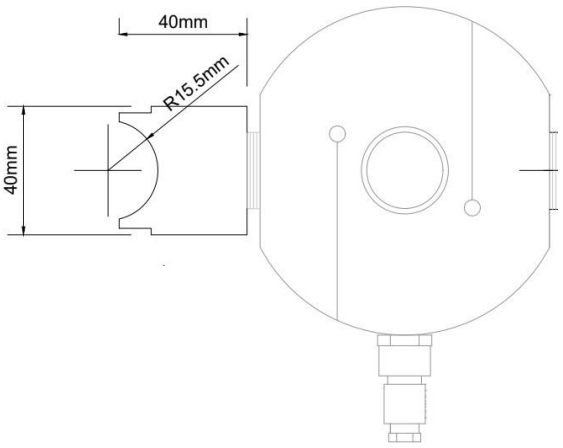

Figure 3.13 - An elevation of how the manufactured connection will connect with the load cell

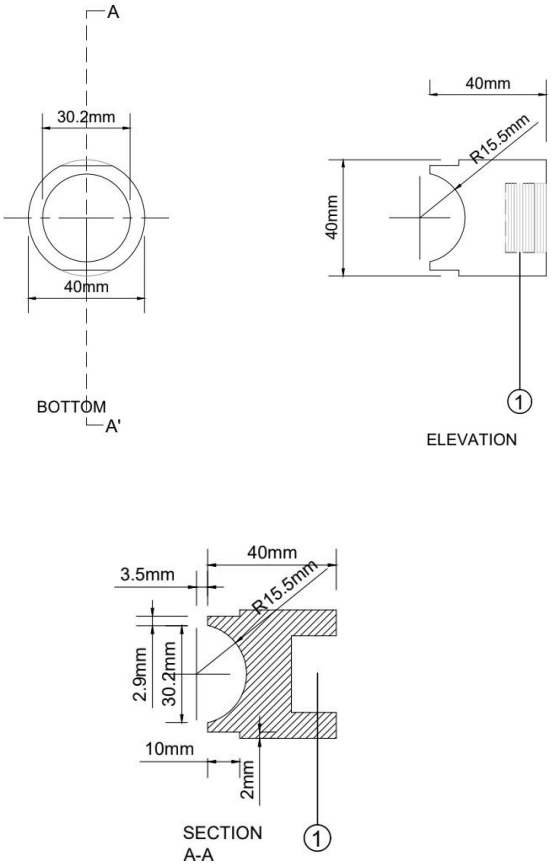

Figure 3.14 - Drawings representing the different views of the manufactured connection. These exact drawings were sent over to the engineering faculty to manufacture the connection from a mild steel cylindrical bar. The numerical label 1 refers to an M24 2mm thread

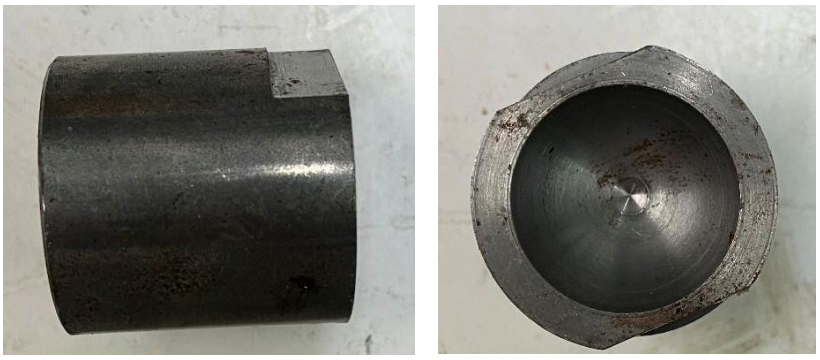

Figure 3.15 - Two photos of the manufactured connection from the above drawings

The load cell to steel arm connection was the other connection which needed to be thought of in this new set-up. A fixed connection in this scenario was required, providing adequate rigidity for the whole experiment.

The load cell from this side was still also an M24 thread with a 2mm pitch, therefore, a M24 bolt with a 2mm pitch was used. This was screwed into an M24x2mm dome nut with a steel plate in between. The dome nut was used so that it keeps the steel plates in place. Importantly, a dome nut was used over a regular nut as the steel arm had an indented area in its centre. Therefore, the dome nut tightened the steel section whilst also touching the steel arm. The steel plates were used so that the steel arm could pass through the section and be tightened in place from the other axis through some bolts.

Since a fixed connection was required between the load cell and the arm, the plates needed to be bolted in such a way that they were restrained from rotating in both directions. This was done through superimposing the dimensions of the steel arm and the load cell. M8 bolts were placed at a very accurate distance so that the screw restrained the load cell with the nut (allowing for 0.5mm of tolerance after the distance between flats was drawn). This accuracy to cut through the plates was achieved through using a milling machine. Although no formal calculations were carried out for this connection design, engineering judgement was applied based on an understanding of the force distribution within the setup.

The steel arm was restrained through the threaded bolts across the plates. The plate tightening the system together was identical to this once described, however, there was no 24mm hole present for the dome nut. The plates were used for the horizontal and vertical arm. The drawings and manufactured plates can be seen on Figure 3.16 and Figure 3.17.

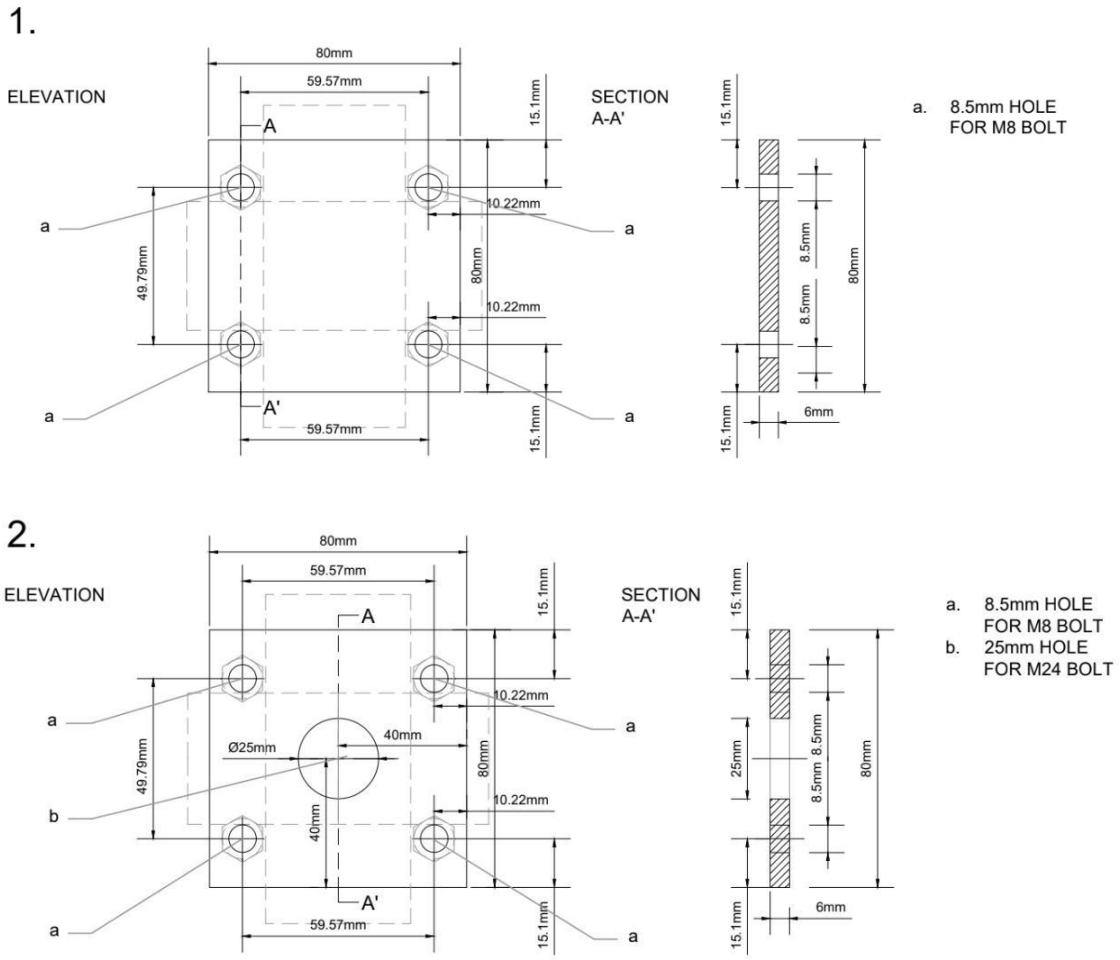

Figure 3.16 - The above are the drawings of the 2 plates which have been cut with the milling machine at the engineering faculty

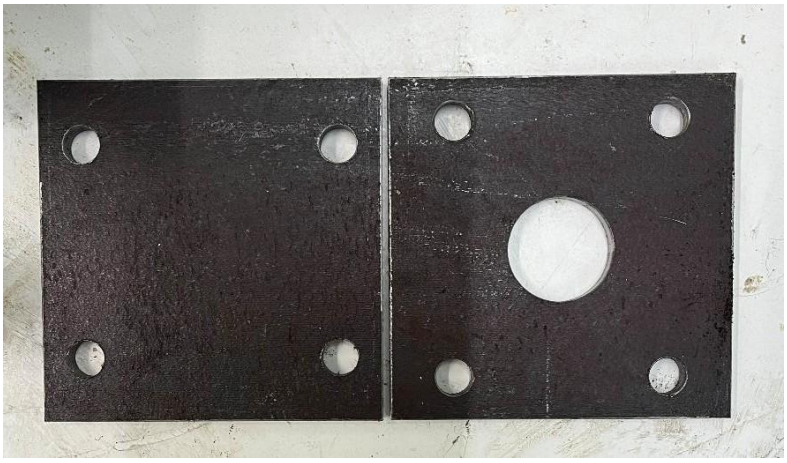

Figure 3.17 - A photo of the 2 different types of plates which were cut by the milling machine.

3.4.1.1. Changing the size of the current set-up

As can be seen in the previous section, the load cell and the new designed connection needed to be installed on the current shear box apparatus. This meant that the steel arms needed to be extended through a threaded rod. Connecting the threaded rod to the equipment was done by designing a steel coupler of 50mm in length. The thread and diameter of the coupler were designed to match both the threaded rod and the original connection to the shear box at M18 1.5mm thread (see Figure 3.18 and Figure 3.19). This coupler was designed for both the vertical and horizontal arms, making a total of four couplers designed.

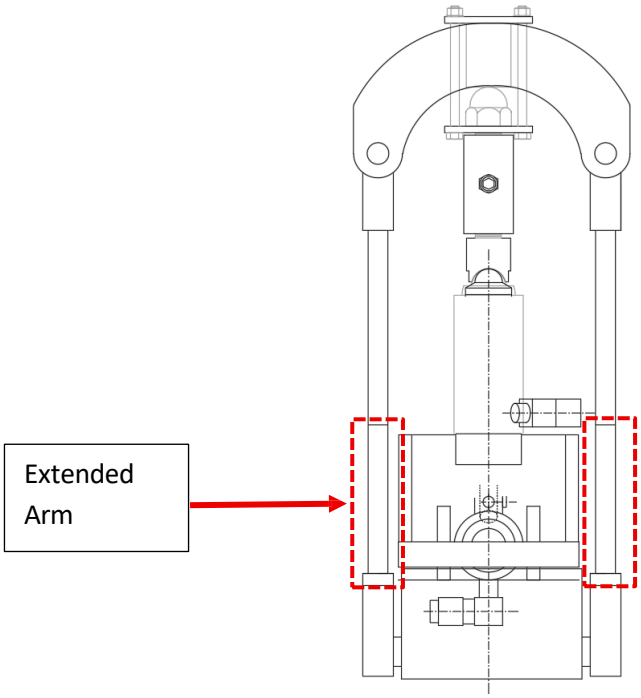

Figure 3.18 - An elevation view of the engineered drawings of the extended set up

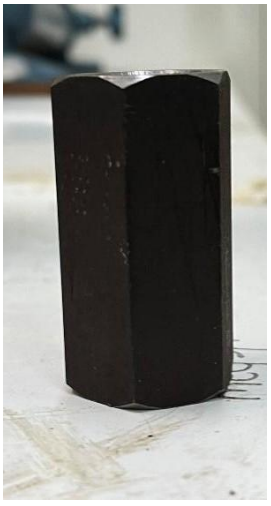

Figure 3.19 - A photo of the designed steel coupler

3.4.2. Connection of LVDT in set-up

The linear variable digital transformer measured relative horizontal and vertical displacement of the separate components of the shear box. It has replaced the dial gauges which were used in Section 3.2. In order to achieve their desired accuracy, the sensors needed to be fixed in place. This was done by 3D printing stands that fit the exact dimensions of the sensor. As the sensor passed through the stand, the stand can be tightened from the top with a screw, making sure it doesn't move further. A hole was designed for the stand to adjust the connection of the stand with the shear box.

The stands were drawn on AutoCad 3D and Rhino so that an .stl file can be generated (see Figure 3.20). This was then sent over to a printing supplier so that the 3d prints can be generated through a plastic filament (see Figure 3.31).

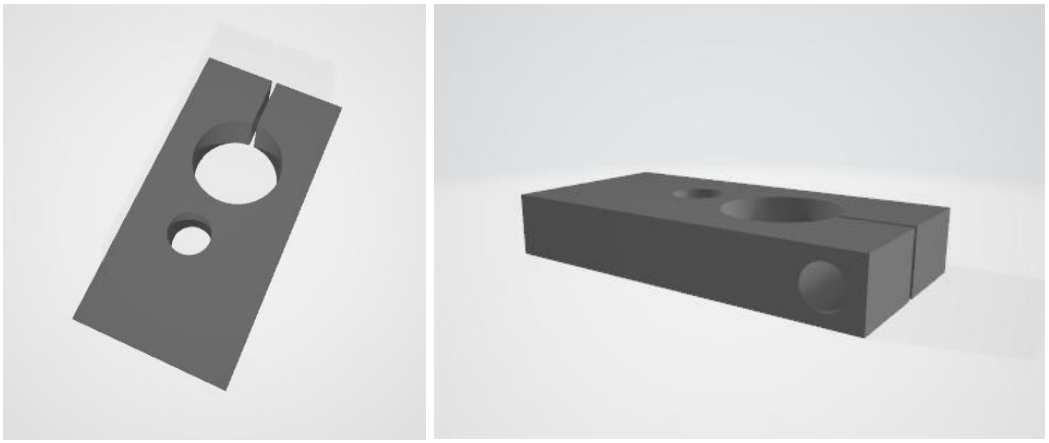

Figure 3.20 - A photo from the STL file, which was sent over for 3d printing

Figure 3.21 - The final 3d printed version of the stand

Following the set-up of all four data inputs, the complete set up was tested with the dedicated PC to see if digitized values were being correctly recorded and producing meaningful results.

3.5. Testing Procedure

With the equipment ready calibrated, the testing procedure adopted was the one indicated by ISRM. Despite this, the ISRM procedure only takes into consideration rock being sheared against rock, without the presence of an infill material. This presented the challenge that Constant Normal Loading (CNL) would not be achieved. This was a method where the normal load applied on the test remained the same, however the presence of dilation from the asperities didn't allow this to occur with the specified equipment, as in this case, load application was manually controlled throughout the test.

The LabVIEW software was set up to take multiple readings per second. This was done through the polynomial:

$$T = Ai^B \qquad \textit{Eq. 3-2}$$

Where i was the reading number and A and B were constants. Since the software was programmed in minutes, A was set to 0.05 and B was set to 1. This ensured that readings were taken every 3 seconds automatically by the software. This both removed human error when taking synchronized readings as well as increased the ease of taking more readings for improved accuracy.

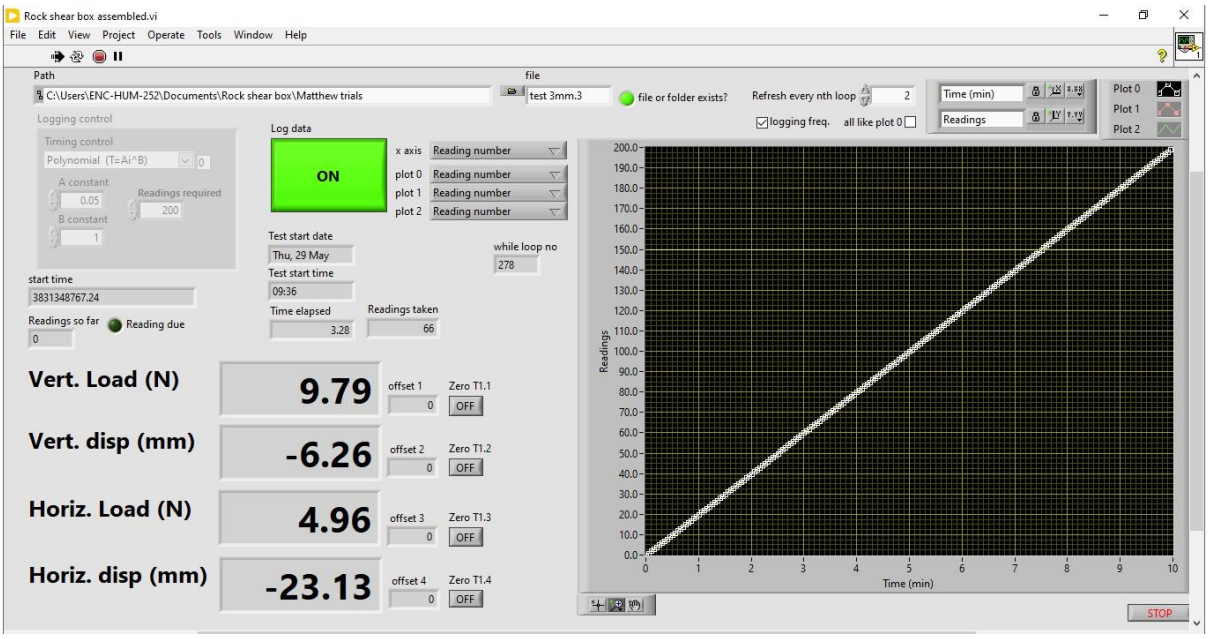

Figure 3.22 - A photo of the LabVIEW interface as it is tabulating readings

In the final tests, the cured plaster samples were prepared for testing. The bottom specimen was smeared with the right amount of clay. The known mass of the required volume of the infill thickness was smeared across the discontinuity surface. Spacers were used to provide uniform thickness throughout the specimen. This specimen with the clay sample was then placed in the shear box. A sample of the clay which was smeared was always taken so that the water content of the sample at that point in time could be calculated.

3.6. Preliminary core trials and observations

For the preliminary trial test, the rock specimen was chosen after careful analysis of type of rock, the quality of rock extraction, and rock discontinuity from a borehole core. This was because of the regularity of rock extraction from a borehole core. Had rock been chosen directly from the field, this would have been prone to surface weathering. Regularity within testing procedure was crucial for early equipment trials.

The dimensions of the specimen under test were understood. This was determined by the dimension of the encapsulation area which can be seen from Figure 3.1 and Figure 3.24. This dictated the size constraints of the test specimen. The Lower Globigerina Limestone specimen which was used was then cut to fit the shear box. Importantly, when cutting the rock specimen, the discontinuity was not touched. This was because the shear strength of the discontinuity was going to be tested, meaning it needed to be present (see Figure 3.23).

Figure 3.23 - A photo adjusting the actual size of the rock to fit the mould. The discontinuity is not cut out.

The rock specimens were tied to eachother through a series of rubber bands. This kept the contact area the same, preventing the rock from moving. A solution of plaster and water could easily be prepared and poured into the mould former with the rock specimen upright there. This was because the geometry of the rock did not fit perfectly within the circular rock specimen which was cut.

Releasing agent oil was placed on the surface of the mould former before the solution was poured. This would help the solidified mould to be removed from the mould former. As time passed, the mould would harden, keeping the rock specimen perfectly in place and upright.

The plaster solution was then poured into the mould when the rock was in a vertical position. The mould was sealed in all axes so that no plaster would seep outwards. When it was poured, the plaster solution would take up the negative volume of the mould where the rock was present. This ensured that the rock specimen was subsequently kept in place as a normal and shear force was applied. Plaster

was also used as it hardens quickly, providing a very good stand for the rock. The plaster would also not crack and not affect the main rock specimen under test. This can be seen on Figure 3.24.

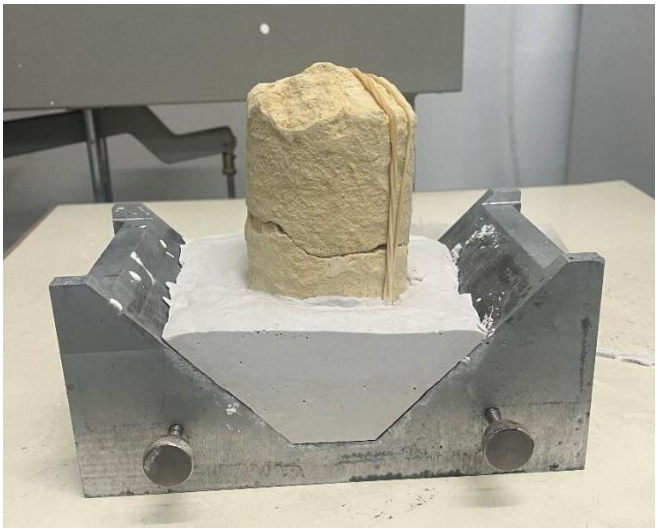

Figure 3.24 - A photo showing the rubber bands used to keep the rocks in place as the mould is being cast. This plaster solution holding the rock specimen is then encased in the Direct Shear Box as shown in Figure 3.1.

When the plaster base of the rock solution had hardened, the same process was then repeated on the other base of the rock. This allowed a mould to be formed on both the top and the bottom of the rock (see Figure 3.25).

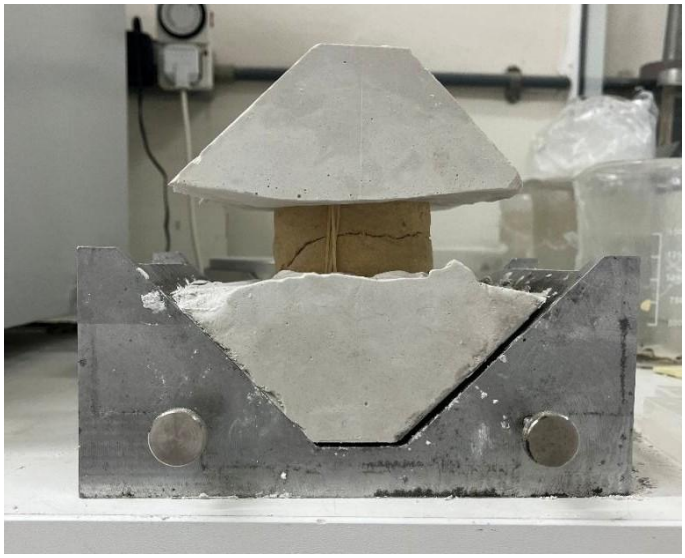

Figure 3.25 - A photo of the moulds in place with each other. Following this, the sample can be placed in the shear box.

The rock specimen was then placed inside the direct shear box for the ISRM preliminary test procedure.

From this test, the difficulty in sourcing the same Lower Globigerina Limestone and testing the infill thickness was anticipated. Therefore, alternative sources to simulate rock and discontinuities started being evaluated.

3.7. Simulating Rock

To address these limitations, it was decided to simulate the rock by substituting it with Plaster of Paris and pouring it in a mould of a chosen geometry. This was because the compressive strength of Lower Globigerina Limestone is comparable to that of Plaster of Paris after several days of curing. In reality, the anticipated results are likely to be more conservative than those for the Lower Globigerina Limestone (*Barbieri, 2021),* since the Lower Globigerina Limestone is slightly stronger. Figure 3.26 shows how the UCS (Unconfined Compressive Strength) values for Lower Globigerina Limestone range between 5Mpa and 20 MPa. The Plaster of Paris from the research of Barbieri (2021) ranges between 5-7 MPa.

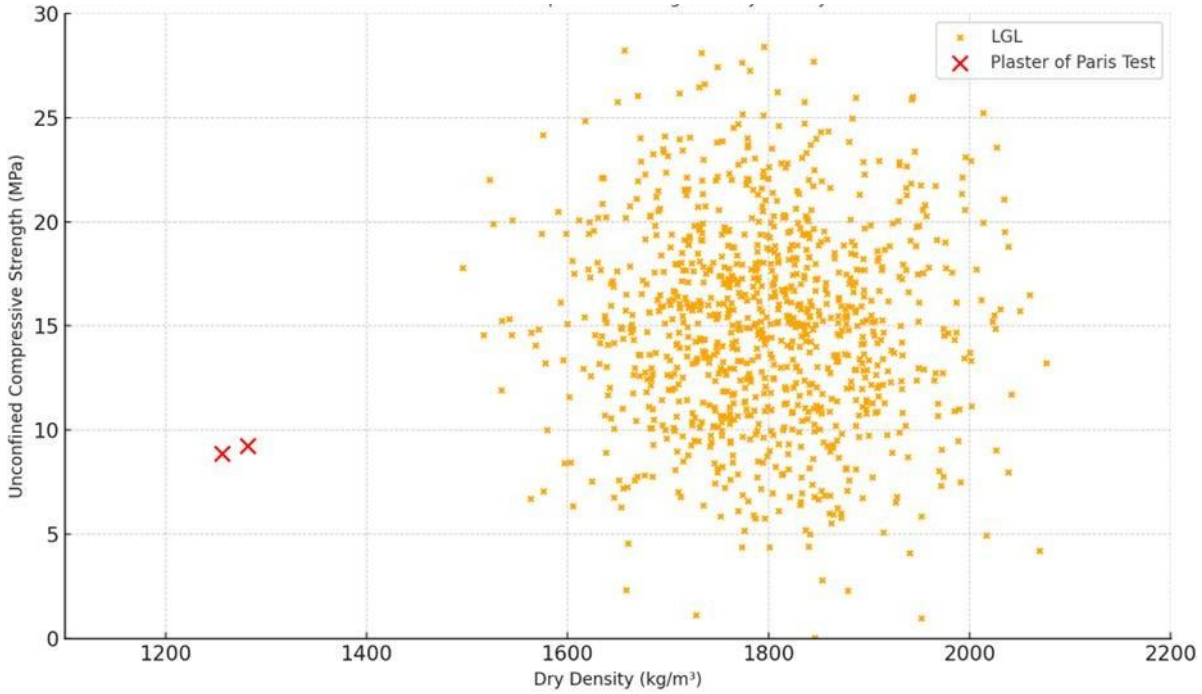

Figure 3.26 - Unconfined Compressive Strength vs Dry Density of LGL (Barbieri, 2021) and mean Plaster tests

The Plaster of Paris was used because this allowed both the discontinuity and the compressive strength to be consistent throughout experimentation. This was because the plaster test specimen were prepared under controlled mix proportions within a controlled lab environment rather than extracted from the ground. This, therefore, reduced the number of variables being present when assessing the situation at the contact area (through using a mould) and strength within each respective test. Reducing such variables would aid the actual variables of the infill material and thickness to take for the change in readings.

Other materials like concrete, would produce stronger specimens, which would not be representable of Lower Globigerina Limestone. The curing of plaster would be uniform for a specific time frame. This contrasts with other materials like concrete, which would be very sensitive to its hydration environment, reintroducing the heterogeneity. Aggregates are also not needed in plaster, creating a smooth texture, which was desired for the experimental set-up and uniform contact area.

3.7.1. Plaster Applicability

Despite the analysis carried out by Barbieri (2021), where a ratio of 1:0.5 (plaster:water) was used, the strength of the plaster needed to be confirmed. This was because different types of plaster and different water-content ratios would yield different Unconfined Compressive Strengths (UCS). Therefore the UCS value of this plaster-water ratio would need to be compared to a database of information of UCS tests on Lower Globigerina Limestone. A plaster to water ratio of 1:0.6 was used for this experimentation, as extra workability was achieved with more water for specimen forming.

Whilst the specimen were prepared, extra volume of the solution was poured into 50x50mm cube moulds. These would then be compressed in the compression machine on the same day that the actual specimen would be tested in the shear box test (see Figure 3.27 and Figure 3.28. This would give an understanding of the compressive strength of the specimen under test. The Plaster of Paris would therefore a representation of whether it would be a comparable alternative to the Lower Globigerina Limestone.

a)  b) 

Figure 3.27- a) A photo of the 50x50mm plaster specimen under the compression machine. b) A photo of the shear failure which the paster specimen went under the compression machine

Test No.	Date of Casting	Date of Test	No. of Days	UCS (MPa)
1	29.04.2025	28.05.2025	29	8.30
2	29.04.2025	28.05.2025	29	9.78
3	29.04.2025	28.05.2025	29	10.73
4	29.04.2025	28.05.2025	29	9.00
5	30.04.2025	29.05.2025	29	8.58
6	30.04.2025	29.05.2025	29	9.07
Average				**9.24**

Table 1 – Database of UCS tested values

A database of Lower Globigerina Limestone (LGL) strength values was analysed from Solidbase Laboratories Malta, which have a database of the strength values of the Maltese rock formation. The statistical mean LGL UCS value from the Solidbase Database was 12.15 MPa. This rock was slightly stronger than the 9.24 MPa average which resulted from the cube testing.

Apart from this method, more properties relating to the Plaster of Paris were found, such as the Bulk Density, and Dry Density. These were found by extracting plaster volumes from an already tested plaster specimen (see Figure 3.28 and Figure 3.29). These were found by taking further measurement on cubical volumes of hardened plaster trimmed back from the same specimens that were used in the shear box.

Figure 3.28 - The plaster volumes being extracted from the already tested specimen

The plaster was cut out to a known volume, weighed and placed in the compression machine. The properties were then found as seen in Table 2. The plasters variables compared relatively well to the Lower Globigerina Limestone variables.

Test No.	Bulk Density (kg/m^3)	Moisture Content (%)	Void Ratio	Dry Density (kg/m^3)
1	2052.00	60	1.11	1282.5
2	1905.90	60	1.27	1191.2

Table 2 – Properties of extracted rock

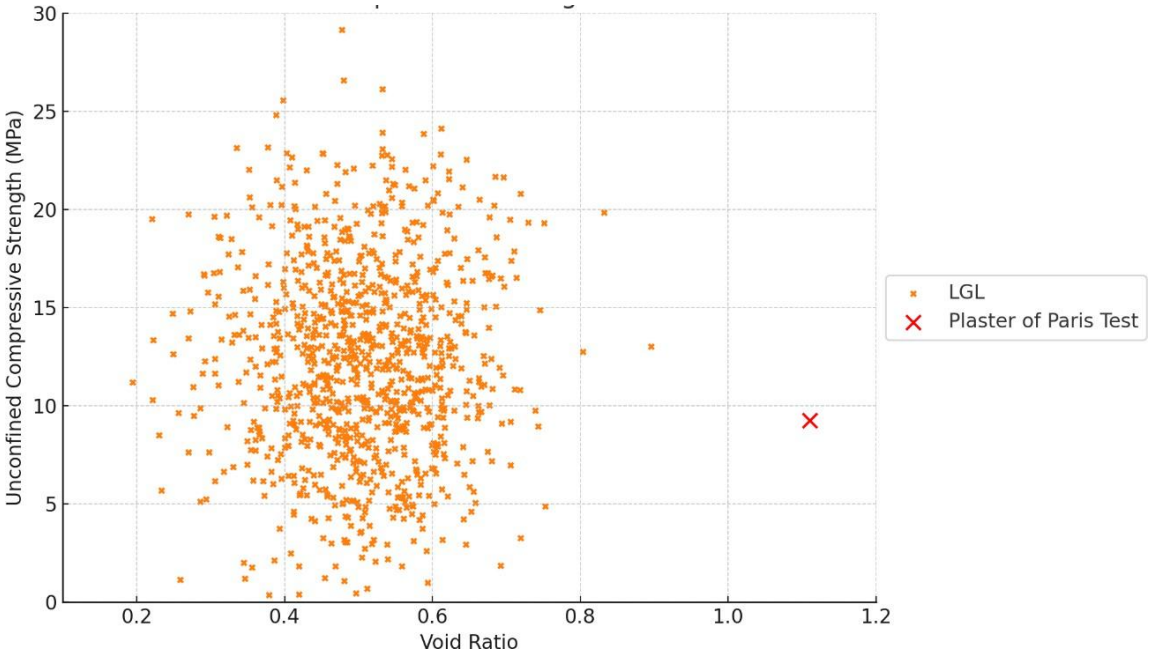

Figure 3.29 - Unconfined Compressive Strength vs Void Ratio of LGL and mean Plaster test value (Barbieri, 2021)

3.7.2. Geometry Applicability

The chosen geometry of the mould stemmed from the study of Patton (1971) who relates inclination angles and asperity heights of saw-tooth discontinuities which was discussed in the literature. Eq. 2-14 depicts this in Section 2.3.2.1. However, this doesn't consider the infill material. The discontinuity was designed to have a 5mm asperity height and an 18.5-degree angle. This geometry was chosen based on the research of Indraratna (2010), so that a comparative study could potentially be done, who also included clay infill with plaster discontinuity replicas of this geometry for his testing procedure. The 18.5 degree should lie in the transitional range where sliding and breakage interact *(Indraratna, 2010).* The 5mm also ensures the interlocking effect so that a noticeable dilation can be present. Smaller asperity height will not produce noticeable dilation whilst greater asperity heights will produce premature asperity failure *(Indraratna, 2010).*

Patton (1971) shows how the asperity inclination between 15-20 degrees represents a zone where both dilation and shear can be captured without the induced brittle failure. In the experimentation of Indraratna (2010), this same range was confirmed. The chosen conditions would therefore reflect the mechanical interaction between the clay infill and the discontinuity surface. Indraratna (2010) also showed how this study is also present and relevant when an infill thickness is present. These results helped to understand how soft materials like clay affect jointed rock mass stability. This study also used a plaster set-up to simulate rock.

The selection of the 5mm asperity height and 18.5 degree angle reflets typical conditions in weathered rock. The simplified geometry corresponds to a Joint Roughness Coefficient (JRC) value estimated within the range of 12-15 (from observing Figure 2.11 in Literature Review), as defined by Barton and Choubey (1977). This is based on the angle and spacing of the saw-tooth asperities. This JRC range is consistent with the findings of Barbieri (2021) who reported JRC values of 12.5-14.2 in X and Y scanning direction on weathered Globigerina Limestone. Therefore the simplified geometry represents a plausible discontinuity profile found in Malta.

Through a replication of such geometry, detailed assessment of how roughness and infill interact during shearing. The practicality of this includes how the discontinuity roughness and infill will influence the slope stability failure. This is common in weathered jointed rock masses where the clay will reduce the effect of the cohesion and friction angle. The test geometry quantifies how the infill modifies the shear response. This set up will not only mirror realistic geometries in slopes and excavations, however, will also serve as a platform for calibrating numerical models in slope stability.

3.7.3. 3D Printed Mould

The mould to create the replicated rock through plaster was 3D printed (see Figure 3.30). This needed to be thought out both from an experimental point of view as well as by understanding the workability and issues of creating a mould, and how removing the mould may affect the experiment. In theory, the contact area should only be between the discontinuity interfaces. However, this would provide the problem that perpendicular faces between the 3D print would be present. The mould would be impossible to remove without damaging the plaster, meaning a variability of cut-out edges would be formed between one experiment and another. This problem was tackled by creating chamfered edges. This allowed for the mould to be removed easily, consistently keeping the same contact area within one experiment and another, despite the chamfered edges creating an irregularity when calculating the contact area.

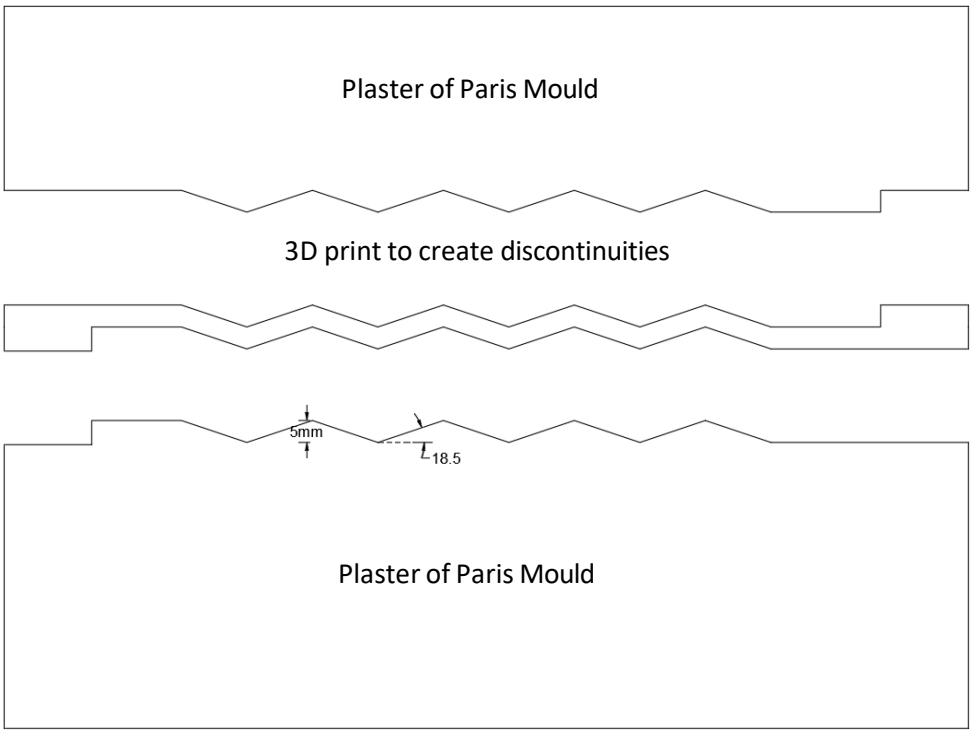

Figure 3.30 - A drawing of how the test specimen will be created through pouring the plaster mix into the negative space occupying the print. The 3d print is designed in such a way that the negative space between the top and bottom mould will interlock with each other

The Plaster of Paris mould was prepared several days before the experiment was carried out. A curing time of 28 days is a conventional benchmark in concrete testing. The application of 28 days or more served to ensure a complete moisture loss and material stabilisation in the plaster. Plaster of Paris typically reaches its functional strength within a few days *(Barbieri,2021)*. The extended curing time was adopted as a conservative measure to eliminate incomplete drying. This duration was verified through preliminary testing shown in Section 3.7.1.

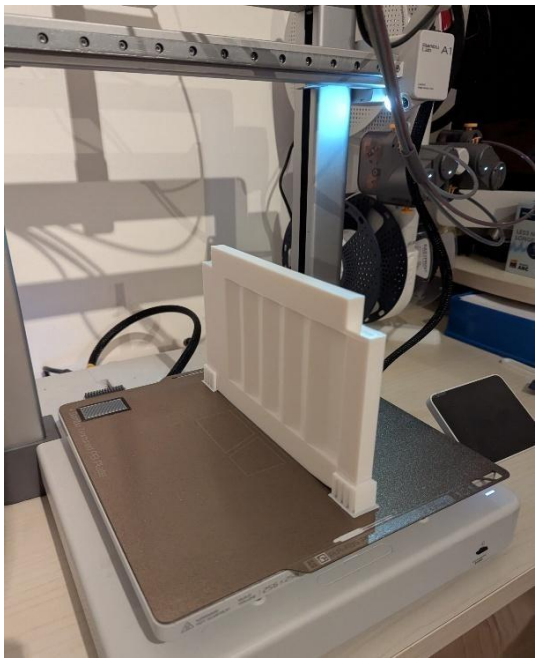

Figure 3.31 - A photo of the mould being 3D printed

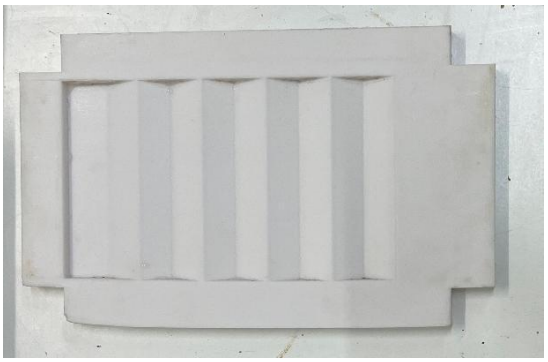

Figure 3.32 - The 3D printed mould

Following the 3D prints being prepared, they were then used to prepare the mould for the test specimen.

3.7.4. Mould Preparation

The plaster mould was made from a ratio of 1:0.6 (plaster: water). This brought about the desired compressive strength which neared the 12 MPa as well as the desired workability of the mix to be poured into the mould. This was mixed with a mixer so that no clumps of unmixed plaster would be present. This can be seen below in Figure 3.33.

Figure 3.33 - The plaster mix was placed in the mixer so that any clumps of unmixed plaster were removed

The steel mould representing the geometry of the shear box (seen in Figure 3.25) was clamped together with the 3d print dividing the space, ensuring tightness all round. Release agent was placed on the 3d prints and the steel mould, so that the cured plaster mould would be easier to separate from the 3d print. The tightened mould was then placed on a vibrating table, which would be switched on as the solution was poured into the mould. The vibrating table minimised the air bubbles which could form when working with plaster. These were not desired as they alter the contact area from one mould to another.

The plaster was left to cure for 2 hours until the steel mould was unscrewed outwards and the 3d print was separated from the solidified mould. The two separated plaster specimens were left to cure for several days until testing was done. Figure 3.34 and Figure 3.35 show this process.

a) 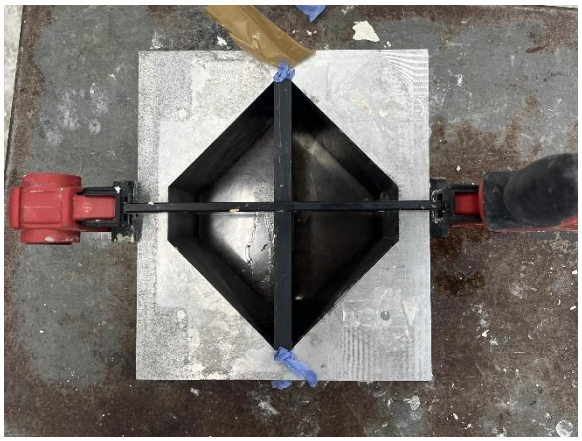 b) 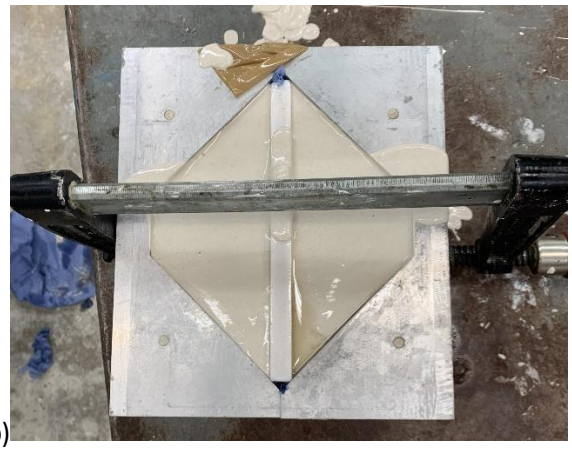

Figure 3.34 – a) The steel mould clamped together with the print acting as the divider between the space, right before the mixture was poured. b) A photo of the plaster seFng after it was poured into the mould. This was left to set for 2 hours.

a)  b) 

Figure 3.35 – a) A photo of the plaster after it had set, and the steel mould was removed. After removing this, the 3d print would then be removed. b) A photo of the discontinuity created on the plaster of Paris face, with the 5mm asperity and 18.5- degree orientation discussed earlier

3.8. Sampling the Clay

3.8.1. Location of Blue Clay

The clay which was used for testing was extracted from a site in Santa Maria Estate, Mellieha (Figure 3.36, Figure 3.37, Figure 3.38 and Figure 3.39). This was the same clay which was used in the study of Cassar (2020), where its properties were analysed. It required a preparation process prior to being used for experimentation. The Blue Clay under test was found at 50 asml and a moisture content ranging from 40-50%.

Figure 3.36 - The location of the extracted Blue Clay used in the experimentation. The red circle marks the exact location. (Cassar, 2020)

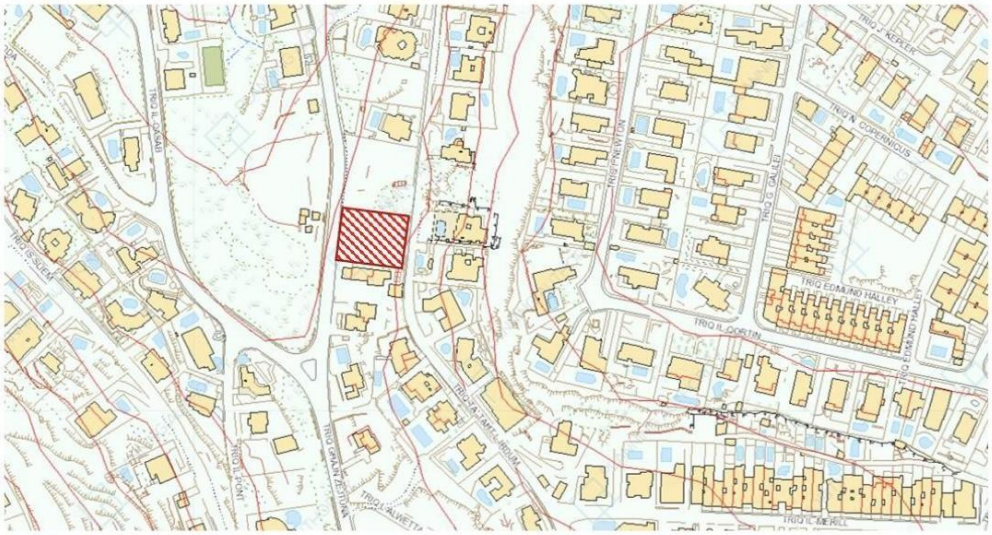

Figure 3.37 - Location of sample collection highlighted on topographical map with a difference in 10m between from and back of site (Cassar, 2020)

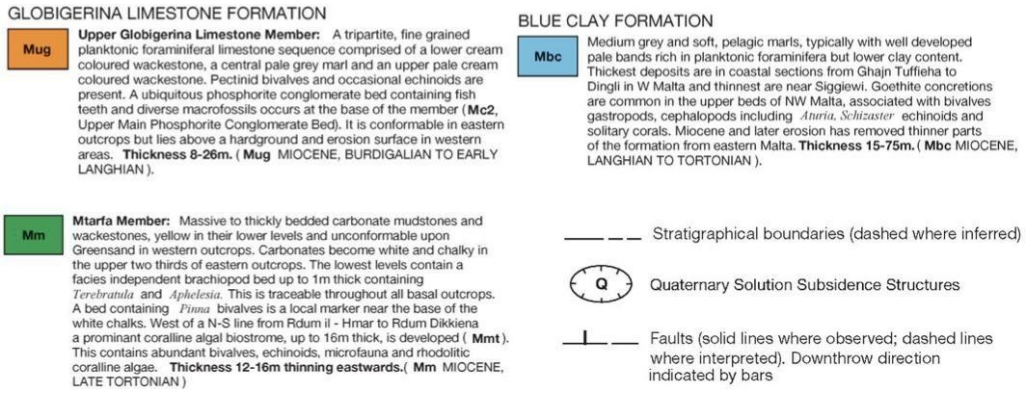

Figure 3.38 - A photo explaining the location of the site in red with a legend of the geological map

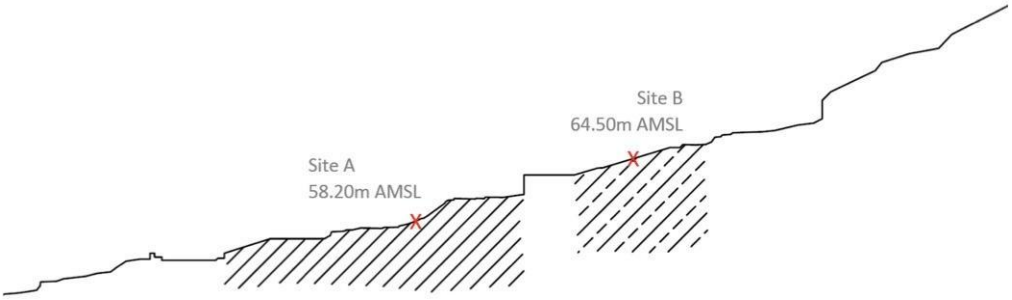

Figure 3.39 - A photo depicting the topography of the site. The clay used for this experimentation was from Site A

3.8.2. Preparing the Blue Clay for testing

The Blue Clay was firstly put in a container, where distilled water was then added. This allowed the clay to swell. Following this, the clay was then put in a mixer for 24 hours (see Figure 3.40). A pillar drill was used to form a slurry from the clay and distilled water solution. The mixer was formatted such that it would be mixing for 45 minutes and resting for 15 minutes for the entirety of the 24 hours.

Figure 3.40 - A photo of the clay being mixed into a slurry using a pillar drill for 24 hours

After this, the slurry was then passed through a sieve of 63 µm. This process was done to separate the sand particles which would be present within the Blue Clay.

The distilled water which was on top of the mix was then siphoned. Following this, a sample of the slurry was placed in a container. The container was placed on an electronic balance before so that the actual mass of the slurry would be known. This mix was then placed in an oven which was set between 100-105 degrees Celsius for 24 hours. This temperature ensured that the un-siphoned remaining distilled water which was originally placed in the mix was then evaporated so that the dry weight of the mixture could be tabulated. This was done through Eq. 3-3 below from the phase relationships:

$$w = \frac{M_w}{M_s} * 100\% \qquad \textit{Eq. 3-3}$$

Where M_w is the mass of water, M_s is the mass of soil and w is the water content value.

Trays of slurry were then placed into the oven. The greater surface area from the trays allowed for evaporation within each slurry to happen quicker. The trays were left in the oven at 105 degrees overnight. The clay was then crushed into finer particles so that it would be easier to re-mix with distilled water. Once again, using the water content phase relationship, the mass of distilled water per tray which was needed to reach the desired water content was then calculated (see Figure 3.41).

a) 

b) 

c) 
d) 

Figure 3.41 – a) Measuring the amount of slurry poured into a container whose mass had already been found. b) After the clay was dried, its dry mass was noted and it was broken down into very fine pieces. c) The known mass of fine clay, was further crushed through a mortar and paste . d) A known mass of distilled water was added so that the clay at the right water content is sampled

The desired ratio of clay-water mix was then worked such that a homogeneous mix was formed for the tests, removing lumps which would be present from poorly crushed clay samples.

a) 
b) 

Figure 3.42 -The clay samples before it is worked. b) The clay samples after it is worked

A water content of 45% was desired. This was based of the research of Cassar (2020), where a good plasticity was reached at the 45% water content for the same type of clay used. Different water contents were assembled for the same clay, confirming the 45% as the optimal workability.

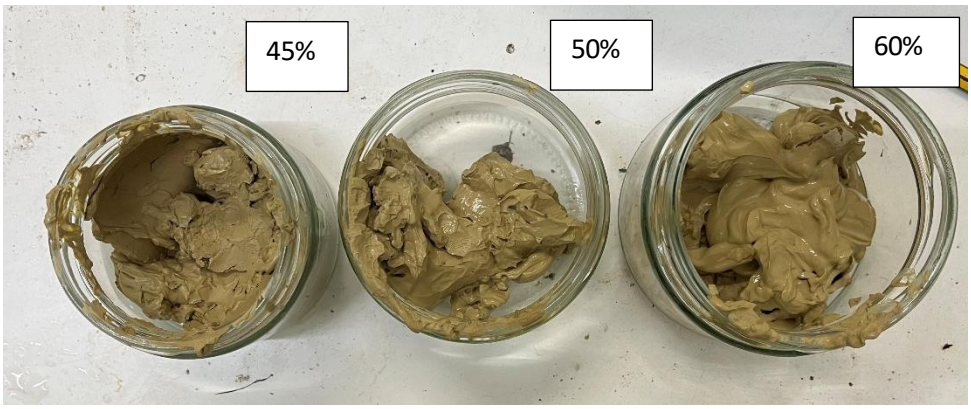

Figure 3.43 - 3 different samples were prepared at different water contents where the 45% was chosen to be the most workable and used for the entirety of the tests

The required volume of clay for each test was found. This was done by firstly, calculating the area of the face of the 3d mounds. This area was multiplied by the infill height to determine the volume required. Three different volumes for three different clay infills were calculated. Therefore, the amount of slurry needed for a test at 45% water content was found. This was done through the void ratio where:

$$e = \frac{V_v}{V_s}$$

Where V_v is the volume of air and water (all voids are filled with water as 100% saturation is assumed) and V_s is the volume of soils.

3.9. Specimen Preparation

After the specimens were cured for approximately 28 days, they were ready to be used for experimentation.

Figure 3.44 - A photo of the specimens before testing

The known mass of the required volume of clay was smeared on the bottom specimen. Spacers were placed on the edges of the specimen so that the volume was kept consistent throughout the preparation process. This was further aided by compressing the top specimen to the bottom specimen. Uneven clay smearing would allow the extra localised clay volume to be pushed out of the edges in this process. This extra volume was then re spread on areas with evident less clay presence.

Clay was only applied to the bottom specimen (see Figure 3.45). This decision was made because the clay mix had a relatively low water content (45%), which reduced its adhesiveness. Applying both surfaces risked the clay detaching or falling off the top specimen during placement or testing. Applying to only the bottom ensured consistent coverage while preventing any displacement during assembly.

a)  *b)* 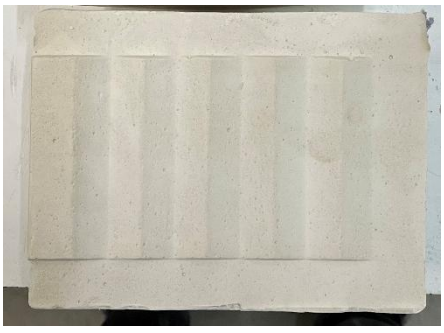

Figure 3.45 - a) A photo of the bottom specimen smeared with clay. b) The top specimen

The top part of the shear box and the top specimen were weighed (Figure 3.46). This was because under the test, the normal force from the hydraulic pumps on the specimen would not take into consideration the normal force induced by the self-weight of these two objects. These would therefore be added to the normal force calculation.

a) 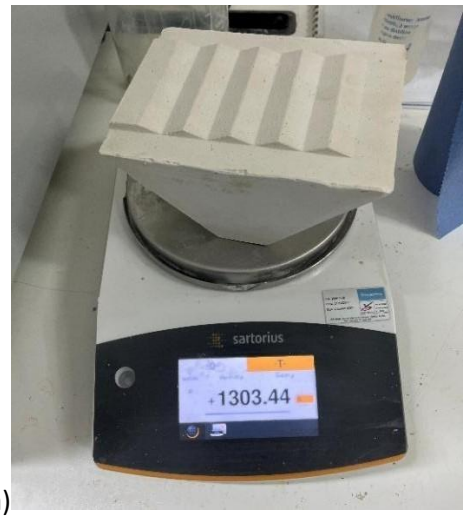

b) 

Figure 3.46 – a) Finding the mass of the top specimen. b) Finding the mass of the top part of the shear box

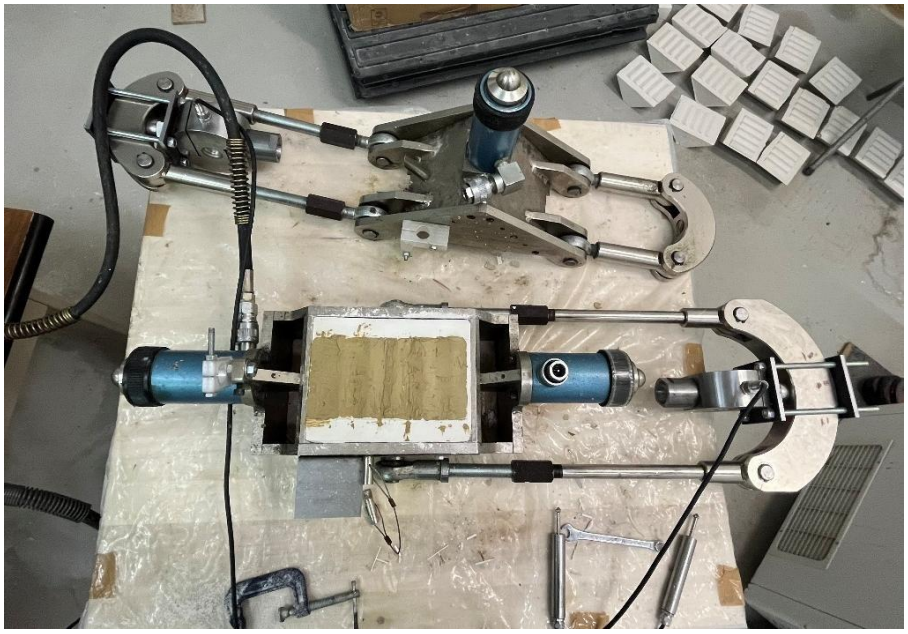

Figure 3.47 - The bottom specimen as it is placed in the shear box

Once the shear box was set up (see Figure 3.48, Figure 3.49, Figure 3.50), the sensors secured and the software was giving an output, a normal force was applied by the hydraulics before the software started running. The initial normal force was targeted to be 4 to 10 kN for respective tests, serving as a reference point. However, due to manual operation of the hydraulic levers, precise application was challenging. To mitigate this, the change in normal force during testing was monitored through displacement readings, ensuring that any variations originated only from dilation or compression rather than additional applied load.

The shearing rate was adopted by the ISRM standards which were mentioned in Section 3.2.1 where 0.1-0.2 mm/min was maintained throughout. Shearing was manually kept constant throughout the entire of the process, however this was dependent on human error. As mentioned in Section 3.2.1, the

ISRM standard recommends a strain rate of 10-15%. Only 6% was achieved in this test due to equipment limitations.

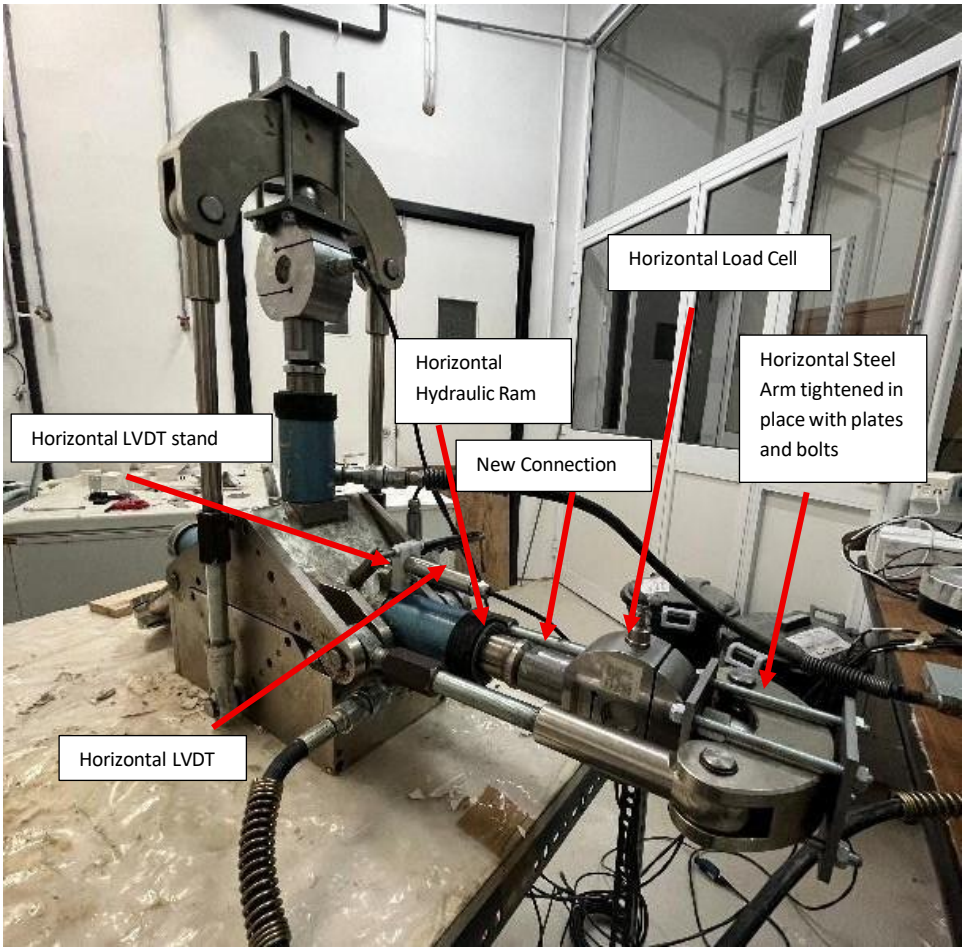

Figure 3.48 - A photo of the modified equipment during an experiment

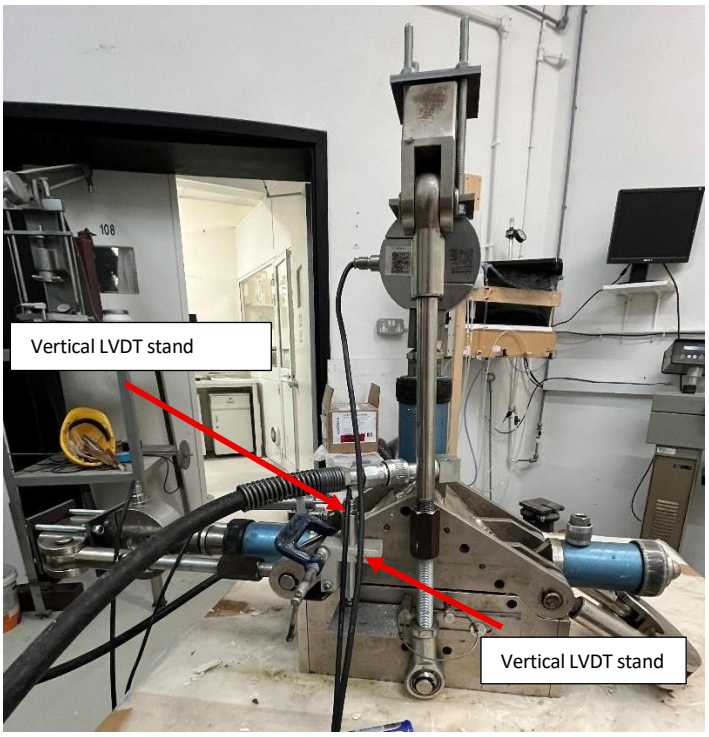

Figure 3.49 - A photo of the modified equipment during an experiment

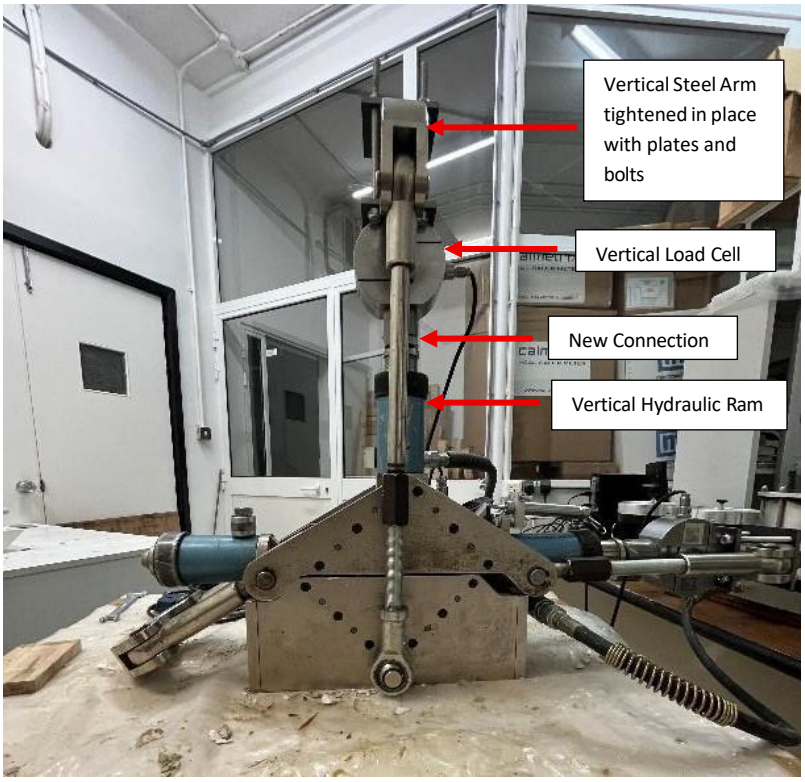

Figure 3.50 - A photo of the modified equipment during an experiment

Figure 3.51 - A photo of the specimens after test

The test was stopped once a sufficiently large shear force was induced on the hydraulic pump. This was based on the manual force on the lever which was connected to the horizontal ram, not producing any further increase in value to the horizontal load cell.

Once the experimented was terminated, the valves of both pumps were released so that no force on the specimen would be present. This allowed for careful demounting of the top specimen, enabling the specimen halves to be separated with minimal disturbance.

Following the experiment, the failure on the specimen was noted (as seen above Figure 3.51). Samples of the clay were once again taken after experimentation. This was done so that an understanding of how much water was lost during the setting up time and shearing process would be understood (more detail on this is mentioned in Section 4 and Section 5). Re-testing on the same specimen was never done because of the deformation which occurred on the specimen.

The recorded data from the software was then analysed. The results were correlated with the data logger inputs, indicating what each output represented. The data was cleaned by zeroing values when necessary. Results such as the Strain % were calculated as the shear displacement value from the sensor in relation to the total shearing distance (the sheared length of the mould was 175mm). The stresses were calculated from Eq. 3-1. Graphs of Shear Strain vs Time, Shear Stress vs Shear Strain, Normal Displacement vs Shear Strain and Shear Stress vs Normal Stress were then plotted through Microsoft Excel.

4. Results and Discussion

4.1. Estimates of the Clay's Undrained Strength

The undrained strength of the clay, of which shearing behaviour depends, was found by pocket penetrometer tests and by pocket shear vane test on specimens of the slurry. This was an important procedure as the shearing would be governed by the undrained strength of the clay.

Undrained conditions were selected because short-term loading conditions of clay in a natural, saturated state were aimed at. Pore water does not have the time to dissipate, highlighting how clay will be present in its undrained shear strength. Drained tests provide more long-term stability application, which was not focused on in this research. The undrained strength therefore provides a more realistic measure of the clay's behaviour under the rapid loading provided by the direct shear box apparatus in this experiment.

The clay samples were smeared inside a glass container. This container was first wiped thoroughly with acetone prior to smearing the clay. The container was thoroughly knocked on a surface so that the any voids within the clay was removed. The top of the container was then wiped with a scalpel to have a smooth surface. Figure 4.1 below shows the clay in the container.

Figure 4.1 - A photo of the smooth clay surface inside the container

The pocket shear vane was inserted into the middle of the container (see Figure 4.2). The container was clamped to the surface. The pocket shear vane was inserted sufficiently so that the entire depth of the vane would be inside the clay. In fact, the size of the vane itself was chosen both so that the depth of the vane would fit in the container and so that the radius of the vane would be sufficient to rotate within the container.

Once the vane was inserted, it was given a manual twist. The vane was rotating within the clay until one complete revolution of 360 degrees was completed. The reading on the shear vane was then tabulated.

Figure 4.2 - A photo of the shear vane test as it was being inserted inside the container

The pocket penetrometer test was then carried out (see Figure 4.3). This was carried out by inserting the tip of the penetrometer into the clay sample. A force required to penetrate the clay generated a dial reading on the penetrometer. This reading was then taken note of.

Figure 4.3 - A photo of the pocket penetrometer test as it was being inserted inside the container

The large penetrometer was used for measuring the undrained strength of the clay. The results using the pocket Penetrometer were as follows:

Test No.	Penetrometer Size	Penetrometer Reading	Undrained Strength, S_u (kPa)
Test 1	Large (x 25)	0.25	6.25
Test 2	Large (x 25)	0.25	6.25
Test 3	Large (x 25)	0.4	10
Average			**7.5**

Table 3 – Penetrometer test of undrained clay samples

The Pocket Shear Vane test was also used to determine the undrained strength of the clay. The results on the Shear Vane test were as follows:

Test No.	Shear Vane Size	Shear Vane Reading	Undrained Strength, S_u (kPa)
Test 1	Small (x 21.18)	0.7	14.8
Test 2	Medium (x 10.84)	1.7	18.4
Average			**16.6**

Table 4 – Shear Vane test of undrained clay samples

The results of the undrained strength of the clay needs to be analysed by looking at the Plasticity Index and Atterberg testing results of the clay under test. These results were published by Cassar (2020) (Figure 4.4).

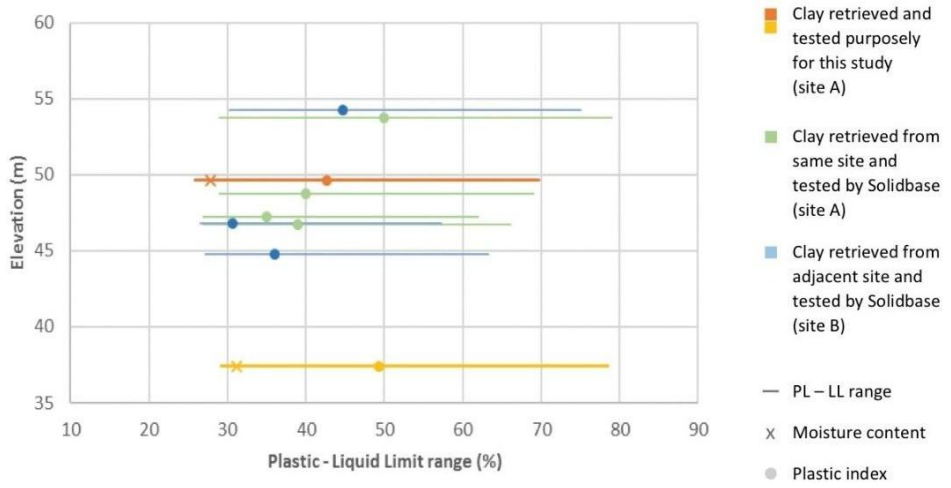

Figure 4.4 - The Atterberg Testing carried out by Cassar (2020). The red marking is the disturbed Blue Clay used throughout experimentation

The Plasticity Index (PI) of the clay under test was found to be 45. This was calculated through:

$$PI = PL - LL \qquad \textit{Eq. 4-1}$$

With the PL (75) and LL (25) extracted values from Figure 4.4.

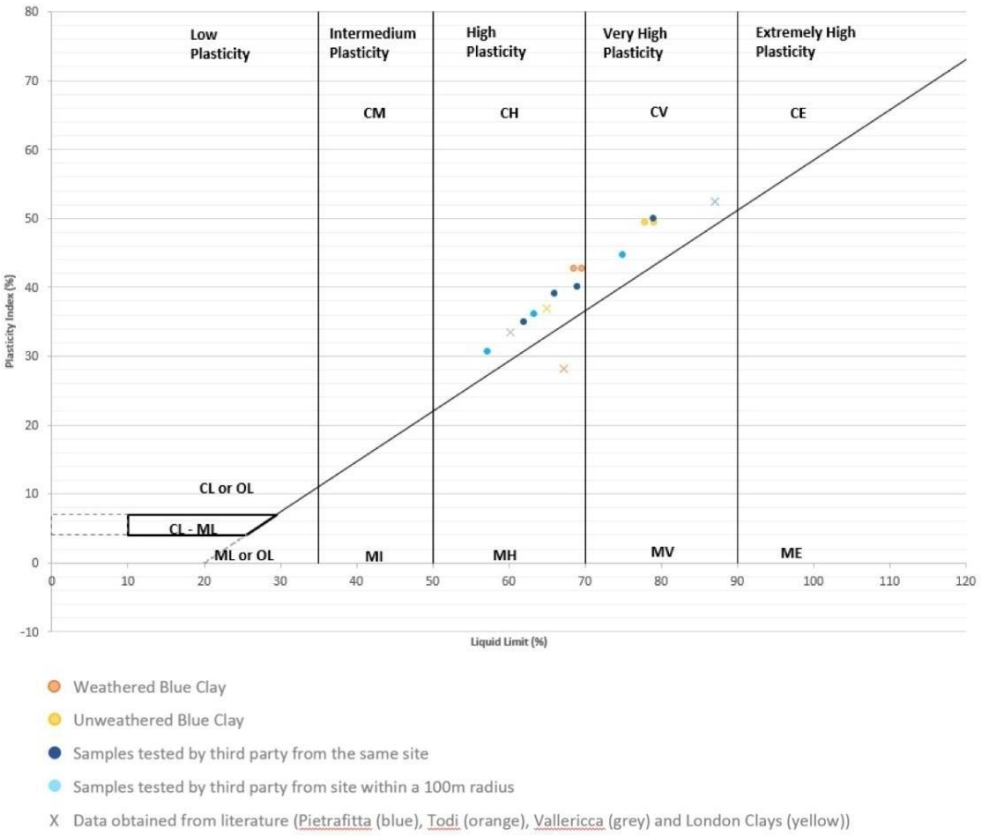

Figure 4.5 - The plasticity chart for the Blue Clay throughout experimentation

By correlating the PI and Liquid Limit to Figure 4.5, it can be concluded how the clay has a high plasticity. What was present during the experiments has been altered by the placing process. It has dried in the meantime, and the water could have absorbed the plaster.

4.2. Overview

The main results together with a discussion and interpretation are presented in this section.

Shearing along a discontinuity occurs through frictional forces, especially in planar faces where there is direct contact. When this occurs, the roughness of the surface influences the frictional force present. This is further affected by the presence of asperities and undulations, as this resistance is further increased.

The clay infill will alter the discontinuity surface interaction. In planar surfaces with no asperities, the shearing could occur along the rock-clay interface or within the material. This is dependent on the relative strength. When asperities are introduced, the clay will shear or compress depending on the water content and stiffness, and also on the discontinuity aperture. Wider gaps will inherently allow more deformation when compared to smaller gaps.

The dimensions of the test specimen were selected to ensure consistency across all tests and were based on the limitations of the laboratory setup, particularly the size of the shear box and the hydraulic system. while literature acknowledges that specimen size can influence shear behaviour, particularly in relation to scale effects and asperity spacing, the specimens in this study were sized to maintain the same asperity frequency and distribution across all tests. This ensured that any variation in response could be more confidently attributed to the infill thickness and not to changes in scale. The asperity geometry was also scaled proportionally with the specimen, maintaining consistent ratios across the tested surfaces.

To cover the above considerations, several infill thicknesses were considered whilst keeping the asperity size constant in all specimens tested. The chosen range varied between 0mm (the asperity faces were in direct contact), to 10mm, where the infill thickness was larger than the space required for the asperities to move relative to eachother without colliding. The 10mm infill was selected to simulate a dominant clay-filled discontinuity, where the clay infill governs the shearing behaviour. In between, intermediate thicknesses of 1,3, and 5mm were considered, where the latter value is equal to the asperity height. The clay infill thickness was controlled by measuring a consistent mass of clay for each specimen, as mentioned in 3.8.2. This approach ensured that the volume and therefore the thickness of clay remained constant across all the tests. To further assist this, spacers were used along the specimen edges to contain the clay during smearing and compression, allowing for even redistribution.

A specimen having a 10mm thick infill and smooth discontinuity sides was also tested so as to test a discontinuity that is predominantly affected by the clay infill rather than the discontinuity faces. Similarly another specimen with a Plaster to Plaster contact with no infill was tested to obtain a baseline measurement whereby the clay infill does not feature. The initial contact area for the testing procedure was taken as 15750mm^2 which was based off the geometry of the mould.

Smooth-surface tests were conducted for the 0mm and 10mm infill only, as they represented the two extremes of interface behaviour, the direct plaster to plaster contact (no infill) and complete governed clay infill (full infill). The intermediate thicknesses stated earlier were only tested using asperity surfaces, as the study aimed to investigate how clay interacts with discontinuity geometry. Including the intermediate thicknesses for smooth surfaces was considered less critical since, without asperities,

the shearing resistance is already minimized. The focus was thus placed on the more representative rough-surface condition.

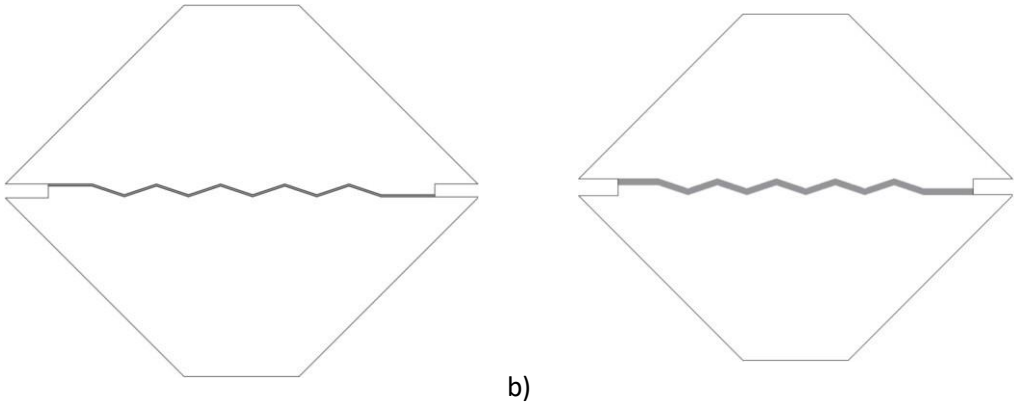

a) b)

Figure 4.6 – a) A drawing of the 1mm infill and the plaster mould b) A drawing of the 3mm infill and the plaster mould

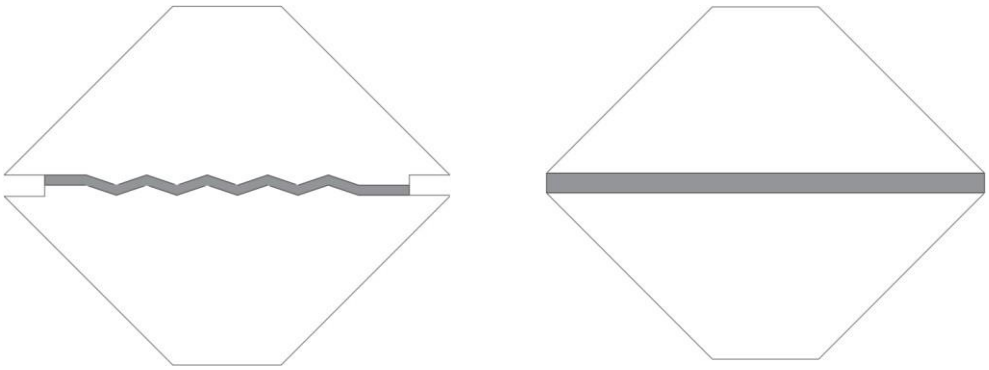

a) b)

Figure 4.7 – a) A drawing of the 5mm infill and the plaster mould b) A drawing of the 10mm infill and the plaster mould with no asperities

The stream of data from the two orthogonal sets of sensors (load cell and displacement sensor measuring load and deformation in each of the horizontal and vertical directions) results were acquired by the national instruments datalogger and displayed in real time on screen, whilst being recorded in a text file compiled through the bespoke virtual interface (*.vi) written specifically for this purpose using LabVIEW software.

Further processing of this data was then carried out in Microsoft Excel, where all the necessary corrections were made and where all the resultant stresses and strains were calculated. These were then used to understand the mechanical behaviour of each test. The results were processed as follows:

The Time vs Shear Strain gives an indication of the rate at which the hydraulic pumps were operated to create the necessary forces that cause shearing action at the discontinuity faces. This is because the shearing rate has an effect on the dissipation of pore water pressure. A fast shearing rate is likely to impose undrained conditions within the clay, whereas slower rates will give better understanding of

drained conditions. Drained tests would take hours. However, undrained conditions were targeted throughout this experimentation. This graph is to therefore give an indication of the strain rate.

The Normal Displacement against Shear Strain gives an understanding of whether the fissure represented by the two plaster casts and clay infill is undergoing changes in volume (compression or dilation). This has a direct effect on the instantaneous contact area as the normal force is being applied, and will indicate the type and amount of work done in having the simulated fissure surfaces sheared against eachother.

The Shear Stress against Shear Strain gives an understanding of mechanical properties of the soil and its interaction with the Plaster of Paris casts. Properties such as the peak strength, residual strength and post-peak behaviour can be evaluated from this curve.

Finally the graph of Shear Stress against Normal Stress allows the strength characteristic of the discontinuity assemblage to be determined, in this case using a Mohr-Coulomb fit to define the strength envelope. Further to this, the resultant stress path from this curve allows investigation into the stress history of the clay infill and provides insight into the various mechanisms that evolved during shearing action.

4.3. Results of individual tests

4.3.1. Results of 1mm Infill Thickness

A total of 3 tests were performed at different initial normal stress (0.42 MPa, 0.54 MPa and 0.58 MPa), applied on the Plaster of Paris casts. As stated in Section 3.9, the initial normal forces were targeted to range between 4-10kN, however were difficult to achieve manually. The normal forces were just a mere starting point for every test and shouldn't have affected the accuracy or behaviour in any way.

The force values were converted to stresses by taking into consideration the contact area of the test specimen which was 15750 mm^2. This contact area was then adjusted as horizontal displacement was present when shearing occurred.

Test No.	Applied Force (kN)	Stress (MPa)
1	9.14	0.58
2	8.51	0.54
3	6.61	0.42

Table 5 – 1mm tests

This range does not follow the ISRM suggested Methods of having well-separated values, however this was due to the limitations of the manual shear box apparatus, due to human error which limiting the range of stresses.

It was after the normal force was applied that the software started recording readings. This was done to avoid capturing initial compression displacements that occur during the application of the normal load. Such displacements would not be representative of the clay behaviour, but reflect the immediate mechanical response to the applied load.

The tests at 0.54 MPa and 0.58 MPa normal stress do not differ significantly from another. They were retained to observe the shear response in relation to small increments.

From Figure 4.8, the specimen with the smallest normal force was sheared at the fastest rate, with 11% strain in 7 mins suggesting that pore pressures within the clay had very little time to reach equilibrium and therefore implying undrained clay behaviour. This aligns well with the discussion in Section 3.2.1, where it was highlighted that the maximum strain achieved during the experiments was limited to 6-11% due to equipment limitations. Contrasting this, the slowest test (0.57MPa) shows a smoother stress response (6% strain in 10 minutes). In general, a stable gradient is present for the majority of all 3 tests, except for the last part of the test at the highest pressure.

For all three tests in Figure 4.8, no shear strain was recorded within the first minute. This was primarily due to a temporary incomplete loading path as the testing procedure commenced, and shear was applied. Specifically, the hydraulic ram had to interlock with the connection for the displacement sensor to record readings. Until this interlock occurred, no displacement – and hence no shear strain, could be recorded. In contrast, the load cell was already registering force, allowing shear stresses to be calculated.

To ensure accuracy and clarity in the presentation of results, the graph in Figure 4.8 was filtered to exclude this initial segment where the equipment was not fully engaged. This ensured that the plotted

data reflects only the active shearing behaviour after the displacement sensor began recording reliably. Further discussion on this limitation is presented in Chapter 6 under Further Research.

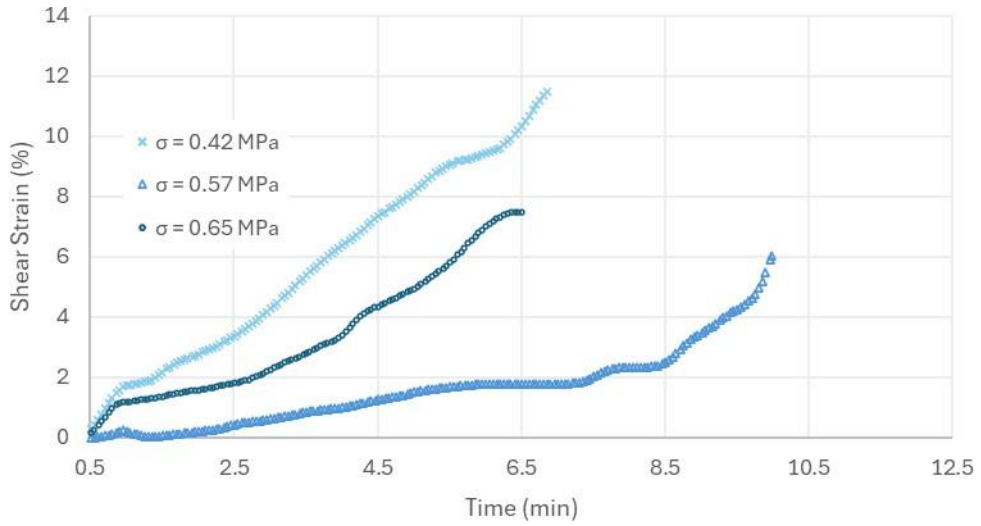

Figure 4.8 - Shear Strain(%) against Time (min) for 1mm.

Figure 4.11 shows consistent hardening behaviour with the lowest shear stress present in the test specimen with lowest initial σ_n. When referring back to the literature in Section 2.3, strain hardening behaviour suggests the behaviour of normally consolidated clay which is consistent to the methodology of preparing the clay as a slurry to remove its stress history.

Importantly, this behaviour is relevant up until the shear strain value of around 8.5%. This is a critical strain level, as originally it was assumed that this strain represented the point where the two plaster faces of the asperities made contact and subsequently started being sheared against eachother. However, after careful analysis of all the results and comparing these with measurements taken on the apparatus, it was concluded that this strain level represents the point where the steel body of the lower half of the shear box comes into contact with the hinge of the loading yoke moving the upper half. This can be seen on Figure 4.9.

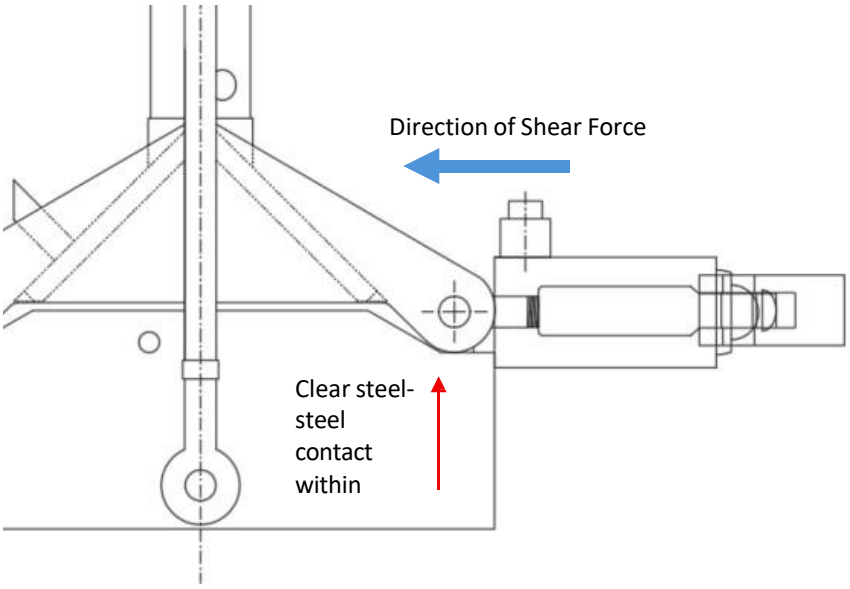

Figure 4.9 - Steel-to-Steel contact present whilst shearing in the latter stages of the test

In this regard, all results after this particular strain level (8.5%) should be ignored, as these represent forces and displacements in the steel body and not in the specimen. This concept is spoken about in more detail in Chapter 0(Further Research). The strain values at the early stages are also marked on Figure 4.11 having no tabulated readings due to the error discussed in the previous paragraph.

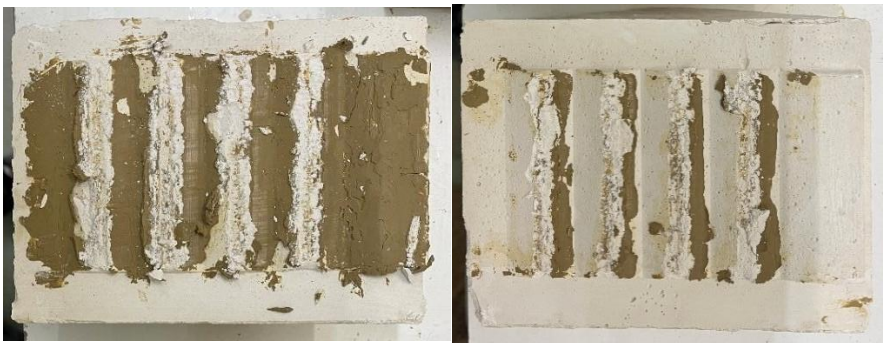

Figure 4.10 - Bottom and top specimens for Test 1 after experimentation

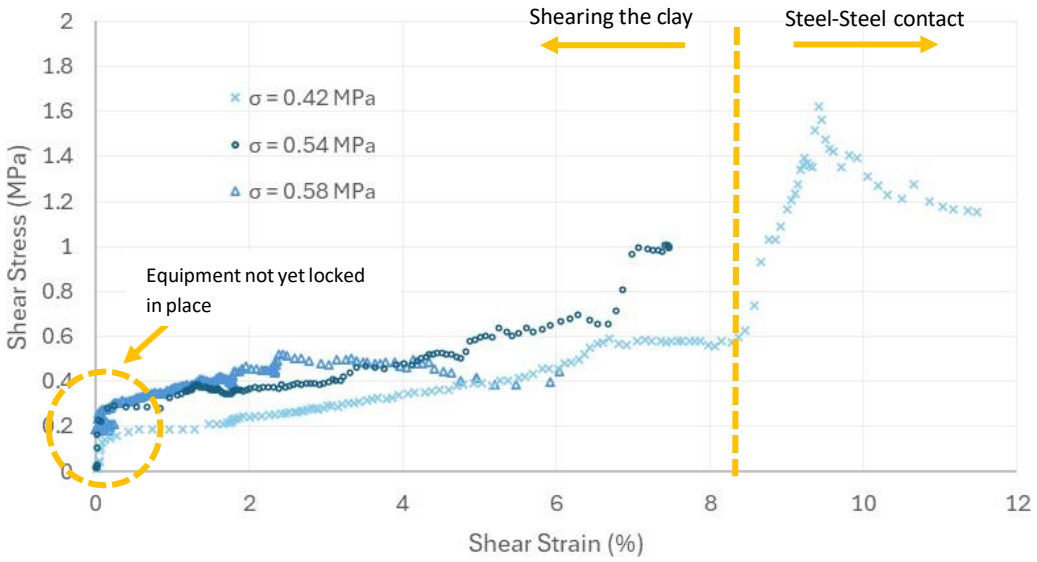

Figure 4.11 - Shear Stress (MPa) vs Shear Strain (%) for 1mm

All the three graphs in Figure 4.12 show initial gradual dilation. Although a peak is reached and some reduction in normal displacement is observed, the values never fall below the initial starting point – confirming that no actual compression occurred during the tests. This interpretation is supported by the absence of negative displacement values in Figure 4.12, verifying that clay primarily exhibited dilative behaviour throughout the shearing process.

Once again, the relevance of the graph is questioned just after the 8.5% strain mark where the steel-steel contact occurred. The change in behaviour on the graphs is evident around 5% strain, as circled in the Figure 4.12. This is because the clay likely completes shearing over the full asperity.

Subsequently, specimen behaviour changes from riding up the asperities to riding down the asperities (5-7%), changing behaviour from dilation to compression. The strain value of the asperities with respect to the total shearing length is approximately 8%, meaning this consistent early failure could be a result of several errors within the equipment. This may include zeroing of sensors, showing the earlier behaviour of the asperities.

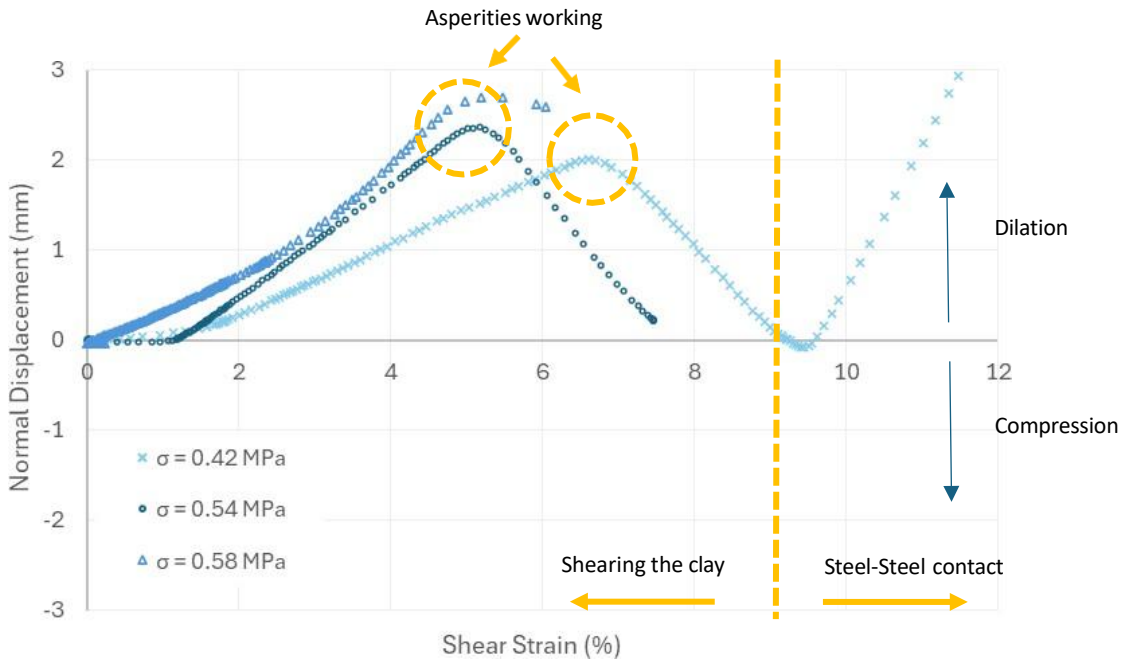

Figure 4.12 - Normal displacement (mm) vs shear strain (%) for 1mm

Figure 4.13 shows an increase of shear stress vs normal stress. A smooth path is present in all tests, albeit with some deviation at the end, as shown in 0.42 MPa test. This is representative of shear stress being lost as the normal force was increased in the end. This is highlighting some mechanical fault in the horizontal arm. The 0.54 MPa test shows a fault midway through the experiment. These consistent errors throughout highlight the error present of the equipment, which is the steel-to-steel contact.

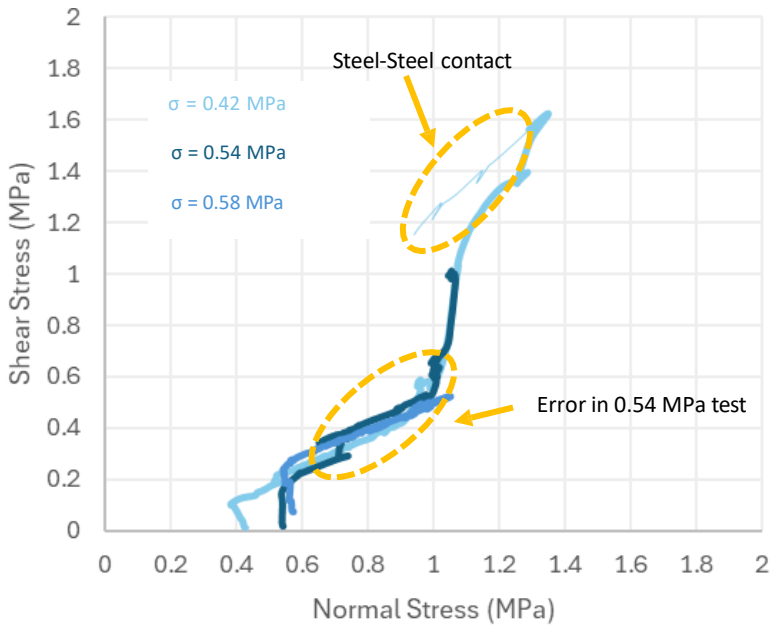

Figure 4.13 - Shear Stress (MPa) vs Normal Stress (MPa) for 1mm at different initial σ

4.3.2. Results of 3mm Infill Thickness

The 3mm infill thickness was the size chosen to understand how the intermediate clay thickness will affect the discontinuities. This is mathematically exactly halfway between the 1mm and 5mm thickness as discussed in Section 4.1.

Test No.	Applied Force (kN)	Stress (MPa)
8	4.41	0.28
9	5.67	0.36
10	6.93	0.44

Table 6 – 3mm tests

Figure 4.14 provides further evidence of the problem related to the initial stages of the test, where the specimen assemblage was subject to rapid shearing action as contact with the displacement sensor was achieved. Before this happened, tabulation of the shear strain values was not possible. This is shown circled in yellow on Figure 4.14.

The gradient of this graph then stabilises up until the 8% strain value where the shearing slows down. This indicates how this manual shearing slowed down and was not consistent. The initial rapid shearing stage, is most evident in the 0.44 MPa test. The test carried out at 0.36 MPa normal stress is showing a slow-fast-slow shearing rate based on the change in gradient of the graph, compromising consistency throughout this particular experiment. It is important to note that the shearing was applied manually during the test, which introduced some variability in the loading rate. Although equipment setup aimed to minimise this, minor inconsistencies in manual control were unavoidable.

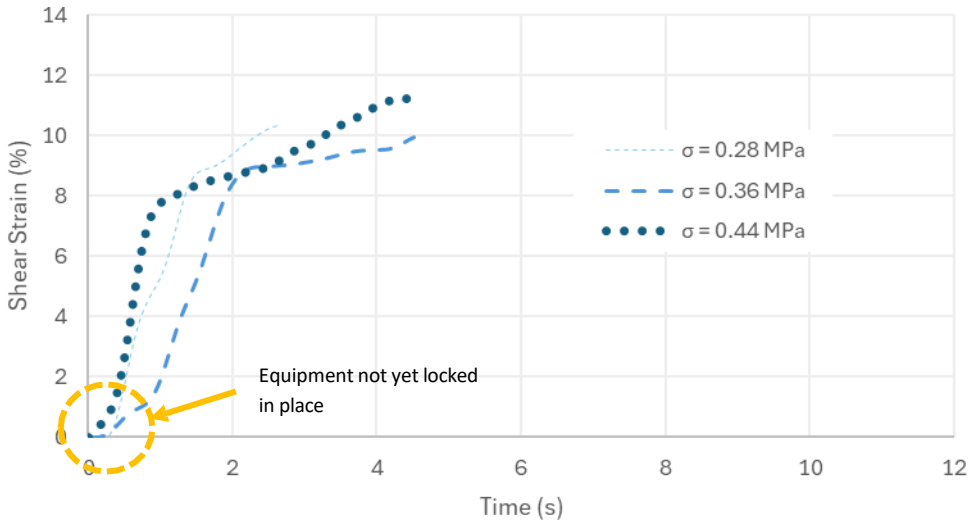

Figure 4.14 - Shear Strain (%) vs Time (min) for 3mm thickness

From Figure 4.15, the lower stresses of 0.28MPa and 0.36MPa are very comparable with each other. All three tests show clear expected strain hardening behaviour. The strain values after the 8.5% mark are once again considered redundant because of the steel-steel interaction of the equipment which distorted the results obtained.

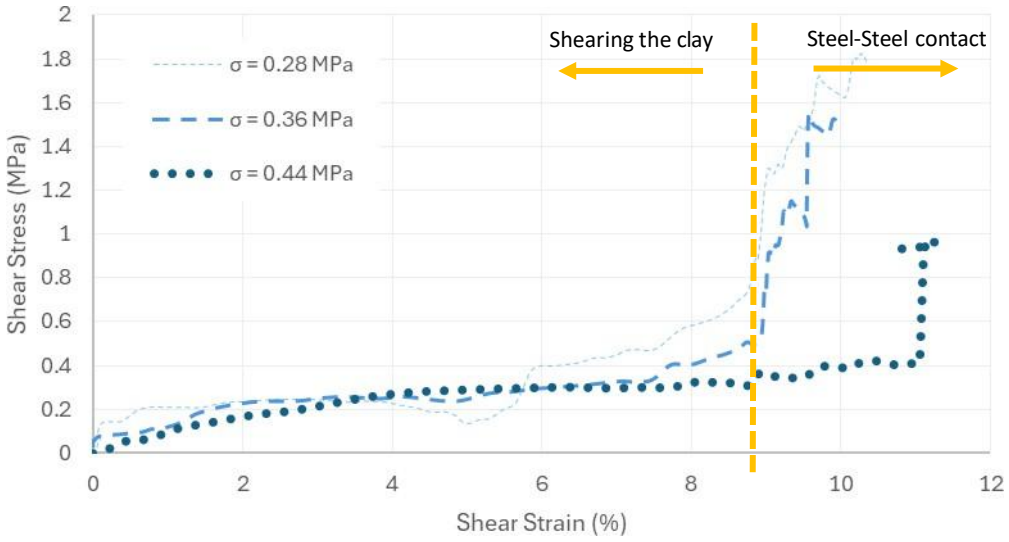

Figure 4.15 - Shear Stress (MPa) vs Shear Strain (%) for 3mm

In terms of normal displacement, two tests show an initial compression. This is expected for normally consolidated clays *(Schofield & Wroth, 1968),* and furthermore, because at this thickness of infill, dilation may be delayed until the asperities come sufficiently close to each other, after compressing the clay in between. The 0.44 MPa test is the most unique from the tests, as its shape is the least comparable from the other 2 in Figure 4.16. This highlights the probability of slip failure or equipment fault which has influenced the readings taken during the test. A point of contraflexure, where compression changes to dilation can be seen at 5.5% strain on both tests. These are circled on Figure 4.16 and highlight the influence of the asperities working. This is because the specimen have sheared up a set of asperities and now start riding down. The thicker effect of the 3mm produces a less notable point of contraflexure as oppose to the 1mm test.

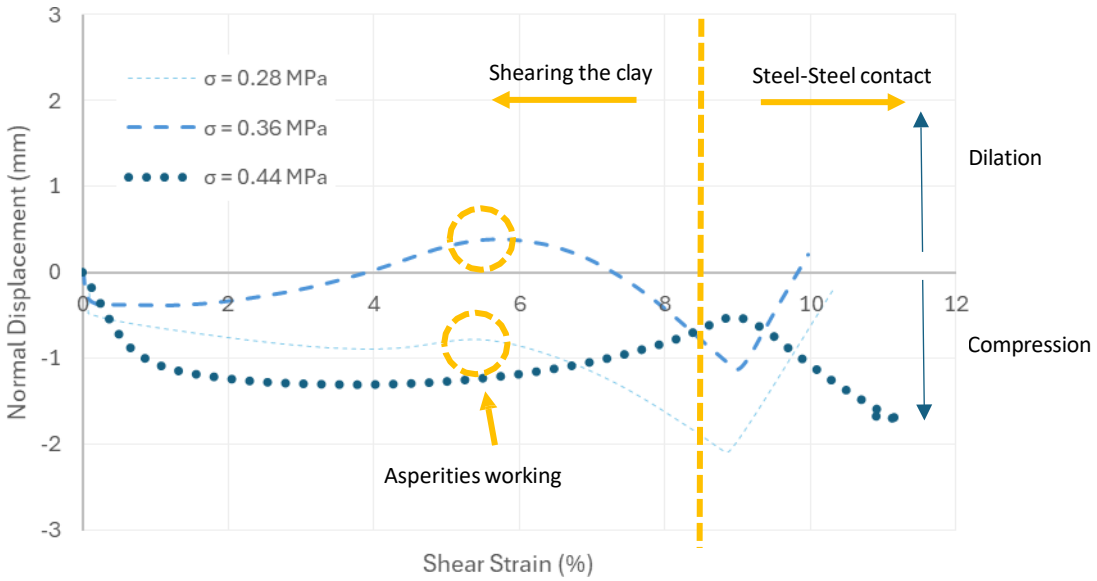

Figure 4.16 - Normal Displacement (mm) vs Shear Strain (%) for 3mm

Figure 4.17 below shows relative consistent stress path, with the irregularities circled. The 0.44 MPa test appears to have the most deviation, especially in the early stages. This highlights the presence of

an early fault in the equipment or test. Minor slippage is also present in the circled areas from all three graphs, possibly from a slight instability or equipment lag.

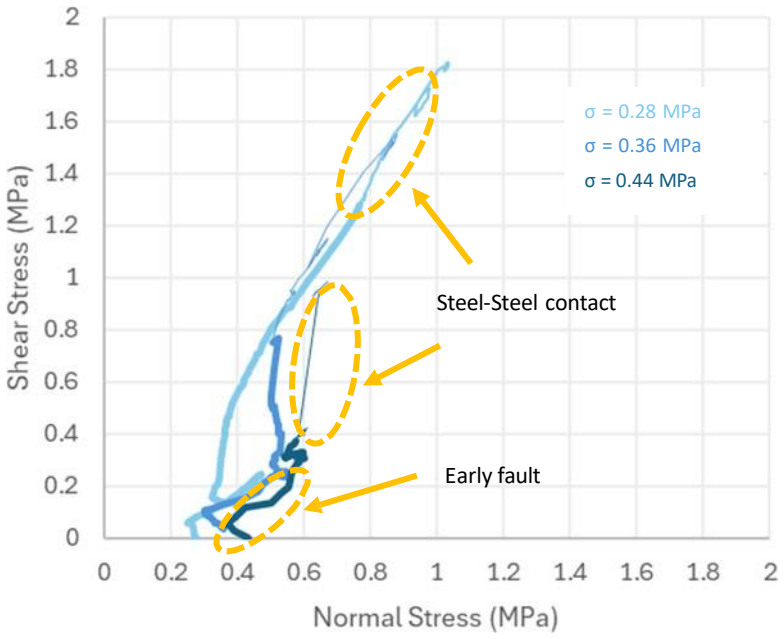

Figure 4.17 - Shear Stress (MPa) vs Normal Stress (MPa) for 3mm at different initial σ

4.3.3. Results of 5mm Infill Thickness

The 5mm infill thickness indicates an infill thickness which is of the same size as the chosen asperity height. In this case, it is expected that the influence of the clay infill would be more dominant, and shearing action would be limited mostly to the clay infill. This is because at this simulated fissure aperture, no direct contact between asperities would be possible as these move relative to each other. However, in practice, this may not be the case, because as a normal force is applied, some of the clay is compressed, possibly moving outwards, reducing the infill volume, and creating contact points for the asperities of the two casts.

Test No.	Applied Force (kN)	Stress (MPa)
4	5.83	0.37
5	10.71	0.68
6	4.41	0.28

Table 7 – 5mm tests

From Figure 4.18, the circled location is showing very clearly how the initial shear force being applied on the equipment is not causing any shear strain, as the displacement sensor has not been locked in place as yet. The 0.37 MPa test shows how the shearing rate is similar mostly for this, whereas for the 0.28 MPa test, a slow shearing rate is present initially when compared to the others, which then accelerates. The applied stresses for these tests were not uniform due to limitation of the manual shear box setup and human error during the application of the hydraulic load. As discussed previously, the normal stress was difficult to control precisely, and the values shown were the actual starting points achieved for each test.

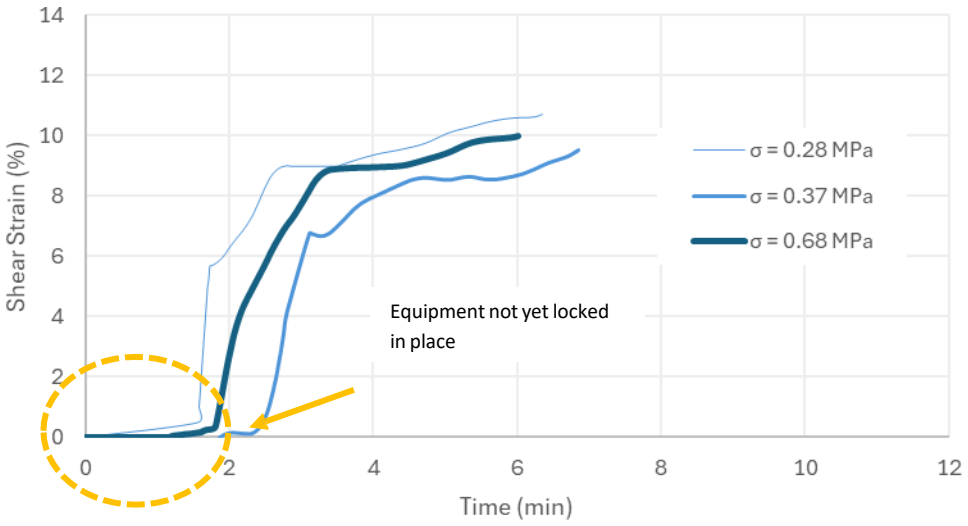

Figure 4.18 - Shear strain (%) vs time (min) for 5mm

In Figure 4.19, the lowest normal stress (0.28 MPa), is showing a delayed reaction to strain hardening, which could indicate a possible slip in the initial shearing stages *(Schofield & Wroth, 1968)*. The other 2 stresses (0.37 MPa and 0.68 MPa) show much more clearly the strain hardening response whilst shearing. This relationship is more evident in the 0.68MPa graph, which indicates that in the 0.37MPa graph, there may have been some material roughness or other factors which resulted in the noise within the data. The graph is once again redundant after the marked 8.5% shear strain location as

shearing is occurring on the steel-to-steel interface. In general, Figure 4.19 presents clear normally consolidated clay behaviour *(Schofield & Wroth, 1968)* which matches well with the general methodology of removing the stress history of the clay sample when making it a slurry.

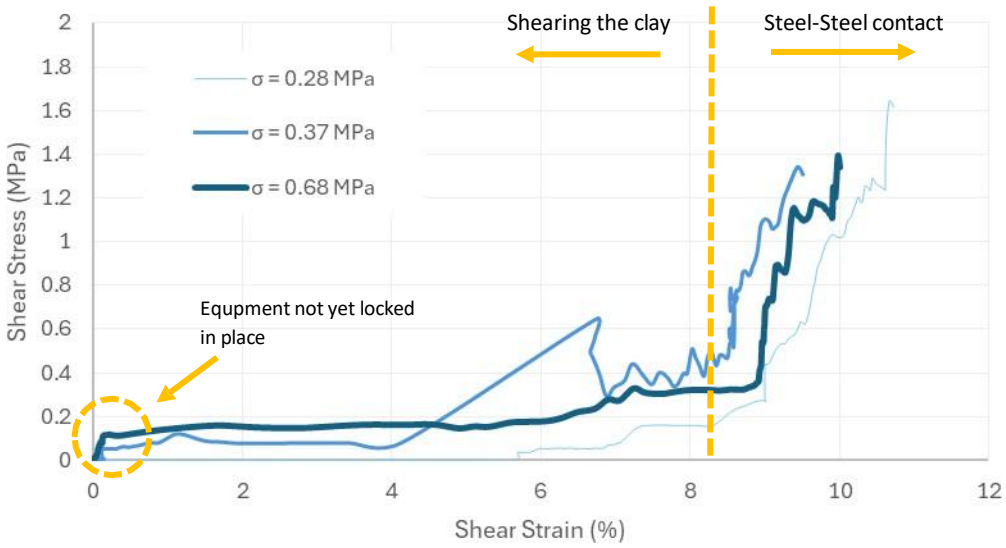

Figure 4.19 - Shear Stress (MPa) vs Shear Strain (%) for 5mm

From the normal displacement against shear strain, only the test having initial stress of 0.37 MPa shows dilation in the beginning, which then proceeds to show compression comparing its behaviour to the other two. The initial compression is expected for normally consolidated clays. The initial dilation in the 0.37 MPa test is not a usual occurrence for normally consolidated clays. For this reason, a form of interface slip is predicted to have resulted in this behaviour. There is no evidence of the asperities of the clay having an effect in this scenario as the clay thickness is the same as the asperity height (5mm). The dilation is because the normal stress was not sufficiently high to suppress it at 0.37 MPa. Dilation happens not only in relation to the degree of over consolidation, but also in relation to the confining pressure, in this case the normal stress.

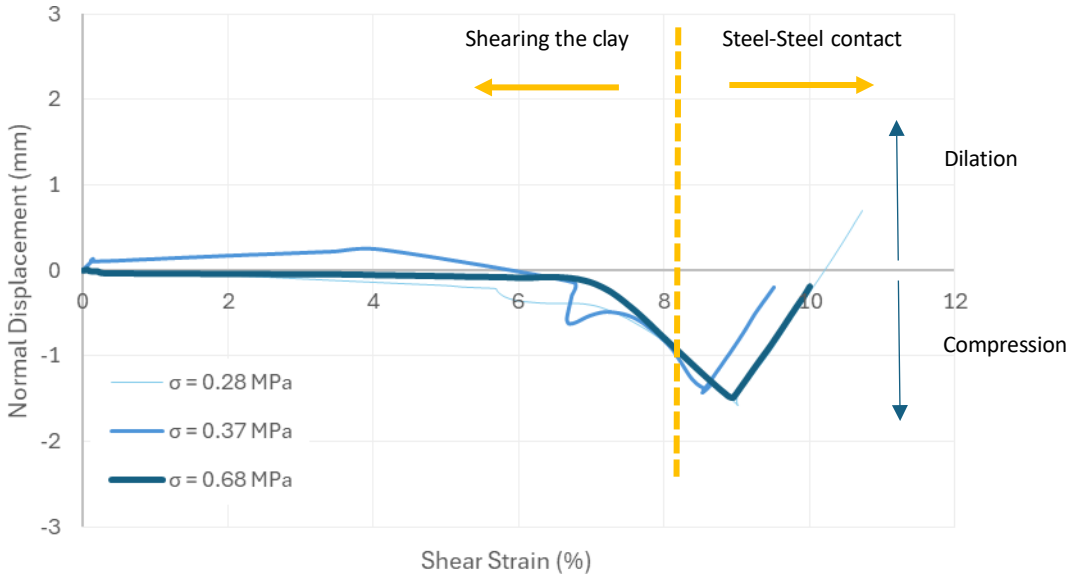

Figure 4.20 - Normal Displacement (mm) vs Shear Strain (%) for 5mm

From Figure 4.21, the 0.28 MPa test presents a very clean and clear stress path. This contrasts with the 0.37 MPa test which shows very erratic behaviour, strongly suggesting the presence of a mechanical fault or misalignment in the apparatus.

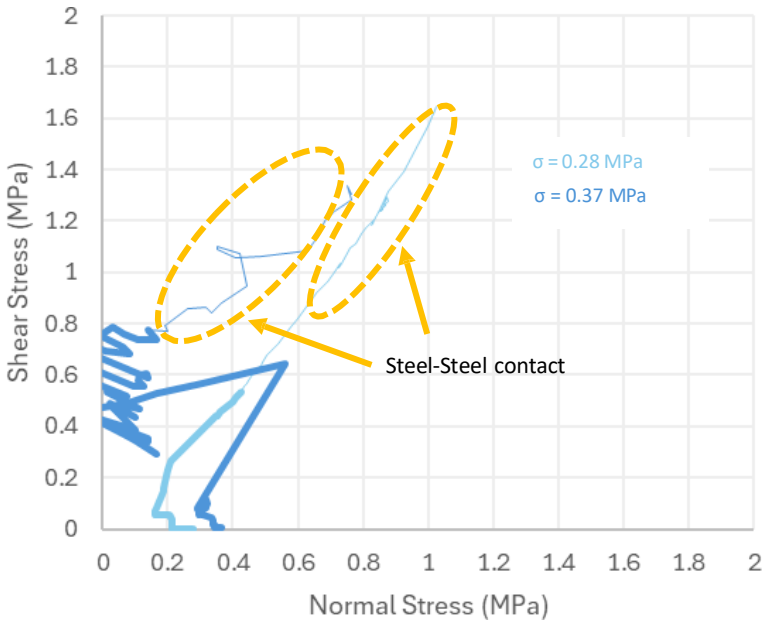

Figure 4.21 - Shear Stress (MPa) vs Normal Stress (MPa) for 5mm at different initial σ

4.3.4. Results of tests on casts with no infill

This test was carried out to understand if the 1mm clay infill had an effect on the mechanical behaviour or whether the thin volume of infill can be considered redundant. Only one test was carried out due to time limitations.

Test No.	Applied Force (kN)	Stress (MPa)
7	8.82	0.56

Table 8 - No infill test

The recorded readings begin slightly before the first minute, since strain accumulation is not yet being recorded until displacement sensor is engaged in place. After readings started being recorded, the specimen was originally sheared slowly and this was then followed by a slightly accelerated response. The increased shearing rate is likely due to the slight resistance to the frictional forces between the plaster cast being overcome *(Bhardwaj et al., 2022)*.

The shearing rate is much less critical for interaction between two plaster casts in direct contact *(Bhardwaj et al., 2022).* This is because material behaviour is less dependent on induced pore water pressures, because of its cementitious nature. In contrast, the dissipation of pore pressure has a direct effect on the behavioural patter of the infill material. In the case of plaster, the material is unlikely to have a drained or undrained state. The effects of the shearing rate will only slightly effect results due to heat build up from the frictional forces, and therefore this effect can be considered redundant in this case. The shearing rate can be see on Figure 4.22.

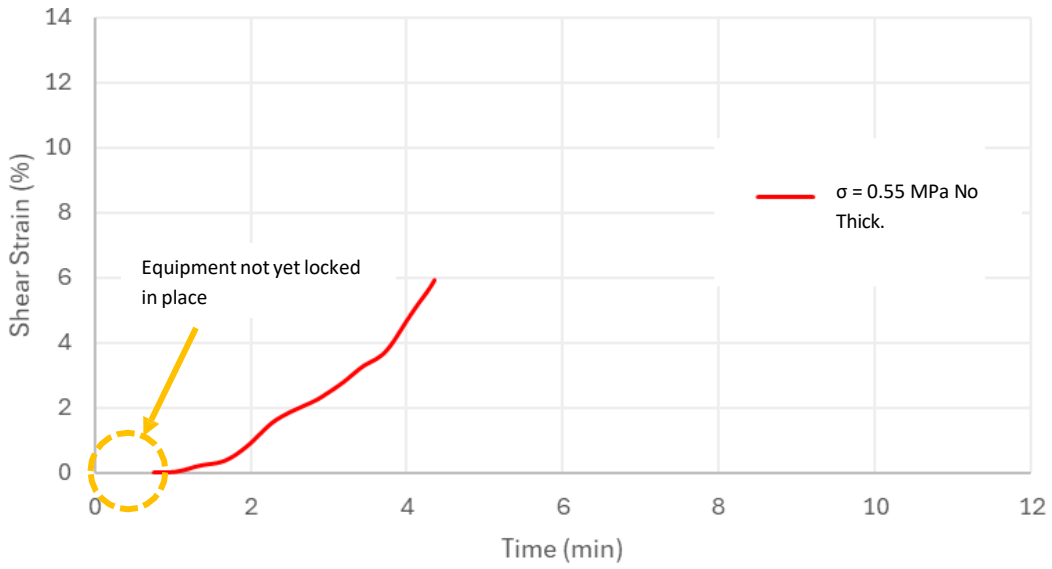

Figure 4.22 - Shear Strain (%) vs Time(min) for no thickness

As can be seen from Figure 4.23, the shear stress rises quickly, which then starts presenting strain softening behaviour. The friction between the 2 surface is very high, from surface roughness and asperity interlock. This is also because of the plaster inherently being a strong material in itself *(Bhardwaj et al., 2022).* However, as the specimens are being sheared against eachother, the plaster

gets smoother and the asperities get flatter. The 8.5% strain value has not been reached in this scenario, therefore the test results are all valid. This can be seen on Figure 4.23.

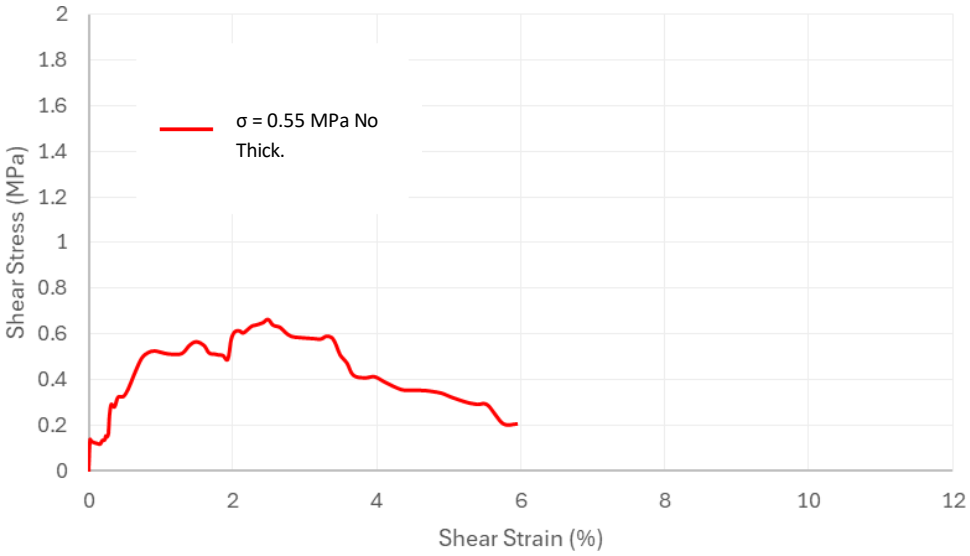

Figure 4.23 - Shear Stress(MPa) vs Shear Strain (%) for no thickness

From Figure 4.24, only pure dilation is present, likely due to the interaction of the asperities. The plaster is stiff and does not have deformable properties found in clay, which can also cause dilation. This suggests that the behaviour is solely from the asperities. There is also no distinct turning point present within the graph suggesting that the asperities progressively flatten. The curve is then expected to flatten for the rest of the test from this shear-induced shaving. This anticipated behaviour is expected based on the general understanding of the equipment and testing procedure.

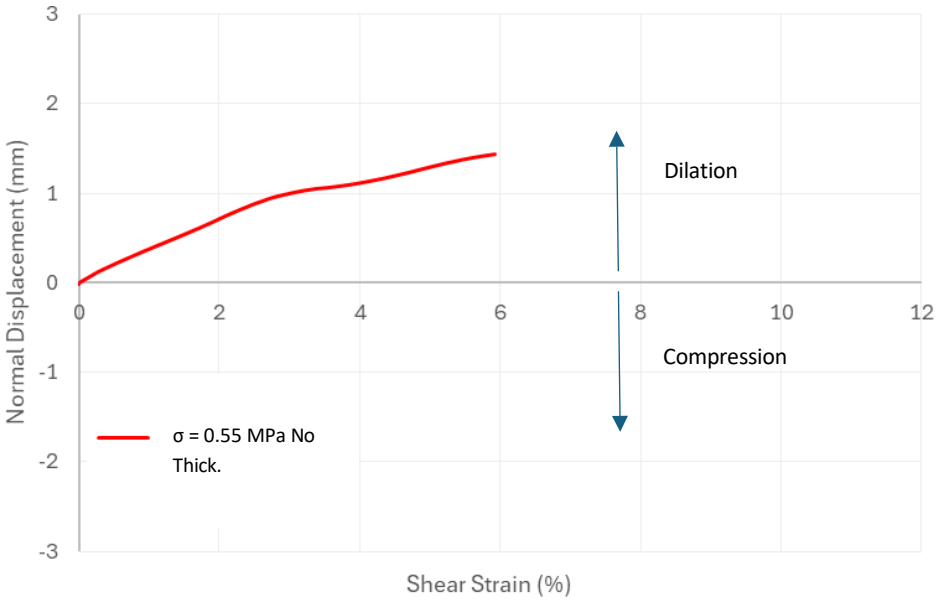

Figure 4.24 - Normal Displacement (mm) vs Shear Strain(%) for no thickness

Figure 4.25 - The test results showing how the asperities have been sheared off

Figure 4.26 shows the expected increase in shear and normal stress. The linear behaviour is present throughout the testing procedure up until the circled area where the graph starts to curve downwards. This decline may be a result of the plaster asperities which were progressively sheared off during the test procedure. The curve aligns well with this hypothesis as the loss of shear strength is a result of the asperities being degraded or flattened. The fact that the shear strain never reached 8.5% confirms that steel-to-steel contact is not the reason for this type of behaviour.

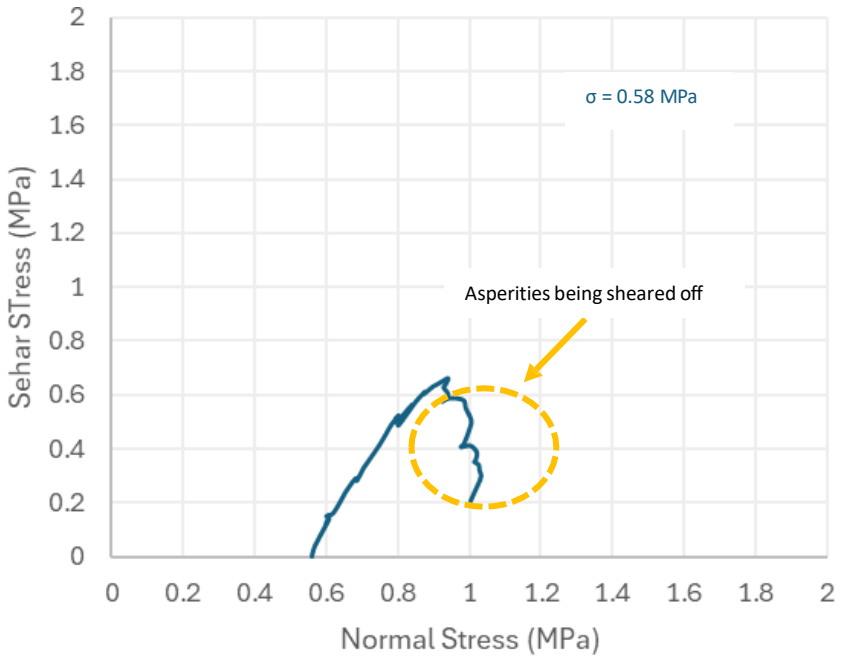

Figure 4.26 - Shear Stress (MPa)vs Normal Stress (MPa) for no infill thickness 0.58 MPa initial σ

4.3.5. Results of 10mm Thickness

An assemblage of two smooth plaster casts with no asperities but with 10mm infill was also tested. Only one of this test was carried out because of the large clay volume which this test requires. The sampling process of the clay was very time consuming and time constraints limited the amount of tests which were done.

This test was done so that shearing is done solely on the clay, highlighting the effects of the thickness in relation to the asperities for the other tests. The contat area was now greater having a value of 19418 mm^2.

Test No.	Applied Force (kN)	Stress (MPa)
11	6.80	0.35

Table 9 – 10mm thickness test

In Figure 4.27, the circled part of the graph shows that there is a delayed initial strain reading. This is once again due to the of need to stabilize the equipment before the actual test begins. The equipment is then sheared rapidly as can be deduced from the relatively steep gradient. This gradient then flattens indicating that the clay is sheared less rapidly towards the end. In general, this test was of very short duration, lasting around 3 minutes.

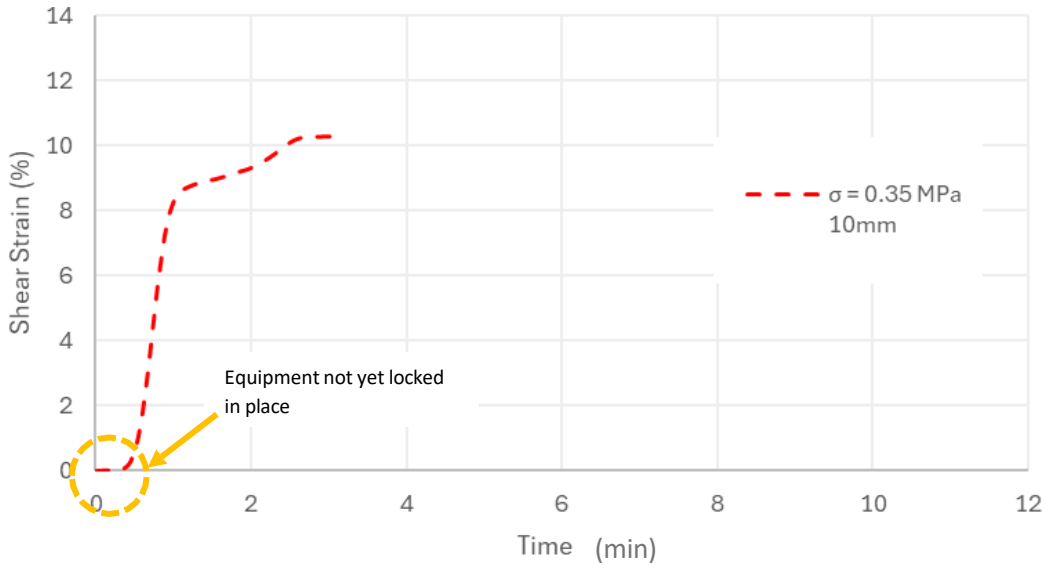

Figure 4.27 - Shear Strain (%) vs Time (min) for 10mm thickness

In this case, there were no asperities present, so no plaster-plaster contact is present at any point during the test. The shear strength of the clay results in the increase in shear strength of Figure 4.28. As can be seen, the rapid increase in shear strength at around the 8.5% mark is once again due to the result of the steel of the upper box being put in contact with the steel of the lower box. The original hypothesis was that this 8.5% mark was the result of the plaster-plaster contact from the asperities. However, in this scenario, no asperities were present so this could not be the case. Therefore, following further analysis of results and photo references of the tests, it could be seen how the individual parts

of the top and bottom parts of the shear box were colliding with eachother. This concluded that there was a mechanical error, and the behaviour was not due to the asperities.

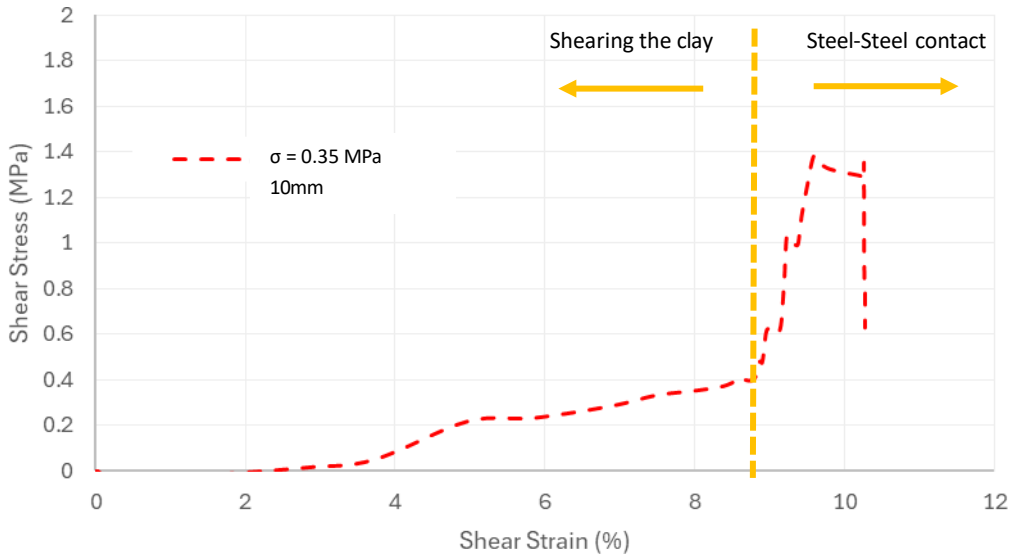

Figure 4.28 - Shear Stress (MPa) vs Shear Strain (%) for 10mm thickness

This hypothesis is once again confirmed by looking at Figure 4.29. Originally the compression is consistent with normally consolidated behaviour of clay. Following this, the 8.5% shear strain is showing how the equipment material under test stops compressing and starts dilating rapidly. This is the result of the top element of the shear box being pushed up by the steel-to-steel contact. The fact that no asperities were present indicates that it is very unlikely for dilation to be induced by the clay or plaster properties in any way. This hypothesis is also confirmed from this behaviour being present in all other tests of Section 4.3.

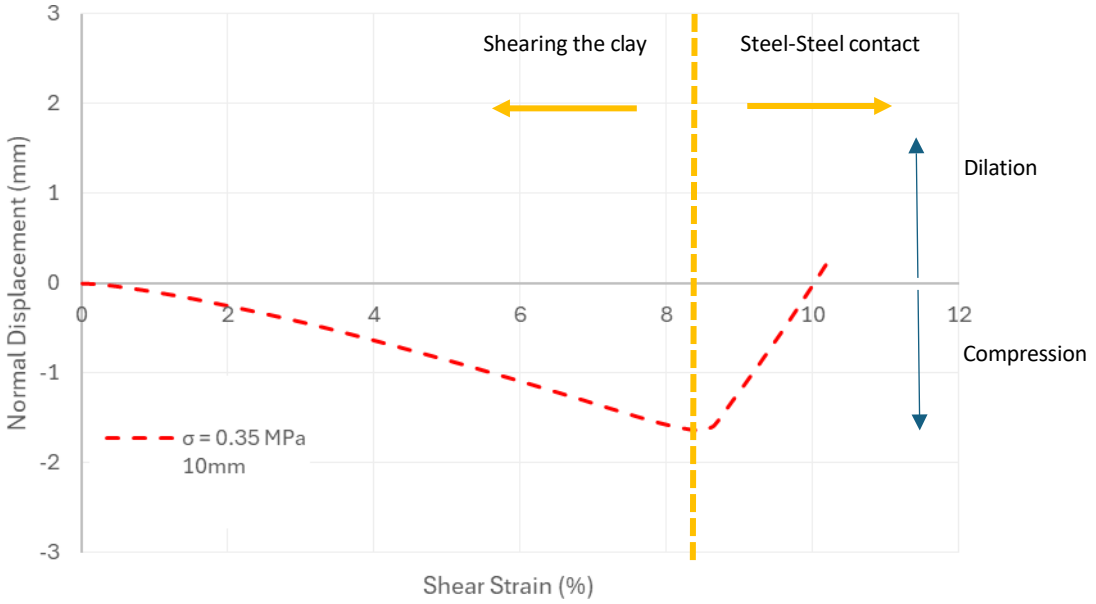

Figure 4.29 - Normal Displacement (mm) vs Shear Strain (%) for 10mm thickness

Figure 4.30 shows how an initial slip, evident because the 0.35 MPa drops instantly, as indicated. A linear relationship is then observed, highlighting that most of the test results behaved consistently. However, a rapid drop in shear stress, indicates that a mechanical fault in the equipment is present, likely due to the steel-to-steel contact.

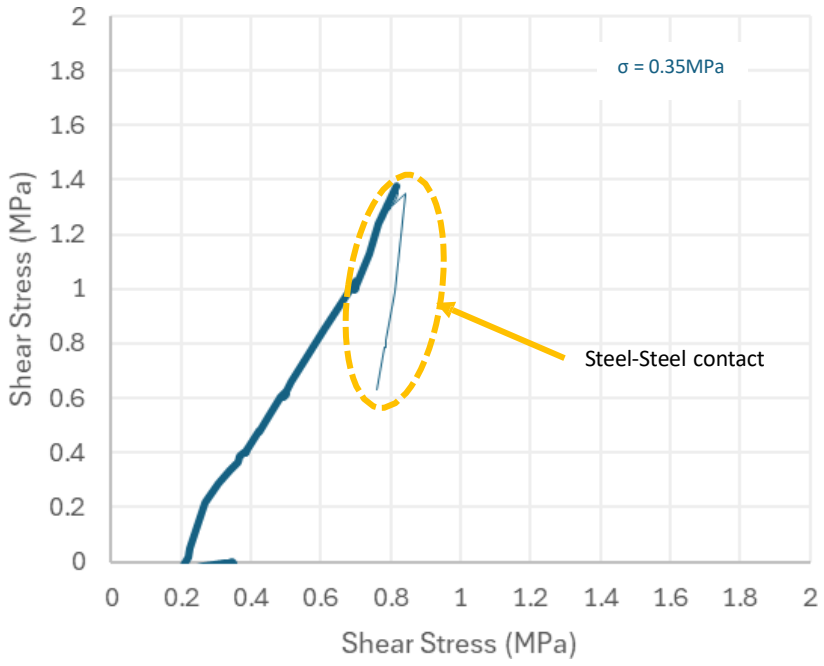

Figure 4.30 - Shear Stress (MPa) vs Normal Stress (MPa) for 10mm thickness 0.35 MPa initial σ

4.3.6. Superimposition of Results

This section presents a comparison of the results obtained from the direct shear tests performed on the specimen casts having varying clay infill thicknesses: no infill, 1mm, 3mm, 5mm and 10mm, the latter having no asperities in the plaster, unlike all the others.

The superimposed plots of shear stress vs shear strain and normal displacement vs shear strain allow the behaviour of the joints to be compared under similar normal stresses. Although it was difficult to apply perfectly consistent normal stresses due to the manual operation of the hydraulic pump levers connected to the shear box, efforts were made to analyse results with the closest matching values to ensure meaningful comparison.

The results indicate that infill thickness significantly influences the mechanical response of the joint. When no clay infill was present, the asperities were sheared off, resulting in a distinct peak stress followed by post-peak softening. The 1mm clay infill allowed asperity interlock to persist, contributing to higher shear strength. However, beyond the 3mm infill thickness, the interlocking effect diminished substantially. For the 10mm infill, shear strength was governed solely by clay behaviour. These trends are reflected in both the shear stress and normal displacement.

Comparing the tests with 1mm infill to those with no infill, on Figure 4.31, the 1m thickness creates a boundary preventing the plaster-plaster contact *(Indraratna et al., 2012)*. The clay surface resists the shearing force differently to the plaster, lowering its peak stress. The shear stress increase of the 5mm infill thickness within the test happens at a later stage than the 3mm infill. This is because of the strain mobilization which would require a longer period of time to overcome a greater volume of clay.

By gradually analysing the tests from no thickness to 10mm thickness, a gradual decline in shear stress can be seen with respect to every thickness. The 3mm and 5mm graphs have produced greater variability in results. Some of the irregularities and noise observed in the graphs between the 7-9% strain may stem from minor equipment sensitivity. Nonetheless, the overall trend remains clear and does not significantly affect the interpretation of the test outcomes.

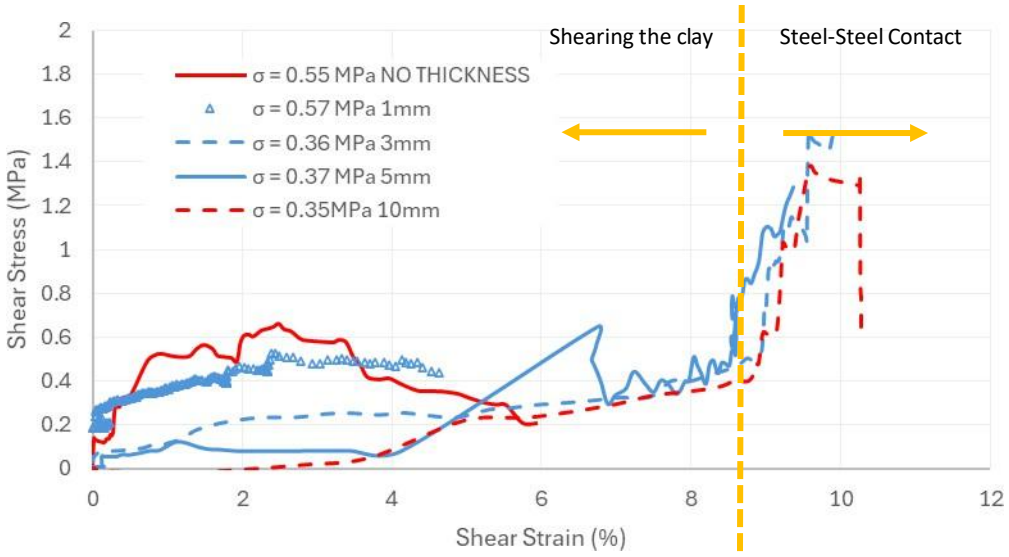

Figure 4.31 - Shear Stress vs Shear Strain for all thickness

Figure 4.32 shows that dilation is more present in the tests on plaster casts with 1mm infill. This is because the clay undergoes volumetric expansion during shearing. In contrast, the plaster-to-plaster shows only pure dilation. This indicates that shear force on the clay transitions from shearing which is sheared between the clay and the asperities, to a state where all shearing occurs solely within the clay (10mm test). The clay therefore acts as a lubricant for the asperities to ride from the top of one part to another.

The initial compression of the 3mm clay is the expected behaviour of normally consolidated clays *(Indraratna et al., 2012)*. Points of contraflexure have been labelled for the 1mm and 3mm tests. These are marked in the individual tests of Section 4.3.1 and Section 4.3.2, as well as in the superimposition of results in Figure 4.32. These points of contraflexure can be seen at the same strain location for both of these tests. This location indicates when the asperities are working with respect to the geometry of the asperities.

This result was not present when there was no infill thickness, which initially was of concern. However, the asperities were shaved off in the process due to the high frictional forces present in the plaster-to-plaster experiment. The clay reduces the friction, allowing the asperities to engage without shearing each other off. The early steel-to-steel contact in the equipment suggests that the asperities are engaging earlier than expected, which is consistent with the absence of clay to reduce friction between surfaces.

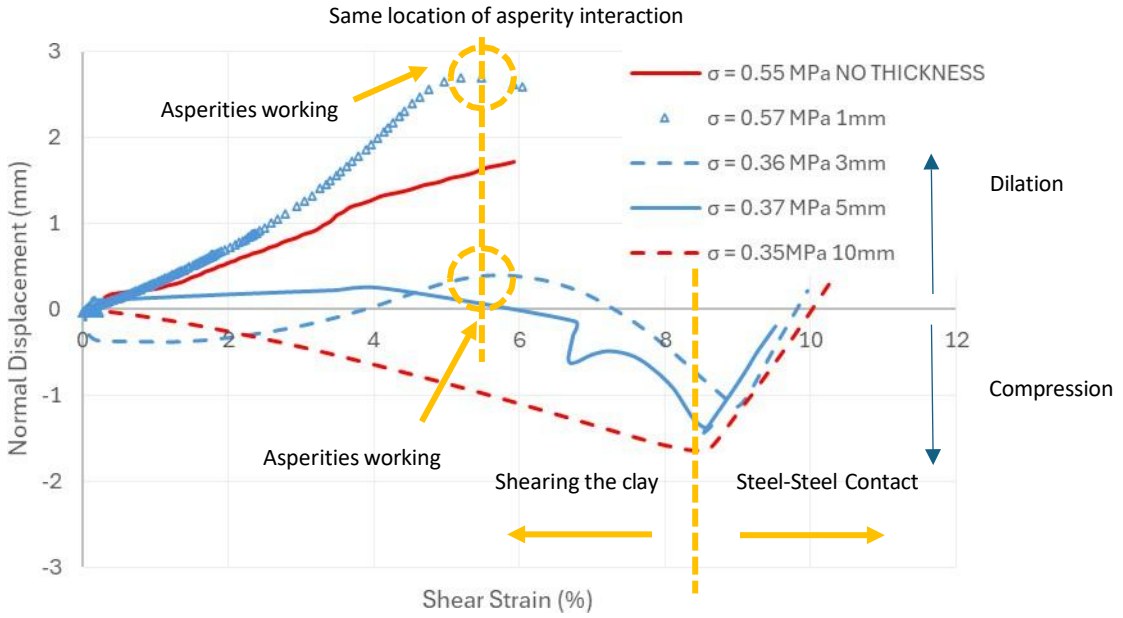

Figure 4.32 - Normal Displacement vs Shear Strain for all thicknesses

All graphs display a rapid change in results from the 8.5% strain mark onwards. This consistent error is due to the steel-to-steel interaction which has been discussed. On the basis of measurements taken on the apparatus itself, the calculated shear strain value at steel-to-steel contact was estimated at 9.3%. This was arrived at by calculating the distance of travel required for the two halves to make contact, relative to the full extent of the surfaces being sheared, in the direction of shearing. This aligns very well to the consistent irregularities observed at the 8.5% mark. The superimposition of results has

helped to identify this error. This is because the test of the 10mm infill thickness, having no asperities, also provided this behaviour, in spite of this being initially attributed to asperity contact.

When looking at Figure 3.30 (Methodology) the level of strain at which the chosen asperity profiles (on opposite faces) make contact occurs at 8.3% Strain. This confused the interpretation of the spike in shear stress to be representative to plaster-to-plaster behaviour. The plaster asperities appear to begin engaging around the 5% strain mark, as indicated by the emergence of point of contraflexure in the normal displacement data in Figure 4.32.

The test on plaster casts having 5mm infill thickness was purposely carried out as the effect of the asperities was not expected to be seen for this thickness, due to the thickness being the same dimensions as the asperities. The results support this hypothesis.

However, overall, it was expected that these points of contraflexure within the Normal Displacement vs Shear Strain graphs will occur at the 8.3% Strain values and not at the 5% Strain Value. This is because the 8.3% strain value corresponds to the calculated point at which the opposing asperities on the plaster specimens should first come into contact, based on the shear strain relative to the total shearing length of the mould. This indicates a possible zeroing error of displacement sensors.

4.3.7. Mohr Coulomb failure criterion

The Mohr Coulomb failure criterion has been drawn up for all three thicknesses, the 1mm, 3mm and 5mm. This is analysis is based on Eq. 2-1, where the cohesion is found from the y-intercept of the linear best-fit line and the residual friction is found from the inverse tan of the gradient.

In theory, the Mohr–Coulomb envelope requires a substantial number of data points and filtering to produce reliable results. However, due to time constraints and experimental limitations, only three tests were carried out per thickness. Additionally, inaccuracies introduced by manual loading and equipment limitations further affected the quality of the data. The normal force in this study was also not kept a as a constant because of the dilation from the asperities. This violates the assumption of constant normal stress which is typically required in tests leading to the determination of a Mohr-Coulomb failure envelope. As a result, the derived Mohr–Coulomb parameters are subject to high uncertainty and should be interpreted cautiously. Time constraints also limited the repeated tests on plaster-to-plaster interaction and 10mm clay infill tests.

Other types of analysis such as the study done by Indraratna (2010) (refer to Eq.. 2-13), would require analysing the drop in peak shear strength from the infill material to the plaster. Due to equipment limitation, the peak shear stress could not be achieved as the steel-steel contact terminated the test prematurely and hence compromised the reliability of the experiment

Figure 4.33 present a Mohr-Coulomb failure criterion at 1% strain. This location was chosen as a reference point for drawing the failure envelope due to the early termination of several tests before peak shear stress could be reached,

A notable issue is the negative cohesion in the 3mm test. This is physically unrealistic and likely caused by variability from limited data. The friction angle at 1% Strain has also rapidly changed from 27.4 degrees in 3mm test, to notably lower in 13.9 degrees for the 5mm test and finally to 30 degrees in 1mm test. This lack of consistency is a result of inaccurate data for this analysis.

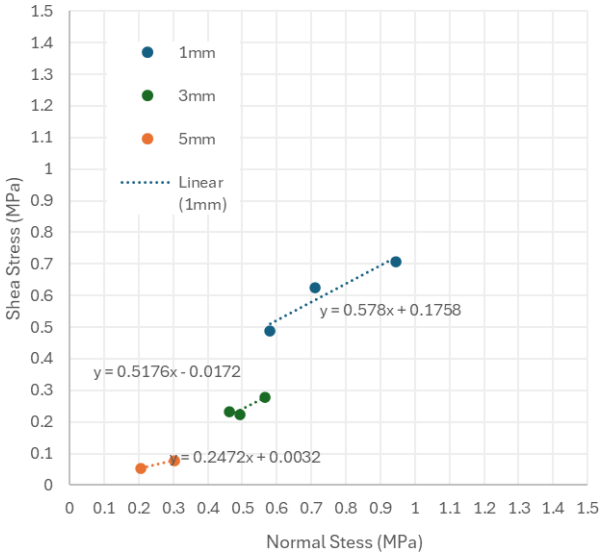

Figure 4.33 - Mohr Coulomb failure criterion at 1% Strain for all thickness

The results obtained generally align with expected behaviour in shear testing of infilled discontinuities. Thinner infills ranging from 1mm to 5mm allowed more interaction between asperities, leading to higher shear strength and some dilatant behaviour. In contrast, thicker infills (10 mm) behaved more like pure clays. These findings conform the significant role of infill thickness and asperity interaction in controlling joint behaviour.

While some variation as observed, particularly in friction angles and cohesion, this was attributed to experimental limitations such as manual loading and early test termination. Despite these, the trends remain consistent. Different infill materials or natural rock surfaces would produce varied results, especially in stiffness and failure modes. These outcomes reinforce the relevance of material selection and control in shear testing.

5. Conclusion

This dissertation aimed to investigate how clay infill thickness influences the shear behaviour of plaster cast discontinuity replicas to mimic weak rock masses such as Maltese Lower Globigerina Limestone. The approach involved direct shear testing across a range of clay thicknesses (1mm, 3mm and 5mm), whilst retaining the asperity geometry for all tests. Tests were also carried out when no infill thickness was present and when a clay volume of 10mm without asperities was present. This allowed infill thickness and its effect on shear strength and deformation to be explored. Despite equipment limitations, particularly load control and strain measurement, the results showed consistent trends that offer meaningful insight into joint behaviour in the presence of weak infills.

The use of Plaster of Paris was intended to simulate the mechanical profile of weathered Lower Globigerina Limestone. While not identical in mineralogy, the plaster offered a uniform and repeatable medium with a comparable texture and surface profile, allowing consistent casting of asperities. The mechanical comparability was supported by UCS tests showing an average value of 8.3MPa, which is comparable to the UCS 12.15MPa average of LGL from the Solidbase database. In addition to strength, the stiffness of the plaster was approximated using normal load-displacement behaviour during shear box testing, providing insight into the elastic response of the material. While no direct stiffness comparison was made with natural limestone, the consistent results obtained across all plaster specimens ensured reliable mechanical performance for the experiment. However, the plaster does not replicate the mineralogical interlock, pore structure or time-dependent deformation which is seen in natural rock. These limitations affect the material's behaviour under long-term or variable stress conditions, but the plaster remains effective for exploring immediate mechanical interaction between infill and discontinuity geometry.

The chosen geometry of 5mm height and 18.5 degree inclination was developed to reflect a simplified version of rough undulating joint surfaces which are commonly observed in weathered Maltese Limestone. This configuration aligns well with the observations of Barbieri (2021) on Local Globigerina Limestone. Thus, while not a direct replica, the simplified geometric profile of the specimen serves as a plausible analogue to simulate a particular but realistic limestone discontinuity scenario.

The Mohr-Coulomb analysis was performed for the 1mm, 3mm and 5mm tests at 1% Strain levels due to early test termination. These aimed to extract shear strength values for each respective infill thickness. The reliability was limited due to the equipment constraints and inherent variability in the test data. The 3mm showed a negative cohesion value, being mechanically unrealistic and attributed to inconsistent data. The friction angle varied unpredictably with the 5mm test showing an angle of 13.9 degrees, which is notably lower than the 27.4 degree and 30 degree tests for the 3mm and 1mm tests respectively. The variations highlight the unreliability of the Mohr-Coulomb parameters from this dataset, particularly under low confining stress.

Dilation is evident in the normal displacement vs shear strain graphs. The data indicated an increase in volume as a result of the top specimen riding up the bottom specimen during the shearing process. The normal vs shear strain graph also depicts points of contraflexure around the 5% strain mark. This strain level corresponds to the location where the asperities go from riding up the asperity, to riding down the asperity. It is notable to point out that a greater point of contraflexure is evident when there is less clay volume, with the 1mm test providing the most evident response. The 5mm test does not show this behaviour because the thickness matches the asperity height. The no infill thickness also

does not show these points of contraflexure as the asperities are being shaved off during the experiment. The 8.5% strain mark depicts the point in the test where the equipment limitation is present, which is consistent in all tests of all clay thicknesses. At this location, the steel-steel contact of the top and bottom specimen effects the results of the test.

The testing procedure confirmed that increasing clay thickness reduces shear strength, with the 1mm and 3mm infills showing clearer asperity interaction than the 5mm. The 10mm test served to isolate the clay's behaviour in the absence of asperities. Despite variations in results due to manual loading and testing limitations, the trends across thicknesses support this interaction.

The experimental results revealed consistent trends across varying infill thicknesses, supporting the hypothesis that clay infill alters joint shear behaviour. Notably, the 1mm infill demonstrated a significant reduction in strength compared to the no-infill test, confirming that even minimal clay presence affects joint resistance. The transition to behaviour dominated by clay properties in the 10mm test highlights the influence of infill volume on joint mechanics. These support a broader understanding of shear behaviour in weak rock discontinuities and help quantify the mechanical transition from rock-to-rock to clay shearing.

Photo evidence and post-test analysis confirmed that asperities were often shaved off during testing. This highlighted the clay's crucial role in facilitating asperity engagement depending on thickness. This has important implications for understanding joint behaviour under undrained conditions particularly in cases where clay infill may modify contact between opposing joints.

The relevance of these findings extends to excavation design. In practice, rock wedges with clay-filed discontinuities pose significant risk and challenges in slope excavations. The tests conducted under presumed undrained conditions reflect the likely behaviour of clay-infilled joints during early stages of excavation when drainage has not occurred. Therefore, understanding the reduction in shear strength due to clay infill is critical for assessing slope stability.

Testing irregularities did limit the accuracy of findings, especially at higher strain levels. However, this provides a foundation for future research. In conclusion, the results were largely as expected, supporting the literature of clay behaviour. The mechanical response was strongly dependent on the infill thickness, and the transition from asperity interaction to infill-dominated behaviour was clearly reflected in the results. The results provide a stronger understanding of how varying infill conditions affect joint performance and offer a useful way for simulating the behaviour of weak rock discontinuity in geotechnical analysis. Future research should extend tests to long-term loading, address surface mineralogy and include a wider range of normal stress conditions to improve applicability.

6. Further Research and Limitation

6.1. Limitations

Before and after all three tests, the water content of the clay was tabulated. This produced a significant change in water content which had an effect on the accuracy of the readings. This occurred during the preparation time of the test and setting up the shear box which approximated to around an hour. Within this time frame, the plaster started rapidly absorbing the moisture content from the clay because of its hygroscopic properties. The small volume of infill increases the surface area to volume ratio which accelerated the moisture absorption rate within the clays.

At high normal and shear stresses, the accuracy of readings is questioned. This is because the top part of the shear box moved during shear, and as a result, the load cell assembly directly overhead lost its verticality and went out of alignment. The arm holding the load cell and hydraulic ram creating the vertical force remained pin-connected to the bottom half of the shear box, whereas the top part of the same arm moved, inducing an eccentricity in the loading. The load cell was seen to rotate as a result, creating a sideways component. Therefore, the reading from the load cell was not an accurate representation of the normal force produced at high levels of shear. This same misalignment also caused the plates holding the load cell in position to bend, suggesting that the connection system can be improved much further, to eliminate this effect. This can be seen in Figure 6.2 and Figure 6.3.

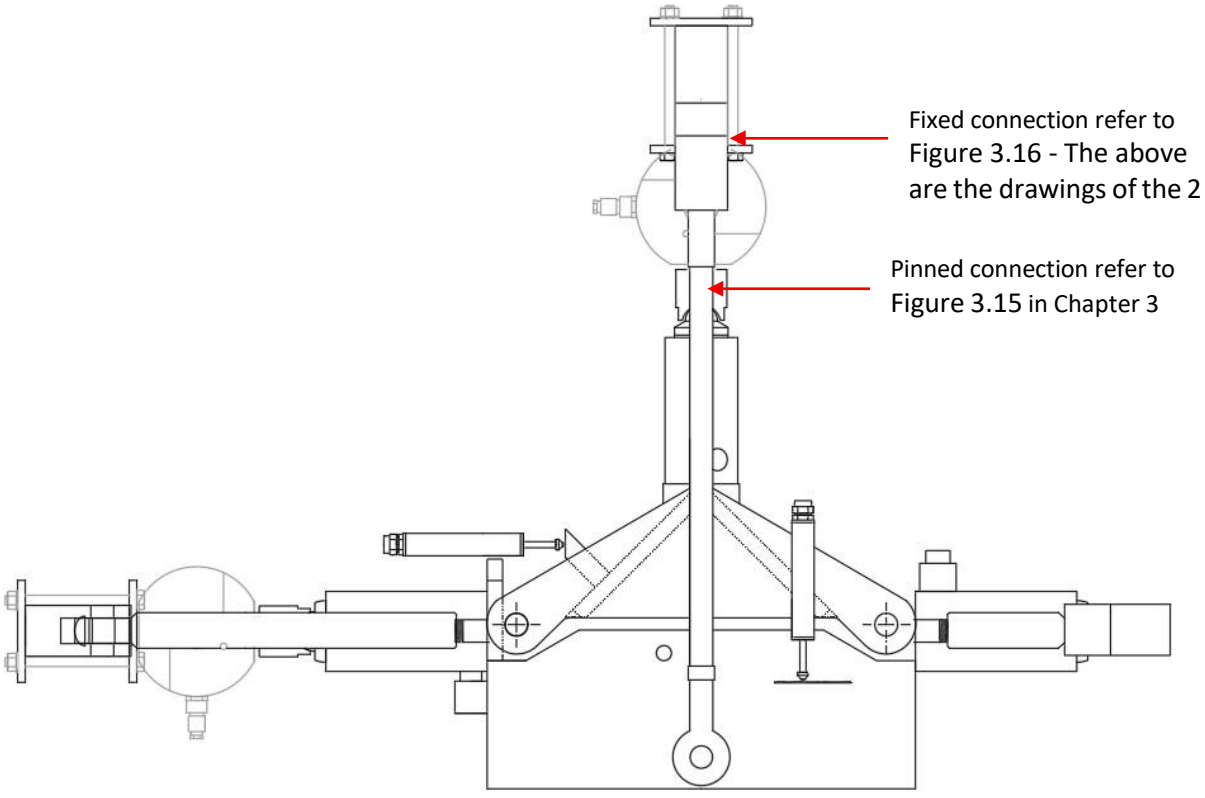

Figure 6.1 - An elevation of the new designed shear box before the connections rotated

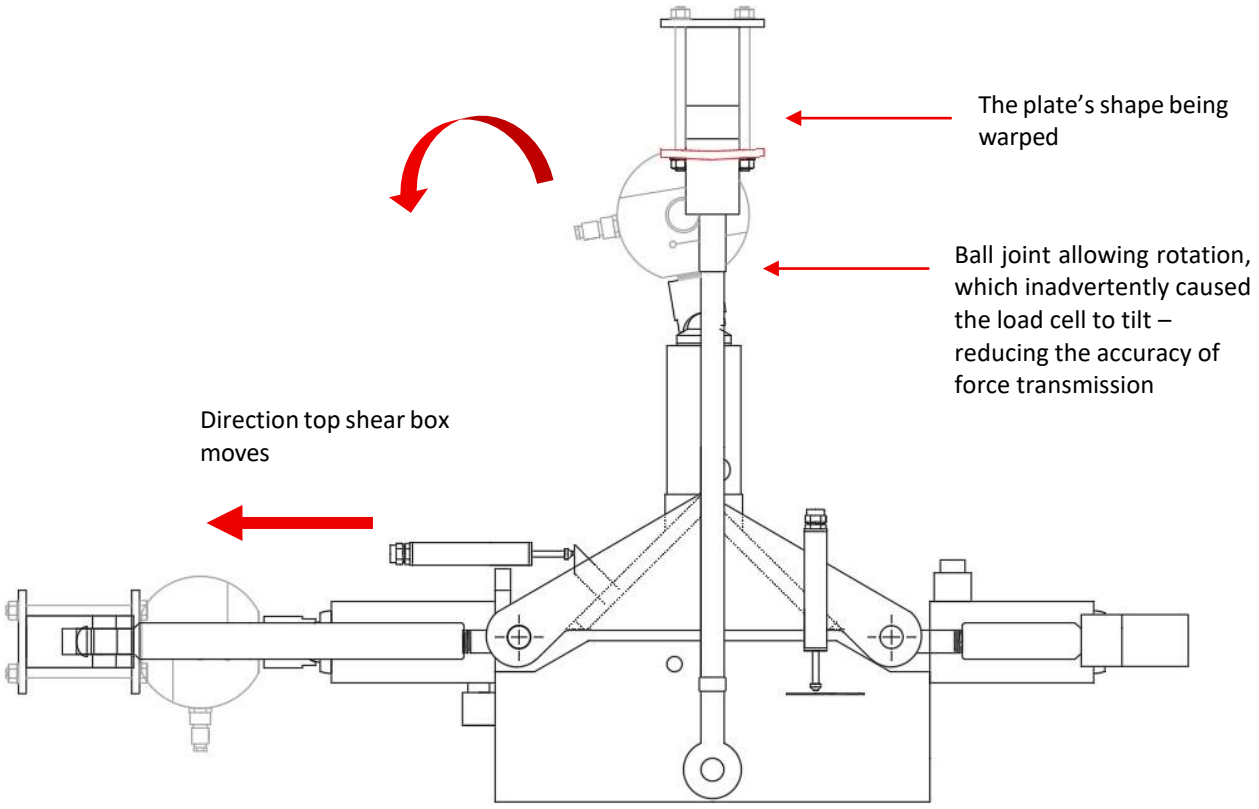

Figure 6.2 - An elevation of how the connections rotated within the experiment, creating less accurate readings

Figure 6.3 - The plate connecting the load cell to the arm visibly bent after testing

6.2. Further Research

Re-Modifying the equipment

The steel connections which were designed for this experiment proved to be unsuccessful and should be further improved. Figure 6.4 below labels the locations and types of the connections which were used in this experimental set-up.

Figure 6.4 shows the suggested modifications, which are split up into a total of six different areas. Location 2 and 5 should be identical. The suggestion to switch the connection of the bottom part of the load cell (2 and 5) from pinned to fixed has been developed from the general mechanical understanding of the equipment. The top part of the shear box is moving perpendicular to the applied normal load as it is being sheared. This causes the hydraulic ram to move with it. Therefore, it is important that the connection between the ram and the load cell is fixed, so that a direct vertical force with no eccentricity is created. This will allow the load cell to measure the identical normal force which is being applied on the specimen, even at high stresses and high displacement values.

Connections 1 and 4, as seen on Figure 6.4, need to however move to allow for the shearing to occur, and hence they are recommended to be pinned connections. In reality, the rotation of the load cells and plates was far more critical in locations 1 and 2, however it is still recommended to change 4 and 5 and use the same design. This is because the movement of the shear box is occurring parallel to the connections in steps 4 and 5.

Suggested Modified Equipment

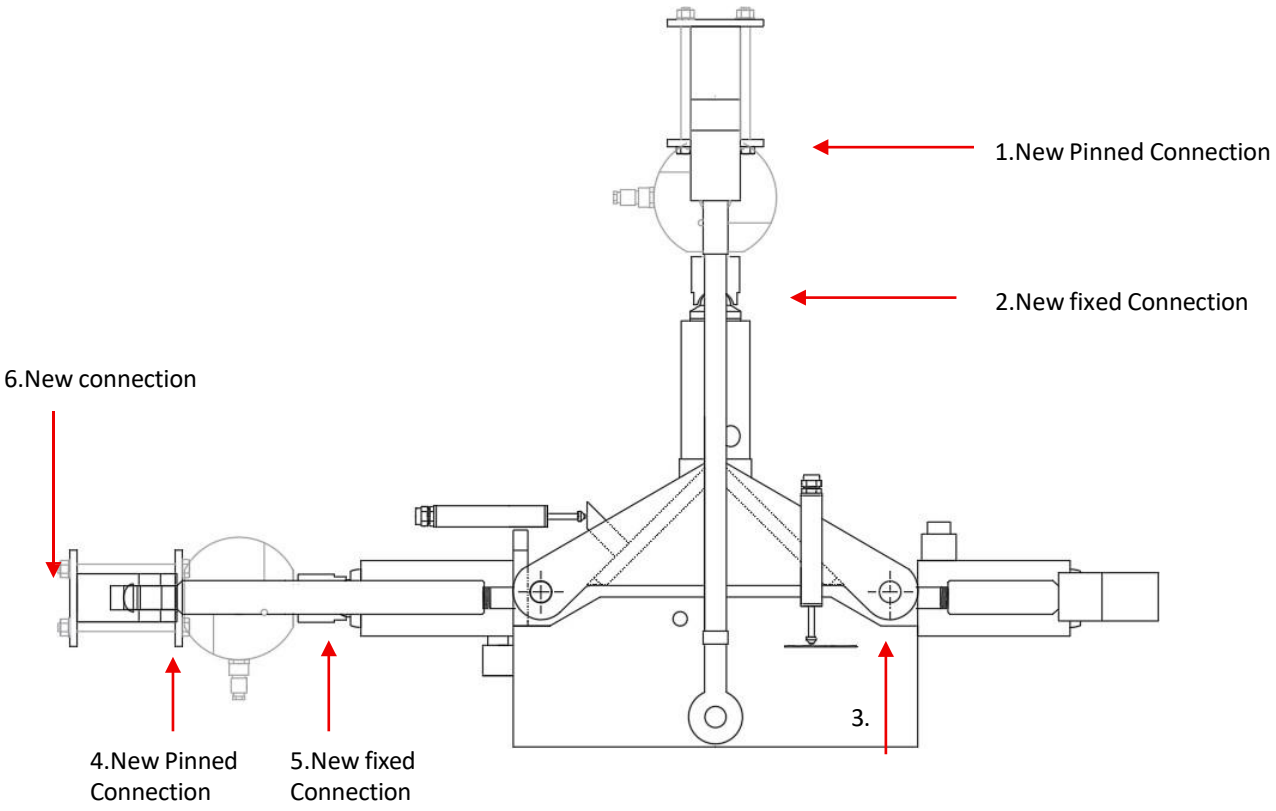

Figure 6.4 - Explaining the new suggested location and types of pinned connection

The recommendation to change connections 4 and 5 is due to the self-weight of the arm which is acting perpendicular to the connections, causing a slight rotation of the connection none the less. The force diagram and its effects on the shear box can be seen in Figure 6.5.

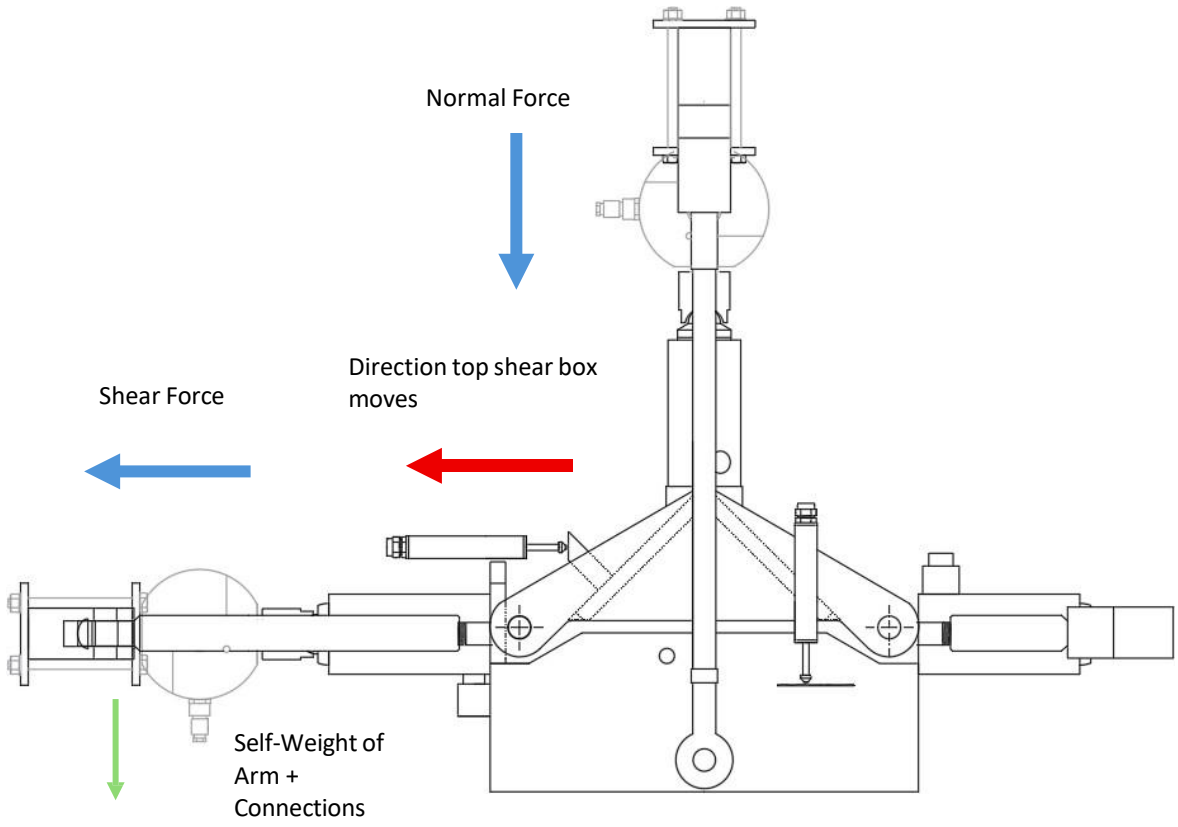

Figure 6.5 - Main forces Normal and Shear Force in Blue which showcase their direction in relation with respect to the movement of the top part of the shear box. The green arrow indicates the less apparent force of self-weight within the set-up

A new mode of compressing the equipment prior to starting the test needs to be considered in the location 6 on Figure 6.4. This is because the initial stages of the testing procedure were considered redundant due to the shear force being increased rapidly until the hydraulic ram locks with the designed steel connection of location 6. This is evident in all results in Section 4 of Shear Strain vs Time. It will be ideal that the whole system is compressed in place from before the testing procedure begins. To avoid sensor misalignment or lack of contact, the entire system should be gently seated in position prior to testing. This ideally does not induce a significant normal stress, however is an essential step to ensure that displacement sensor is properly engaged from the start of data acquisition.

Location 3, as seen in Figure 6.6, provides another limiting factor with respect to the testing procedure. This is because as the specimen was being sheared the top steel element of the shear box started rubbing against the bottom incline section of the shear box. This essentially meant that the tabulated readings towards the end of the testing procedure, produce the shear strength values of shearing steel against steel and not the material under test. The exact location and this behaviour is specified in Section 4. Whether this presents the opportunity to modify the shear box further or to modify the geometry of the moulds produced needs to be further analysed.

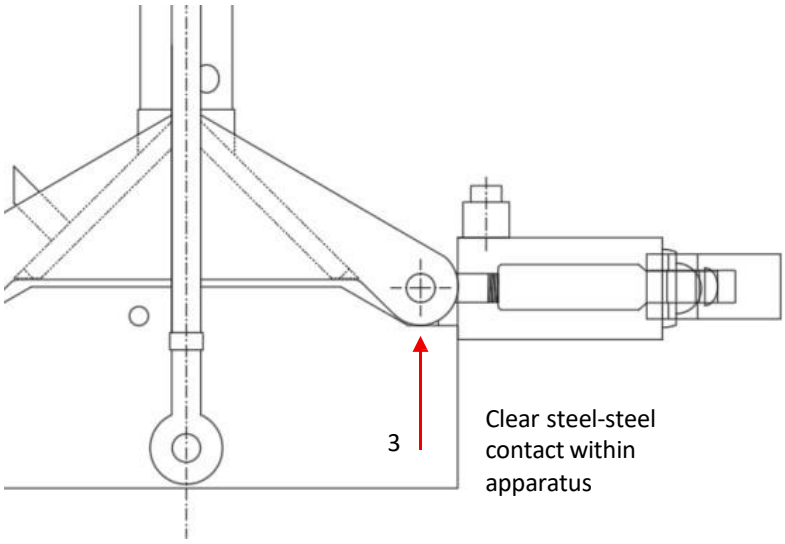

Figure 6.6 - Close up of steel-steel contact

Varying the infill material and its properties

Moreover, other parameters may be varied from this study. The infill material, which was analysed, was a soil made primarily out of blue clay sediments. The reality is that the infill material will be made up of several different types of rock and sand particles. The possibility of varying different percentages of clay with other types of rocks is something which can be further studied. Following this, varying the grain size distribution of each respective rock sediment, together with the presence of water.

The water content of the clay is an area which could be further studied upon. The 45% was chosen from a workability point of view, so that a paste of Blue Clay can be adopted. In reality, different clays of 50% and 60% could easily have been used for experimentation, indicating a relationship between how the strength behaviour would change as more water is added to a clay mix.

Varying the material of the replica

The Plaster of Paris produced a good representation of Lower Globigerina Limestone. However, this had the direct effect of evaporating the water content of the clay because of its hygroscopic properties. Therefore the consistency can be maintained more by using other materials to make up the moulds such as reconstituted limestone.

However, it is acknowledged that the use of plaster introduces certain limitations when compared to real rock such as Lower Globigerina Limestone. Differences in mechanical behaviour, including a generally more brittle failure mode and reduced resistance to sustained loading, mean that plaster may not full replicate the complex deformation mechanism observed in natural rock.

Additionally, the absence of interface mineralogy, which plays a significant role in rock joint behaviour further limits the fidelity of the results. While plaster provides a consistent and workable substitute for controlled lab testing, its applicability under field-scale stress levels must be interpreted with caution.

The geometry of the mould could also be changed and understanding how the same thickness and material would change with different inclination angles and asperity heights. As discussed in Section 4, the strain of the specimens against eachother in relation to the geometry of the mould could be seen as a determining factor. The spike in shear strength is consistent with this shear strain location.

Using a different apparatus testing different conditions

The current direct shear box does not maintain constant normal loading. A Proportional Integral Derivative (PID), controller coupled with a pressure sensor, can be installed on the normal loading member of the equipment. This system would continuously monitor and adjust the applied force. As the normal force begins to increase (as observed in this experiment), the PID system would respond by regulating the pressure to a constant value. This will provide a different area of results for the same test procedure.

7. References

Aladejare, A. E., Ozoji, M. T., Idris, A. M., Lawal, A. I., & Onifade, M. (2022). Empirical estimation of rock mass deformation modulus of rocks: Comparison of intact rock properties and rock mass classifications as inputs. *Arabian Journal of Geosciences, 15*(11). doi:10.1007/s12517-022-10190-7

Al-Obaidi, A. (2018). *Soil Mechanics Notes – Chapter 6.* Unpublished Report.

Alonso, E., Alejano, L. R., Varas, F., Fernández-Manín, G., & Carranza-Torres, C. (2003). Ground response curves for rock masses exhibiting strain-softening behaviour. *International Journal for Numerical and Analytical Methods in Geomechanics, 27*(13), 1153–1185. doi:10.1002/nag.315

Balmer, G. G. (1952). *A Study of Stress Conditions in Rock Using Photoelastic Models. Vicksburg, Mississippi: U.S. Army Corps of Engineers, Waterways Experiment Station*.

Bandis, (1983). Fundamentals of rock joint deformation. *International Journal of Rock Mechanics and Mining Sciences & Geomechanics Abstracts, 20*(6), 249-268.

Bandis, (1981). Experimental Studies of Scale Effects on Shear Strength and Deformation of Rock Joints.

Barbieri, N. (2020). Assessing Shear Strength of Rock Discontinuitites through laboratory testing on replicas. Master's Thesis, University of Malta.

Barton, N. (1973). Review of a New Shear-Strength Criterion for Rock Joints. *Engineering Geology, 7*, 287–332.

Barton, N. R. (1973). A review of the shear strength of filled discontinuities in rock. *Symposium on Rock Mechanics, Bergmekanikk.* Oslo: Norwegian Group for Rock Mechanics.

Barton, N. R. (1976). The shear strength of rock and rock joints. *International Journal of Rock Mechanics and Mining Sciences & Geomechanics Abstracts, 13*(9), 255–279. doi:10.1016/0148-9062(76)90003-6

Barton, N. R., & Bandis, S. C. (1982). Effect of block size on the shear behavior of jointed rocks. *Paper presented at the 23rd U.S. Symposium on Rock Mechanics (USRMS).* Berkeley, California: American Rock Mechanics Association (ARMA).

Barton, N. R., & Bandis, S. C. (2017). Characterization and modelling of the shear strength, stiffness and hydraulic behaviour of rock joints for engineering purposes. In X.-T. Feng (Ed.), *ISRM Suggested Methods and Guidelines: Volume 1* (pp. 1–26). Cham: Springer.

Barton, N. R., & Choubey, V. (1977). The shear strength of rock joints in theory and practice. *Rock Mechanics and Rock Engineering, 10*(1–2), 1–54. doi:10.1007/BF01261801

Bhardwaj, S., & Rao, K. S. (2022). The Shear Strength Behaviour of Natural Joint Infill. *Research Square (Preprint Platform)*. doi:10.21203/rs.3.rs-1535717/v1

Bieniawski, Z. T. (1974). Estimating the Strength of Rock Materials. *Journal of the South African Institute of Mining and Metallurgy*, 312–320.

Bieniawski, Z. T. (1989). *Engineering Rock Mass Classifications: A Complete Manual for Engineers and Geologists in Mining, Civil, and Petroleum Engineering.* New York: John Wiley & Sons.

Bishop, A. W., Green, G. E., Garga, V. K., Andresen, A., & Brown, J. D. (1971). A study of the influence of progressive failure on the peak strength of a clay. *Géotechnique, 21*(4), 343–358.

Cassar, D. (2020). An Investigation into the One-Dimensional Compression Properties of the Reconstituted and Intact Blue Clay of the Maltese Islands. University of Malta.

Chattopadhyay, B. C. (1972). Residual strength of cohesive soils.

de Toledo, P. E., & de Freitas, M. H. (1993). The strength and dilatancy of dry sand and the mechanical consequences of particle breakage. *Géotechnique, 43*(3), 541–555.

Dhadse, G. D., Ramtekkar, G., & Bhatt, G. (2024). Thin layer interface: An alternative modeling consideration in soil-structure interaction system. *Research on Engineering Structures and Materials*. doi:10.17515/resm2024.16me0926rs

ERA. (2025). *National Plan-Geology*. Retrieved from ERA: https://era.org.mt/topic/national-plan-geology/

Fathipour-Azar, H. (2023). Shear strength criterion for rock discontinuities A comparative study of regression approaches. *Rock Mechanics and Rock Engineering*. doi:10.3390/app10124095

Fredlund, D. G. (2021). *An Introduction to Unsaturated Soil Mechanics.* Hoboken, New Jersey: John Wiley & Sons, Inc.

Frühwirt, T., Pötschke, D., & Konietzky, H. (2021). Simulation of direct shear tests using a forces on fracture surfaces (FFS) approach. *Environmental Earth Sciences, 80*(312). doi:10.1007/s12665-021-09606-6

Galea, P. (2007). Seismic history of the Maltese islads and considerations on seismic risk. *Annals of Geophysics, 50*(6).

Gauci, R., & Scerri, S. (2019). A Synthesis of Different Geomorphological Landscapes on the Maltese Islands. In R. Gauci, *Landscapes and Landforms of the Maltese Islands* (pp. 49–61). Cham. doi:10.1007/978-3-030-15456-1_5

Giwangkara, G. G., Mohamed, A., Nor, H. M., Khalid, N. H., & Mudiyono, R. (2020). Analysis of internal friction angle and cohesion value for road base materials in a specified gradation. *Journal of Advanced Civil and Environmental Engineering, 3*(2), 58–65. doi:10.30659/jacee.3.2.58-65

Goodman, R. E. (1970). *Methods of Geological Engineering in Discontinuous Rocks.* San Francisco: West Publishing Company.

Hoek, E. (2007). Chapter 3: Rock Mass Classification. In *Practical Rock Engineering.* Toronto: Rocscience Inc.

Hoek, E. (2007). *Practical Rock Engineering.* Toronto: Rocscience.

Hoek, E., & Bray, J. (n.d.). *Rock Slope Engineering* (Third ed.). London.

Hoek, E., & Brown, E. (2019). The Hoek Brown failure criterion and GSI - 2018 edition. *Journal of Rock Mechanics and Geotechnical Engineering*(3), 445-463. doi:10.1016/j.jrmge.2018.08.001

Hoek, E., Marinos, P., & Barton, N. (1997). Practical Estimates of Rock Mass Strength. In *Proceedings of the International Symposium on Rock Stress, 1997* (pp. 1–8). Rotterdam: Balkema.

Hudson, J. A., & Priest, S. D. (1983). Discontinuity frequency in rock masses. *International Journal of Rock Mechanics and Mining Sciences & Geomechanics Abstracts, 20*(2), 73–89. doi:10.1016/0148-9062(83)90329-7

Hvorslev, M. J. (1936). Fundamentals of Soil Strength: A Study of the Strength of Cohesive Soils. Copenhagen: Technical University of Denmark.

Indraratna, B. (2010). *Ground Improvement Techniques and Applications.* New York: Nova Science Publishers.

Indraratna, B., Oliveira, D., & Brown, E. T. (1998). A shear-displacement criterion for rock joints. *Géotechnique*. doi:10.1680/geot.8.P.094

Indraratna, B., Premadasa, W., Nemcik, J., & Jayanathan, M. (2012). Shear Strength model for sediment-infilled rock discontinuitites and field applications. *ANZ 2012 Conference Proceedings* (pp. 1250-1255). Perth: Australian Geomechanics Society.

Irfan, T. Y., Sham, A. T., & Tang, K. Y. (1993). A soil–rock model for the shear strength of decomposed rock. *Quarterly Journal of Engineering Geology and Hydrogeology, 26*(4), 321–330.

Jaber, J., Conin, M., Deck, O., Moumni, M., Godard, O., & Kenzari, S. (2020). Investigation of the mechanical behavior of 3D printed polyamide-12 joints for reduced scale models of rock mass. *Rock Mechanics and Rock Engineering, 53*(6), 2687–2705. doi:10.1007/s00603-020-02064-9

Jaeger, J. C. (1959). The strength of rocks. *Advances in Physics, 8*, 82–139.

Kaiser, P. K., & Bawden, W. F. (1995). *Ground Support in Mining and Underground Construction.* Rotterdam: A.A. Balkema.

Karademir, T., & Dışkaya, B. (2024). Composite Sand–Clay infrastructural soil fills: Characteristic consolidation and hydraulic properties. *Journal of Advanced Research in Natural and Applied Sciences*. doi:10.28979/jarnas.1411201

Kenney, T. C. (1967). Residual strength of mineral mixtures. *Géotechnique, 17*.

Kenney, T. C. (1967). Residual strength of mineral mixtures. *Géotechnique, 17*(3), 255–272.

Liu, S. H. (2006). Simulating a direct shear box test by DEM. *Canadian Geotechnical Journal, 43*(2), 155–172. doi:10.1139/T05-097

Lupini, J. F., Skinner, A. E., & Vaughan, P. R. (1981). The drained residual strength of cohesive soils. *Géotechnique, 31*(2), 181-213. doi:10.1680/geot.1981.31.2.181

Main, G., Schembri, J., Gauci, R., Crawford, K., Chester, D., & Duncan, A. (2018). The hazard exposure of the Maltese Islands. *Natural Hazards, 92*(2), 829–859. doi:10.1007/s11069-018-3227-x

Malik, A., & Singh, A. (2019). Triaxial and direct shear tests to estimate the parameters of rock-joints and rock-shotcrete interface. *Vietrock2019 – An ISRM Specialized Conference.* Hanoi: ISRM (International Society for Rock Mechanics and Rock Engineering).

Mantovani, M., Devoto, S., Forte, E., Mocnik, A., Pasuto, A., Piacentini, D., & Soldati, M. (2013). A multidisciplinary approach for rock spreading and block sliding investigation in the north-western coast of Malta. *Landslides, 10*(5), 611–622. doi:611–622

Miller, R. P. (1965). *Rebound Test for Rock Strength.* Vicksburg, Mississippi: U.S. Army Engineer Waterways Experiment Station.

Mogi, K. (1966). Pressure dependence of rock strength and transition from brittle fracture to ductile flow. *Bulletin of the Earthquake Research Institute, University of Tokyo, 44*, 215–232.

Mokhtarian, H., Moomivand, H., & Moomivand, H. (2020). Effect of infill material of discontinuitites on the failure criterion of rock under triaxial compressive stresses . *Theoretical and Applied Fracture Mechancis*.

Muralha, J., Grasselli, G., Tatone, B., Blümel, M., Chryssanthakis, P., & Jing, L. (2014). ISRM Suggested Method for Laboratory Determination of the Shear Strength of Rock Joints: Revised Version. *Rock Mechanics and Rock Engineering, 47*(1), 291–302. doi:10.1007/s00603-013-0519-z

Patton, F. D. (1966). Multiple modes of shear failure in rock. *Proceedings of the 1st Congress of the International Society for Rock Mechanics.* Lisbon: International Society for Rock Mechanics (ISRM).

Patton, F. D., & Deere, D. U. (1967). Closure to discussion of 'Multiple failure surfaces in model slopes'. *Proceedings of the 1st International Conference on Rock Mechanics.* Lisbon: International Society for Rock Mechanics (ISRM).

Pedley, H. M., House, M. R., & Waught, B. (1976). *The Geology of Malta and Gozo.*

Rocha, M. (1964). The shear strength of rockfill. *Proceedings of the 8th International Congress on Large Dams.* Edinburgh: International Commission on Large Dams (ICOLD).

Schofield, A., & Wroth, P. (1968). *Critical State Soil Mechanics.* London: McGraw-Hill.

Skempton, A. N. (1972). The behaviour of saturated clays in landslides and embankment failures. *Géotechnique, 22*(3), 195–213.

Skempton, A. N., & Hutchinson, J. N. (1969). Stability of natural slopes and embankment foundations. Mexico City: British National Society of the International Society of Soil Mechanics and Foundation Engineering.

Skempton, A. N., & Petley, D. J. (1968). The strength along structural discontinuities in stiff clays. *Géotechnique, 18*(1), 9–26.

Skinner, A. E. (1969). A note on the influence of interparticle friction on the shearing strength of a granular material. *Géotechnique, 19*(1), 150–157.

Terzaghi, K., & Peck, R. B. (1967). *Soil Mechanics in Engineering Practice.* New York: John Wiley & Sons.

Ulusay, R., Hudson, J. A., & al., e. (2007). *The Complete ISRM Suggested Methods for Rock Characterization, Testing and Monitoring: 1974–2006.* Lisbon: International Society for Rock Mechanics (ISRM).

Venkateswarlu, B., & Singh, M. (2022). Shear strength of the soil-rock mixture deposits: Applicability of Barton and Kjaernsli shear strength model. *Acta Geotechnical*. doi:10.1007/s11440-022-01692-5

Voight, B. (1973). Correlation of residual friction angle with plasticity index.

Wang, S., Hagan, P. C., & Cao, C. (2023). Rockbolting. In *Ground Support in Underground Mining* (pp. 61-102). Amsterdam: Elsevier. doi:10.1016/B978-0-12-810552-8.00002-7

Wesley, L. D. (1977). Residual strength of clays in relation to clay mineralogy. *Géotechnique*.

Wickham, G. E., Tiedemann, H. R., & Skinner, E. H. (1972). Support determination based on geologic predictions. *Proceedings of the Rapid Excavation and Tunneling Conference (RETC).* New York: AIME (American Institute of Mining, Metallurgical, and Petroleum Engineers).

Zheng, B., Qi, S., Huang, X., Guo, S., Wang, C., Zhan, Z., & Luo, G. (2020). An advanced shear strength criterion for rock discontinuitites considering size and low shear rate. *Applied Sciences, 10*(12), 1-20. doi:10.3390/app10124095

8. Appendix

8.1. Test Results

Test 1

Date of Test:	20.05.2025
Date of Mould:	25.04.2025

Moisture Content Before:	46.25%	Moisture Content After:	32.73%
Void Ratio Before:	1.23	Void Ratio After:	0.87

Infill Thickness:	1mm
Mass Specimen:	1.26 kg
Initial Normal Stress:	0.58 MPa

Before Shearing:

Figure 8.1 - Bottom and top specimens for Test 1 before experimentation

After Shearing:

Figure 8.2 -Bottom and top specimens for Test 1 after experimentation

Test 2

Date of Test:	22.05.2025
Date of Mould:	28.04.2025

Moisture Content Before:	43.%	Moisture Content After:	31.62%
Void Ratio Before:	1.16	Void Ratio After:	0.84

Infill Thickness:	1mm
Mass Specimen:	1.34 kg
Initial Normal Stress:	0.54 MPa

Before Shearing:

Figure 8.3 - Bottom and top specimens for Test 2 before experimentation

After Shearing:

Figure 8.4- Bottom and top specimens for Test 2 after experimentation

Test 3

Date of Test:	22.05.2025
Date of Mould:	28.04.2025

Moisture Content Before:	48.8%	Moisture Content After:	34.16%
Void Ratio Before:	1.29	Void Ratio After:	0.91

Infill Thickness:	1mm
Mass Specimen:	1.3 kg
Initial Normal Stress:	0.43 MPa

Before Shearing:

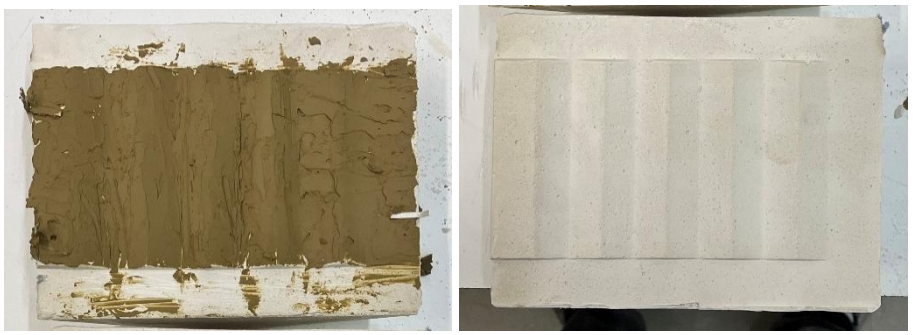

Figure 8.5- Bottom and top specimens for Test 3 before experimentation

After Shearing:

Figure 8.6- Bottom and top specimens for Test 3 after experimentation

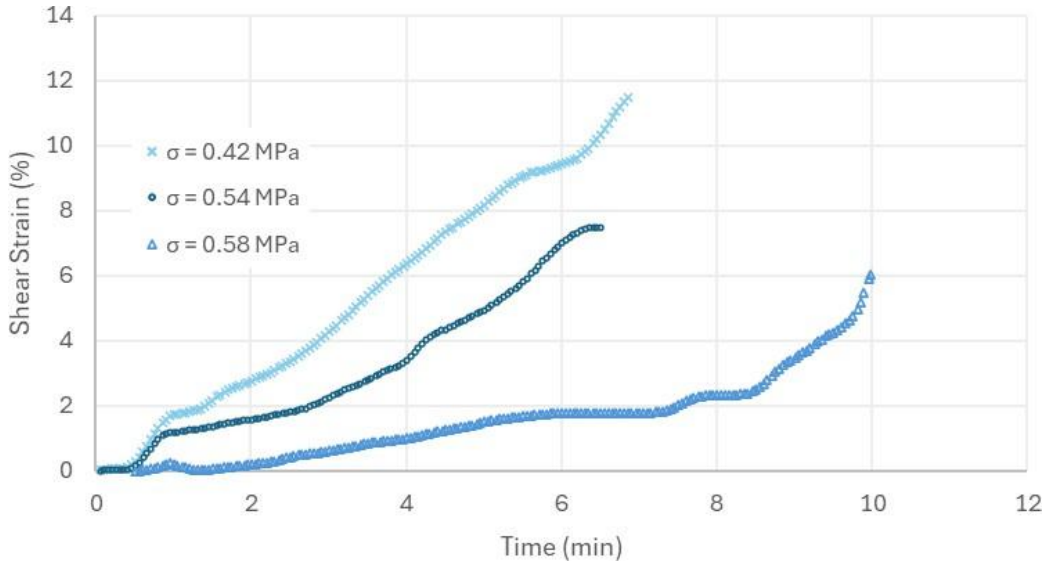

Figure 4.8- Shear Strain (%) vs Time (mins) for 1mm

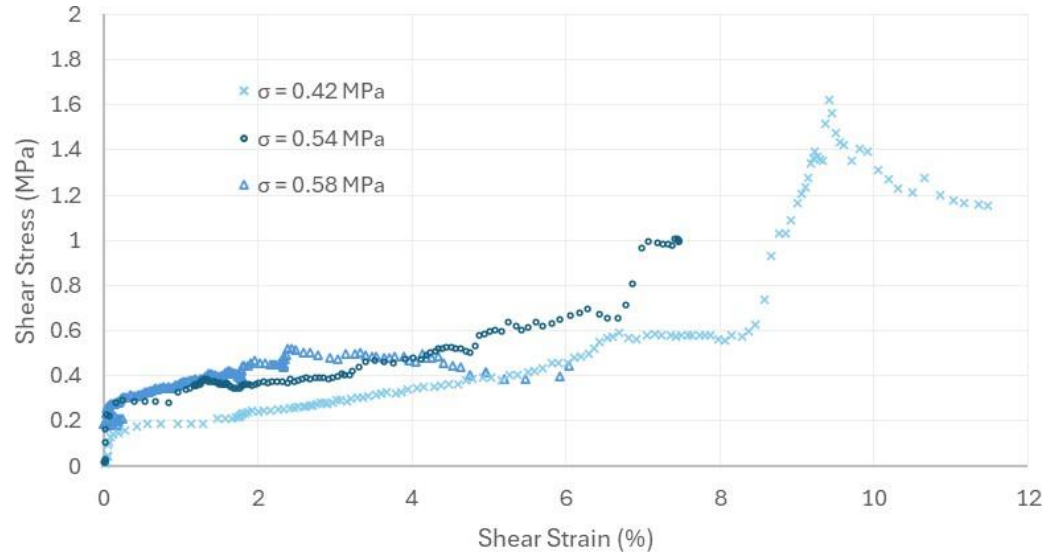

Figure 4.11 - Shear Stress (MPa) vs Shear Strain (%) at different initial normal loads for 1mm thickness

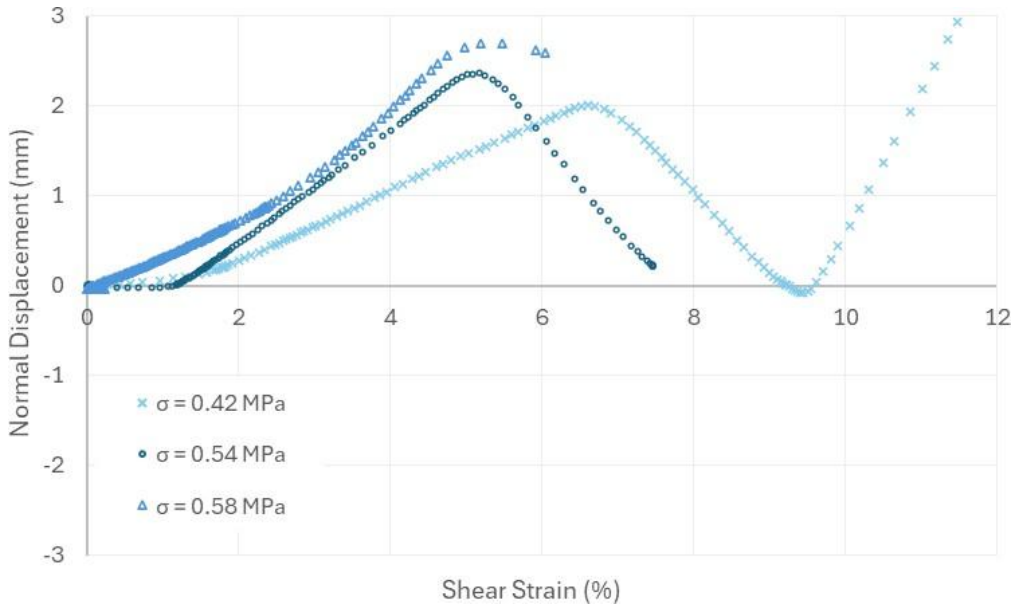

Figure 4.12 - Normal displacement (mm) vs shear strain (%) for 1mm

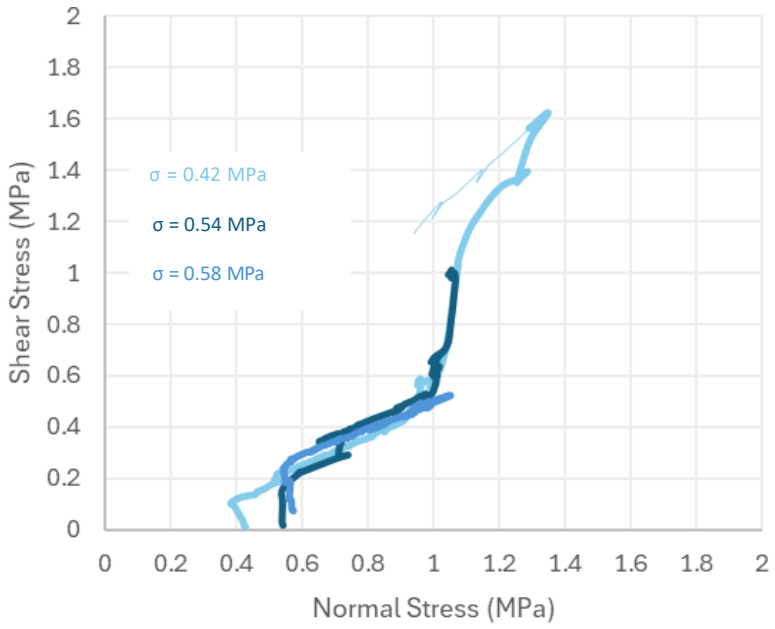

Figure 8.13 - Shear Stress (MPa) vs Normal Stress (MPa) for 1mm at different initial σ

Test 4

Date of Test:	28.05.2025
Date of Mould:	28.04.2025

Moisture Content Before:	46.5%	Moisture Content After:	39%
Void Ratio Before:	1.23	Void Ratio After:	1.03

Infill Thickness:	5mm
Mass Specimen:	1.36 kg
Initial Normal Stress:	0.37 MPa

Before Shearing

Figure 8.7- Bottom and top specimens for Test 4 before experimentation

After Shearing

Figure 8.8- Bottom and top specimens for Test 4 after experimentation

Test 5

Date of Test:	28.05.2025
Date of Mould:	29.04.2025

Moisture Content Before:	48.35%	Moisture Content After:	44.35%
Void Ratio Before:	1.28	Void Ratio After:	1.18

Infill Thickness:	5mm
Mass Specimen:	1.27 kg
Initial Normal Stress:	0.68 MPa

Before Shearing:

Figure 8.9- Bottom and top specimens for Test 5 before experimentation

After Shearing:

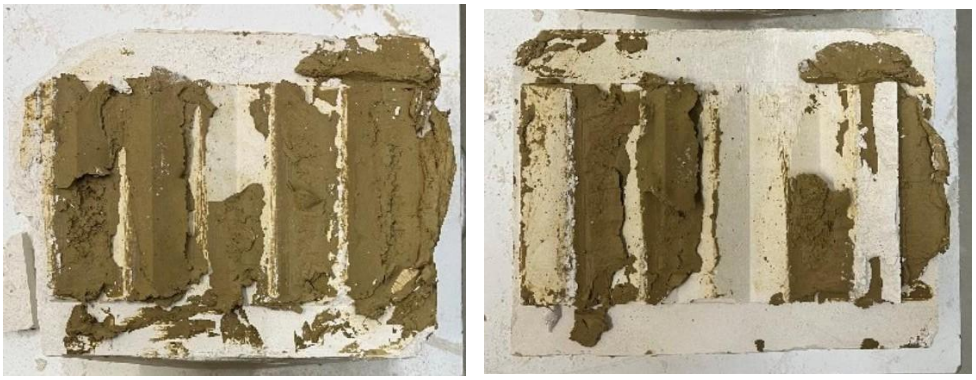

Figure 8.10- Bottom and top specimens for Test 5 after experimentation

Test 6

Date of Test:	28.05.2025
Date of Mould:	25.04.2025

Moisture Content Before:	50.05%	Moisture Content After:	44.8%
Void Ratio Before:	1.33	Void Ratio After:	1.19

Infill Thickness:	5mm
Mass Specimen:	1.3 kg
Initial Normal Stress:	0.28 MPa

Before Shearing:

Figure 8.11- Bottom and top specimens for Test 6 before experimentation

After Shearing:

Figure 8.12- Bottom and top specimens for Test 6 after experimentation

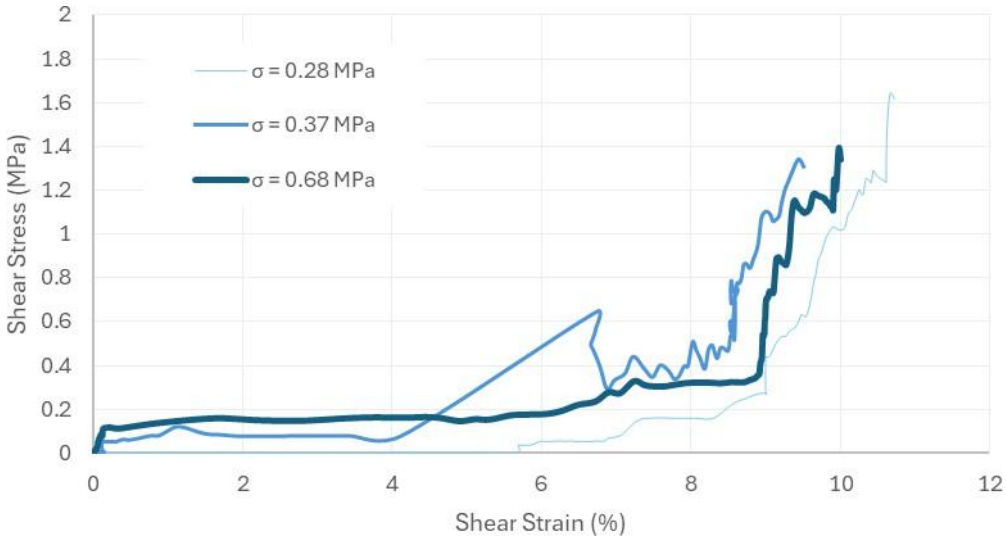

Figure 4.18-Shear Strain (%) vs time (min) for 5mm

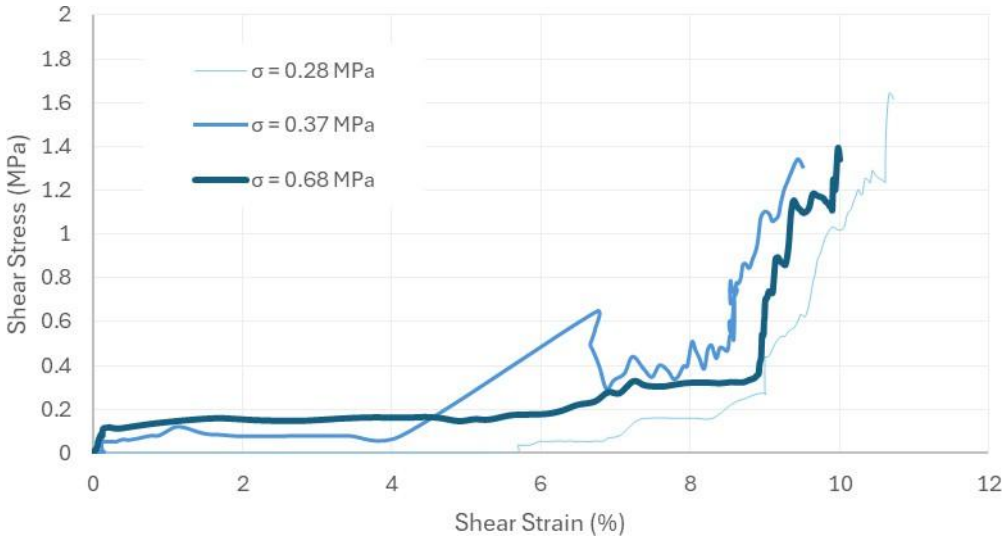

Figure 4.19 - Shear Stress(MPa) against Shear Strain (%) for 5mm clay infill

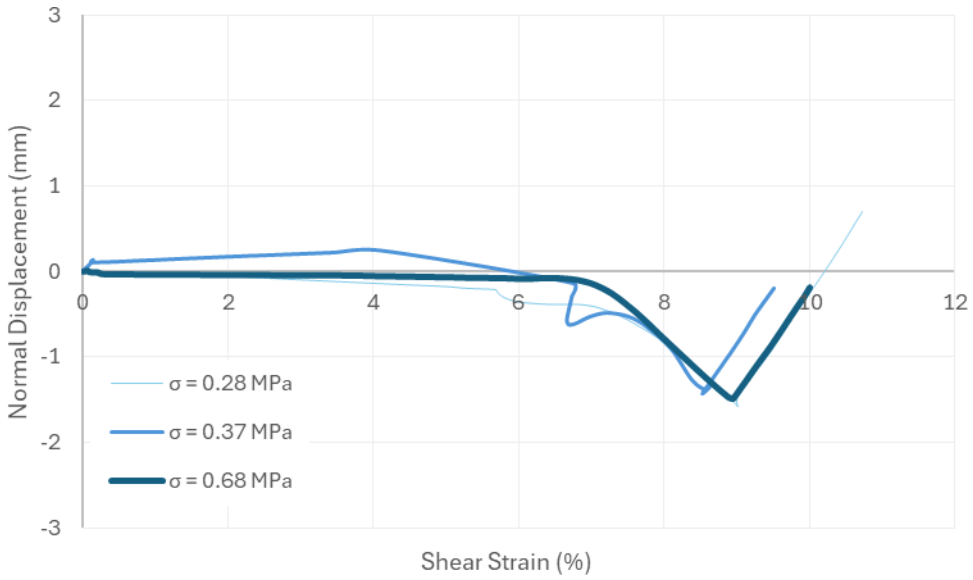

Figure 4.20 – Normal Displacement (mm) vs Shear Strain (%) for 5mm

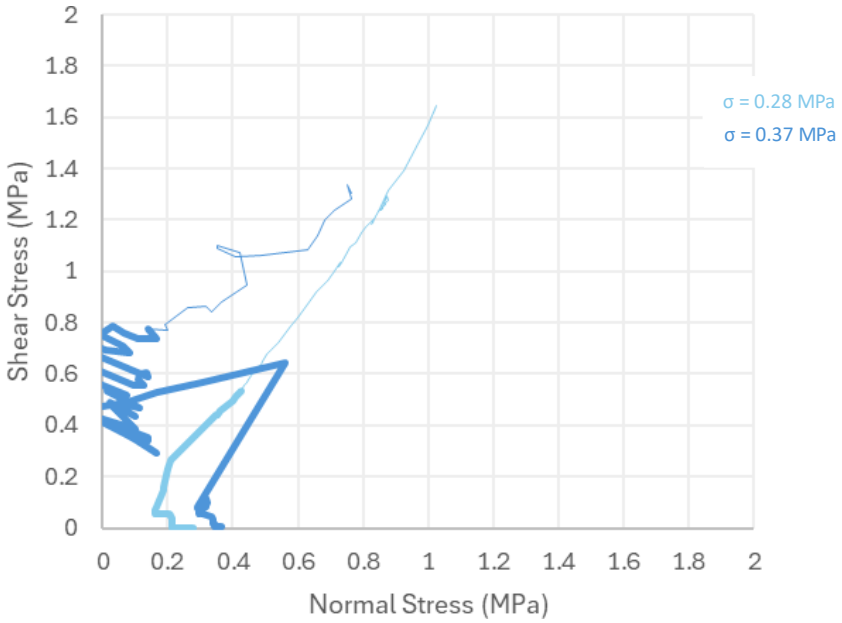

Figure 4.21 – Shear Stress (MPa) vs Normal Stress (MPa) for 5mm

Test 7

Date of Test:	28.05.2025
Date of Mould:	29.04.2025

Moisture Content Before:	0	Moisture Content After:	0
Void Ratio Before:	0	Void Ratio After:	0

Infill Thickness:	0mm
Mass Specimen:	1.26 kg
Initial Normal Stress:	0.56 MPa

Before Shearing:

Figure 8.13- Bottom and top specimens for Test 7 before experimentation

After Shearing:

Figure 8.14- Bottom and top specimens for Test 7 after experimentation

Figure 4.27 - Shear Strain (%) vs Time (min) for 10mm thickness

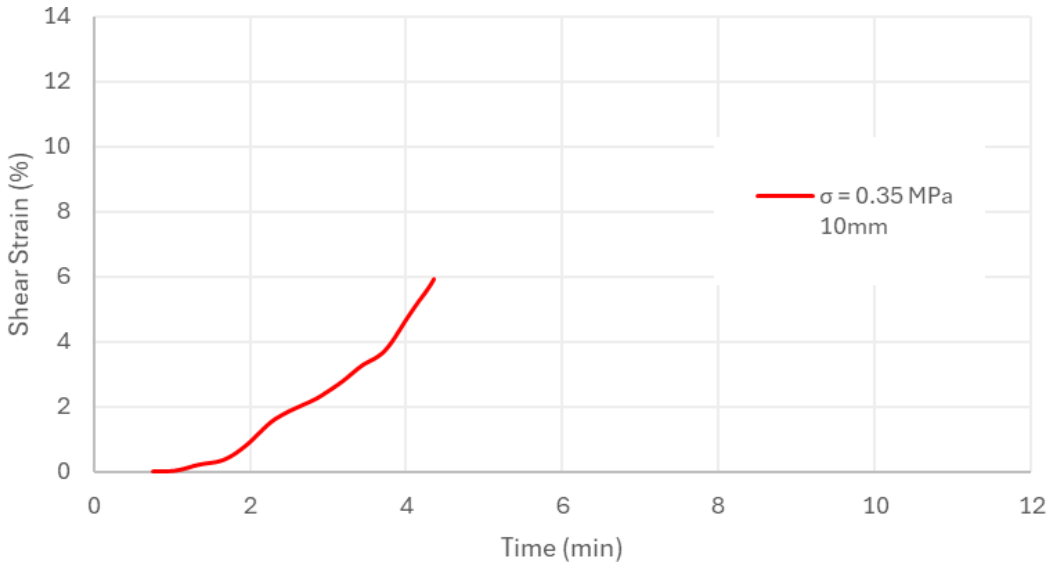

Figure 4.22 - Shear Strain (%) vs Time(min) for no thickness

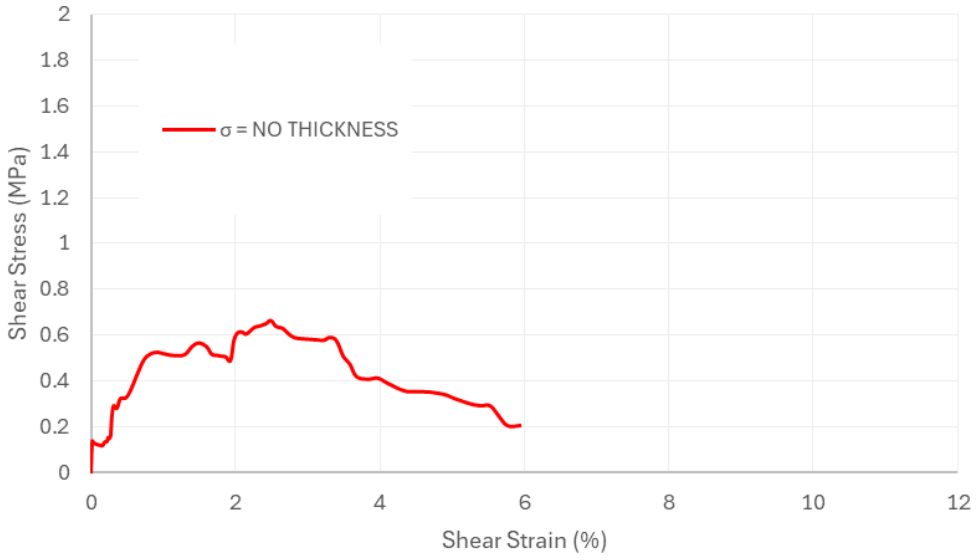

Figure 4.23 - Shear Stress(MPa) vs Shear Strain (%) for no thickness

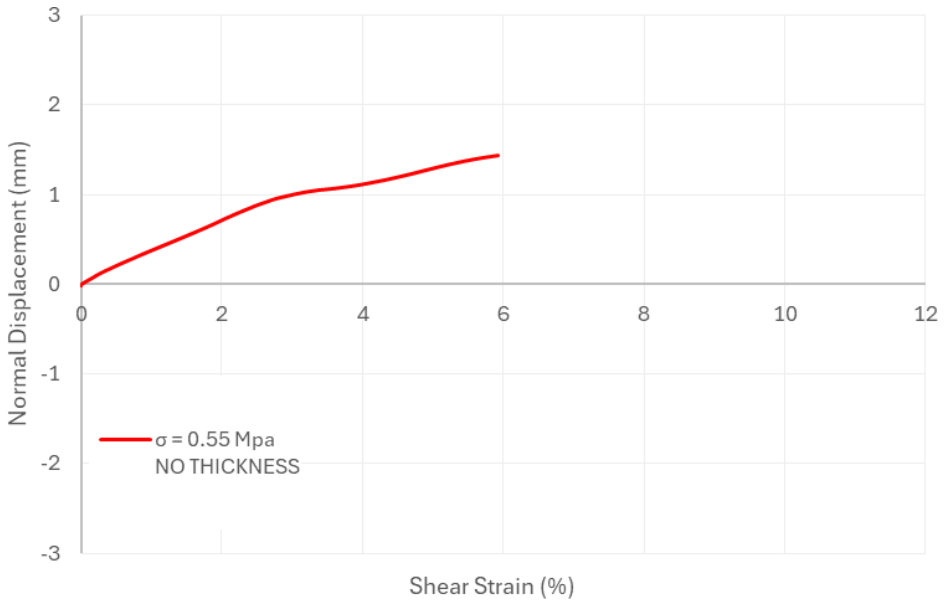

Figure 4.24 - Normal Displacement (mm) vs Shear Strain (MPa) for no thickness

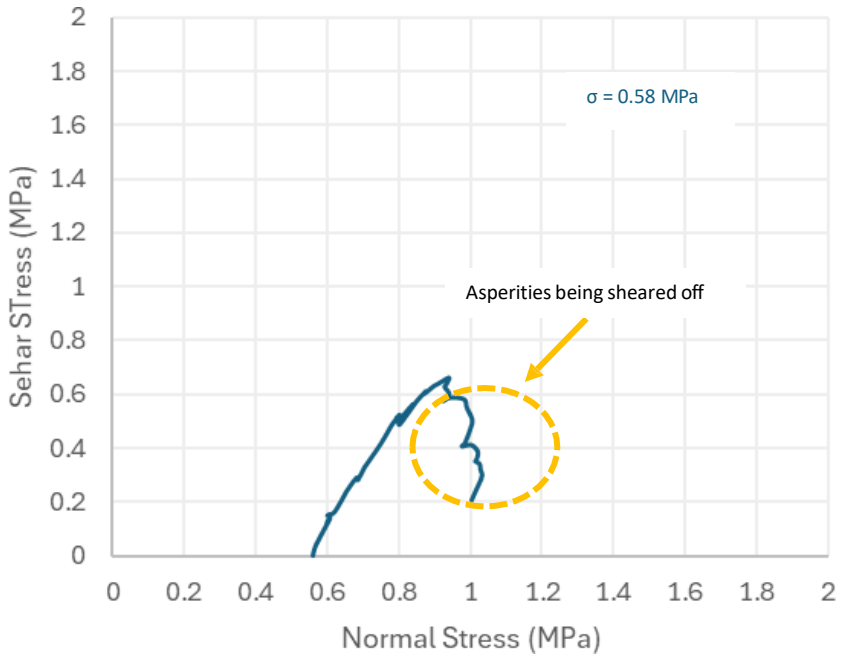

Figure 4.26 - Shear Stress (MPa)vs Normal Stress (MPa) for no infill thickness 0.58 MPa initial σ

Test 8

Date of Test:	29.05.2025
Date of Mould:	29.04.2025

Moisture Content Before:	51.63%	Moisture Content After:	41.61%
Void Ratio Before:	1.37	Void Ratio After:	1.10

Infill Thickness:	3mm
Mass Specimen:	1.29 kg
Initial Normal Stress:	0.28 MPa

Before Shearing:

Figure 8.15- Bottom and top specimens for Test 8 before experimentation

After Shearing:

Figure 8.16- Bottom and top specimens for Test 8 after experimentation

Test 9

Date of Test:	29.05.2025
Date of Mould:	30.04.2025

Moisture Content Before:	52.74%	Moisture Content After:	43.47%
Void Ratio Before:	1.4	Void Ratio After:	1.15

Infill Thickness:	3mm
Mass Specimen:	1.16 kg
Initial Normal Stress:	0.36 MPa

Before Shearing:

Figure 8.17- Bottom and top specimens for Test 9 before experimentation

After Shearing:

Figure 8.18- Bottom and top specimens for Test 9 after experimentation

Test 10

Date of Test:	29.05.2025
Date of Mould:	30.04.2025

Moisture Content Before:	47.3%	Moisture Content After:	41.92%
Void Ratio Before:	1.25	Void Ratio After:	1.11

Infill Thickness:	3mm
Mass Specimen:	1.263 kg
Initial Normal Stress:	0.44 MPa

Before Shearing:

Figure 8.19- Bottom and top specimens for Test 10 before experimentation

After Shearing:

Figure 8.20- Bottom and top specimens for Test 10 after experimentation

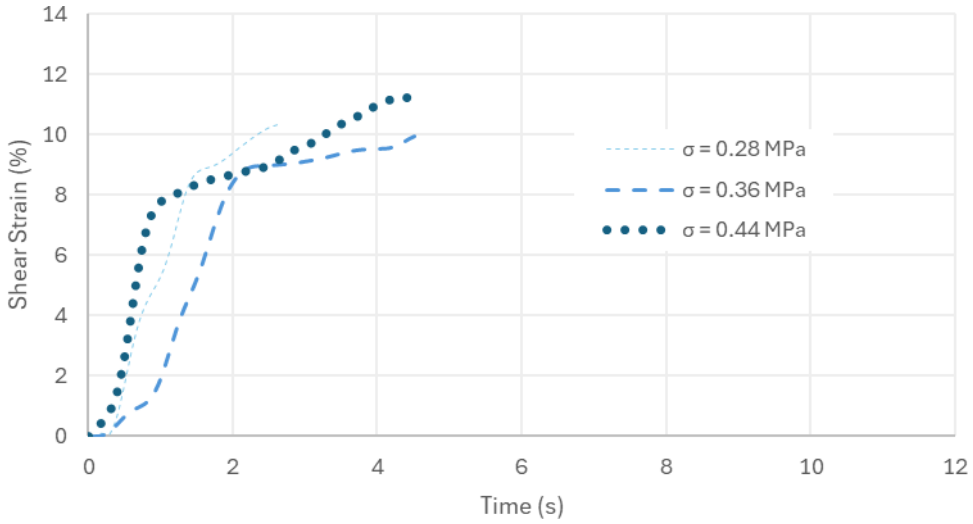

Figure 4.14 - Shear Strain (%) vs Time (min) for 3mm

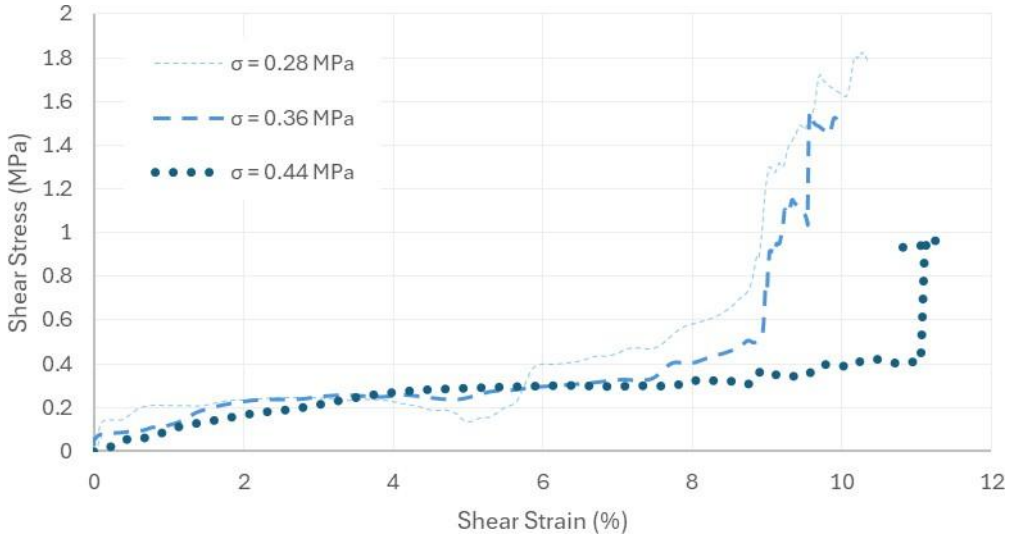

Figure 4.15 – Shear Stress (MPa) vs Shear Strain (%) for 3mm

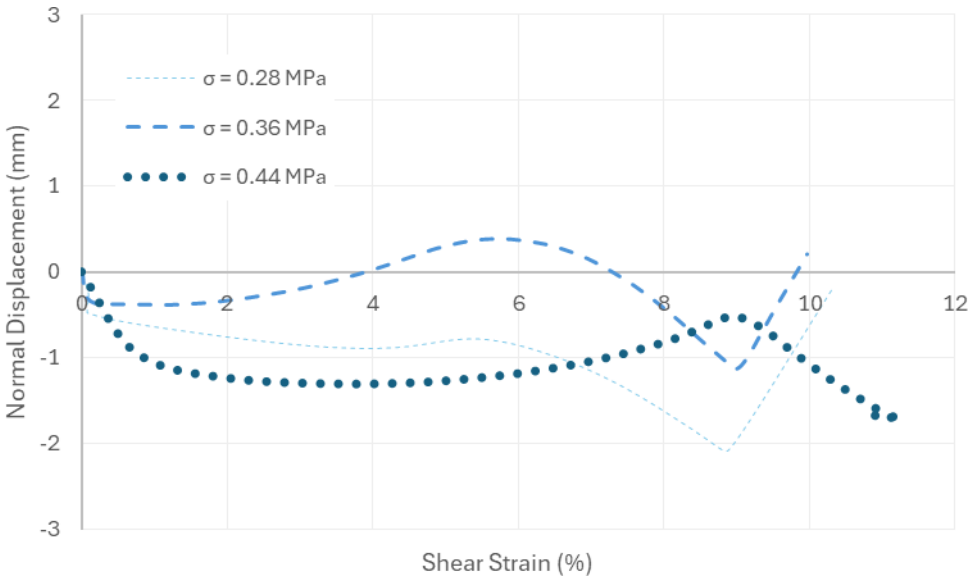

Figure 4.16 – Normal Displacement (mm) vs Shear Strain (%) at 3mm thickness

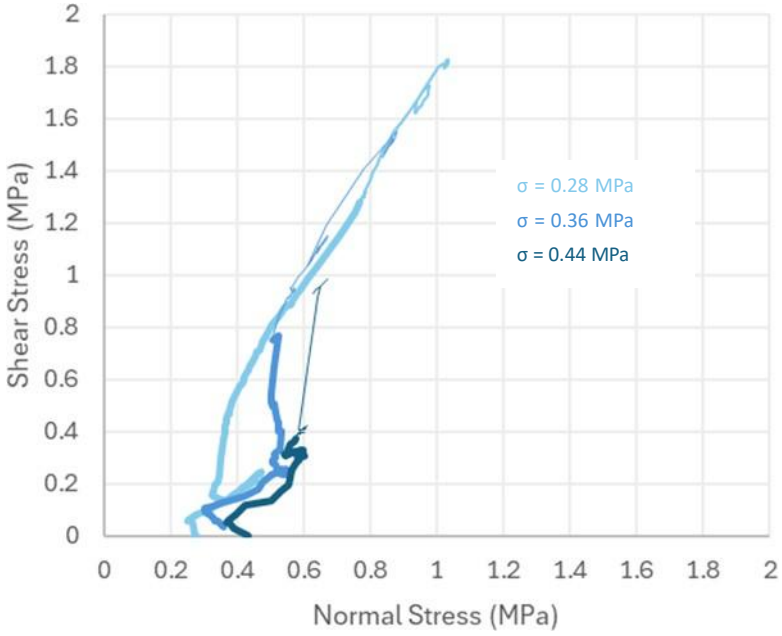

Figure 4.17 - Shear Stress (MPa) vs Normal Stress (MPa) for 3mm at different initial σ

Test 11

Date of Test:	03.06.2025
Date of Mould:	02.05.2025

Moisture Content Before:	52.7%	Moisture Content After:	48.6%
Void Ratio Before:	1.4	Void Ratio After:	1.29

Infill Thickness:	10mm
Mass Specimen:	0.905 kg
Initial Normal Stress:	0.35 MPa

Before Shearing:

Figure 8.21- Bottom and top specimens for Test 11 before experimentation

After Shearing:

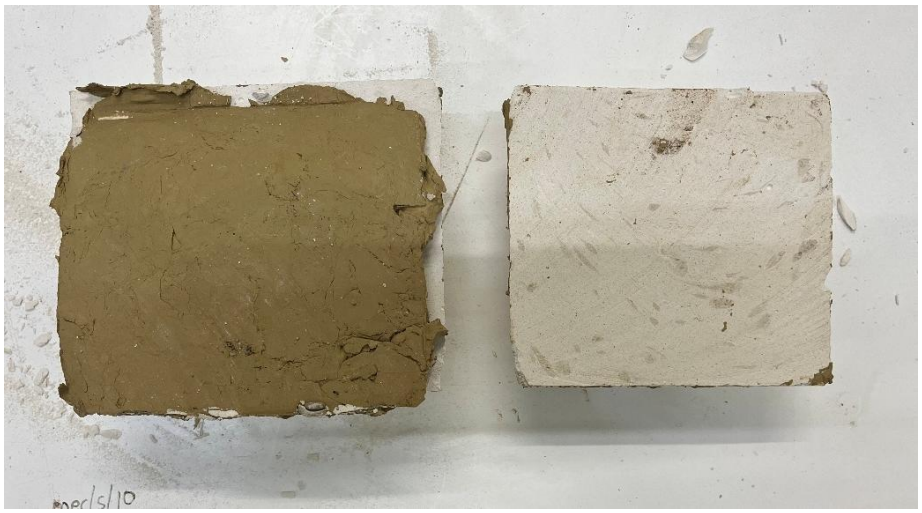

Figure 8.22- Bottom and top specimens for Test 11 after experimentation

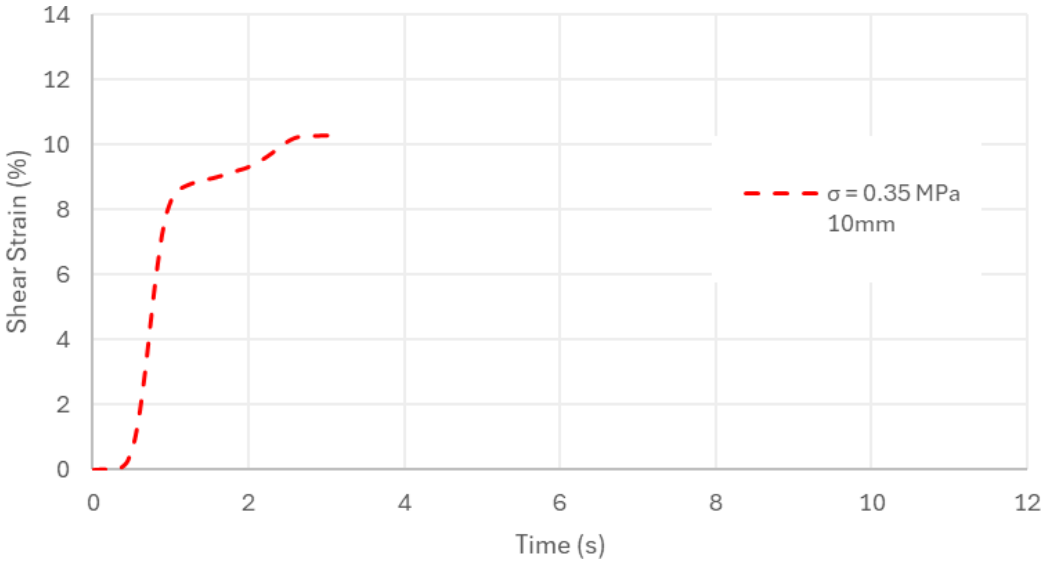

Figure 4.27 - Shear Strain (%) vs Time (min) for 10mm thickness

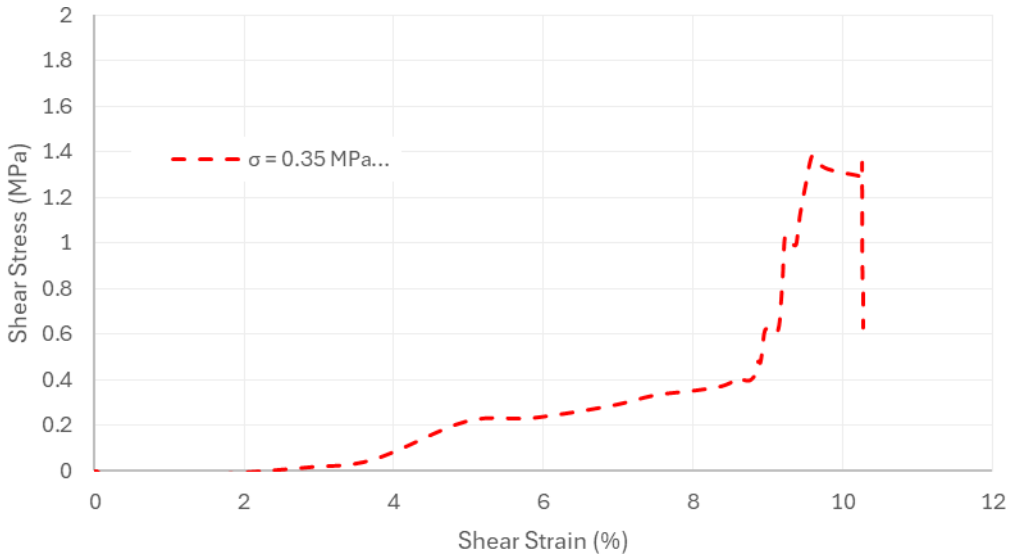

Figure 4.28 - Shear Stress (MPa) vs Shear Strain (%) for 10mm thickness

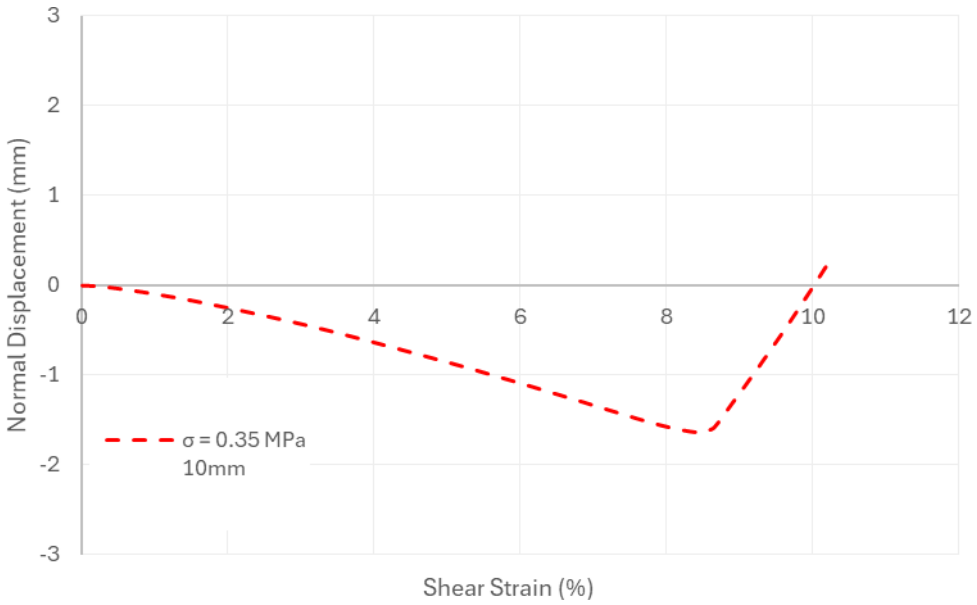

Figure 4.29 - Shear Strain (MPa) vs Normal Displacement (mm) for 10mm thickness

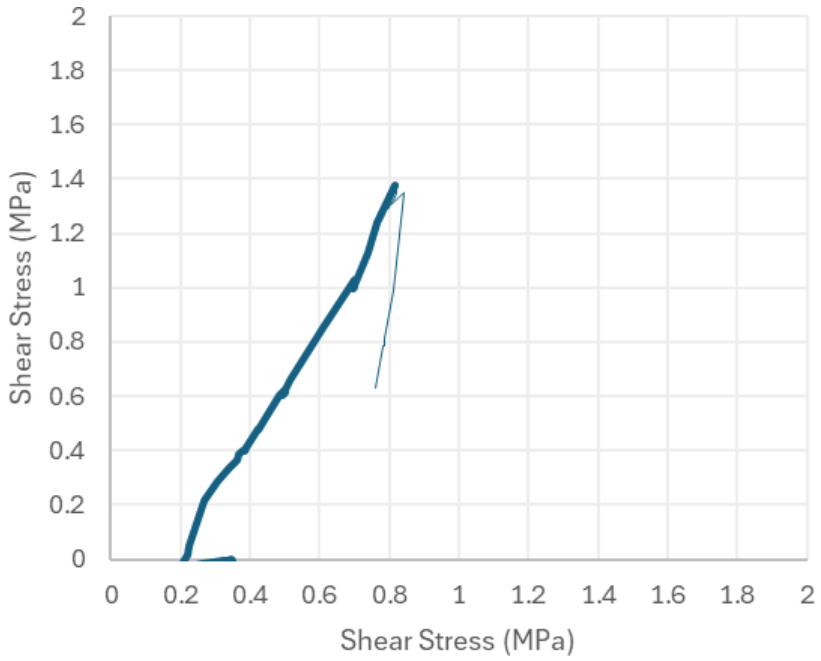

Figure 4.30 - Shear Stress (MPa) vs Normal Stress (MPa) for 10mm thickness 0.35 MPa initial σ

8.2. Equipment Specifications

77 Rock Mechanics
Classification, strength and durability

ELE International

Rock Shear Strength

The engineering strength and slope stability of a rock formation is directly related to the strength of any fault line within it, therefore it is essential to obtain data concerning such weakness at the design stage.

Portable Shear Box Assembly

The technique enables the engineer to select specimens of rock from exposed faces or bore holes, observe orientation of fault lines, then set and test the fault in the shear box.

The apparatus consists of a diagonally split box assembly. The upper half incorporates a vertical ram for compressive loading, and the lower half, two horizontal rams for reversible shearing action. The force applied by the horizontal ram is aligned with the centre of the box and the discontinuity in the specimen. Pressure is applied to the rams by means of hand-operated hydraulic pumps and load is indicated on two Bourdon tube gauges. An adjustable low friction pressure maintainer incorporated into the loading system allows a constant load to be maintained during the test. The pressure maintainer is supplied with a foot pump.

Specification	
Maximum sample size	
Irregular	125 x 115 mm face area
Cores	101 mm diameter
Load application	Hydraulic via two single speed hand pump/reservoir assemblies
Load gauge	Two x 150 mm dia dual-marked scale 50 kN x 1 kN and 11 000 lbf x 200 lbf
Horizontal displacement	Dial gauge 25 mm travel x 0.01 mm
Weight	45.5 kg

Ordering Information

EL77-1030
Portable Shear Box Assembly

Accessory

EL77-1100 **Crystacal Plaster** for casting specimens in position. Weight 25 kg bag

EL77-1030 Portable Shearbox Assembly

Rock Durability

Slake Durability Apparatus

ASTM D 4644

This apparatus provides a means of predicting the durability of rock to weakening and disintegration when subjected to the simulated effects of climatic slaking. The system incorporates a motor drive unit mounted on a base board with quick-release drive assemblies capable of revolving two or four specimen test drums at a speed of 20 revolutions per minute. The test drums are supported on water lubricated bearings allowing unobstructed clearance below the drum.

Two drums manufactured from a corrosion resistant material are supplied with two water troughs.

Specification		
Dimensions (l x w x h)		1320 x 368 x 267 mm
Drums	Length	100 mm
	Diameter	140 mm
	Mesh	2 mm
Weight		20 kg

Ordering Information

EL77-0510/01
Slake Durability Apparatus
For 220 – 240 V AC, 50 – 60 Hz, 1 ph

EL77-0510 series Slake Durability Apparatus

Portable Shear Box Assembly
EL77-103

Operating instructions

1. Description

1.1 The portable shear box assembly is designed to accept rock samples of no more than 155 mm x 125 mm (4.5 x 5 in) in face area or, alternatively, cores up to 102 mm (4 in) diameter.

1.2 It can be seen that the shear box consists of two halves, the lower (1) being fixed with two rams (2) for reversible shearing, and the upper (3) fitted with a ram (4) for normal load application.

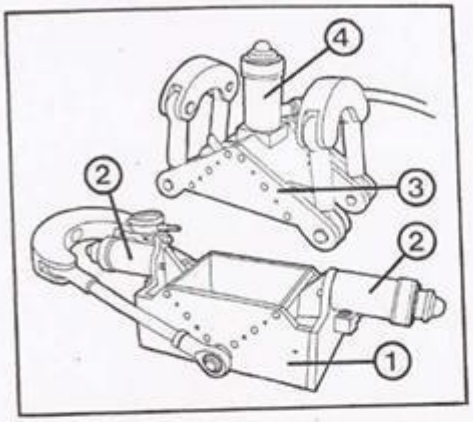

1.3 The loads exerted on the rams during testing are indicated by Bourdon tube load gauges (5) and they are worked independently by hand-operated hydraulic pumps. The gauges are calibrated in both S.I. and Imperial Units.

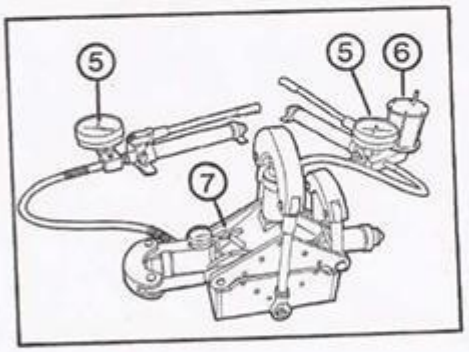

1.4 One of the most important additions to the shear box is an adjustable low friction pressure maintainer (6) which has been incorporated into the normal loading system, thus allowing a constant normal load to be achieved throughout the duration of the test.

1.5 Clamp attachment and anvil are provided so that a dial gauge (7) can be mounted to record horizontal movement of the box.

1.6 The mould is for casting a sample into a suitable form to be accepted by the shear box. It is of aluminium main construction with heavy duty perspex sides to allow inspection of the sample for correct alignment. The sides are detachable to facilitate removal of the bonded sample. A sample locating clamp (8) is supplied with each mould. Two moulds are recommended for normal field use and are supplied in the standard kit.

2. Operation

2.1 Sample preparation

2.1.1 Select the discontinuity or plane of weakness to be studied from the recovered borehole cores or similar samples.

2 **Portable Shear Box Assembly**
EL77-103

2.1.2 Prepare the sample for test by sawing or fracturing the core some 40 to 60 mm (1.5 to 2.5 in) on either side of the selected discontinuity. The two parts of the sample so formed are then bound together with wire (9).

2.1.3 The sample is now in a form suitable for mounting in the mould, as shown in the diagram.

2.2 Sample mounting

2.2.1 Prepare a quick-setting plaster such as Crystacal medium (EL77-110). Coat the mould formers with mould release oil to facilitate sample removal after the setting of the mounting medium.

2.2.2 Place the clamp with the wire bound specimen gripped in its jaws (10) across the half mould which contains the retaining screws in its inclined faces (11) taking care that the intended shear plane is aligned with the mid position of the inspection slot (12) in the vice and the sight markings on the perspex sides. Position the shear plane in the horizontal plane until a central symmetry for even normal loading is achieved. The design of the sample locating clamp and its closing movement to grip the specimens is such that it enables a rapid procedure for mounting.

2.2.3 Screw the retaining screws in so that they will locate approximately 5 mm into the bonding medium (13). Remove the specimen with the clamp attached. Treat the inside of the mould and screws with release oil and pour a sufficient quantity of the selected bonding mixture into the half mould so that its level reaches the top edge of the mould when the sample is replaced, thus immersing the lower half of the sample in the wet mix. Vibrate the mould vigorously to achieve good compaction of the bonding material around the sample without contaminating the shear plane.

2.2.4 Allow the bonding medium to set hard.

2.2.5 Remove the perspex sides and fix them onto the other half mould. Apply release oil in the inner surfaces as previously. Fill the mould with wet bonding mixture as accurately as possible so that little addition or removal of the mix is required due to the more difficult access. Remove the sample locating clamp from the specimen. Slide the mould with the bonded specimen onto the second half of the sample. It may be necessary to slightly

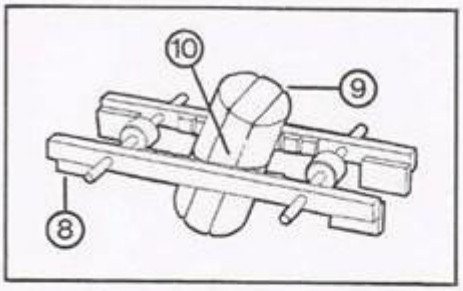

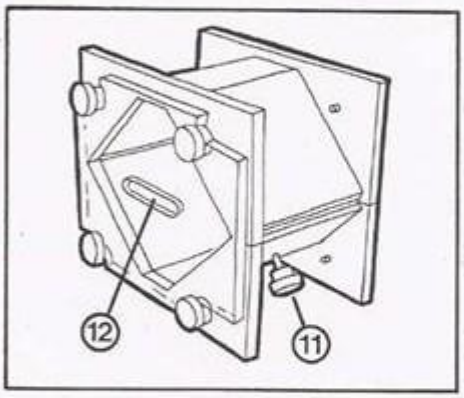

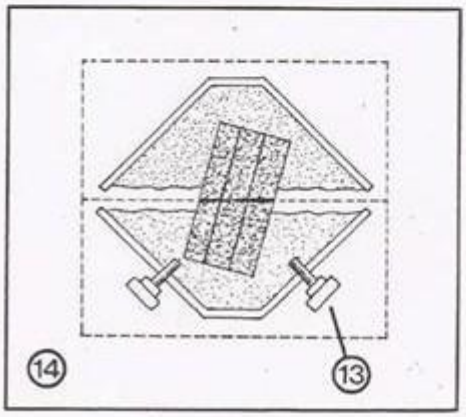

loosen the four bottom screws holding the perspex sides to allow easy passage of the upper mould. When the upper half of the mould is properly seated tighten all eight screws to obtain the accurate alignment and dimensions required.

2.2.6 Add or remove small amounts of wet mix with a palette knife through the inspection side slots to bring the bonding flush with the top edge of the mould. The sample is suitable for testing after being left overnight to ensure adequate hardening of the bonding.

Figure 14 shows a cross-section through the mould with the specimen in position in the bonding in both halves of the mould.

2.3 Sample loading

2.3.1 Make hydraulic connections in the manner illustrated in the second drawing. The adjustable pressure maintainer is included in the vertical ram circuit, with a pressure gauge being fitted in each of the loading circuits.

2.3.2 Place the mounted sample in the lower section of the box, and position the upper section on top of it. Bring the vertical yoke into position over the spherical seating of the upright ram and apply a small vertical load by means of pressure from the vertical load hand pump with a low air pressure in the maintainer. Once the joint surfaces are held firmly in this manner, cut the wire constraint on the sample. Use a pair of flat tin snips or similar, to gain access to the sample through the small amount of clearance.

2.3.3 Affix the dial gauge to the frame of the lower section (15) so that the relevant horizontal movement of the segments can be monitored.

2.3.4 Engage one horizontal yoke, depending on direction of shear, with a ram and apply a small positive pressure using the shear load hand pump.

2.4 Test procedure

2.4.1 The vertical load maintaining unit is basically a hydraulic intensifier, the low pressure side being a pneumatic reservoir (accumulator). Its operation is best appreciated by initial trial and error usage, but the principal operational mode is as follows:

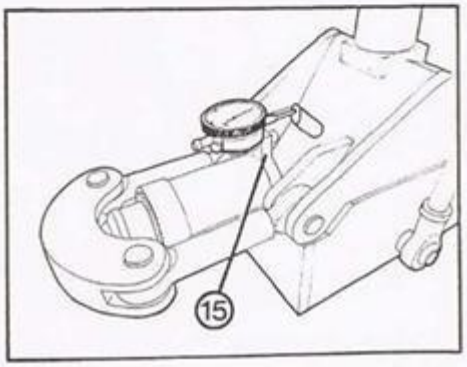

4 **Portable Shear Box Assembly**
EL77-103

Test procedure (continued)

The hydraulic and pneumatic pressures are balanced by means of the hydraulic hand pump and a portable air pump respectively, such that the maintainer float lower edge rises approximately half way up the viewing ports in the outer body at the required load (indicated on the gauge). The air pump for this use can be a car foot pump, motorcycle pump, gas cylinders or similar appliance.

Under no circumstances should the float lower edge be allowed to stay above the half way level of the ports (16) (at which the maintainer is most effective) at the start of any test, at a particular vertical load setting.

To unload, always reduce the hydraulic pressure by the pump pressure release valve (17) (there is no need to deflate the air reservoir; the remaining air pressure helps to seal the oil spill side of the system). The oil spill from the maintainer is returned to the tank via outside piping.

Keep the device upright to avoid oil spillage in transit.

Precaution

Do not pump the hydraulic unit carelessly so that pneumatic reservoir float is driven up against the top without a balancing air cushion.

Using the technique described above, apply the required vertical load to the sample.

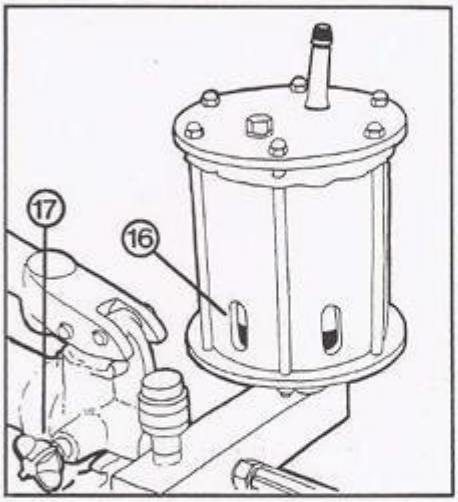

2.4.2 Apply a shearing load to the sample by use of the second hand pressure pump, the dial gauge being monitored to ensure that a reasonable uniform rate of displacement is achieved during shearing. Very occasionally during the shearing operation it may be found necessary to slightly re-adjust the vertical load to maintain its original value.

2.4.3 Record the level of vertical load and the peak shearing strength indicated by the maximum auxiliary pointer.

2.4.4 Continue shearing beyond this peak so that a reliable average residual shear strength value can be obtained, changing shear direction where necessary. Note also the displacements corresponding to the residual shear strength readings.

The displacement required for a residual value varies with different rock types but displacement of about 10 mm (0.4 in) are generally sufficient.

It should be noted that in order to preserve near axial symmetry of normal loading, shearing should not be carried for more than 10 mm (0.4 in) from the neutral position, in either direction.

2.4.5 Repeat the process for a series of vertical loads, the corresponding peak and residual shear values being obtained.

2.4.6 Using the measured sample area and the recorded loads, calculate values of stress so that plots of peak and residual shear stress against normal stress can be made. If values of cohesion are calculated, note that the ram friction and the upper box weight should be taken into account as zero errors.

8.3. Calibration Certificate

Micrometre

Certificate No. I4054225

Measurement and Calibrations Services Unit
MRA049B, Marsa Industrial Estate,
Marsa MRS3000. Malta
tel.: +356 21226841, +356 21226844
fax.: +356 23331204

CALIBRATION CERTIFICATE

This document certifies that the instrument detailed below has been calibrated by the Measurement & Calibration Services Unit of Inspectra Ltd. All measurement results reported in this certificate were obtained following standard operating procedures. The reference standards are indicated in section 5 from which starts the traceability chain of the Measurement & Calibration Services Unit laboratory. The traceability chain proceeds uninterrupted towards national or international standards of the *International System of Units (SI)*. They relate only to the calibrated item and they are valid for the time and conditions of calibration, unless otherwise specified.

This certificate cannot be reproduced unless in full and with the written consent from the Measurement & Calibration Services Unit of Inspectra Ltd. This certificate applies only to the instrument detailed in section 2 and only for this calibration.

1. GENERAL INFORMATION

DATE OF ISSUE	22/04/2025
CUSTOMER	University of Malta
ADDRESS	Department of Civil & Structural
POST CODE	MSD 2080
CONTACT PERSON	Nicholas Azzopardi
ORDER NUMBER	4768
DATE OF CALIBRATION	09/04/2025
DATE OF NEXT CALIBRATION	09/04/2026
CONFORMITY STATEMENT	Required
DECISION RULE APPLIED	As per manufacturer's specification

2. INSTRUMENT DETAILS

(Info provided by the customer)

TYPE		External Micrometer (Digital)
MANUFACTURER		Mitutuyo
MODEL		N/A
SERIAL NO		2241
IDENTIFICATION NO		N/A
RESOLUTION	(mm)	0.001
MAXIMUM RANGE/s	(mm)	25
CALIBRATED RANGE/s	(mm)	2.27 to 25

3. AMBIENT CONDITIONS

	START	END
TEMPERATURE °C	20.5	20.3
RELATIVE HUMIDITY %	58	57.7

4. APPROVAL

CERTIFICATE COMPILED BY	Amel Masilungan	Laboratory technician
CERTIFICATE APPROVED BY	Jacob Spiteri	Laboratory Manager

5. EQUIPMENT

TYPE	SERIAL NO	CERTIFICATE NO	NEXT CALIBRATION
Therm/Hygrometer	Probe: 24000104 Readout: 5231264	250-1062-24-1 260-247-24-1	Jun-25
Gauge Blocks	0805861	I3117523	Mar-25

6. MEASUREMENT TRACEABILITY

The measurements are traceable to international standard units of length through a series of comparisons.

Compiled By:

Approved By:

Measurement and Calibrations Services Unit
MRA049B, Marsa Industrial Estate,
Marsa MRS3000. Malta
tel.: +356 21226841, +356 21226844
fax.: +356 23331204

7. PROCEDURE

The procedure used is MCSU_SOP 19 Ver.1, which is extracted from the documents; "Geometrical product specifications (GPS) — Dimensional measuring equipment: Micrometers for external measurements — Design and metrological characteristics" issued by International Organization for Standardization, ISO 3611:2010 (E); and "Taratura di micrometri per esterni" issued by Ente Nazionale Italiano di Unificazione, UNI 9191:1988.

8. RESULTS

Nominal Dimension	Error of Indication	Expanded Uncertainty	Tolerance	Conformity
(mm)	(mm)	(mm)	(±)	[*]
0.00	0.000	0.0008	0.00254	C
2.27	0.000	0.0009	0.00254	C
4.54	0.001	0.0010	0.00254	C
6.81	0.000	0.0012	0.00254	C
9.08	0.001	0.0013	0.00254	C
11.35	0.001	0.0015	0.00254	C
13.62	0.000	0.0018	0.00254	C
15.89	0.000	0.0020	0.00254	C
18.16	0.000	0.0021	0.00254	C
20.43	0.000	0.0024	0.00254	C
22.70	0.001	0.0026	0.00254	C
25.00	0.000	0.0027	0.00254	C

[*] In this section is indicated the compliance with specified limits. Possible cases are:

C: The calibrated item complies with the stated specification at the measured point.

NC: The calibrated item does not comply with the stated specification at the measured point.

In tolerance/Not in tolerance statement is based on simple acceptance rule (Refer to ILAC-G8:09/2019 Guidelines on Decision Rules and statement of conformity).

9. EXPANDED UNCERTAINTY

The Expanded Uncertainty U quoted in section 8 is the product of the standard uncertainty to a coverage factor taken as 2 for a probability of 95.45% and is calculated in accordance to document JCGM 100:2008.

The quoted expanded uncertainty applies only for the calibration done, the instrument specified above, under the stated conditions at MCSU Lab and using the standards specified above, It does not include influences which may be present during the normal day to day operation of the instrument but not mentioned in this report.

END

Compiled By:

Approved By:

Certificate No. I4055925

Inspectra Lab
MRA049B, Marsa Industrial Estate,
Marsa MRS3000. Malta
tel.: +356 21226841, +356 21226844
fax.: +356 23331204

CALIBRATION CERTIFICATE

This document certifies that the instrument detailed below has been calibrated by the Inspectra Lab within Inspectra Ltd., which is an NAB-Malta accredited laboratory Reg. No. 009. The certificate fulfills all the requirements of ISO/IEC 17025:2017 for calibration laboratories.

All measurement results reported in this certificate were obtained following standard operating procedures. The reference standards are indicated in section 5 from which starts the traceability chain of the Measurement & Calibration Services Unit laboratory. The traceability chain proceeds uninterrupted towards national or international standards of the International System of Units (SI). They relate only to the calibrated item and they are valid for the time and conditions of calibration, unless otherwise specified.

This certificate cannot be reproduced unless in full and with the written consent by the Inspectra Lab within Inspectra Ltd. This certificate applies only to the instrument detailed in section 2 and only for this calibration.

1. GENERAL INFORMATION

DATE OF ISSUE	22/04/2025
CUSTOMER	University of Malta
ADDRESS	Department of Civil & Structural Engineering Faculty for the Built Environment, Msida
POST CODE	MSD 2080
ORDER NUMBER	093/25
DATE OF CALIBRATION	08/04/2025
CONFORMITY STATEMENT	Not Required

2. INSTRUMENT DETAILS

(Info provided by the customer)

TYPE		Electronic Balance
MANUFACTURER		AND
MODEL		GX-10K-EC
SERIAL NO		149101759
IDENTIFICATION NO		N/A
LOCATION		Civil Engineering Lab
CLASS		N/A
RESOLUTION	(g)	0.01
MAXIMUM CAPACITY	(g)	10100
CALIBRATED RANGE/s	(g)	1000 to 10000

3. AMBIENT CONDITIONS

	START	END	UNCERTAINTY
TEMPERATURE °C	21.2	21.0	0.4
RELATIVE HUMIDITY %	57.3	59.3	2.8

4. APPROVAL

CERTIFICATE COMPILED BY	Arnel Maallungan	Laboratory technician
CERTIFICATE APPROVED BY	Jacob Spiteri	Laboratory Manager

5. EQUIPMENT

TYPE	MANUFACTURER	SERIAL NO	CERTIFICATE NO	NEXT CALIBRATION
Thermo-Hygrometer	Rotronic	Probe: 24000104 Readout: 5231264	250-1062-24-1 260-247-24-1	Jun-25
1mg - 5kg M1 Masses	Sinergica Soluzioni	D7189	LAT117-24-M-4246	Dec-25
10kg M1 Mass	Sinergica Soluzioni	D7190	LAT117-24-M-4212	Dec-25
Stopwatch	Fastime	MCSU 253	411L/23/T	May-25

Compiled By:

Approved By:

Inspectra Lab
MRA049B, Marsa Industrial Estate,
Marsa MRS3000. Malta
tel.: +356 21226841, +356 21226844
fax.: +356 23331204

6. MEASUREMENTS TRACEABILITY

The measurements are traceable to international standard units of Mass. The reference equipment used have been calibrated by laboratories accredited to ISO 17025, as specified in section 5.

7. PROCEDURE

The procedure used is MCSU_SOP 08 current version, which is extracted from the documents; "Guidelines on the Calibration of Non-Automatic Weighing Instruments" issued by the European Association of National Metrology Institutes, EURAMET/cg-18/v.04, edition November 2015.

	An Initial check was carried out. The "as found" readings were:				An adjustment was carried out. The readings after adjustment were:	
	Nominal Mass	Reading	Tolerance	Need for adjustment	Nominal Mass	Reading
	(g)	(g)	(g)		(g)	(g)
Minimum load	1000	999.93	N/A	N/A	1000	999.95
Half Load	5000	4999.36	N/A	N/A	5000	4999.43
Maximum load	10000	9999.15	N/A	N/A	10000	9999.23

Note Tolerance limit not specified or readings within tolerance limits. However an adjustment was still carried out as agreed with client.

8. RESULTS

8.1 Stabilization Time (s)	6
8.2 Loading/Unloading Time (s)	12

8.3 Eccentricity Test
Test carried out to determine the most likely difference that eccentric loading can have on the reading.

Nominal Mass	Error (E_{ecc})	uncertainty ($u\ E_{ecc}$)
(g)	(g)	(g)
2000	0.16	0.046

Positions of load for common rectangular and circular platforms

8.4 Repeatability Test
Test consists in the repeated deposition of the same load on the platform for a number of repetitions n, under identical conditions of handling the load and the instrument and under constant test conditions.

Nominal Mass	Standard Deviation	uncertainty (u_{stat})
(g)	(g)	(g)
5000	0.00	0.003
10000	0.00	0.003

8.5 Linearity Test
The purpose of this test is an appraisal of the performance of the instrument over the whole weighing range

Nominal Mass	Error of Indication	Expanded Uncertainty
M_{conv} (g)	ΔM (g)	U (g)
0	0.00	0.004
1000	-0.07	0.047
2000	-0.10	0.094
3000	-0.16	0.140
4000	-0.26	0.187
5000	-0.28	0.232
6000	-0.37	0.278
7000	-0.40	0.325
8000	-0.39	0.371
9000	-0.47	0.418
10000	-0.71	0.464

Compiled By:

Approved By:

Inspectra Lab
MRA049B, Marsa Industrial Estate,
Marsa MRS3000, Malta
tel.: +356 21226841, +356 21226844
fax.: +356 23331204

9. EXPANDED UNCERTAINTY

The Expanded Uncertainty U quoted in section 8 is the product of the standard uncertainty to a coverage factor taken as 2 for a probability of 95.45% and is calculated in accordance to document JCGM 100:2008 and EA-4/02 M:2022.

The reported expanded uncertainty applies only for the calibration done, the instrument specified above, under the stated ambient conditions at client's premises, in the stated working area and using the identified masses specified above. It does not include any other influences which may be present during the normal day to day operation of the instrument but not mentioned in this report. The reported expanded uncertainty budget is not included in the conformity calculation.

END

Compiled By:

Approved By:

Calibration Horizontal LVDT								
Ref. Value	Raw	After Equation	Ref. Value	Raw	After Equation	Ref. Value	Raw	After Equation
0	-39.010	-0.31565	-20	-368.400	4.90492	-4	-88.200	0.46397
0	-39.010	-0.31565	-20	-368.500	4.90650	-4	-88.170	0.46350
0	-39.030	-0.31533	-22	-403.400	5.45964			
-2	-54.190	-0.07506	-22	-403.300	5.45806			
-2	-54.240	-0.07426	-22	-402.700	5.44855			
-2	-54.310	-0.07316	-22	-402.700	5.44855			
-4.002	-88.480	0.46841	-20	-368.200	4.90175			
-4.002	-88.490	0.46857	-20	-368.200	4.90175			
-4.002	-88.490	0.46857	-20	-368.200	4.90175			
-5.999	-122.500	1.00760	-18	-333.300	4.34861			
-5.999	-122.500	1.00760	-18	-333.300	4.34861			
-5.999	-122.500	1.00760	-18	-333.300	4.34861			
-7.999	-157.600	1.56391	-16	-298.300	3.79389			
-7.999	-157.500	1.56232	-16	-298.200	3.79231			
-7.999	-157.500	1.56232	-16	-298.200	3.79231			
-10	-192.400	2.11546	-14	-263.000	3.23441			
-10	-192.400	2.11546	-14	-262.900	3.23283			
-10	-192.400	2.11546	-14	-262.900	3.23283			
-12	-228.900	2.69396	-11.99	-228.000	2.67969			
-12	-228.900	2.69396	-11.99	-227.900	2.67811			
-12	-228.900	2.69396	-11.99	-227.900	2.67811			
-14	-262.700	3.22966	-10	-193.000	2.12497			
-14	-262.700	3.22966	-10	-193.000	2.12497			
-14	-262.600	3.22807	-10	-192.900	2.12339			
-15.99	-298.800	3.80182	-8	-157.800	1.56708			
-15.99	-298.800	3.80182	-8	-157.800	1.56708			
-15.99	-298.800	3.80182	-8	-157.700	1.56549			
-18	-333.300	4.34861	-6	-122.900	1.01394			
-18	-333.300	4.34861	-6	-122.900	1.01394			
-20	-368.400	4.90492	-6	-122.800	1.01236			

Trial Test Horizontal LVDT								
Rev. Value	Raw	After Equation	Rev. Value	Raw	After Equation	Rev. Value	Raw	After Equation
0	-0.353	-1.06012	-20	5.1949	-21.05797	-4	0.7641	-5.08679
0	-0.353	-1.06012	-20	5.1956	-21.06049	-4	0.764	-5.08643
0	-0.352	-1.06372	-20	5.1954	-21.05977	-4	0.7642	-5.08716
-2	0.2027	-3.06318	-22	5.7527	-23.06860	-2	0.2087	-3.08481
-2	0.2024	-3.06210	-22	5.753	-23.06968	-2	0.2093	-3.08697
-2	0.203	-3.06426	-22	5.7541	-23.07365	-2	0.2098	-3.08878
-4	0.7586	-5.06697	-20	5.1938	-21.05400	0	-0.339	-1.11058
-4	0.7579	-5.06445	-20	5.1954	-21.05977	0	-0.339	-1.11058
-4	0.7584	-5.06625	-20	5.195	-21.05833	0	-0.339	-1.11058
-6	1.3116	-7.06030	-18	4.6395	-19.05598			
-6	1.3128	-7.06463	-18	4.6402	-19.05851			
-6	1.313	-7.06535	-18	4.6401	-19.05815			
-8	1.8685	-9.06769	-16	4.0889	-17.07130			
-8	1.8686	-9.06805	-16	4.088	-17.06806			
-8	1.8681	-9.06625	-16	4.0867	-17.06337			
-10	2.4235	-11.06823	-14	3.5326	-15.06607			
-10	2.4234	-11.06787	-14	3.5325	-15.06571			
-10	2.4229	-11.06607	-14	3.5322	-15.06463			
-12	2.9779	-13.06661	-12	2.9766	-13.06193			
-12	2.9776	-13.06553	-12	2.9775	-13.06517			
-12	2.9768	-13.06265	-12	2.9763	-13.06085			
-14	3.5337	-15.07004	-10	2.4239	-11.06968			
-14	3.5335	-15.06932	-10	2.4249	-11.07328			
-14	3.5336	-15.06968	-10	2.4248	-11.07292			
-16	4.0855	-17.05905	-8	1.8704	-9.07454			
-16	4.0862	-17.06157	-8	1.8699	-9.07274			
-16	4.085	-17.05724	-8	1.8699	-9.07274			
-18	4.6409	-19.06103	-6	1.3169	-7.07941			
-18	4.6416	-19.06355	-6	1.3166	-7.07833			
-18	4.6418	-19.06427	-6	1.3165	-7.07796			

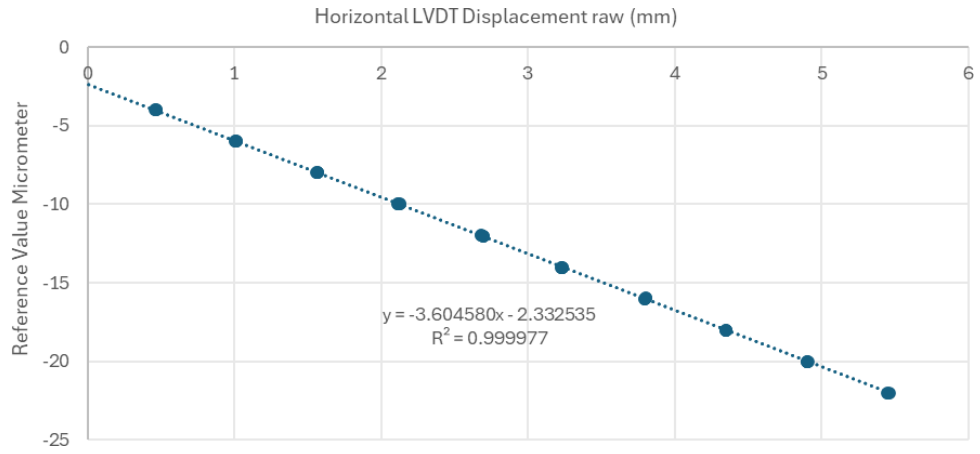

Figure 8.23 - A photo of the tabulated readings for the calibration of the Horizontal LVDT

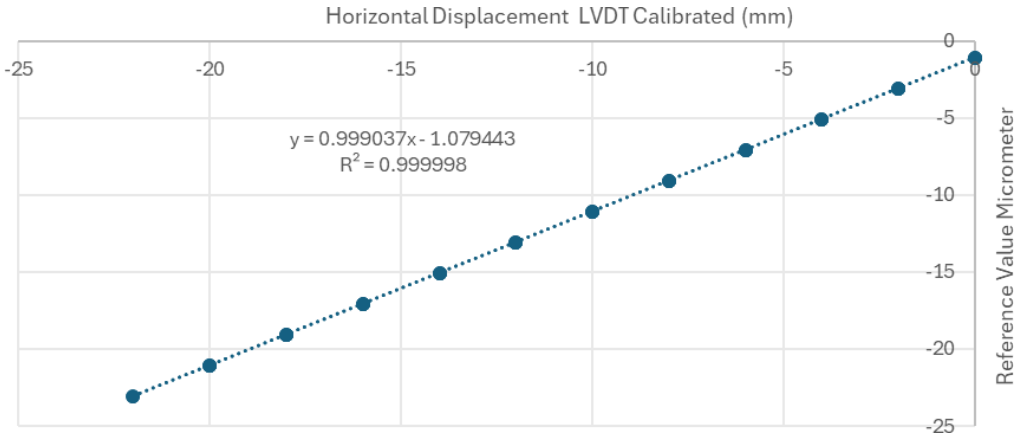

Figure 8.24 -The gradient of the plotted line is 1 when corrected to 3 d.p. giving a fairly accurate representation of the sensor. This is because in this scenario, the equipment is calibrated.

Note: The Horizontal LVDT was calibrated against an inbuilt equation y=-63.094673-58.925694 on Labview

Calibration Vertical LVDT					
Ref. Value	Raw	Ref. Value	Raw	Ref. Value	Raw
0	0.1082	-20	5.5446	-4	1.192
0	0.1081	-20	5.5448	-4	1.1919
0	0.1082	-20	5.5444	-4	1.1914
-2	0.6492	-21	5.8003	-2	0.6477
-2	0.6482	-21	5.8016	-2	0.6475
-2	0.6479	-21	5.8014	-2	0.647
-4.001	1.196	-20	5.5368	0	0.105
-4.001	1.1959	-20	5.5367	0	0.1053
-4.001	1.1961	-20	5.5371	0	0.1052
-6	1.7387	-18	4.9966		
-6	1.7385	-18	4.9956		
-6	1.7393	-18	4.9955		
-8	2.2852	-16	4.4553		
-8	2.2857	-16	4.4548		
-8	2.2859	-16	4.4543		
-10	2.8311	-14	3.909		
-10	2.8318	-14	3.9084		
-10	2.8317	-14	3.9082		
-12	3.3719	-12	3.3681		
-12	3.3717	-12	3.3674		
-12	3.3714	-12	3.3671		
-14	3.9102	-10	2.8219		
-14	3.9101	-10	2.8223		
-14	3.9103	-10	2.8223		
-16	4.4539	-8.001	2.2805		
-16	4.454	-8.001	2.2798		
-16	4.4549	-8.001	2.2805		
-18	4.9968	-6.001	1.74		
-18	4.9964	-6.001	1.7398		
-18	4.9964	-6.001	1.7398		

Trial Test Vertical LVDT								
Ref.Value	Raw	Actual Value	Ref.Value	Raw	Actual Value	Ref.Value	Raw	Actual Value
0	0.0278	0.29842	-20	5.5369	-19.99102	-4	1.1913	-3.98663
0	0.0867	0.08150	-20	5.5357	-19.98660	-4	1.1914	-3.98699
0	0.0992	0.03546	-20	5.5353	-19.98513	-4	1.1914	-3.98699
-2	0.6393	-1.95367	-21	5.7958	-20.94452	-2	0.6463	-1.97945
-2	0.639	-1.95256	-21	5.7966	-20.94747	-2	0.6466	-1.98055
-2	0.6388	-1.95183	-21	5.7969	-20.94857	-2	0.6457	-1.97724
-4	1.1876	-3.97300	-20	5.5375	-19.99323	0	0.1097	-0.00321
-4	1.1872	-3.97153	-20	5.5376	-19.99360	0	0.1089	-0.00026
-4	1.1869	-3.97042	-20	5.5374	-19.99286			
-6	1.7271	-5.95992	-18	4.9916	-17.98274			
-6	1.7273	-5.96066	-18	4.9922	-17.98495			
-6	1.7269	-5.95919	-18	4.9926	-17.98642			
-8	2.275	-7.97778	-16	4.4506	-15.99029			
-8	2.2748	-7.97704	-16	4.4505	-15.98992			
-8	2.2751	-7.97815	-16	4.4504	-15.98955			
-10	2.8143	-9.96397	-14	3.9056	-13.98311			
-10	2.8146	-9.96507	-14	3.9065	-13.98643			
-10	2.8154	-9.96802	-14	3.9068	-13.98753			
-12	3.3642	-11.98919	-12	3.3651	-11.99251			
-12	3.3641	-11.98882	-12	3.3648	-11.99140			
-12	3.3642	-11.98919	-12	3.3648	-11.99140			
-14	3.9129	-14.01000	-10	2.8167	-9.97281			
-14	3.9128	-14.00963	-10	2.817	-9.97391			
-14	3.9124	-14.00815	-10	2.8175	-9.97575			
-16	4.4506	-15.99029	-8	2.2767	-7.98404			
-16	4.4505	-15.98992	-8	2.2763	-7.98257			
-16	4.4504	-15.98955	-8	2.276	-7.98146			
-18	4.9972	-18.00336	-6	1.7333	-5.98276			
-18	4.9962	-17.99968	-6	1.7329	-5.98128			
-18	4.9955	-17.99710	-6	1.7325	-5.97981			

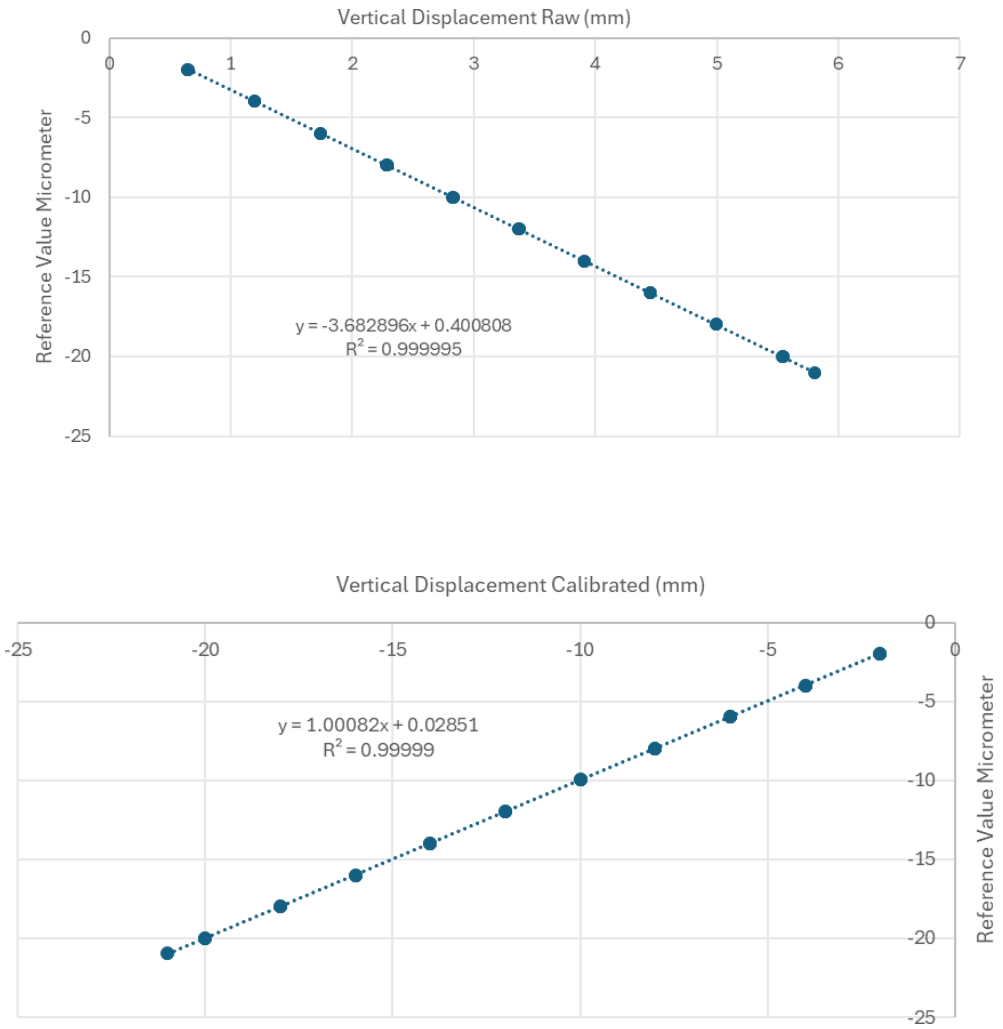

Figure 8.25 - Two graphs of the calibration and the trial test for the vertical LVDT, respectively. A RMS of 0.999995 and a gradient of 1.0008 also provide a fairy well-calibrated set-up

Calibration
Horizontal Load Cell

Ref. Value	Raw	Ref. Value	Raw	Ref. Value	Raw	Ref. Value	Raw	Ref. Value	Raw	Ref. Value	Raw	Ref. Value	Raw
0	-0.149	10	-0.561	25	-1.181	40	-1.799	45	-2.002	30	-1.384	15	-0.766
0	-0.149	10	-0.561	30	-1.386	45	-2.002	45	-2.002	30	-1.384	15	-0.766
0	-0.149	15	-0.769	30	-1.386	45	-2.006	40	-1.797	30	-1.384	15	-0.766
0	-0.149	15	-0.768	30	-1.389	45	-2.004	40	-1.797	30	-1.384	15	-0.766
0	-0.149	15	-0.768	30	-1.388	45	-2.004	40	-1.797	30	-1.384	15	-0.766
0	-0.149	15	-0.768	30	-1.387	45	-2.002	40	-1.797	30	-1.384	15	-0.766
0	-0.149	15	-0.77	30	-1.387	45	-2.002	40	-1.796	30	-1.384	15	-0.766
0	-0.149	15	-0.77	30	-1.386	45	-2.006	40	-1.796	25	-1.177	15	-0.766
0	-0.149	15	-0.77	30	-1.386	45	-2.005	40	-1.796	25	-1.177	10	-0.56
0	-0.149	15	-0.769	30	-1.386	45	-2.004	40	-1.796	25	-1.177	10	-0.56
0	-0.149	15	-0.768	30	-1.386	45	-2.004	40	-1.796	25	-1.177	10	-0.56
5	-0.356	15	-0.768	35	-1.594	50	-2.208	40	-1.796	25	-1.177	10	-0.56
5	-0.356	20	-0.975	35	-1.593	50	-2.207	35	-1.593	25	-1.177	10	-0.56
5	-0.355	20	-0.975	35	-1.593	50	-2.207	35	-1.593	25	-1.177	10	-0.56
5	-0.355	20	-0.974	35	-1.592	50	-2.207	35	-1.591	25	-1.177	10	-0.56
5	-0.355	20	-0.974	35	-1.592	50	-2.209	35	-1.591	25	-1.177	10	-0.56
5	-0.355	20	-0.974	35	-1.591	50	-2.209	35	-1.591	20	-0.97	10	-0.56
5	-0.355	20	-0.974	35	-1.595	50	-2.208	35	-1.59	20	-0.97	5	-0.356
5	-0.355	20	-0.974	35	-1.594	50	-2.208	35	-1.59	20	-0.971	5	-0.356
5	-0.355	20	-0.977	35	-1.593	50	-2.209	35	-1.59	20	-0.971	5	-0.356
5	-0.355	20	-0.977	35	-1.593	50	-2.209	35	-1.59	20	-0.972	5	-0.355
5	-0.355	20	-0.976	35	-1.592	50	-2.209	35	-1.59	20	-0.972	5	-0.355
10	-0.561	25	-1.181	40	-1.801	50	-2.208	35	-1.59	20	-0.972	5	-0.355
10	-0.561	25	-1.18	40	-1.799	50	-2.208	35	-1.59	20	-0.972	5	-0.355
10	-0.563	25	-1.18	40	-1.798	45	-2.005	30	-1.383	20	-0.972	5	-0.355
10	-0.562	25	-1.183	40	-1.797	45	-2.004	30	-1.383	20	-0.972	5	-0.355
10	-0.562	25	-1.183	40	-1.797	45	-2.003	30	-1.383	20	-0.972	5	-0.355
10	-0.561	25	-1.182	40	-1.801	45	-2.002	30	-1.383	20	-0.972	5	-0.355
10	-0.561	25	-1.182	40	-1.8	45	-2.002	30	-1.384	15	-0.765	0	-0.149
10	-0.561	25	-1.181	40	-1.799	45	-2.002	30	-1.384	15	-0.766	0	-0.149

Ref. Value	Raw
0	-0.149
0	-0.149
0	-0.149
0	-0.149
0	-0.149
0	-0.149
0	-0.149
0	-0.149
0	-0.149
0	-0.149
0	-0.149
0	-0.149
0	-0.149
0	-0.149

Trial Test Horizontal Load Cell											
Ref. Value	Raw	Act. Value	Ref. Value	Raw	Act. Value	Ref. Value	Raw	Act. Value	Ref. Value	Raw	Act. Value
5	-0.356	5.0217	15	-0.769	15.0450	30	-1.389	30.0922	45	-2.002	44.9695
5	-0.356	5.0217	15	-0.769	15.0450	30	-1.387	30.0437	45	-2.002	44.9695
5	-0.356	5.0217	15	-0.769	15.0450	30	-1.387	30.0437	45	-2.005	45.0423
5	-0.356	5.0217	15	-0.768	15.0208	30	-1.387	30.0437	45	-2.004	45.0181
5	-0.356	5.0217	20	-0.975	20.0446	30	-1.387	30.0437	45	-2.004	45.0181
5	-0.356	5.0217	20	-0.975	20.0446	30	-1.386	30.0194	45	-2.003	44.9938
5	-0.355	4.9974	20	-0.974	20.0203	30	-1.386	30.0194	45	-2.003	44.9938
5	-0.355	4.9974	20	-0.974	20.0203	30	-1.386	30.0194	45	-2.003	44.9938
5	-0.355	4.9974	20	-0.976	20.0689	30	-1.386	30.0194	45	-2.002	44.9695
5	-0.355	4.9974	20	-0.976	20.0689	35	-1.592	35.0190	50	-2.207	49.9448
5	-0.355	4.9974	20	-0.975	20.0446	35	-1.591	34.9947	50	-2.207	49.9448
5	-0.355	4.9974	20	-0.975	20.0446	35	-1.591	34.9947	50	-2.207	49.9448
10	-0.562	10.0212	20	-0.975	20.0446	35	-1.591	34.9947	50	-2.207	49.9448
10	-0.561	9.9970	25	-1.181	25.0441	35	-1.595	35.0918	50	-2.207	49.9448
10	-0.561	9.9970	25	-1.18	25.0199	35	-1.594	35.0675	50	-2.207	49.9448
10	-0.561	9.9970	25	-1.18	25.0199	35	-1.593	35.0432	50	-2.207	49.9448
10	-0.561	9.9970	25	-1.18	25.0199	35	-1.592	35.0190	50	-2.207	49.9448
10	-0.561	9.9970	25	-1.18	25.0199	35	-1.592	35.0190	50	-2.207	49.9448
10	-0.561	9.9970	25	-1.18	25.0199	35	-1.592	35.0190	50	-2.207	49.9448
10	-0.561	9.9970	25	-1.183	25.0927	40	-1.797	39.9943	45	-2.002	44.9695
10	-0.561	9.9970	25	-1.184	25.1170	40	-1.797	39.9943	45	-2.002	44.9695
10	-0.561	9.9970	25	-1.183	25.0927	40	-1.797	39.9943	45	-2.002	44.9695
10	-0.561	9.9970	25	-1.182	25.0684	40	-1.797	39.9943	45	-2.002	44.9695
15	-0.768	15.0208	25	-1.18	25.0199	40	-1.799	40.0428	45	-2.002	44.9695
15	-0.768	15.0208	25	-1.18	25.0199	40	-1.801	40.0913	45	-2.001	44.9453
15	-0.768	15.0208	30	-1.386	30.0194	40	-1.8	40.0671	45	-2.001	44.9453
15	-0.768	15.0208	30	-1.386	30.0194	40	-1.799	40.0428	45	-2.001	44.9453
15	-0.768	15.0208	30	-1.386	30.0194	40	-1.798	40.0185	45	-2.001	44.9453
15	-0.768	15.0208	30	-1.386	30.0194	40	-1.798	40.0185	45	-2.001	44.9453
15	-0.769	15.0450	30	-1.386	30.0194	45	-2.002	44.9695	40	-1.795	39.9457

Ref. Value	Raw	Act. Value	Ref. Value	Raw	Act. Value	Ref. Value	Raw	Act. Value
40	-1.795	39.9457	25	-1.176	24.9228	10	-0.559	9.9484
40	-1.801	40.0913	25	-1.176	24.9228	10	-0.559	9.9484
40	-1.8	40.0671	25	-1.177	24.9471	10	-0.56	9.9727
40	-1.796	39.9700	25	-1.177	24.9471	10	-0.56	9.9727
40	-1.795	39.9457	25	-1.177	24.9471	10	-0.56	9.9727
40	-1.795	39.9457	25	-1.177	24.9471	10	-0.56	9.9727
40	-1.796	39.9700	25	-1.177	24.9471	10	-0.56	9.9727
40	-1.796	39.9700	25	-1.177	24.9471	10	-0.56	9.9727
35	-1.589	34.9462	20	-0.971	19.9475	5	-0.356	5.0217
35	-1.589	34.9462	20	-0.971	19.9475	5	-0.356	5.0217
35	-1.589	34.9462	20	-0.971	19.9475	5	-0.356	5.0217
35	-1.589	34.9462	20	-0.971	19.9475	5	-0.355	4.9974
35	-1.59	34.9704	20	-0.971	19.9475	5	-0.355	4.9974
35	-1.59	34.9704	20	-0.971	19.9475	5	-0.355	4.9974
35	-1.59	34.9704	20	-0.971	19.9475	5	-0.355	4.9974
35	-1.59	34.9704	20	-0.971	19.9475	5	-0.355	4.9974
35	-1.59	34.9704	20	-0.971	19.9475	5	-0.355	4.9974
35	-1.59	34.9704	20	-0.971	19.9475	5	-0.355	4.9974
30	-1.383	29.9466	15	-0.765	14.9480	0	-0.149	-0.0021
30	-1.383	29.9466	15	-0.765	14.9480	0	-0.149	-0.0021
30	-1.383	29.9466	15	-0.765	14.9480	0	-0.149	-0.0021
30	-1.383	29.9466	15	-0.765	14.9480	0	-0.149	-0.0021
30	-1.383	29.9466	15	-0.765	14.9480	0	-0.149	-0.0021
30	-1.383	29.9466	15	-0.765	14.9480	0	-0.149	-0.0021
30	-1.383	29.9466	15	-0.766	14.9722	0	-0.149	-0.0021
30	-1.383	29.9466	15	-0.766	14.9722	0	-0.149	-0.0021
30	-1.383	29.9466	15	-0.766	14.9722	0	-0.149	-0.0021
30	-1.383	29.9466	15	-0.766	14.9722	0	-0.149	-0.0021
25	-1.176	24.9228	10	-0.559	9.9484			
25	-1.176	24.9228	10	-0.56	9.9727			

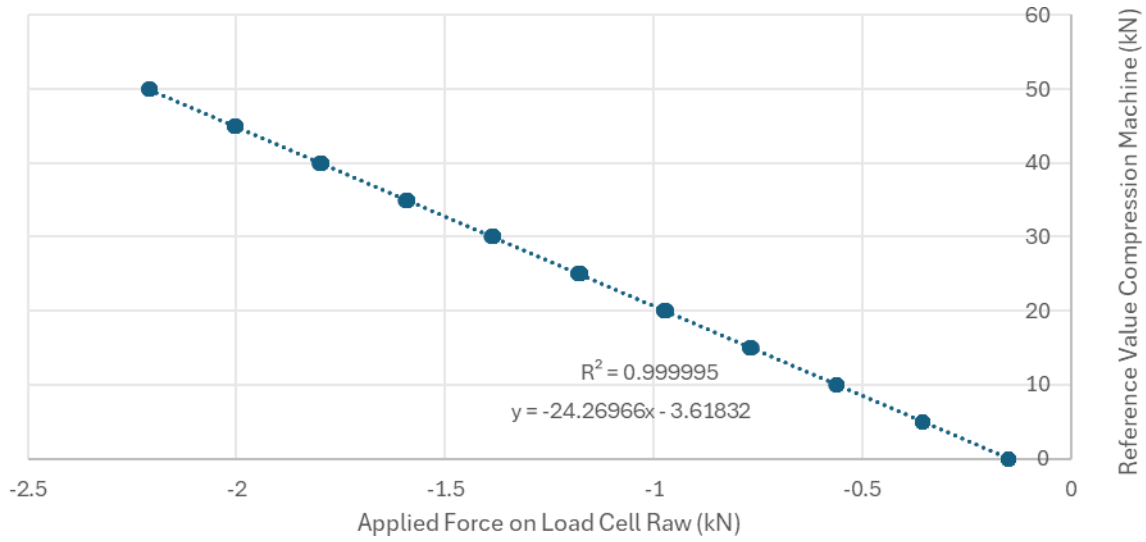

Figure 8.26 - A photo of the best straight line plotted after the calibration, with its accuracy at 0.999995 Root Mean Square

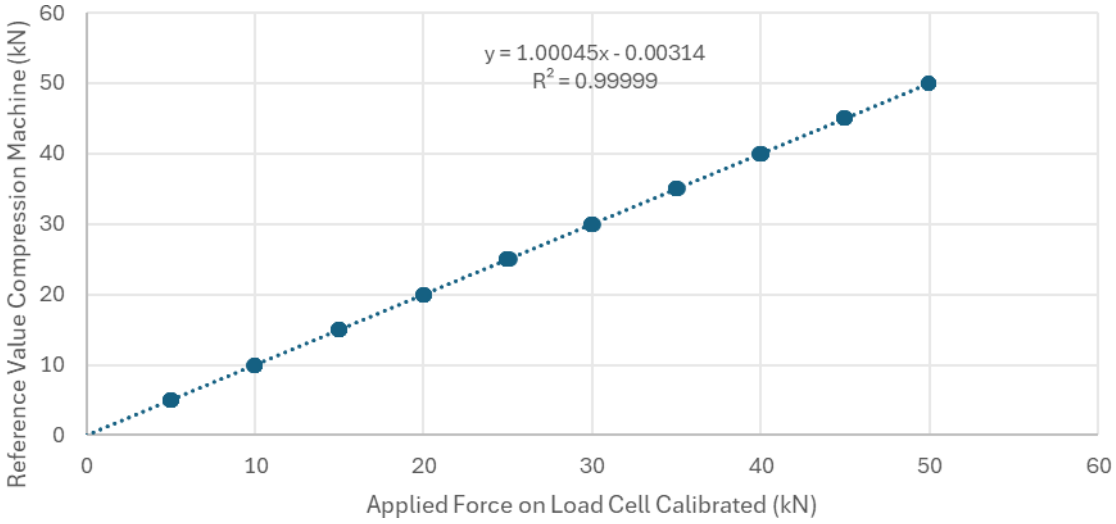

Figure 8.27 A photo of the Trial Test on the Horizontal Load Cell, where the calibration of the apparatus is verified. This showed how the calibration was done successfully

Calibration Vertical Load Cell

Ref.Val.	Raw	Ref.Val.	Raw	Ref.Value	Raw	Ref.Value	Raw	Ref.Value	Raw	Ref.Val.	Raw	Ref.Value	Raw
0	-0.084	15	-0.696	30	-1.308	40	-1.719	45	-1.921	30	-1.309	15	-0.695
0	-0.082	15	-0.696	30	-1.31	45	-1.922	40	-1.716	30	-1.309	15	-0.696
0	-0.081	15	-0.695	30	-1.31	45	-1.921	40	-1.717	25	-1.106	15	-0.697
0	-0.081	15	-0.696	30	-1.309	45	-1.921	40	-1.717	25	-1.105	10	-0.491
0	-0.081	15	-0.697	30	-1.311	45	-1.921	40	-1.717	25	-1.105	10	-0.491
0	-0.081	15	-0.696	30	-1.309	45	-1.924	40	-1.715	25	-1.104	10	-0.49
0	-0.081	15	-0.695	30	-1.308	45	-1.922	40	-1.717	25	-1.106	10	-0.489
0	-0.081	15	-0.696	30	-1.309	45	-1.922	40	-1.717	25	-1.106	10	-0.49
0	-0.08	15	-0.697	30	-1.309	45	-1.921	40	-1.721	25	-1.106	10	-0.489
0	-0.08	20	-0.902	30	-1.309	45	-1.92	40	-1.721	25	-1.105	10	-0.489
5	-0.285	20	-0.901	35	-1.516	45	-1.921	40	-1.719	25	-1.105	10	-0.487
5	-0.285	20	-0.9	35	-1.515	50	-2.123	40	-1.719	25	-1.104	10	-0.49
5	-0.284	20	-0.9	35	-1.513	50	-2.124	35	-1.517	25	-1.103	5	-0.285
5	-0.286	20	-0.902	35	-1.513	50	-2.123	35	-1.515	20	-0.902	5	-0.285
5	-0.285	20	-0.902	35	-1.512	50	-2.125	35	-1.513	20	-0.901	5	-0.284
5	-0.284	20	-0.902	35	-1.518	50	-2.124	35	-1.513	20	-0.9	5	-0.286
5	-0.284	20	-0.902	35	-1.516	50	-2.124	35	-1.512	20	-0.9	5	-0.285
5	-0.284	20	-0.899	35	-1.514	50	-2.125	35	-1.518	20	-0.902	5	-0.284
5	-0.285	20	-0.899	35	-1.514	50	-2.124	35	-1.516	20	-0.902	5	-0.284
5	-0.285	25	-1.106	35	-1.513	50	-2.125	35	-1.514	20	-0.902	5	-0.284
10	-0.491	25	-1.105	40	-1.716	50	-2.125	35	-1.514	20	-0.902	5	-0.285
10	-0.491	25	-1.105	40	-1.717	45	-1.922	35	-1.513	20	-0.899	5	-0.285
10	-0.49	25	-1.104	40	-1.717	45	-1.921	30	-1.308	20	-0.899	0	-0.084
10	-0.489	25	-1.106	40	-1.717	45	-1.921	30	-1.31	15	-0.694	0	-0.082
10	-0.49	25	-1.106	40	-1.715	45	-1.921	30	-1.31	15	-0.696	0	-0.081
10	-0.489	25	-1.106	40	-1.717	45	-1.924	30	-1.309	15	-0.696	0	-0.081
10	-0.489	25	-1.105	40	-1.717	45	-1.922	30	-1.311	15	-0.695	0	-0.081
10	-0.487	25	-1.105	40	-1.721	45	-1.922	30	-1.309	15	-0.696	0	-0.081
10	-0.49	25	-1.104	40	-1.721	45	-1.921	30	-1.308	15	-0.697	0	-0.081
15	-0.694	25	-1.103	40	-1.719	45	-1.92	30	-1.309	15	-0.696	0	-0.081

Trial Test Vertical Load Cell											
Ref.Value	Raw	Actual Value	Ref.Value	Raw	Actual Value	Ref.Value	Raw	Actual Value	Ref.Value	Raw	Actual Value
0	-0.128	1.13304	15	-0.746	16.24467	30	-1.365	31.38074	45	-1.981	46.44347
0	-0.128	1.13304	15	-0.746	16.24467	30	-1.364	31.35629	45	-1.981	46.44347
0	-0.128	1.13304	15	-0.746	16.24467	30	-1.364	31.35629	45	-1.982	46.46792
0	-0.128	1.13304	15	-0.746	16.24467	30	-1.364	31.35629	45	-1.981	46.44347
0	-0.128	1.13304	15	-0.747	16.26912	30	-1.364	31.35629	45	-1.981	46.44347
0	-0.128	1.13304	15	-0.747	16.26912	30	-1.367	31.42965	45	-1.98	46.41901
0	-0.128	1.13304	15	-0.747	16.26912	30	-1.367	31.42965	45	-1.98	46.41901
0	-0.128	1.13304	15	-0.746	16.24467	30	-1.366	31.40520	45	-1.982	46.46792
0	-0.128	1.13304	15	-0.746	16.24467	30	-1.366	31.40520	45	-1.982	46.46792
0	-0.128	1.13304	15	-0.746	16.24467	30	-1.365	31.38074	45	-1.982	46.46792
5	-0.335	6.19470	20	-0.952	21.28187	35	-1.571	36.41795	50	-2.192	51.60294
5	-0.335	6.19470	20	-0.953	21.30633	35	-1.57	36.39350	50	-2.19	51.55403
5	-0.334	6.17025	20	-0.953	21.30633	35	-1.569	36.36905	50	-2.188	51.50513
5	-0.334	6.17025	20	-0.952	21.28187	35	-1.571	36.41795	50	-2.187	51.48068
5	-0.334	6.17025	20	-0.952	21.28187	35	-1.571	36.41795	50	-2.186	51.45622
5	-0.334	6.17025	20	-0.952	21.28187	35	-1.57	36.39350	50	-2.186	51.45622
5	-0.334	6.17025	20	-0.954	21.33078	35	-1.57	36.39350	50	-2.186	51.45622
5	-0.334	6.17025	20	-0.956	21.37968	35	-1.57	36.39350	50	-2.185	51.43177
5	-0.334	6.17025	20	-0.956	21.37968	35	-1.57	36.39350	50	-2.185	51.43177
5	-0.334	6.17025	20	-0.955	21.35523	35	-1.569	36.36905	50	-2.185	51.43177
10	-0.54	11.20746	25	-1.159	26.34354	40	-1.776	41.43071	45	-1.979	46.39456
10	-0.54	11.20746	25	-1.159	26.34354	40	-1.775	41.40626	45	-1.979	46.39456
10	-0.54	11.20746	25	-1.158	26.31908	40	-1.775	41.40626	45	-1.979	46.39456
10	-0.539	11.18300	25	-1.158	26.31908	40	-1.776	41.43071	45	-1.979	46.39456
10	-0.539	11.18300	25	-1.158	26.31908	40	-1.778	41.47962	45	-1.979	46.39456
10	-0.539	11.18300	25	-1.158	26.31908	40	-1.777	41.45516	45	-1.979	46.39456
10	-0.539	11.18300	25	-1.158	26.31908	40	-1.776	41.43071	45	-1.979	46.39456
10	-0.539	11.18300	25	-1.159	26.34354	40	-1.776	41.43071	45	-1.98	46.41901
10	-0.539	11.18300	25	-1.162	26.41689	40	-1.776	41.43071	45	-1.98	46.41901
10	-0.539	11.18300	25	-1.162	26.41689	40	-1.775	41.40626	45	-1.98	46.41901

40	-1.771	41.30845	25	-1.155	26.24573	10	-0.537	11.13410
40	-1.772	41.33290	25	-1.155	26.24573	10	-0.538	11.15855
40	-1.772	41.33290	25	-1.155	26.24573	10	-0.538	11.15855
40	-1.776	41.43071	25	-1.155	26.24573	10	-0.538	11.15855
40	-1.776	41.43071	25	-1.155	26.24573	10	-0.538	11.15855
40	-1.776	41.43071	25	-1.155	26.24573	10	-0.538	11.15855
40	-1.776	41.43071	25	-1.155	26.24573	10	-0.538	11.15855
40	-1.776	41.43071	25	-1.155	26.24573	5	-0.332	6.12134
40	-1.776	41.43071	25	-1.153	26.19682	5	-0.332	6.12134
40	-1.775	41.40626	20	-0.95	21.23297	5	-0.333	6.14579
35	-1.571	36.41795	20	-0.95	21.23297	5	-0.333	6.14579
35	-1.571	36.41795	20	-0.95	21.23297	5	-0.332	6.12134
35	-1.571	36.41795	20	-0.95	21.23297	5	-0.333	6.14579
35	-1.57	36.39350	20	-0.95	21.23297	5	-0.333	6.14579
35	-1.57	36.39350	20	-0.95	21.23297	5	-0.333	6.14579
35	-1.569	36.36905	20	-0.949	21.20852	5	-0.333	6.14579
35	-1.569	36.36905	20	-0.947	21.15961	5	-0.333	6.14579
35	-1.569	36.36905	20	-0.948	21.18406	0	-0.128	1.13304
35	-1.569	36.36905	20	-0.948	21.18406	0	-0.128	1.13304
35	-1.568	36.34460	15	-0.744	16.19576	0	-0.128	1.13304
30	-1.361	31.28294	15	-0.744	16.19576	0	-0.128	1.13304
30	-1.361	31.28294	15	-0.744	16.19576	0	-0.128	1.13304
30	-1.361	31.28294	15	-0.744	16.19576	0	-0.128	1.13304
30	-1.361	31.28294	15	-0.744	16.19576	0	-0.128	1.13304
30	-1.361	31.28294	15	-0.744	16.19576	0	-0.128	1.13304
30	-1.361	31.28294	15	-0.744	16.19576	0	-0.128	1.13304
30	-1.361	31.28294	15	-0.744	16.19576	0	-0.128	1.13304
30	-1.361	31.28294	15	-0.744	16.19576			
30	-1.362	31.30739	15	-0.744	16.19576			
30	-1.361	31.28294	10	-0.536	11.10965			
25	-1.155	26.24573	10	-0.537	11.13410			

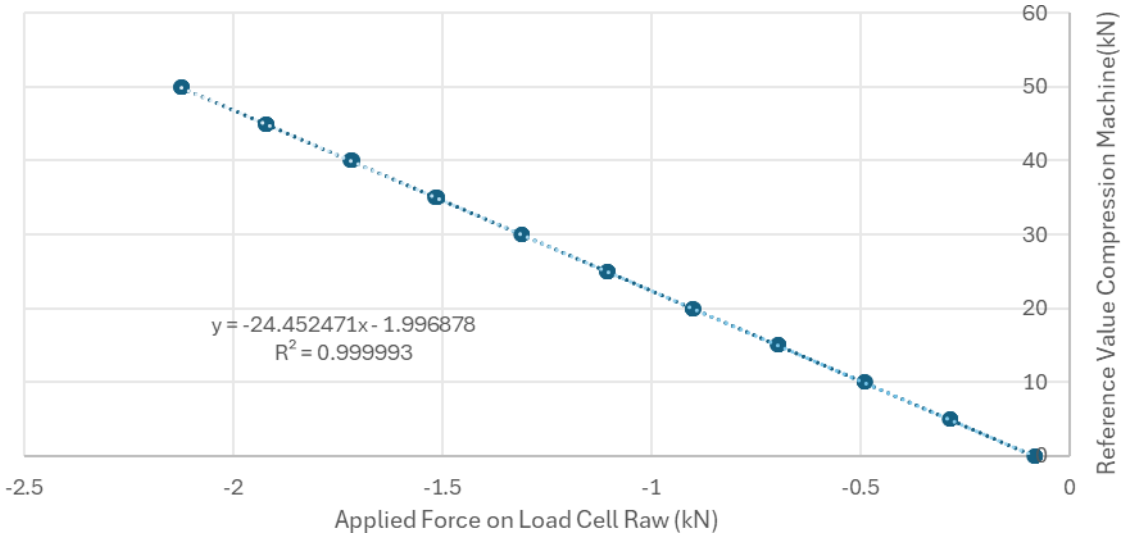

Figure 8.28 - A photo of the calibration equation of the Vertical Load Cell. A Root Mean Square of 0.999993 is achieved

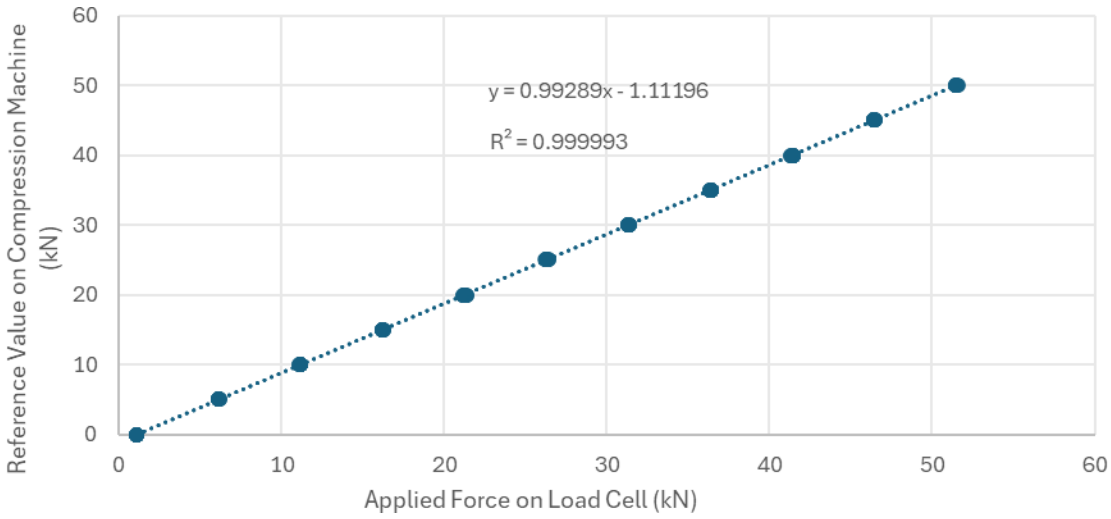

Figure 8.29 - A photo of the test where the calibration equation is verified. The gradient achieved is 0.99289. This showed how the calibration was done successfully